UNIVERSITY OF SOUTHAMPTON

FACULTY OF ENGINEERING, SCIENCE AND MATHEMATICS

School of Ocean and Earth Science

Observations and modelling of the variability of the Solent-Southampton Water estuarine system

by

Anne Levasseur

Thesis for the degree of Doctor of Philosophy

April 2008

UNIVERSITY OF SOUTHAMPTON

ABSTRACT

FACULTY OF ENGINEERING, SCIENCE AND MATHEMATICS
SCHOOL OF OCEAN AND EARTH SCIENCE

Doctor of Philosophy

OBSERVATIONS AND MODELLING OF THE VARIABILITY OF THE SOLENT-SOUTHAMPTON WATER ESTUARINE SYSTEM

by Anne Levasseur

Understanding the effect of physical forcing on estuarine functioning is of major importance to determine the rate of exchange of water, sediments, pollutants and nutrients between the continent and the ocean. The combination of numerical models and discrete datasets is used to describe and investigate processes of natural variability in the partially-mixed, non-turbid, macrotidal Solent-Southampton Water estuarine system (UK).

The estuarine circulation and the response of wind forcing is examined using a three dimensional, free surface, finite volume and finite element grid model. Results from short-term (three months) simulations have been compared against data (ADCP measurements, tidal elevations and salinity distributions) collected in spring 2001 in Southampton Water and the Solent. The model reproduces the unique tidal curve of Southampton Water and the partially-mixed conditions prevailing in the upper estuary. The contribution of the local wind forcing (wind intensity $\leq$ 12 m s^{-1}) to changes in water level is estimated to be up to 6 cm in Southampton Water in the model. The modelled salinity stratification varies over a semi-diurnal cycle with the highest stratification occuring at mid-ebb. Wind forcing is more efficient in altering stratification at ebb than flood.

The temporal and spatial variability of light attenuation is also investigated. Turbidity is demonstrated to be the major contribution to light attenuation using a time-series of discrete data collected in 2001, 2002 and 2003. A typical seasonal cycle of the coefficient of light attenuation is revealed, with a minimum in May-June and a maximum occuring in September-October. A second dataset of continuous measurements (10-minute interval) demonstrates the spring-neap modulation of the turbidity. The mouth of Southampton Water is more exposed to tidal mixing and therefore more turbid than the mid-estuary.

A five-compartment zero-dimensional pelagic ecosystem model including a sediment compartment has been developed to assess the impact of the variability of the light attenuation on the timing and the magnitude of the spring phytoplankton bloom. Using high resolution irradiance forcing and a constant coefficient of attenuation k set to the minimum May-June value, simulations compare well with discrete data of chlorophyll *a*, and less successfully with zooplankton and Dissolved Inorganic Nitrogen. A sensitivity analysis indicates that interranual variability in the phytoplankton spring bloom originates in order of importance from 1) parameterization of k 2) the variation of the seasonal cycle of surface irradiance 3) the intrinsic dynamics determined by the combination of fixed parameters of the ecosystem model.

Contents

List of Tables

List of Figures

DECLARATION OF AUTHORSHIP

I, Anne Levasseur, declare that the thesis entitled 'Observations and modelling of the variability of the Solent-Southampton Water estuarine system' and the work presented in the thesis are both my own, and have been generated by me as the result of my own original research. I confirm that:

- this work was done wholly or mainly while in candidature for a research degree at this University;
- where any part of this thesis has been previously been submitted for a degree or any other qualification at this University of any other institution, this has been clearly stated;
- where I have quoted from the work of others, the source is always given. With the exception of such quotations, this thesis is entirely my own work;
- I have acknowledged all main sources of help;
- where the thesis is based on work done by myself jointly with others, I have made clear what was done by others and what I have contributed myself;
- Parts of this work have been published before as:

  Levasseur A., Shi L., Wells N., Purdie D., Kelly-Gerreyn B. A three-dimensional hydrodynamic model of estuarine circulation with an application to Southampton Water, UK. *Estuarine, coastal and shelf science*, 2007, vol. 73, issue 3-4, pp 753-767.

Signed: Anne LEVASSEUR
Date: 14th August 2008

Graduate School of National Oceanography Centre, Southampton

This PhD dissertation by

Anne Levasseur

has been produced under the supervision of the following persons

Supervisors:

Dr. Duncan A. Purdie

Dr. Boris A. Kelly-Gerreyn

Chairs of Advisory Panel:

Prof. Andreas Oschlies

Prof. Harry Bryden

Member of Advisory Panel:

Dr. Neil C. Wells

Acknowledgements

I am most grateful to my supervisors Duncan Purdie and Boris Kelly-Gerreyn for their supervision, more specifically the planning of the experiments, careful proof-reading of the thesis draft, detailed comments on the results, encouragement to present my research in conferences, and all advice provided during the completion of this research project. Thanks to Neil Wells for his help on the analysis of the outputs from the hydrodynamic model, help in finding useful references and data, and comments on the research paper.

Lei Shi initiated the modelling work of this study area at the University of Southampton by developing the three-dimensional hydrodynamic model. I am grateful to Lei Shi for his help in getting started with the hydrodynamic model.

Many people from the department have been helpful at various stages of this project. I especially want to mention Peter Killworth for his encouragement during the initial stage of the first simulation with the hydrodynamic model, Joël Hirshi for the preparation of the upgrade report and talk, Cathy Lucas for her help on zooplankton data, Joanna Waniek for her help on the analysis of ADCP data, Harry Bryden for stimulating discussion on tides in Southampton, Andreas Oschlies for his feedback and modelling tips during my panel meeting, Ivan Haigh for his help in finding useful references, and Ben Ward who provided me with the numerical code of the genetic algorithm and helped me to use it.

Thanks to my fellow PhD students and my colleagues for support, friendship and matlab tips: Laure Grignon, Kirsty Edgar, Rebecca Bell, Phil Wallhead, Sarah Bennett, Chris Jeffery, Turky Al-Said, Hao Zuo, Yining Chen, Alice Lefebvre, Cédric Boulard, Sally Hunter, Sinhué Torres-Valdés, Anna Hickman, Jo Hopkins, Raquel Diez, Leyla Hazeem, Chris Smith-Duque, Clara Bolton, Richard Marsh, Jörg Frommlet, Aurélie Devez, Guillaume Charria and Myriam Glessmer.

Additional encouragement were coming for farther field than Southampton, many thanks to Laurence Kerrien, Pierre-André Kerrien, György Hetényi, Elsa Petrellezzi, Benoît Taisne, Maïté Depas, Natty Bounzeky, Jennyfer Miot and Olivier Favez.

Lastly, I thank my parents Claude and Elisabeth Levasseur and my brother Nicolas Levasseur who have encouraged me all the way.

This research project was supported by the University of Southampton.

Abbreviations

ADCP : Acoustic Doppler Current Profiler
BP : Before Present
CDOM : Colored Dissolved Organic Matter
CO_2 : Carbon Dioxide
DIN : Dissolved Inorganic Nitrogen
DW : Dry Weight
MNR : Mean Neap Range
MSR : Mean Spring Range
NAO : North Atlantic Oscillation
NTU : Nephelometric Turbidity Unit
NWNetley : North West Netley
PAR : Photosynthetically Active Radiation
POL CS3 : Proudman Oceanographic Laboratory Continental Shelf 3
SPM : Suspended Particulate Matter
SST : Sea Surface Temperature
TBT : Tributyl Tin
VOC : Volatile Organic Compound

Chapter 1

Introduction

1.1 General overview

Estuaries are the transition zone between rivers and coastal seas, where river water enriched with nutrients and particles of terrestrial origin is mixed with saline water from the adjacent ocean. Several definitions of estuaries exists and the three predominant classifications are based on topography, river flow or tidal action (Dyer, 1997). Estuaries are an important part of the coastal environment with a total of 18800 km^2 defined as estuarine habitat along the European coast bordering the Atlantic Ocean and the North Sea, the highest percentage (27.9 %) found in the U.K. (Davidson et al., 1991). Estuaries are generally short-lived features on geological time-scales. Most of them have been formed following the inundation of river valleys during the last transgression in the Holocene (between 17000 years and 6000 years BP) (Bokuniewicz, 1995). Both the addition of sediment by river inputs and hydrodynamic-induced erosion determines the shape of estuaries. Their morphology constantly evolves to adjust to those changes.

Estuarine waters are characterized by a very high salinity gradient horizontally. They constitute a very stressful environment for the ecosystem, but paradoxically they are one of the most productive areas of the world ocean due to the high nutrient concentrations (McLusky and Eliott, 2004). Numerous recreational and commercial fish species are estuary-dependent since the sheltered conditions and the high level of nutrients maximise the rate of survival of their juvenile stages (Le Pape et al., 2003). The intertidal areas are feeding grounds for migratory birds which can refuel and rest during their journey (Andrews, 1989).

River inputs, atmospheric forcing and tides are the main drivers of estuarine circulation. In turn variations in the physical environment determine the rate of

sediment accumulation and influence ecosystem functioning. These forcings interact together in a non-linear way and create a highly dynamic environment.

1.2 Time-scale of physical processes

Estuaries are affected by hydrodynamic processes ranging in time from minutes to seasons. Turbulence, waves and internal waves are phenomena of short duration, from seconds to minutes. Tides cause the cyclic variation in water level at the semi-diurnal, diurnal and fornightly timescale, with the most important contribution of the M2 tide imposing a 12.42 hour tidal cycle. Seasonal variations in river inputs generate yearly variation in stratification and horizontal gradients in salinity. Transient perturbations can modify the estuarine water circulation regulated by the periodic forcing generated by rivers and tides. For instance, at the scale of a day, occasional high levels of rainfall generates a brief spate of river flow with a time-lag of few days (Dyer, 1975). Atmospheric forcing (wind and change in atmospheric pressure) varies from hourly to daily time-scales in the case of storms.

The competition between turbulence and gravitational circulation driven by the horizontal density gradient determines the rate of exchange between the estuary and the coastal sea. Estuarine flushing rate is a critical parameter which describes the residence time of dissolved nutrients, chemical components, sediments and plankton in the estuary. It is therefore an important indicator of estuarine health, with a high flushing rate limiting accumulation of pollutants and the development of harmful algal blooms (Figueiras et al., 1994). Estuarine flushing has been directly related to species diversity, with higher flushing time being favorable to a higher number of phytoplankton species (Ferreira et al., 2005).

1.3 Impact of human activities

The catchments of most estuaries are densely populated: population densities in coastal regions are about three times higher than the global average (Small and Nicholls, 2003). Estuaries provide a sheltered area for large vessels to transport raw materials and finished products over long distances. Petrochemical industries and oil-refineries are common features along the coast of estuaries. As a result estuaries have been put under increasing pressure by human activities. The use of estuaries by human activities has modified estuarine habitat. The major effects include increase of sediment due to land erosion, overfishing, destruction of

wetlands, eutrophication problems, pollution, and changes in natural flow due to dams and dykes for flood protection (Wolanski, 2007). Eutrophication problems are related to the overenrichment of estuarine water by nutrient load originating from discharge of sewage, fertilisers and pollutants into the estuarine waters (Nixon, 1995). Elevated concentrations of Nitrogen and Phosphorus stimulate plant growth and induce perturbation between production and metabolism of organic matter in the coastal zone with important modifications on the ecosystem and the cycling of biogeochemical elements (Cloern, 2001). As a result eutrophicated waters are depleted in dissolved oxygen, leading to hypoxia and anoxia (Dissolved Oxygen concentration inferior to 2 mg L^{-1} and 0 mg L^{-1} respectively). A critical level of 1 mg L^{-1} of dissolved oxygen is necessary to the survival of benthic and some fish species (McLusky, 1999). Another effect of coastal eutrophication is the development of toxic and nuisance blooms associated with the rapid growth of opportunistic species of algae (Anderson et al., 2002).

In addition to these modifications related to the use of the coastal zone by human activities, changes due to human-induced global warming have been detected in the coastal ocean (Nicholls et al., 2007): Increases in carbon dioxide (CO_2) concentration, changes in Sea Surface Temperature (SST) and sea level, changes in storm intensity, frequency and track, alteration of wave climate and changes in river supply to the ocean.

Increases in atmospheric CO_2 concentration and the subsequent increase in CO_2 in the ocean reduce pH in sea water. Little information exists on its effects on estuaries, however it is likely to impact on biodiversity. Expected modifications include reduced carbonate calcification by marine fauna and flora and increased remineralization of nutrients and dissolution of carbonates minerals in sediments (Riebersell et al., 2000; Raven et al., 2005). For example, reduced calcification of oyster and mussel shells found in European estuaries are expected, thus slowing their growth rate (Gazeau et al., 2007).

Increases in SST causes isolation of nutrients or planktonic food to secondary producers and de-oxygenation events in enclosed waters, as a consequence of increased stratification. Another aspect is the enhancement of phytoplankton primary productivity and microbial processes such as nitrogen fixation and denitrification (Lomas et al., 2002). Increased species richness in fish has been observed to be correlated to temperature increase in the outer Severn estuary (Henderson, 2007). At a larger scale, observations indicate a change in the species distribution of zooplankton such as calanoid copepod species assemblage around

the UK related to a northward movement of warm-water species, and a decrease in the mean number of cold water species (Beaugrand, 2002).

Sea level rise is likely to cause geomorphological changes in estuaries, mainly landward retreat of the estuarine coastline (Crooks, 2004). Intertidal areas are expected to gradually reduce their extension, since man-made stuctures prevent the extension of saltmarshes landwards, a phenomenon referred to as 'coastal squeeze'. Reduced intertidal habitats can have a negative impact on the ecological community, which are mainly shrimps, shorebirds and fish. The impact of this long-term trend has been identified as changes in sediment patterns with accretion and erosion being modified, changes in water quality and modification in water circulation due to a change in tidal pattern.

Climate prediction suggests an increase in extreme events. In particular, changes in storm intensity and more frequent tidal surges are expected along the coast of the North Sea due to changes in wave conditions offshore (Wolf et al., 2002; Lozano et al., 2004; Hulme et al., 2006). Wind climate is related to the North Atlantic Oscillation (NAO), a climate mode of variability quantified by an index calculated as the difference between normalized sea-level pressures representatives of the Azores High and Icelandic Low. A positive NAO index is related to higher wind speeds over the north Atlantic and North sea (Tsimplis et al., 2006). A more frequent positive NAO index since 1973 has been observed (Lozano et al., 2004). Climate projections predict a more frequent positive average NAO value in the following century under the scenario of an increase of greenhouse emissions (Hulme et al., 2006).

Increased river supply to estuaries alters the residence time and intensifies stratification with important consequences for nutrient availability and phytoplankton production (Gillanders and Kingsford, 2002). Other effects include decrease in salinity, increase in vertical stratification and increase in nutrient inputs. Increased nutrient inputs may enhance eutrophication problems in estuaries.

1.4 The Solent-Southampton Water Estuary

1.4.1 Geographical Setting

The Solent estuarine system is the modern evolution of the protoriver Solent which was the main drainage area of the Hampshire basin in the Tertiary and Quaternary (Antoine et al., 2003). The 'Solent river' flowed eastwards and its

pathway was bounded southerly by the Purbeck-Wight chalk ridge (figure 1.1).

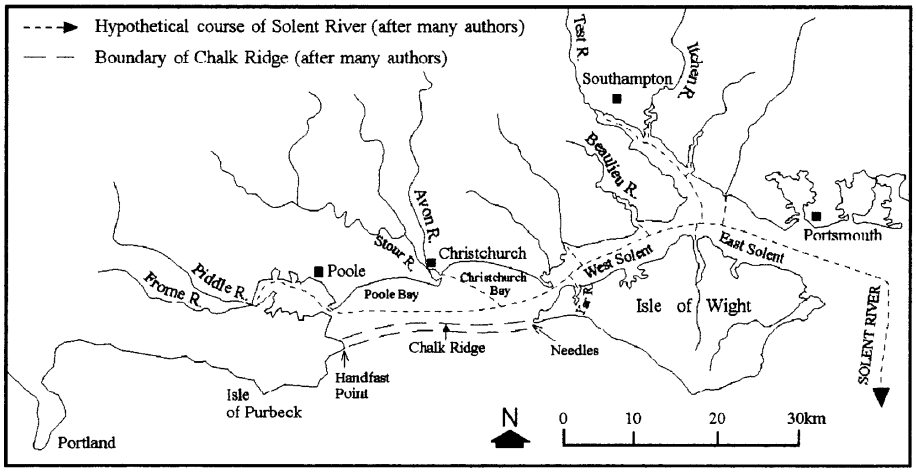

Figure 1.1: The Solent river pathway, Early to Mid-Quaternary. The coastline was approximately located offshore 20 km away from the present-day coastline. Redrawn from Velegrakis et al. (2000).

Before the Flandrian transgression (from 14000 to 7000 years BP), three southerly-flowing tributary rivers incised the chalk ridge. The lowest part of the Solent river was flooded during the Flandrian transgression and resulted first in the formation of Poole bay, followed by Christchurch Bay, and finally in the separation of the Isle of Wight from the mainland (Velegrakis et al., 1999a).

The present-day Solent estuarine system is the largest estuary on the UK south coast. The complex geometrical shape of the coast is made up of barrier spits (Hurst spits and Calshot spits), inter-tidal flats (the shoreline of Southampton Water and Lymington area) and saltmarshes (Porstmouth, Langstone and Chichester Harbours) as denoted on figure 1.2. From north to south, the estuary is defined by Southampton Water, a 2 km wide and 10.3 km long channel fed by three main tributaries: the Test river, Itchen river and Hamble river. The outer estuary separates around the Isle of Wight into the East Solent and the West Solent; both forming a seaway to the English Channel. A deep water channel in the inner estuary is maintained by dredging to 12 metres below the local chart datum. The coast in the Solent area is relatively sheltered from the effect of wave action by the Isle of Wight, and its orientation NW-SE protects it against south-westerly winds.

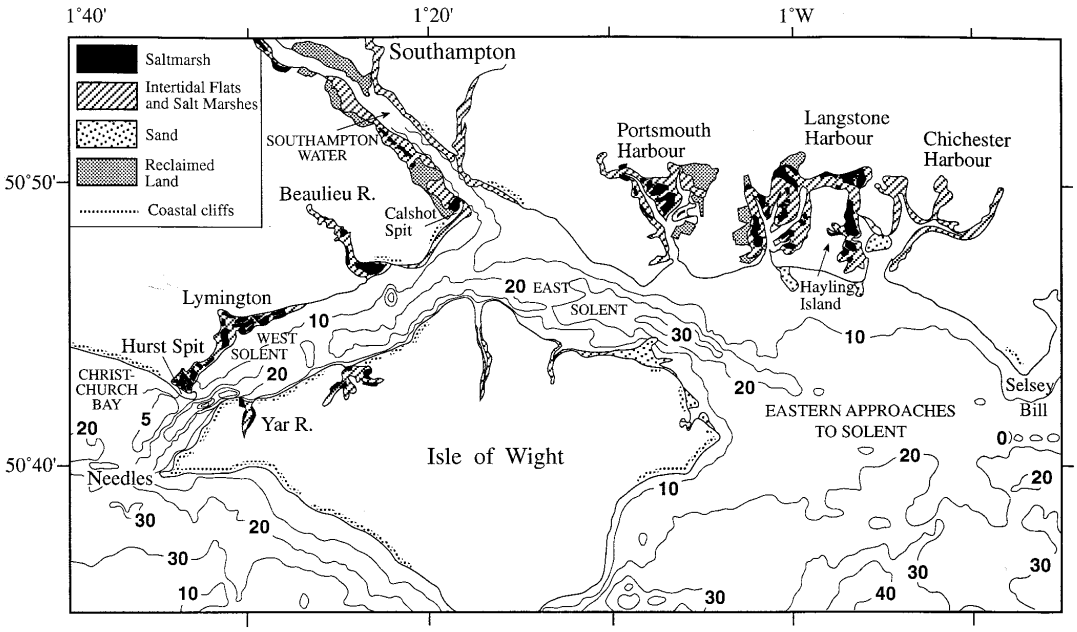

Figure 1.2: Map of the Solent estuarine system, which includes Southampton Water, Western Solent, Eastern Solent, Portsmouth Harbour, Langstone Harbour and Chichester Harbour. The contourlines indicate the bathymetry in metres. Redrawn from Velegrakis (2000).

1.4.2 Estuarine and coastal circulation

The tidal range varies from 1.5 to 3.5 meters in Southampton Water, which classifies it as a macrotidal estuary (Davies, 1964). An increase in the tidal range from west to east is observed in the Solent, due to the presence of the degenerate amphidromic point in Christchurch Bay. The tidal circulation is dominated by the M2 semi-diurnal harmonic constituent. The irregular geometrical shape and the narrow channel configuration result in the amplification of the shallow water tidal constituents M4 and M6. Consequently, this area is characterized by the unique tidal features of both the 'double high water' in the East Solent and Southampton Water, and the 'young flood stand' in the West Solent and Southampton Water (Webber, 1975, 1980). In Southampton Water the tidal cycle beginning at low water displays the following trend (figure 1.3): the flood phase is divided into two sub-phases, separated by the 'young flood stand' when the sea-level rise pauses, creating slack conditions throughout the water column. The maximum flooding rate occurs in the second sub-phase. High water slack conditions prevail for one or two hours due to 'the double high water', before the begining of the ebb phase. The distortion of the tidal wave causes the ebb dominance: ebb currents are faster

than flood currents because of the shorter duration of the ebb phase. As a result, tidal mixing is more intense during the ebb tide because of the higher velocity (Ribeiro et al., 2004) .

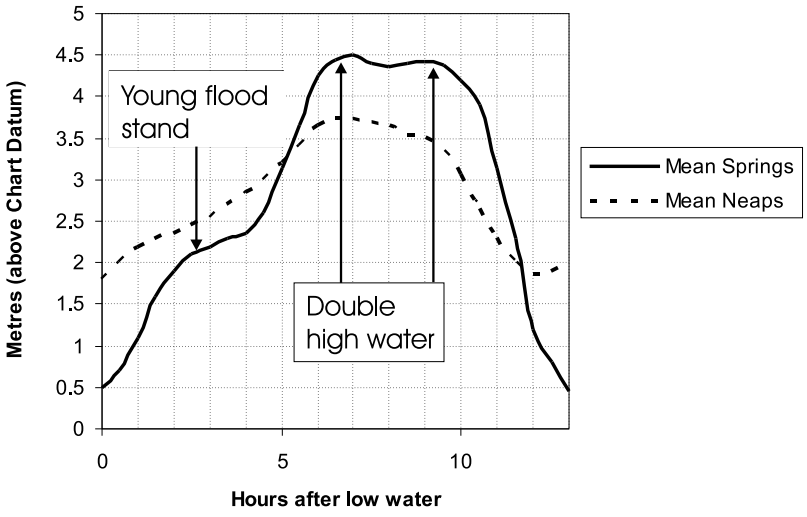

Figure 1.3: Rise and fall of the tide at Southampton, redrawn from Admiralty Charts.

The gravitational circulation in the estuary is caused by a contrast of density between the freshwater input which flows seawards and seawater flowing into the estuary. The resulting residual seaward current reaches typical values of 0.02-0.03 m s^{-1}, and near-bed residual currents of dense sea water of 0.01-0.02 m s^{-1} (Sharples, 2000) . This two-layered circulation induces a vertical stratification of the water column. Tidal mixing acts against the effect of the gravitational circulation by mixing the water column. Hence stratification and destratification conditions alternate in Southampton Water over one tidal cycle. At low water, stratified conditions dominate which are gradually altered during the flood phase. At high water, mixing conditions dominate and salinity exhibits an almost homogeneous vertical distribution which persists during the ebb phase. This typical variation in the semi-diurnal cycle varies spatially from the head to the mouth of the estuary. In the upper estuary (mouth of the Test and Itchen estuary), the proximity of the fresh water sources enhances stratification and large differences between bottom salinity and surface salinity are observed. In contrast, at the mouth of the estuary, there is a small difference between surface and bottom salinity. In addition, fluctuations in the degree of mixing over longer time scales

are generated by the seasonal cycle in the river flows and the fornightly variation in the tidal range.

Another aspect of the estuarine circulation is the transverse gradient in salinity distribution reported by Dyer (1973). Higher salinity values occur on the western side of Southampton Water, overcoming the effect of the Coriolis force which otherwise would promote higher salinity on the eastern side. This results in a landward flow in the central channel and a seaward flow on the shallower eastern side. The river inputs from the Itchen river and topographic effects have been suggested as the main reason for this horizontal variation (Dyer, 1973).

The residual circulation is an index of the water mass exchange and transport between the estuary and the coastal sea. Results from a three-dimensional modelling study of the circulation (Shi and Purdie, 2000) indicates spatial differences in the Solent estuarine system: the connection of Southampton Water with the Solent is characterized by a moderate water exchange of 20-25 % per tidal cycle.

The presence of a semi-permanent residual eddy at the mouth of the estuary generates an assymetry in the seaward and landward residual circulation in Southampton Water. A strong residual current (up to 0.13 m s^{-1}) flowing westwards in the Solent induces a net tidal water flux of 38 km^3 compared with a mean fresh water discharge from the rivers Test and Itchen of 0.52 km^3 over one M2 tidal cycle (Shi, 2000). On longer time scales, spring-neap variation in the tidal amplitude modulates the strength of the stratification which in turn induces spring-neap cyclic variation in the non-tidal residual circulation (Ribeiro et al., 2004).

Semi-permanent eddies have been observed in the eastern approaches to the Solent (Boxall and Robinson, 1987; Salomon and Breton, 1993; Boxall et al., 1995) generated by the interaction between the tidal flow and coastline irregularities. Wind direction has a non-negligible effect on their location (Salomon and Breton, 1993) .

Temperature in the Solent estuarine system is mainly affected by a seasonal cycle and negligible spatial variation occurs with a mean difference of 0.1 ^{o}C between Southampton Water and the Solent (Carr et al., 1980). Thermal stratification occurs locally and is caused by industrial outfalls, the intertidal mud flats and river waters which are warmer in summer and cooler in winter, and temporary meteorological effects like insolation and surface evaporation. The shallower area is more likely to be affected by the diurnal variation in solar heating.

1.4.3 Sediment distribution and transport

1.4.3.1 Seabed sediments and bedload transport

A general variation from east to west characterizes the sediment-type distribution in the Solent-Southampton Water estuary (figure 1.4). Medium and fine grained sediment (ranging from mud to mixed mud and sand) are found in Southampton Water and the eastern Solent while medium to coarse sediment (gravels with variable proportion of coarse sand) are found in the western Solent. Sediment distribution results from complex processes of transport, deposition and erosion determined by the nature of the sediment and the hydrodynamics.

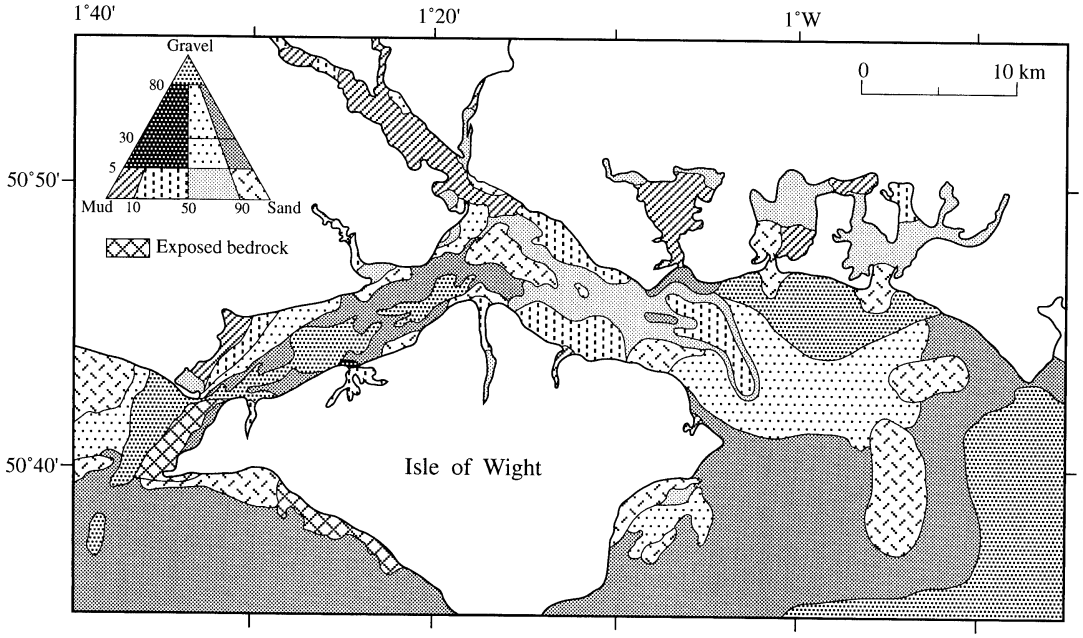

Figure 1.4: Sediment distribution in the Solent system. Lithology follows the classification of Folk. Redrawn from (Velegrakis, 2000)

In Southampton Water, a combination of river flow data, bathymetry and suspended matter concentrations has been used to estimate the sources and sinks of the sediment budget (Bray and Carter, 2003). River inputs contribute to 17000 m^3 per year, cliff erosion to 49000 m^3 per year, and marine inputs at the mouth of the estuary to 79000 m^3 per year respectively. The two main outputs are sediment dredging and seaward movement generated by bedload transport. Tidal currents are the dominant factor determining the rate of bedload transport. Due to the tidal assymetry, medium velocities at flood are associated with transport and resuspension of erodable fine sediment landwards, whereas higher tidal velocities at

ebb are associated with bedload transport of medium to coarse sediment seawards (Teles, 2003).

In the eastern approaches to the Solent, two deposition centres have been identified in the form of sand banks, and one of them is associated with the presence of a recirculation eddy. More generally, bedload transport tends to favour an eastward transport of unconsolidated sediments out of the west Solent (Paphitis et al., 2000; Teles, 2003).

Erosion processes dominate in the West Solent, whereas deposition occurs mainly in the East Solent and Southampton Water (Teles, 2003). Estuarine mixing appears as the main control of fine-grained sediment deposition (Algan and Clayton, 1994). Sedimentation of particle at the bottom occurs preferentially at slack water during the double high water and the young flood stand.

Sedimentation rate was evaluated to be 2-6 mm year^{-1} in Southampton Water by Dyer (1980). Reconstruction of sedimentation rate from a geochronological analysis suggests a sedimentation rate of 20 mm year^{-1} (starting from the 1950's) coincident with the expansion of the Fawley refinery which has lowered to 5 mm year^{-1} (starting from 1990). Variation in sedimentation rate is related to dredging of the estuary and the adjustment of the estuarine circulation and sedimentation to this new bathymetry (Croudace and Cundy, 1997).

1.4.3.2 Suspended sediment

Suspended particles in the estuary are composed of mineral grains and biogenic material. The mineral particles are mainly clay minerals and very fine grains of lithogenic materials (quartz and feldspar). The biogenic material is made up of mainly detritus and increases during periods of intense phytoplankton growth (O'Mahony and Weeks, 2000; Lloyd-Jones, 2002). SPM concentrations averaged over the whole water column are in the range of 10-50 mg L^{-1} in Southampton Water (O'Mahony and Weeks, 2000; Lloyd-Jones, 2002) and in the range of 2.4-30 mg L^{-1} in the Solent (Velegrakis et al., 1999b), which is low compared with other UK estuaries. Thus the Southampton-Solent estuary is classified as a non-turbid estuary, e.g. Uncles et al. (2002).

SPM concentrations are affected by semi-diurnal variation, as well as fortnightly variation and seasonal variation (Lauria, 1998; Velegrakis et al., 1999b; Lloyd-Jones, 2002). SPM levels have been reported to be lower during neap tide, because of the reduced level of tidal mixing, and higher concentrations are generally found at the bottom layer. Variations throughout a tidal cycle indicate

that SPM concentrations are lower at high tide and relatively homogeneous. At ebb, higher concentrations are generally found in the bottom layers with a factor of amplification of 4, as the result of the shear produced by the non-uniform vertical velocity gradients. At low water and flood, SPM concentrations gradually increase. Over longer timescales, seasonal variation in SPM concentrations are caused by the seasonal cycle in river flow with higher SPM concentration in winter.

1.4.4 Nutrient cycling and water quality

The three rivers Test, Itchen and Hamble are the major sources of nutrients and contaminants to the estuary. The proportion of chemical elements reaching the sea is determined by the water residence time and the production or remineralisation of elements by the other components of the food chain. The flushing rate based on the fresh water method in Southampton Water varies from 3 to 40 days (Lauria, 1998). Nitrogen and Phosphorus are essential components of the food chain and are present in estuarine water in both organic and inorganic forms, mainly as ammonium, urea and nitrate for nitrogen and phosphate for phosphorus.

Nitrate and silicate present a conservative dilution-like behaviour and their concentration reduces linearly as the salinity increases towards the mouth of the estuary (Phillips, 1980). By contrast, sewage effluents are the dominant source of ammonium, urea and phosphate concentration to Southampton Water, and local increases in the chemical species occur along the longitudinal salinity gradient (Phillips, 1980; Hydes and Wright, 1999). The concentrations of Nitrogen and Phosphorus components present an annual cycle. The seasonal fluctuation in river flow is the predominant cause of the seasonal cycle in nitrate concentration. By contrast, the seasonal cycles of ammonium, urea and phosphate are strongly influenced by the seasonal cycle of phytoplankton growth. A yearly rate of 74 % and 72.5 % of nitrate and ammonium inputs are exported from Southampton Water to the Solent, respectively (Torres-Valdés and Purdie, 2006).

On a long-term basis, an increase from 342 to 422 μmol m^{-3} and 308 to 393 μmol m^{-3} in nitrate concentration in the Test and Itchen River respectively has been reported from between the periods 1974-1979 and 1990-1997 (Hydes, 2000). Eutrophication occurs only locally in the harbours due to a limited exchange with the sea and generates an overgrowth of green algae and oxygen depletion (Lowthion et al., 1985; Montgomery et al., 1985; Taylor et al., 2001). Dissolved oxygen has been reported to be in the range of 80 % of saturation to 150 % during the productive season in Southampton Water (Phillips, 1980; Shi, 2000), which

maintains the estuary in the range of oxygen saturated or supersaturated conditions, despite the high nutrient inputs from the rivers.

Trace metal elements (cadmium, copper, iron, lead, nickel, and zinc) are discharged into the Solent through industrial (Fawley refinery) and urban wastes entering Southampton Water (Croudace and Cundy, 1997). They tend to contaminate plants and animals through the process of bioaccumulation. A low level of contamination is maintained in the water column of the Solent-Southampton Water estuary and the major trace elements do not exceed Environmental Quality Standard values (Statham, 2000). An exception is the case of tributyl tin (TBT), a chemical component contained in antifouling paint, toxic to marine organisms at high level. This component was banned in 1996 but high concentrations are still present locally. Concentration of trace metals in marine organisms in several indicator species has revealed a low level of contamination (Statham, 2000). Species diversity is lower on the western side of Southampton Water due to chemical stress generated by industrial activities (Lockwood, 1984; Savari et al., 1985). Recent observations indicate a gradient of detrimental impact (physiological and behavioural changes) to the benthic biota from the head to the mouth of the estuary, coincident with high concentration of trace metal elements in sediments (Galloway et al., 2004). Reconstruction of long-term heavy metal inputs to Southampton water from sediment cores is difficult due to both reworking and bioturbation prevailing in saltmarshes and the multiplicity of sources (Cundy et al., 1997).

Organic compounds can be found in three forms in Southampton Water estuary: plant litter, hydrocarbons of domestic and industrial origin which can be incorporated into bottom sediment or suspended particulate matter. Several chlorinated and halogenated organic compounds have been identified as major toxic pollutants. The most studied organic compounds in Southampton Water are Volatile Organic Compounds (VOC) with their spatial and temporal distribution documented by Bianchi (1994) and Bianchi and Varney (1998a). Over 70 individual VOC have been detected in the water column and 100 VOC detected in sediments, mostly aromatics, alkanes/alkenes and organohalogens, which reflects the importance of anthropogenic sources. Methane and dimethylsulphide are the dominant VOC found in sediments and are of natural sources. Phytoplankton blooms are an additional source of VOC. Compared with adsorption by particles, biodegradation within sediments and flushing, volatilisation is the major removal mechanisms of VOC (Bianchi and Varney, 1998b).

1.4.5 Pelagic biota

1.4.5.1 Phytoplankton community structure and dynamics

The Solent-Southampton Water estuary is typically a seasonally diatom-dominated system with diatoms ranging from 63 % to 71 % and dinoflagellate from 23% to 27 % of the total phytoplankton biomass (cell numbers) as documented for years 1996, 1997 and 1998 by the SOuthern NUtrient Survey (SONUS) sampling program (Hydes et al., 2001). Species diversity in terms of number of species recorded is greater in summer. A seasonal succession in species abundance of phytoplankton has been reported by field data and is reviewed for the years 1973-2002 by (Ali, 2003). In summer, alternation between mixed and non-mixed conditions over one tidal cycle allows the coexistence of both diatoms generally found in turbulent waters and dinoflagellates associated with more stratified waters (Lauria et al., 1998).

Phytoplankton blooms characterized by a seasonal peak of chlorophyll *a* concentration which lasts about two weeks usually occur in late spring and summer (Howard et al., 1995; Wright et al., 1997). A major bloom is usually initiated in spring, followed by other blooms until late summer in Southampton Water (O'Mahony and Weeks, 2000) and until early July in the outer estuary (Iriarte and Purdie, 1994). A shift from a diatom-dominated bloom in spring to a dinoflagellate-dominated bloom in summer is generally observed (Kifle, 1992; Hydes et al., 2001; Ali, 2003). Typical values of chlorophyll *a* concentration are in the range of 1-2 mg m^{-3} in winter rising to 10-40 mg m^{-3} in summer (Hydes et al., 2001). The annual rate of primary production for phytoplankton has been calculated to be 176 g C m^{-2} yr^{-1} with 81.7 % of this production in the >3 μm fraction of the phytoplankton, 12.1 % in the 1-3 μm fraction and 6.2 % in the < 1 μm fraction (Iriarte and Purdie, 1994). This indicates a lower rate of primary production compared with the mean value of 223.4 g C m^{-2} yr^{-1} calculated in European estuaries of the Atlantic and North Sea area (Gazeau et al., 2004).

Exceptional bloom events of the photosynthetic ciliate *Mesodinium rubrum* are frequently recorded during summer in Southampton Water, resulting in non-toxic red-tides. These blooms seem to be linked to an increase in temperature and water stability (Crawford et al., 1997). Blooms are mainly located in the inner estuary, in the upper reaches of Southampton Water (Garcia et al., 1993), and form patches (Kifle and Purdie, 1993). This species maintains a high growth rate by adopting a strategy to avoid dispersion offshore during ebb tides: organisms swim

downwards to avoid being transported seaward by surface tidal currents (Crawford and Purdie, 1992). Blooms of *Mesodinium rubrum* can create hypoxic conditions in deep water in the inner estuary (Crawford and Purdie, 1992; Kifle and Purdie, 1993; William, 1996).

1.4.5.2 Factors influencing phytoplankton blooms

Southampton Water is classified as a hypernutrified estuary with the Test river and Itchen River as the main source of nutrient load. Generally, no specific temporal correlation is found between chlorophyll *a* and nutrient concentration in agreement with the general concept that nutrient availibility is rarely the dominant limiting factor of phytoplankton growth in river-influenced marine environments (Cloern, 2001).

In Southampton Water spring blooms appear to be driven by light availability and tidal energy : A typical threshold of 380 W h m^{-2} d^{-1} for mean water column irradiance in the week prior to the bloom has been identified as the most favourable environment for the onset of a bloom event (Iriarte and Purdie, 2004; Holley and Hydes, 2002). Mean water column irradiance I is proportional to the mean daily quantity of photosynthetically active radiation at the surface I_o and inversely proportional to the attenuation coefficient k and the water column depth H (Cloern, 2001) :

$$I = \frac{I_0}{kH} \tag{1.1}$$

Attenuation of sea water varies temporally and spatially, making light availability for photosynthesis vary according to tidal energy (sediment resuspension), changes in river flow and self-shading by phytoplankton itself.

Differences in the nutrient ratio Si:N and Si:P can strongly influence species competition (Sommer, 1994) and may explain the seasonal variation in species composition of the blooms (*cf* a diatom bloom in spring and a dinoflagellate bloom in summer). Phosphorus appears to be the limiting factor of phytoplankton primary production in Southampton Water in summer (Hydes et al., 2001). Altisan (2006) suggests Si as a factor controlling phytoplankton succession with a shift to a flagellate-dominated phytoplankton community when Si is depleted and P as a factor controlling the size fraction of phytoplankton community.

Observations indicate that flagellate-dominated summer blooms occur preferably at neap tides (Crawford et al., 1997) whereas diatom-dominated spring blooms occur generally on spring tides (Iriarte and Purdie, 2004). A modelling study using Lagrangian particle tracking suggests that dinoflagellates using low

motility can actively maintain their vertical distribution irrespective of vertical mixing during neap tides and move upwards in order to benefit from higher light levels (Ross, 2004).

1.4.5.3 Zooplankton and secondary production

Zooplankton distribution, abundance and species have been documented by several authors (Zinger, 1989; Hirst, 1996; Muxagata, 2005). Zooplankton abundance increases significantly in March-April, with a peak of zooplankton biomass generally over two months in August-September, and the lowest abundance found in winter (Hirst, 1996). In terms of spatial variation, the highest zooplankton abundance is generally found in the upper estuary compared with the mid estuary and the mouth of Southampton water. Copepods form the largest community and in 2002 they represented an average of 66 % of the zooplankton biomass in terms of number of organisms; the four other major groups are Cirripedia, Polychaeta, Mollusca and Urochordata, with an annual average in abundance (number of organisms) of 18%, 5%, 5%, 4% respectively (Muxagata, 2005).

Zooplankton secondary production is of major importance in determining carbon flow and understanding the trophic web. Estimates of the production and a model of carbon flow in the pelagic domain of the Southampton estuary indicates a low level of energy flux (Hirst et al., 1999). An assessment based only on the dominant species, calanoid copepods, indicates that this species is a minor contributor of carbon production, possibly explained by seaward drift by flood currents, sea water hydrocarbon contents and high turbidity which may explain the grazing inefficiency of zooplankton (Hirst et al., 1999). A reassessement of carbon flux by Muxagata (2005) estimates a production of 268 mg m^{-3} $year^{-1}$ compared with an estimate of 5720 mg m^{-3} $year^{-1}$ for ciliate, 54925 mg C m^{-3} $year^{-1}$ bacteria and 15345 mg C m^{-3} $year^{-1}$ from primary production.

1.4.6 Benthos

The benthos of the Southampton-Solent estuary reflects the nature of the substratum and the salinity conditions. Due to the high range of habitat and hydrodynamic conditions found throughout the Southampton Water-Solent estuaries, numerous species of scavengers and feeding organisms are found. The various species (along with their common representatives) includes an assemblage of the phyla Porifera (sponges), Cnidaria (anemones), Annelida (polychaete worms), Crustacea (barnacles and crabs), Mollusca (gastropods and bivalves),

Polyzoa, Echinodermata and Tunicata as documented for the Solent and Southampton Water in Barnes et al. (1973). Complementary surveys carried out in other local areas since then have been integrated in recent reviews (Hiscock, 1998; Collins and Mallinson, 2000), where a distinction is made between the substratum. Mud-dominated area are soft sediments dominated by epifauna (burrowing species), more specifically polychaete worms and bivalves molluscs. Large areas are covered by the alien species slipper limpet *Crepidula fornicata* on the mud surface. Their dead shells are very abundant and even tend to modify the nature of the substratum, providing other species like small crabs with an ideal habitat. Patches of oyster are found locally in the eastern Solent. Sand-dominated substrata are generally very mobile but stable areas support a few species of burrowing worms, hermit crabs, gastropods and anemones where mixed sand-hard substrata are found. Stable gravel presents higher diversity with various species of anemones and worms. Rocky shores are very limited along the coast of the Solent-Southampton Water estuary and are colonized by green algae and a few species of crabs and sponges.

The seagrass *Spartina* grows extensively in saltmarshes, and supports a very rich ecosystem. Improvements of effluent quality from 1970 to 1996 has permitted a re-colonisation of denuded saltmarshes in Southampton Water by *Spartina* (May, 2000). Some areas of seagrass bed ecosystem are charaterized by a high degree of species richness with an inventory of 49 species of polychaetes worms, 29 species of amphipods and 15 species of gastropods for a saltmarsh on the Isle of Wight (Samiaji, 2001). The seagrass *Zostera marina* is a notable species of national conservation importance found patchily in intertidal areas along the north coast of the Isle of Wight.

The monitoring of the benthos is of particular importance in order to determine the level of pollution of the estuary, with few species being more tolerant to contaminants in the sediments. The western side of Southampton Water presents a low level of species diversity, due to the higher level of trace metals and hydrocarbons which generate stress for the organisms (Lockwood, 1984; Savari et al., 1985).

1.5 Objectives and thesis overview

As reviewed above, processes of natural variability in the Southampton Water estuary are complex due to the specific configuration and unique tidal circulation.

Observations of the different parts of the ecosystem and sediment transport have highlighted the major role played by the physical environment which is determined by three external forcings: tides, wind and river flow. To understand the processes of natural variability, and the interplay between the various components of the system, it is necessary to account for processes not in isolation, and a numerical model appears as a useful tool to determine impacts of physical forcing on water mass circulation, sediment transport and distribution, and ecosystem variability. One of the aims of this study was to achieve a better description of the impact of physical forcing on the variability of the Solent-Southampton Water estuary. The main objectives of this research were:

- to study the impact of local wind on patterns of water circulation.
- to characterize the processes of natural variability on light penetration in Southampton Water.
- to study the influence of the light variability on the spring phytoplankton blooms.

The original aim of the study was the development of a three-dimensional coupled ecosystem-hydrodynamic model, towards a better understanding of the functioning of the estuarine system. A full three dimensional coupled model has not been completed, however the initial stages of its development (validation of the separate components and applications to Southampton Water) are presented in this thesis. Chapter 1 is an introduction to the importance of physical forcing mechanisms in controlling the spatio-temporal variability of estuarine functioning and present the current knowledge of the Solent-Southampton Water estuary. Chapter 2 introduces a three-dimensional model of the estuarine circulation. In chapter 3, a new application of this model is presented, in order to evaluate the response of water mass circulation to wind forcing. Spatial and temporal changes in light penetration of the water column are investigated in chapter 4. The impact of the variability in attenuation on the timing and amplitude of phytoplankton blooms using an idealised model of the estuarine ecosystem is investigated in chapter 5.

Chapter 2

Description of the 3D numerical hydrodynamic model of estuarine circulation

2.1 Introduction

An unstructured, three-dimensional baroclinic model of estuarine circulation has been adapted from a preexisting 2D hydrodynamic model based on a finite element approach (Shi and Pangen, 1995; Shi, 1996). An unstructured model has the advantage of geometric flexibility to fit the coastline and local grid refinements suitable for simulating flow in the coastal area. Comparisons with finite-difference based models have demonstrated that unstructured grid based models combined with a finite volume or finite element model improve the results in both flow simulation around complex geometric features (Chen et al., 2003) and tidal predictions (Jones and Davies, 2005). The integrated form of the free-surface, primitive equations in sigma coordinates has been used, in order to design a numerical scheme which preserves mass conservation locally and globally. A dry-wet process is included to take into account the tidal flat extension at various stages of the ebb-flood cycle, as estuarine geometry plays a major role in tidal assymetry (Friedrichs and Aubrey, 1988). Freshwater inputs from the three main rivers feeding Southampton Water are included. In the following section, the details of the numerical code are given.

2.2 The governing equations

The system of equations used to simulate the fluid motion are the primitive equations expressed in cartesian coordinates (x increasing eastward, y increasing northward and z increasing downward) and following the hydrostatic assumption and Boussinesq approximation. H is the total water depth defined as $H(x,y,t) = h(x,y) + \xi(x,y,t)$ where ξ is the sea surface elevation:

$$\frac{\partial u}{\partial x} + \frac{\partial v}{\partial y} + \frac{\partial w}{\partial z} = 0 \tag{2.1}$$

$$\frac{du}{dt} - fv = -\frac{1}{\rho_o}\frac{\partial P}{\partial x} + \frac{\partial}{\partial z}(\nu\frac{\partial u}{\partial z}) + \epsilon(\frac{\partial^2 u}{\partial x^2} + \frac{\partial^2 u}{\partial y^2}) \tag{2.2}$$

$$\frac{dv}{dt} + fu = -\frac{1}{\rho_o}\frac{\partial P}{\partial y} + \frac{\partial}{\partial z}(\nu\frac{\partial v}{\partial z}) + \epsilon(\frac{\partial^2 v}{\partial x^2} + \frac{\partial^2 v}{\partial y^2}) \tag{2.3}$$

$$-\frac{1}{\rho}\frac{\partial P}{\partial z} + g = 0 \tag{2.4}$$

$$\frac{dS}{dt} = k(\frac{\partial^2 S}{\partial x^2} + \frac{\partial^2 S}{\partial y^2}) + \frac{\partial}{\partial z}(k_z\frac{\partial S}{\partial z}) \tag{2.5}$$

$$\rho = \rho(T,S) \tag{2.6}$$

u, v and w are the east-west component, south-north component and vertical component respectively, P is the pressure, the density ρ is a polynomial function of the temperature T and salinity S (Millero and Poisson, 1981), f is the Coriolis parameter at the latitude of the Solent with a value of 1.13 10^{-4} s^{-1}, ρ_o is the mean sea water density with a value of 1025 kg m^{-3} and g is the gravitational acceleration with a value of 9.81 ms^{-2}. In structured ocean models, the horizontal eddy viscosity is generally a function of the grid size and varies from 10 to 10^5 m^2 s^{-1}. Large values are associated with ocean models of very large horizontal grid size, and horizontal viscosity is necessary to account for the 3D eddy horizontal motion that is not resolved by horizontal advection only and vertical turbulence. Here the horizontal eddy viscosity ϵ is fixed at 10 m^2s^{-1} due to the high resolution of the grid in the estuary (see section 3.2). The horizontal diffusivity k is treated as a constant with a value of 1 m^2s^{-1}, in the range of values found for the horizontal dispersion coefficient by dye tracing experiments in Southampton Water and the Solent (Riddle and Lewis, 2000). Temperature is not modelled and is kept at its annual mean value of 12.5^oC in Southampton Water (data accessed through the Centre for Environment, Fisheries and Aquaculture Science http://www.cefas.co.uk). The turbulent coefficient ν and k_z are parameterized

with a turbulent closure scheme level 2.5 (Mellor and Yamada, 1974, 1982) as modified by Galperin et al. (1988).

The equation for turbulent energy q^2 and for the mixing length l are

$$\frac{dq^2}{dt} = \frac{\partial}{\partial z}(k_q \frac{\partial q^2}{\partial z}) + 2\nu[(\frac{\partial u}{\partial z})^2 + \frac{\partial u}{\partial z})^2] - \frac{2gk_z}{\rho_o}\frac{\partial \rho}{\partial z} - \frac{2q^3}{B_1 l} \tag{2.7}$$

$$\frac{dq^2 l}{dt} = \frac{\partial}{\partial z}(k_q \frac{\partial q^2 l}{\partial z}) + lE_1\nu[(\frac{\partial u}{\partial z})^2 + \frac{\partial u}{\partial z})^2] - \frac{lE_1 gk_z}{\rho_o}\frac{\partial \rho}{\partial z} - \frac{q^3}{B_1}W \tag{2.8}$$

The wall proximity function is defined as

$$W = 1 + E_2(\frac{l}{kL})^2 \tag{2.9}$$

$$\frac{1}{L} = \frac{1}{\xi + z} + \frac{1}{h - z} \tag{2.10}$$

The turbulent exchange coefficients ν, k_z and k_q are:

$$\nu = lqS_m \tag{2.11}$$

$$k_z = lqS_h \tag{2.12}$$

$$k_q = lqS_q \tag{2.13}$$

The stability function S_m, S_h and S_q depend on the function G_M and G_H:

$$G_M = \frac{l^2}{q^2}[(\frac{\partial u}{\partial z})^2 + (\frac{\partial v}{\partial z})^2] \tag{2.14}$$

$$G_H = \frac{l^2 g}{q^2 \rho_o}\frac{\partial \rho}{\partial z} = -\frac{l^2}{q^2}N^2 \tag{2.15}$$

$$N^2 = \frac{\partial}{\partial z}(\frac{-g(\rho - \rho_o)}{\rho_o}) \tag{2.16}$$

N^2 is the Brunt-Vaisala frequency. G_H has an upper bound of 0.023 for the case of unstable stratification and a lower bound of -0.28 for the case of stable stratification. An algebraic form of the mixing length l is used :

$$l = \frac{1}{\frac{1}{l_1} + \frac{1}{l_2}} \tag{2.17}$$

$$l_1 = K(z + \xi + z_o)\exp \beta_1 \sigma \tag{2.18}$$

$$l_2 = K(H - z + \xi + z_s) \tag{2.19}$$

where K is the von Karman constant ($K = 0.4$), β_1 is an empirical coefficient, H

is the total water depth, z_o is the bed roughness length and z_s is the surface roughness length. Then the stability functions become

$$S_M[6A_1A_2G_M] + S_H[1 - 3A_2B_2G_M - 12A1A2G_H] = A_2 \tag{2.20}$$

$$S[1 + 6A_1^2G_M - 9A_1A_2G_H] - S_H[12A_1^2G_H + 9G_H] = A_1(1 - 3C_1) \tag{2.21}$$

$$S_q = 0.20 \tag{2.22}$$

The empirical constants were assigned the values

$$(A_1, A_2, B_1, B_2, C_1) = (0.92, 0.74, 16.6, 10.1, 0.08) \tag{2.23}$$

$$(E_1, E_2) = (1.8, 1.33) \tag{2.24}$$

The value for the background turbulent coefficients ν and k_z is 1.34 10^{-5} m^2 s^{-1}. At the sea surface ($z = -\xi$), the boundary conditions are:

$$w = -\frac{d\xi}{dt} = -(\frac{\partial\xi}{\partial t} + u\frac{\partial\xi}{\partial x} + v\frac{\partial\xi}{\partial y}) \tag{2.25}$$

$$\frac{\partial(u,v)}{\partial z} = \frac{(\tau_{sx}, \tau_{sy})}{-\rho\nu} \tag{2.26}$$

$$P = Pa \tag{2.27}$$

$$\frac{\partial S}{\partial z} = 0 \tag{2.28}$$

$$q^2 l = 0 \tag{2.29}$$

$$q^2 = B_1^{\frac{2}{3}} u_{\tau_s} \tag{2.30}$$

The momentum flux (equation 2.26) is balanced by the wind stress $\tau_s = (\tau_{sx}, \tau_{sy})$ which is related to the wind speed W_{10} 10 meters above the ocean by $\tau_s = C_s\rho_{air}W_{10}|W_{10}|$.$u_{\tau_s}$ is the friction velocity equal to $(\frac{\tau_{sx}+\tau_{sy}}{\rho})^{\frac{1}{4}}$. ρ_{air} is the air density with a value of 1.2 kgm^{-3} and C_s is a drag coefficient equal to 0.0014 (non-dimensional). Pa is the atmospheric pressure at the sea surface. The net evaporation-precipitation surface flux is ignored, resulting in a zero salinity flux at the surface (equation 2.28).

At the sea bottom $z = h(x, y)$, the boundary conditions are:

$$w = \frac{dh}{dt} = u\frac{\partial h}{\partial x} + v\frac{\partial h}{\partial y} \tag{2.31}$$

$$\frac{\partial(u,v)}{\partial z} = \frac{(\tau_{bx}, \tau_{by})}{-\rho\nu} \tag{2.32}$$

$$\frac{\partial S}{\partial z} = 0 \tag{2.33}$$

$$q^2 l = 0 \tag{2.34}$$

$$q^2 = B_1^{\frac{2}{3}} u_{\tau_b} \tag{2.35}$$

The horizontal velocity is constrained by a quadratic stress law (equation 2.32) $\tau_b = (\tau_{bx}, \tau_{by}) = C_b \rho \sqrt{u_b^2 + v_b^2}(u_b, v_b)$ where (u_b,v_b) is the bed current. u_{τ_b} is the friction velocity equal to $(\frac{\tau_{bx}+\tau_{by}}{\rho})^{\frac{1}{4}}$. C_b is a drag coefficient and is defined by $C_b = \frac{K^2}{ln\frac{z_h}{z_o}}$ where K is the Von Karman constant, z_h is a reference height for the bed current and z_o is the bed roughness height. z_h is the distance from the bottom to the center of the lower layer. The variation of bed roughness height with seabed sediment type is assumed to be negligible and z_o is set to a background value of 0.0001 m.

A no-normal flow condition, a no slip condition and an impermeable boundary condition is applied to constrain the prognostic variables u, v and S along the coastline:

$$\frac{\partial (u, v)}{\partial n} = 0 \tag{2.36}$$

$$(u, v).\vec{n} = 0 \tag{2.37}$$

$$\frac{\partial S}{\partial x} n_x + \frac{\partial S}{\partial y} n_y = 0 \tag{2.38}$$

where $\vec{n} = (n_x, n_y)$ is the normal vector of the boundary line. At the open-ocean boundary, ξ is forced by a predicted water level ξ^* (see section 3.4).

2.3 Sigma coordinate transformation

A sigma coordinate transformation is applied over the vertical to modify the coordinate system from (x,y,z) to (x,y,σ) where σ is defined by:

$$\sigma = \frac{z + \xi}{H} = \frac{z + \xi}{h + \xi} \tag{2.39}$$

σ varies from 0 at the surface to 1 at the bottom. The derivatives of any variable $\phi(x, y, \sigma, t)$ in the new coordinate system are derived from the derivatives $\phi^*(x, y, z, t)$ in the old coordinate system using the following equations obtained after applying the chain rule:

$$\frac{\partial \phi^*}{\partial t} = \frac{\partial \phi}{\partial t} + \frac{\partial \phi}{\partial \sigma}\frac{\partial \sigma}{\partial t} = \frac{\partial \phi}{\partial t} - \frac{\partial \phi}{\partial \sigma}(\frac{\sigma}{H}\frac{\partial H}{\partial t} - \frac{1}{H}\frac{\partial \xi}{\partial t}) \tag{2.40}$$

$$\frac{\partial \phi^*}{\partial x} = \frac{\partial \phi}{\partial t} + \frac{\partial \phi}{\partial \sigma}\frac{\partial \sigma}{\partial x} = \frac{\partial \phi}{\partial x} - \frac{\partial \phi}{\partial \sigma}(\frac{\sigma}{H}\frac{\partial H}{\partial x} - \frac{1}{H}\frac{\partial \xi}{\partial x}) \tag{2.41}$$

$$\frac{\partial \phi^*}{\partial y} = \frac{\partial \phi}{\partial t} + \frac{\partial \phi}{\partial \sigma}\frac{\partial \sigma}{\partial y} = \frac{\partial \phi}{\partial y} - \frac{\partial \phi}{\partial \sigma}(\frac{\sigma}{H}\frac{\partial H}{\partial y} - \frac{1}{H}\frac{\partial \xi}{\partial y}) \tag{2.42}$$

$$\frac{\partial \phi^*}{\partial z} = \frac{\partial \phi}{\partial \sigma}\frac{\partial \sigma}{\partial z} = \frac{1}{H}\frac{\partial \phi}{\partial \sigma} \tag{2.43}$$

The transformed set of equations is then:

$$\frac{\partial \xi}{\partial t} + \frac{\partial Hu}{\partial x} + \frac{\partial Hv}{\partial y} + \frac{\partial w}{\partial \sigma} = 0 \tag{2.44}$$

$$\begin{aligned}\frac{\partial uH}{\partial t} + \frac{\partial u^2 H}{\partial x} + \frac{\partial uvH}{\partial y} + \frac{\partial uw}{\partial \sigma} - fvH = -gH\frac{\partial \xi}{\partial x} - \frac{gH^2}{\rho_o}\frac{\partial}{\partial x}(\int_0^\sigma \rho d\sigma) + \\ \frac{gH}{\rho_o}\frac{\partial H}{\partial x}\int_0^\sigma \sigma\frac{\partial \rho}{\partial \sigma}d\sigma + \frac{\partial}{\partial \sigma}(\frac{\nu}{H}\frac{\partial u}{\partial \sigma}) + F_u\end{aligned} \tag{2.45}$$

$$\begin{aligned}\frac{\partial vH}{\partial t} + \frac{\partial uvH}{\partial x} + \frac{\partial vvH}{\partial y} + \frac{\partial vw}{\partial \sigma} + fuH = -gH\frac{\partial \xi}{\partial y} - \frac{gH^2}{\rho_o}\frac{\partial}{\partial y}(\int_0^\sigma \rho d\sigma) + \\ \frac{gH}{\rho_o}\frac{\partial H}{\partial y}\int_0^\sigma \sigma\frac{\partial \rho}{\partial \sigma}d\sigma + \frac{\partial}{\partial \sigma}(\frac{\nu}{H}\frac{\partial v}{\partial \sigma}) + F_v\end{aligned} \tag{2.46}$$

$$\frac{\partial SH}{\partial t} + \frac{\partial SuH}{\partial x} + \frac{\partial SvH}{\partial y} + \frac{\partial Sw}{\partial \sigma} = \frac{\partial}{\partial \sigma}(\frac{k_z}{H}\frac{\partial S}{\partial \sigma}) + F_S \tag{2.47}$$

where the horizontal diffusion terms are approximated by

$$F_{u,v} = \epsilon H(\frac{\partial^2}{\partial x^2} + \frac{\partial^2}{\partial y^2}).(u, v) \tag{2.48}$$

$$F_S = kH(\frac{\partial^2 S}{\partial x^2} + \frac{\partial^2 S}{\partial y^2}) \tag{2.49}$$

The boundary conditions at the sea surface ($\sigma = 0$) are

$$-\rho\nu\frac{\partial(u, v)}{\partial \sigma} = H(\tau_{sx}, \tau_{sy}) \tag{2.50}$$

$$\frac{\partial S}{\partial \sigma} = 0 \tag{2.51}$$

$$w = 0 \tag{2.52}$$

$$q^2 l = 0 \tag{2.53}$$

$$q^2 = B_1^{\frac{2}{3}} u_{\tau_s} \tag{2.54}$$

and at the sea bottom ($\sigma = 1$)

$$-\rho\nu\frac{\partial(u,v)}{\partial\sigma} = H(\tau_{bx},\tau_{by}) \tag{2.55}$$

$$\frac{\partial S}{\partial\sigma} = 0 \tag{2.56}$$

$$w = 0 \tag{2.57}$$

$$q^2 l = 0 \tag{2.58}$$

$$q^2 = B_1^{\frac{2}{3}} u_{\tau_b} \tag{2.59}$$

A new formulation of the conservation of mass (equation 2.44) is obtained by integrating from surface to bottom and applying the boundary conditions 2.52 and 2.57 :

$$\frac{\partial\xi}{\partial t} + \frac{\partial}{\partial x}[H\int_0^1 u d\sigma] + \frac{\partial}{\partial y}[H\int_0^1 v d\sigma] = 0 \tag{2.60}$$

Equations 2.60, 2.45, 2.46, 2.47, form the basic set of equations for the prognostic variables ξ, u, v, S. The remaining diagnostic variables w, P and ρ are functions of the prognostic variables.

2.4 Fractional-step method

A fractional-step method allows the subdivision of the basic set of equations (equations 2.60, 2.45, 2.46, 2.47) into a succession of simplier one-dimensional or two-dimensional problems and the separate subsets of equations are therefore solved independantly with different numerical methods, as developped by Yanenko (1971).

First step $n\Delta t < t < (n+\frac{1}{3})\Delta t$:

$$\frac{\partial\xi}{\partial t} + \frac{\partial}{\partial x}[H\int_0^1 u d\sigma] + \frac{\partial}{\partial y}[H\int_0^1 v d\sigma] = 0 \tag{2.61}$$

$$\frac{1}{3}\frac{\partial\theta H}{\partial t} + \frac{\partial u\theta H}{\partial x} + \frac{\partial v\theta H}{\partial y} = 0 \tag{2.62}$$

Second step $(n+\frac{1}{3})\Delta t < t < (n+\frac{2}{3})\Delta t$:

$$\frac{1}{3}\frac{\partial\theta H}{\partial t} + \frac{\partial\theta w}{\partial\sigma} = 0 \tag{2.63}$$

Third step $(n+\frac{2}{3})\Delta t < t < (n+1)\Delta t$:

$$\frac{1}{3}\frac{\partial uH}{\partial t} - fvH = -gH\frac{\partial \xi}{\partial x} - \frac{gH^2}{\rho_o}\frac{\partial}{\partial x}(\int_0^\sigma \rho d\sigma) + \frac{gH}{\rho_o}\frac{\partial H}{\partial x}\int_0^\sigma \sigma\frac{\partial \rho}{\partial \sigma}d\sigma + \frac{\partial}{\partial \sigma}(\frac{\nu}{H}\frac{\partial u}{\partial \sigma}) + F_u \tag{2.64}$$

$$\frac{1}{3}\frac{\partial vH}{\partial t} + fuH = -gH\frac{\partial \xi}{\partial y} - \frac{gH^2}{\rho_o}\frac{\partial}{\partial y}(\int_0^\sigma \rho d\sigma) + \frac{gH}{\rho_o}\frac{\partial H}{\partial y}\int_0^\sigma \sigma\frac{\partial \rho}{\partial \sigma}d\sigma + \frac{\partial}{\partial \sigma}(\frac{\nu}{H}\frac{\partial v}{\partial \sigma}) + F_v \tag{2.65}$$

$$\frac{1}{3}\frac{\partial SH}{\partial t} = \frac{\partial}{\partial \sigma}(\frac{k_z}{H}\frac{\partial S}{\partial \sigma}) + F_S \tag{2.66}$$

where θ is (u, v, S). The first step computes the equations including only the horizontal advective term. The second step computes the equations including only the vertical advective term. In both steps the differential equation are approximated by a finite volume method. The third step computes the equations including all remaining terms using a Galerkin approximation and a recursive method.

2.5 Fractional-step method: first time-step

The water column is subdivided in m layers, and $m+1$ levels separated by an equivalent interval (figure 2.1). In the following section, the subscript k refers to the layer, i to the grid nodes, j to the neighbouring nodes (figure 2.2).

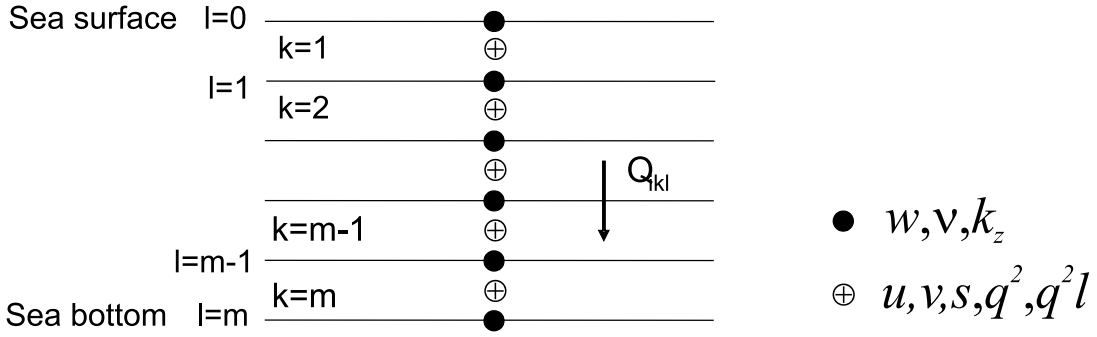

Figure 2.1: Position of the variables on the vertical grid

The variable θ is replaced by the vertically averaged variable over the layer k limited by the interlayer l and $l+1$:

$$\theta_k = \frac{1}{H}\int_{z_l}^{z_{l+1}} \theta dz = \frac{1}{H}\bar{\theta}_k \tag{2.67}$$

This leads to a new set of equations for the first time step (transformation of equations 2.61 and 2.62):

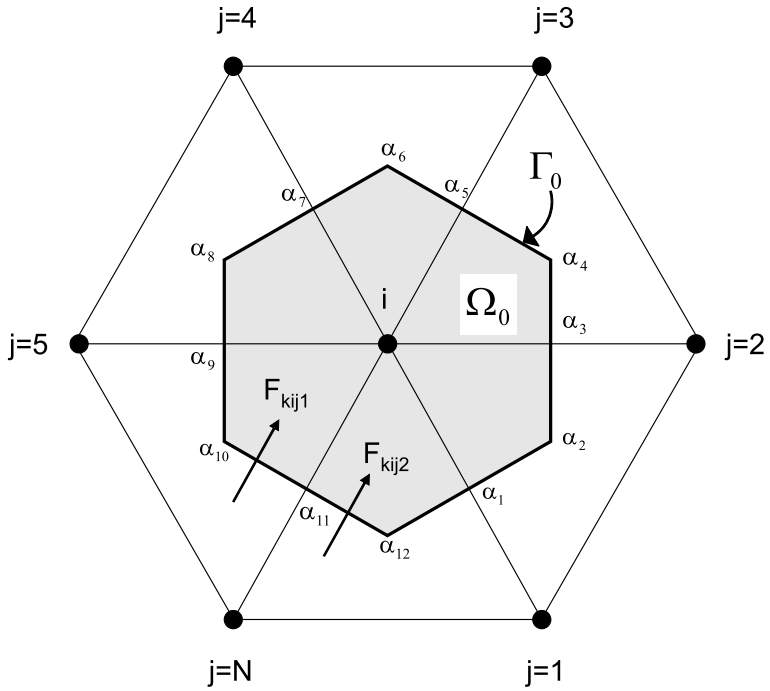

Figure 2.2: Position of the control area over the triangular elements

$$\frac{\partial \xi}{\partial t} + \sum_{k=1}^{m} \frac{\partial H \bar{u}_k}{\partial x} + \frac{\partial H \bar{v}_k}{\partial y} = 0 \tag{2.68}$$

$$\frac{1}{3}\frac{\partial \bar{\theta}}{\partial t} + \frac{\partial u_k \bar{\theta}}{\partial x} + \frac{\partial v_k \bar{\theta}}{\partial y} = 0 \tag{2.69}$$

The numerical procedure is described for equation 2.69 and applies identically to equations 2.68.

The equation is not solved directly, but is integrated over the control area Ω_0 surrounding the grid node i (figure 2.2) with boundary Γ_0 delimited by the baricenter of triangles (α with even indices) and mid-point of triangle edges (α with odd indices). Then we get:

$$\frac{1}{3}\frac{\partial}{\partial t}\int_{\Omega_0} \bar{\theta}_{ik} d\Omega + \int_{\Gamma_0} \bar{\theta}_{ik}(u_{ik}, v_{ik}).\vec{n} d\Gamma = 0 \tag{2.70}$$

The numerical solution for the integrated equation is provided by directly calculating the horizontal flow flux accross the common boundary Γ_0. A detailed description of the horizontal fluxes is given below (see figure 2.3):

$$\int_{\Gamma_0} (u_{ik}, v_{ik}).\vec{n} d\Gamma = \sum_{j=1}^{N} F_{ijk} \tag{2.71}$$

$\vec{n}$ is the vector normal to the contour Γ_0 (figure 2.3). Here F^n_{kij} is the horizontal

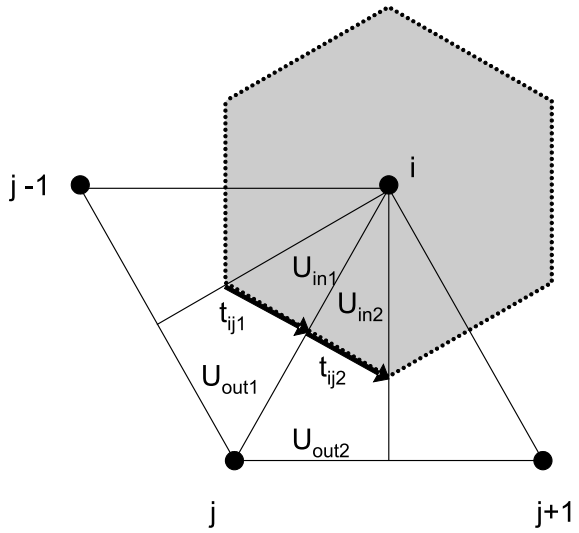

Figure 2.3: Position of the horizontal fluxes. Note that the norm of t_{ij1} and t_{ij2} are unequal when the triangles are not equilateral.

flux crossing the boundary Γ_0 and N is the total number of neighbouring nodes. Along the contour Γ_0, the unit tangential vector (tx, ty) is linked to the unit normal vector (n_x, n_y) by the relationship: $t_x = n_y$ and $ty = -n_x$. Therefore the term $(u_{ik}, v_{ik}).\vec{n}d\Gamma$ in equation 2.70 is calculated following the transformation $(u_{ik}n_x + v_{ik}n_y) = u_{ik}t_y - v_{ik}t_x$, where ($n_x$,$n_y$) is the normal vector of unit length and (tx, ty) is the unit tangential vector. In the following equations the subscript k is ommitted and the tangential vector (non unit) is rescaled to give the length of the segment to integrate over for simplification. The integration over the contour defining the control area is:

$$\sum_{j=1}^{N} F_{ij} = \sum_{j=1}^{N} F_{ij1} + F_{ij2} \tag{2.72}$$

$$F_{ij1} = u_{ij1}t_{ij1y} - v_{ij1}t_{ij1x} \tag{2.73}$$

$$F_{ij2} = u_{ij2}t_{ij2y} - v_{ij2}t_{ij2x} \tag{2.74}$$

where (t_{ij1x}, t_{ij1y}) is the non unit tangential vector of the contour line Γ_0. u_{ij1} and u_{ij2} are defined by a linear equation taking into account the nearest nodes (Shi, 1996):

$$u_{ij1} = \frac{1}{12}(5u_j + 5u_i + 2u_{j-1}) \tag{2.75}$$

$$u_{ij2} = \frac{1}{12}(5u_{j-1} + 5u_i + 2u_j) \tag{2.76}$$

Using an Euler scheme of temporal discretization forward in time and applying a

splitting of fluxes into negative and positive fluxes, equation 2.70 is finally :

$$\frac{\frac{1}{3}(\bar{\theta}_i^{n+\frac{1}{3}} - \bar{\theta}_i^n)\Omega_0}{\frac{1}{3}\Delta t} = \sum_{j=1}^{N} \frac{1}{2}[(F_{ij1}^n - |F_{ij1}^n|)\bar{\theta}_{out1} + (|F_{ij1}^n| - F_{ij1}^n)\bar{\theta}_{in1} + (F_{ij2}^n - |F_{ij2}^n|)\bar{\theta}_{out2} + (|F_{ij2}^n| - F_{ij2}^n)\bar{\theta}_{in2})] \tag{2.77}$$

θ_{out1} and θ_{out2} are the outflow quantities. θ_{in1} and θ_{in2} are the inflow quantities of control area Ω_0. For this application, we use a simple approximation : The outflow quantities from the control volume Ω_0 are θ_i and the inflow quantities are θ_j (Fig. 2.3). Equation 2.77 is therefore:

$$\frac{\frac{1}{3}(\bar{\theta}_i^{n+\frac{1}{3}} - \bar{\theta}_i^n)\Omega_0}{\frac{1}{3}\Delta t} = \sum_{j=1}^{N} \frac{1}{2}(F_{ij}^n - |F_{ij}^n|)\bar{\theta}_i^n + \frac{1}{2}(|F_{ij}^n| + F_{ij}^n)\bar{\theta}_j^n \tag{2.78}$$

No spurious extrema are generated if the solution of equation 2.78 satisfies:

$$min(\bar{\theta}_i^n, \bar{\theta}_j^n, j = 1, N) \leq \bar{\theta}_i^{n+\frac{1}{3}} \leq max(\bar{\theta}_i^n, \bar{\theta}_j^n, j = 1, N) \tag{2.79}$$

After the rearrangement of equation 2.78, the condition for monotonicity as described by equation 2.79 is :

$$1 + \frac{\sum_{j=1}^{N} \frac{1}{2}(F_{ij}^n - |F_{ij}^n|)\Delta t}{\Omega_0} \geq 0 \tag{2.80}$$

The stability condition for equation 2.78 gives finally an upper limit for the time step Δt :

$$\Delta t \leq \frac{-\Omega_0}{\sum_{j=1}^{N} \frac{1}{2}(F_{ij}^n - |F_{ij}^n|)} \tag{2.81}$$

2.6 Fractional-step method: second time-step

Following an identical procedure to the first time step, the equation describing the temporal evolution of the main vertically averaged variables $\bar{\theta}$ is :

$$\frac{1}{3}\frac{\partial \bar{\theta}}{\partial t} + \frac{\partial}{\partial \sigma}\frac{1}{H}\bar{\theta}w = 0 \tag{2.82}$$

where

$$w = \frac{1}{H}[\frac{\partial \xi}{\partial t}(1 - \sigma)] + \frac{\partial}{\partial x}\int_{\sigma}^{1} Hud\sigma + \frac{\partial}{\partial y}\int_{\sigma}^{1} Hvd\sigma \tag{2.83}$$

The equations are integrated over the control area Ω_0 surrounding grid node i at each level k :

$$\frac{1}{3}\frac{\partial}{\partial t}\int_{\Omega_0}\bar{\theta}_k d\Omega + \frac{\partial}{\partial \sigma}\frac{1}{H}\int_{\Gamma_0}\bar{\theta}_k w d\Gamma = 0 \tag{2.84}$$

The interlayer fluxes are approximated following (see figure 2.1):

$$\int_{\Gamma_0} w d\Gamma = Q_{i,k} \tag{2.85}$$

$$Q_{i,k} = \sum_{j=1}^{N}[(1-\sigma_k)\sum_{l=1}^{m}F_{ijl}] + \sum_{l\geq k}^{m}F_{ijl} \tag{2.86}$$

The spatial discretisation of the equations leads to :

$$\begin{aligned}\frac{\frac{1}{3}(\bar{\theta}_k^{n+\frac{2}{3}} - \bar{\theta}_k^{n+\frac{1}{3}})\Omega_0}{\frac{1}{3}\Delta t} = &-\frac{1}{2}\frac{(Q_{i,k+\frac{1}{2}} - |Q_{i,k+\frac{1}{2}}|)}{\delta H_{k+1}^{n+\frac{1}{3}}}\bar{\theta}_{k+1} - \frac{1}{2}\frac{(Q_{i,k+\frac{1}{2}} + |Q_{i,k+\frac{1}{2}}|)}{\delta H_{k}^{n+\frac{1}{3}}}\bar{\theta}_k + \\ &\frac{1}{2}\frac{(Q_{i,k-\frac{1}{2}} - |Q_{i,k-\frac{1}{2}}|)}{\delta H_{k}^{n+\frac{1}{3}}}\bar{\theta}_k + \frac{1}{2}\frac{(Q_{i,k-\frac{1}{2}} + |Q_{i,k-\frac{1}{2}}|)}{\delta H_{k-1}^{n+\frac{1}{3}}}\bar{\theta}_{k-1}\end{aligned} \tag{2.87}$$

where $\delta_k H$ is the new layer thickness inferred from the first step :

$$\delta H_k^{n+\frac{1}{3}} = \delta H_k^n - \Delta t\sum_{j=1}^{N}F_{ijk} \tag{2.88}$$

2.7 Fractional-step method: third time-step

The numerical procedure is described here for equation 2.64 and applies similarly to equations 2.65 and 2.66. Equation 2.64 can be described with two distinctive operators:

$$\frac{\partial u}{\partial t} + R_u = \frac{\partial}{\partial \sigma}(\frac{\nu}{H^2}\frac{\partial u}{\partial \sigma}) \tag{2.89}$$

where

$$R_u = -fv - gH\frac{\partial \xi}{\partial x} - \frac{gH^2}{\rho_o}\frac{\partial}{\partial x}(\int_0^\sigma \rho d\sigma) + \frac{gH}{\rho_o}\frac{\partial H}{\partial x}\int_0^\sigma \sigma\frac{\partial \rho}{\partial \sigma}d\sigma + F_u \tag{2.90}$$

The two operators are solved separately, which means the numerical discretisation for equation 2.89 is

$$u^*_{i,k} = u^n_{i,k} - \Delta t R^n_{u,(i,k)} \tag{2.91}$$

$$u^{n+1}_{i,k} = u^*_{i,k} + \frac{\Delta t}{{H_i}^2}\left(\left(\frac{\nu(k+\frac{1}{2})}{(\sigma_{k+\frac{1}{2}} - \sigma_{k-\frac{1}{2}})}\right)\frac{u^{n+1}_{i,k+1} - u^{n+1}_{i,k}}{\sigma_{k+1} - \sigma_k} - \left(\frac{\nu(k-\frac{1}{2})}{(\sigma_{k+\frac{1}{2}} - \sigma_{k-\frac{1}{2}})}\right)\frac{u^{n+1}_{i,k} - u^{n+1}_{i,k-1}}{\sigma_k - \sigma_{k-1}}\right) \tag{2.92}$$

Equation 2.91 is calculated with a Galerkin method (Wu and Chen, 1985). The transition velocity $u^*_{i,k}$ obtained is then used to solve equation 2.92 following a recursive method (Mellor, 2004, page 25).

2.8 Tidal flat wetting and drying procedure

Balzano (1998) classifies wetting drying schemes according to the following: 1) the criteria for a node to be wet or dry, 2) the computation of water depth between two adjacent cells and 3) the determination of the retention volume. The method used in this study excludes procedure 2) since all prognostic variables are calculated on vertices of the triangles, rather than on a Arakawa-C square grid. At each time step, model grid nodes are tested to determine if they are dry or wet. At ebb, a wet node becomes a dry node if its water depth falls below a predetermined minimum depth of 0.2 m. Computing stops at the wet node and the triangular elements adjacent to it are excluded from the computational domain. The sea surface elevation at the wet node is prescribed at its last value. At flood, a dry node becomes a wet node if the sea surface elevation at two adjacent nodes becomes higher than the prescribed sea surface elevation at the wet node. In this case the triangular element defined by the three nodes is reintegrated into the computational domain and computing restarted at the wet node. At this stage of the model development, no assessment of the volume or mass conservation performance of the wetting-drying scheme exists. However, a detailled investigation of the mass conservation of the numerical model is presented in Shi (2000) by comparing the flux of water entering the model domain and the flux of water going out of the model domain (in the case of the Solent-Southampton Water configuration). Over a 15-day model run and while implementing a constant flux of 24 $m^3\ s^{-1}$ of river flow inputs, a water output flux of 23.9208 $m^3\ s^{-1}$ is recorded at the open-boundary. This reveals the relatively good performance of the numerical model in conserving water volume.

2.9 River inputs

Fresh water discharge is added following a point source method. Freshwater inputs are simulated at a coastal node by introducing a flux of zero salinity in the top layer. To account for the change of water volume, the sigma layers are redefined. The velocity and salinity fields at the new mid-layer depth location are approximated by a piecewise linear interpolation. The momentum associated with the river discharge is assumed to be negligible as suggested by Kourafalou et al. (1996) .

Chapter 3

Modelling the circulation of the Solent-Southampton Water estuary: model validation and impact of wind forcing

3.1 Introduction

Previous numerical models of Southampton Water have mainly focused on describing circulation and mixing patterns in the estuary in either one or two dimensions. Wind generated mixing effects on the gravitational circulation have been tested with a one dimensional model (Ribeiro, 2004). Two dimensional models have been used to simulate salinity and velocity fields (Sylaios and Boxall, 1998), to examine water quality (Jones and Odd, 1995) and to investigate sediment transport but with no consideration of the gravitational circulation or wind forcing (Price and Townend, 2000; Teles, 2003).

Three-dimensional models provide a more realistic representation of the estuarine circulation and allow a more detailed investigation of stratification effects under the main forcing (river flow, wind stress at the sea surface and tides). Shi (2000) developped the three-dimensional hydrodynamic model presented in chapter 2 for the Solent-Southampton Water estuary and carried out a simulation for one year in 1998 made and compared it to data from Southampton Water only. In this chapter, results from 5 short-term simulations of three months in spring 2001 are compared against data available from the Solent -Southampton Water estuary,with each simulation varying in its forcing. The observations were

previously collected in Southampton Water and two tide gauge stations located in the eastern and western approaches to the Solent (figure 3.1). In addition, model runs are used to examine the role of a high-frequency (hourly) wind forcing on the sea surface slope and vertical stratification in the estuary.

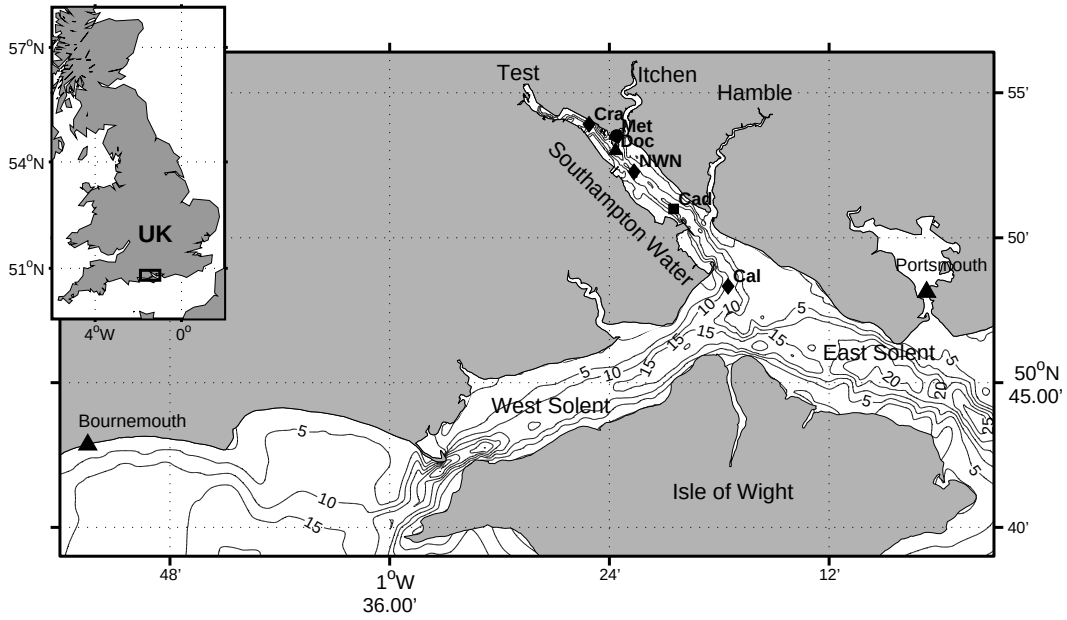

Figure 3.1: Black square indicates the location of velocity measurements at Cadland (Cad). Black triangles indicates tide gauge at Dockhead (Doc), Bournemouth (Bournemouth) and Portsmouth (Portsmouth). Black diamonds indicate salinity measurements at Cracknore (Cra), NWNetley (NWN), Calshot (Cal) navigation buoys. The black circle indicate the location of the meteorological station (Met). Coutourlines delineate the bathymetry in meters (0 m corresponds to the local Chart Datum in Southampton Water).

3.2 Model grid and bathymetry

The computational domain covers Southampton Water, the west and east Solent and it extends offshore to the coastal area around the Isle of Wight. The bathymetry was obtained from Admiralty Charts (figure 3.2). The grid consists of 1417 nodes forming a mesh of triangles with variable size ranging from 0.002 km^2 in the upper estuary to 7.89 km^2 along the open ocean boundary. The time-step is constrained by the grid geometry and intercell fluxes (equation 2.81). Here the

minimum grid size has been determined as a compromise between the need for high spatial resolution and the computational time. The vertical resolution is 5 layers of equal thicknesses.

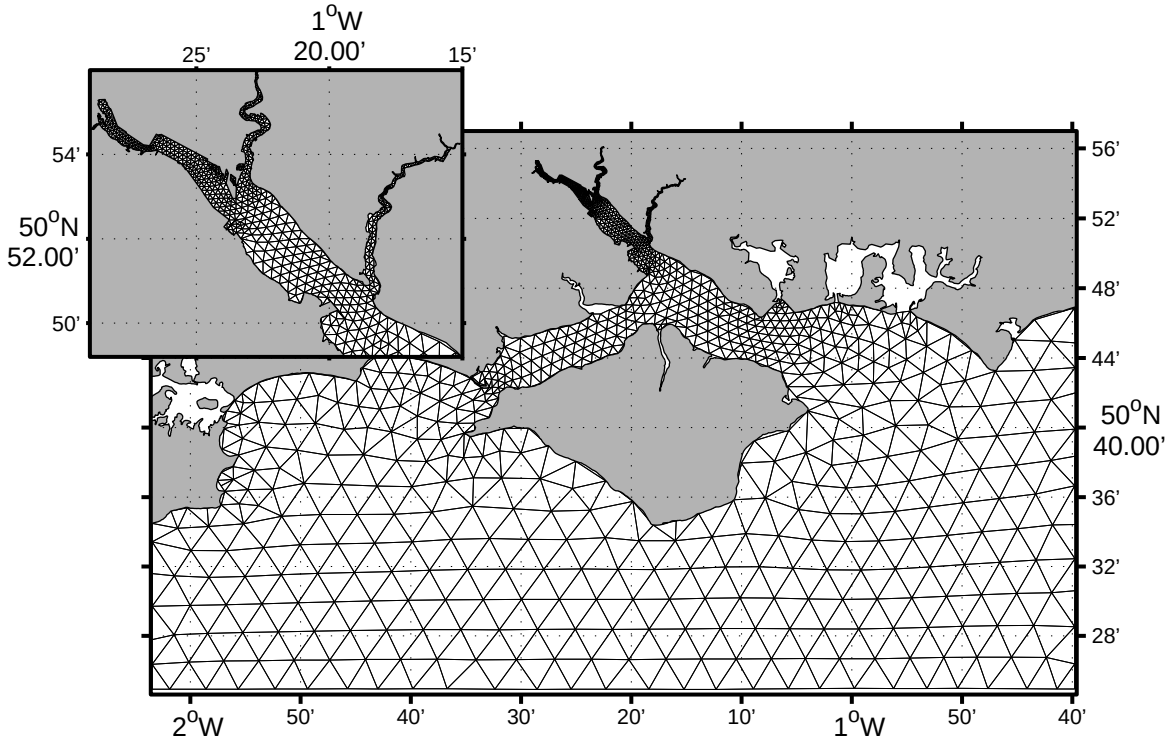

Figure 3.2: Model area and unstructured triangular mesh of the Solent estuarine system.

3.3 Meteorological forcing and river inputs

Hourly wind measurements at 25 metres above the Ordnance Survey British datum for 2001 are provided by a coastal meteorological station (see location on figure 3.1). These data have been reduced to the common reference height of 10 metres using the following relationship (Ribeiro, 2004):

$$W_{10} = \frac{W_{25}}{1.06} \tag{3.1}$$

where W_{25} is the wind recorded at 25 metres height. Wind stress derived from equation 2.26 is applied uniformly over the whole model domain.

River flow from the two main tributaries of Southampton Water are provided by the UK Environment Agency. Time-varying fresh water inputs from the Test and Itchen rivers are simulated with daily mean flow recorded 5 km and 7 km

upstream from the model domain respectively. The mean river flow rate from March to June 2001 was 12.2 ± 1.1 m^3 s^{-1} for the Itchen river and 26.5 ± 3.2 m^3 s^{-1} for the Test river. A constant annual mean river flow rate (0.47 m^3 s^{-1}) was used for the Hamble river due to limited access to data.

3.4 Open-ocean boundary conditions

Current and sea surface elevation within the model domain are driven by an elevation specified condition at the open-ocean boundary nodes. The sea surface elevation is prescribed as a sum of the contribution of n major tidal constituents:

$$\xi^*(x,y,t) = \sum_{i=1}^{n} A_i f_i cos(\omega_i t + (V_i + u_i) - g_i) \tag{3.2}$$

where ω_i is the angular speed, f_i and u_i are the nodal adjustment coefficients and phase angle respectively, A_i is the amplitude, g_i is the phase lag on Equilibrium Tide at Greenwich and V_i is the phase angle in the Equilibrium Tide. The amplitude, phase and angular speed of 26 tidal constituents are obtained from the regional Proudman Oceanographic Laboratory Continental Shelf 3 (POL CS3) model which has a resolution of 1/9 degree latitude and 1/6 degree longitude (Flather, 1978; Flather et al., 1979; Flather, 2000) . The dataset consists of the 5 diurnal constituents Q_1, O_1, P_1, S_1, K_1, the 10 semi-diurnal constituents $2N_2$, μ_2, N_2, ν_2, M_2, λ_2, L_2, T_2, S_2, K_2, and the 11 shallow-water constituents $3M_2S_2$, MNS_2, MSN_2, $2SM_2$, MN_4, M_4, MS_4, M_6, $2MS_6$, $2SM_6$, $2MN_6$. More specifically, the amplitude A_i and the phase e_i for each constituent vary in space and are derived at each boundary node from the coarser POL CS3 model by linear interpolation.

Salinity is prescribed at the open-ocean boundary as a constant value of 34.5 following previous measurements made in the eastern aproaches to the Solent (Kelly-Gerreyn et al., 2006). The open ocean boundary is implemented passively: at each open-ocean node, if fluxes yield a gain in water volume, water goes out of the cell. If fluxes indicate a decrease in water volume, water goes into the model domain with the prescribed value of 34.5 . This procedure ensures mass conservation at the boundary.

3.5 Model spin-up

The model simulation starts from 10th February 2001 12:00 with a time step of 5.5 s and lasts 90 days. This duration aims at investigating the variation in estuarine circulation at the time scale of the fornightly tidal cycle, the semi-diurnal tidal cycle, making use of existing long-term time-series of ADCP measurement, tidal data and salinity measurements from Southampton Water. The length of the simulation does not cover a complete year but is sufficiently long to test the response of the estuarine circulation to the decrease in salinity that occurs during a seasonal cycle in river flow. The model is initially at rest with the sea surface elevation set at 1.20 m. The initial salinity has a constant value of 34.5 over the whole domain. The initial value for the turbulent coefficients ν and k_z is the background value set at 1.34 10^{-5} m^2 s^{-1}. Model outputs are recorded every 495 seconds. 10 days of simulation takes 3 hours on a 3 GHz PC.

The model is expected to adjust to the initial conditions, before stabilising and reaching an equilibrium state when variation in the model solution varies periodically under the effect of the periodic forcing (tides and seasonal freshwater inflow from the rivers). The model reaches an equilibrium state with respect to the sea surface elevation and velocity field after two tidal cycles. The adjustment of the salinity field takes longer and is achieved when an estuarine plume characterized by a marked spatial and vertical salinity gradient forms (figure 3.3).

The stratification adjusts under the effect of the periodic tidal forcing at the boundary, the wind effect and the seasonal change in river flow. To address the question of the spin-up time necessary before analysing the results, the reference run A1 was compared with a simulation where the salinity is zero everywhere (run A2). Additional runs were made to decouple the effect of the wind and river flow on the equilibrium state (run B, C and D). The runs are described in table 3.1.

	A1	A2	B	C	D
river	**daily river flow**	**daily river flow**	constant river flow	**daily river flow**	constant river flow
wind	**hourly wind**	**hourly wind**	**hourly wind**	no wind	no wind
initial salinity	34.5	0	34.5	34.5	34.5

Table 3.1: List of model runs. Bold fonts are used to distinguish the temporally varying forcing.

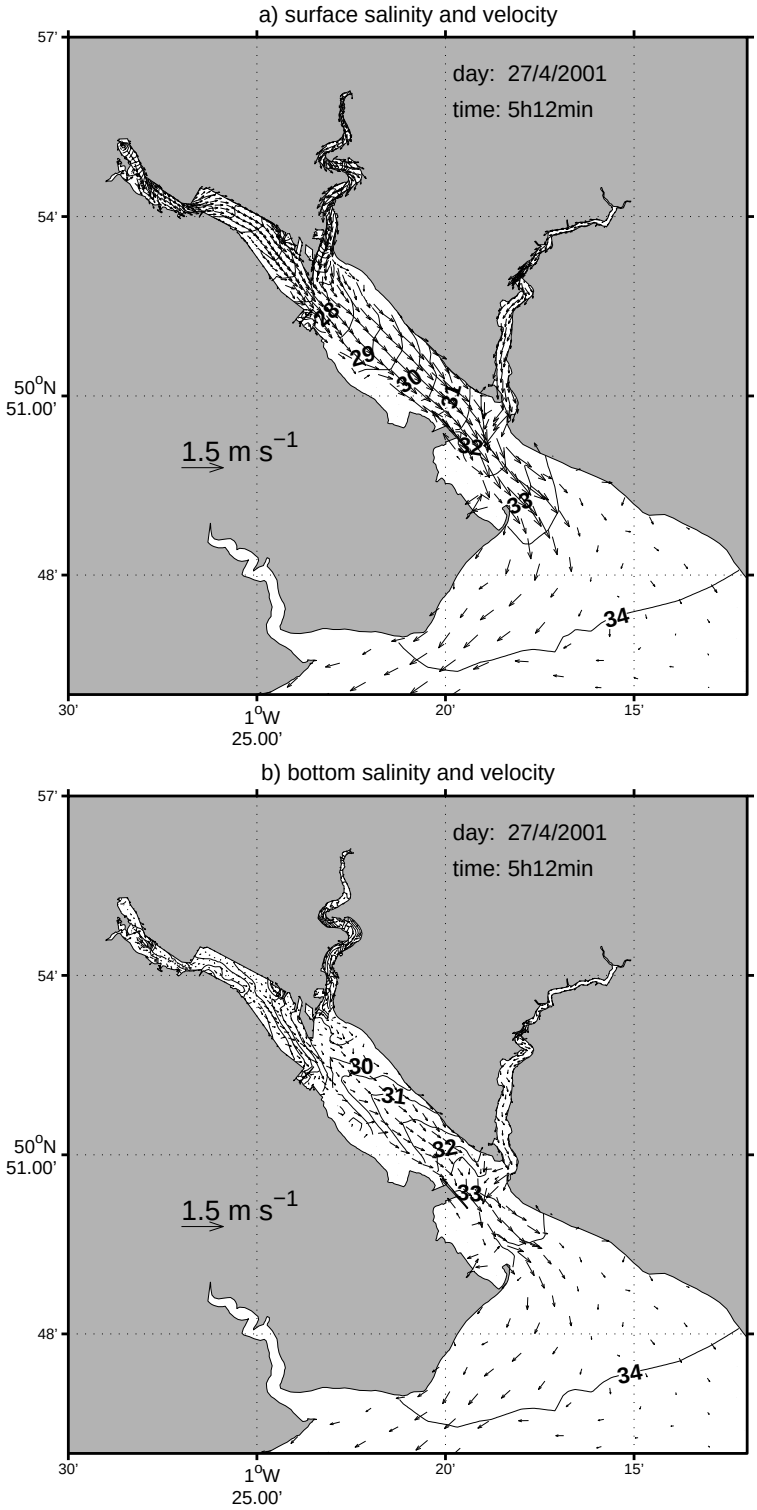

Figure 3.3: Illustration of the baroclinic structure (horizontal and vertical salinity gradient) by a snapshot of the salinity and velocity field for a) surface layer and b) bottom layer 1 hour 12min after first high tide of the day on 27th April 2001 (flood tide). Isocontour intervals are 0.5 salinity units with labels every one unit in the main channel of Southampton Water.

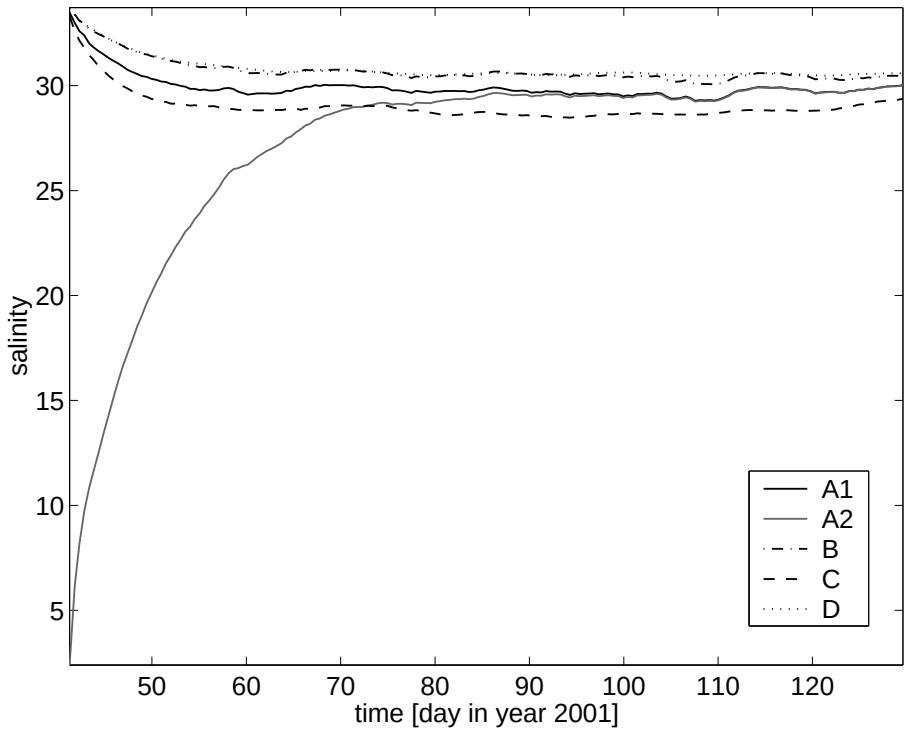

Figure 3.4: Volume averaged concentration of salt over the whole model domain. A low-pass filter with a cutoff of 12.5 hours was applied to remove fluctuation due to the M2 tidal cycle. Legend refers to the simulations carried out (table 3.1).

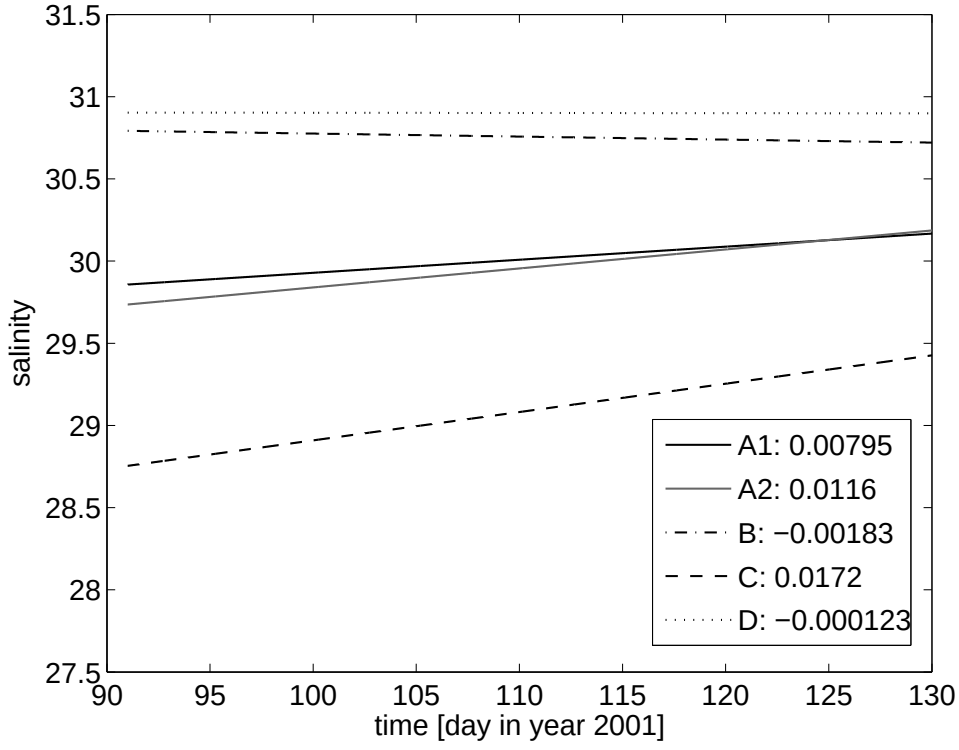

Figure 3.5: Trend line of the volume averaged salinity from day 90 to day 130 in year 2001. The legend gives the slope for each run.

The salt concentration was averaged over the whole domain as an indicator of the adjustment processes for stratification (figures 3.4 and 3.5). A linear trend is calculated from day 90 to day 130 to estimate variation in the equilibrium state. By comparing run A1 and run A2, the impact of the initial value for salt on the adjustment time of the stratification was examined. The model solution adjusts more rapidly in the case of run A1 where the initial value for salinity is higher, closer to the coastal ocean salinity which represents a higher volume of water in the model domain. The adjustment of the salinity field in run A2 occurs later and reaches an equilibrium after 50 days of simulation. In the following sections, it is therefore assumed that a spin-up time of 50 days was sufficient for the model to form an estuarine gradient starting from a constant initial value for salinity, and therefore model stratification was adjusted after day 90. In the following section, simulation A1 is considered for comparison with the observations.

Without wind forcing and under constant fresh water inputs (run D) the model equilibrium state only varies according to the tidal forcing imposed at the boundary and the slope from day 90 to day 130 of the simulation is -0.0001. Without wind forcing and with time-varying fresh water inputs (run C), the equilibrium state is fresher. This fresher state is explained by higher river flow rate in winter compared with the mean annual river flow rate. The trend from day 90 to day 130 is positive (0.017) since the input of fresh water is reduced as the simulation progresses in time towards summer.

When wind forcing is added (runs B and A1), significant changes occur in the equilibrium state compared with simulation without wind forcing (runs D and C respectively). In the case of a constant flux of fresh water from the main rivers (comparison between run B and D), wind forcing at the surface generates a minor deviation from the equilibrium state for salinity, the two curves diverging notably for a period of ten days starting at day 104 and day 120 (figure 3.4). The slope of the curve B is -0.0018 from day 90 to day 130 (figure 3.5). In the case of time-varying fresh water fluxes from the two main rivers (comparison between runs A1 and C), the wind forcing yields a saltier volume averaged salinity (an addition of 1 unit approximately). The slope of the volume averaged salinity in run A1 between day 90 and day 130 is 0.0079, indicating that wind forcing generates more exchange at the open-ocean boundary and therefore weakens the effect of the seasonal decrease in fresh water inputs.

3.6 Results for sea surface elevation

3.6.1 Dockhead

Figure 3.6a shows sea surface elevations at Dockhead (see location on figure 3.1) reproduced from day 113 to day 123 in 2001, representative of a successive spring-neap cycle. Model results describe the following trend: the tidal curve is dominated by the M2 tide which consists of a 12.42 hour tidal cycle. The tidal range varies from 2 m during neap tides to 4 m during spring tides. The slackening effect, known as the 'young flood stand' occuring 2.5 hours after the beginning of the flood, and the extension of high water, which produces the 'double high water', are simulated by the model. Overestimation of the young flood stand occurs at the transition from spring to neap (from day 115 to day 122) with the modelled tidal curve indicating a reversal of the circulation at mid flood. The other discrepancy is the overestimation of the double high water by up to 0.4 m (figure 3.6 b). The tidal prediction from Admiralty Tables shows a similar discrepancy with the observations (overestimation of the 'young flood stand and the double high water) but less pronunced than the model results (figure 3.6 a).

A tidal harmonic analysis was conducted over a 40 day time series, starting at day 90 in year 2001 using the T_TIDE tidal package (Pawlowicz et al., 2002). Results for the most significant constituents are compared with time series recorded by the tide gauge station at Dockhead and presented in table 3.2. The error between model and observations is given by the measure of the relative error defined as the absolute difference between modelled amplitude and observed amplitude divided by the observed amplitude, and expressed as a percentage of error. An error in amplitude between model and observations of less than 15 % is obtained for the semi-diurnal components N2, M2, S2, and the shallow-water components M6 and 2MS6.

The Mean Spring Range ($MSR = 2(M2 + S2)$) and the Mean Neap Range ($MNR = 2(M2 - S2)$) are derived from the amplitude of the two semi-diurnal constituents S2 and M2 . The modelled MSR and MNR reach an amplitude of 3.26 m and 1.46 m respectively compared with an observed amplitude of 3.7 m for the MSR and 1.85 m for the MNR. This gives a relative error of 12 % in the amplitude of the MSR and 16 % in the MNR. The amplitudes of the two most important shallow-water quarter-diurnal constituents M4 and MS4 are simulated with an error of less than 34 % , while the two most important sixth-diurnal constituents in amplitude 2MN6 and M6 are simulated with an error of less than 10%. The

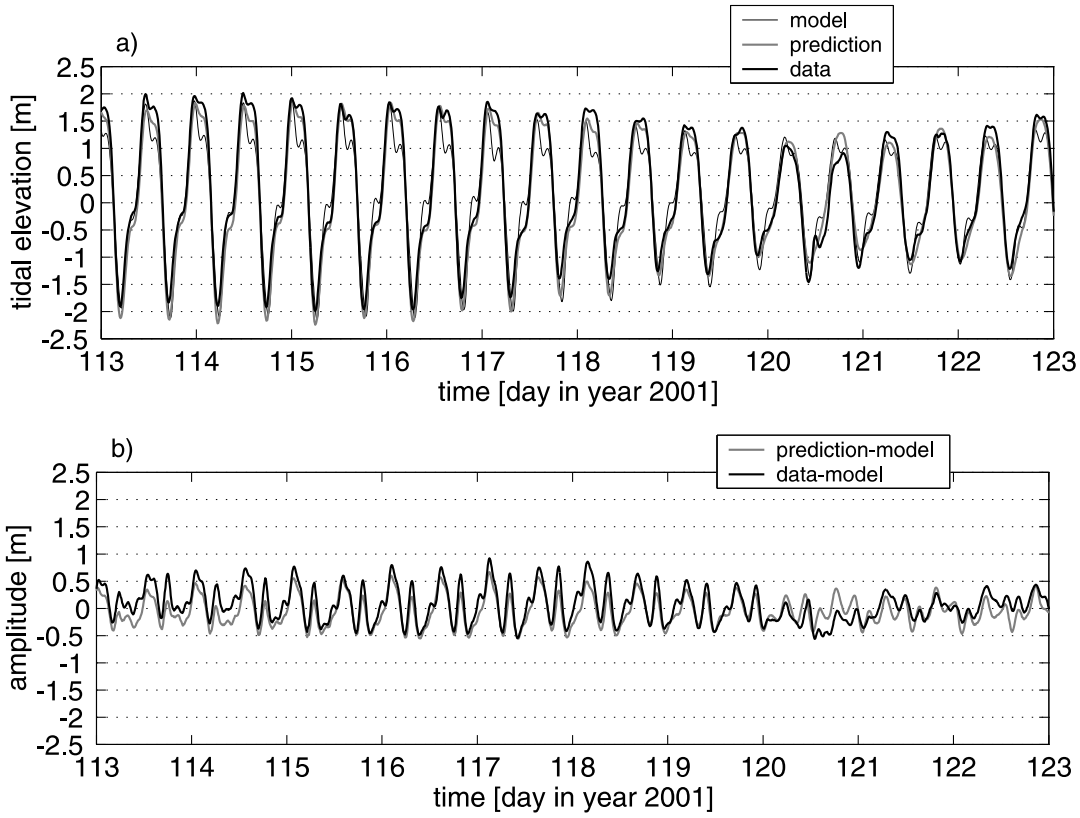

Figure 3.6: a) Sea surface elevation from model results (thin black line), from the Admiralty Tide Prediction (grey line) and from the tide gauge (black line) at Dockhead. b) The grey line indicates the difference between model results and the Admiralty Tide Prediction. The black line indicates the difference between tide gauge measurements and the model results.

tidal constituent	modelled amplitude [m]	observed amplitude [m]	amplitude error relative to observation	modelled phase [degree]	observed phase [degree]	phase difference [degree]
O1	0.45	0.4	14%	17.29	327.45	49.84
K1	0.04	0.08	51%	120.72	97.46	23.26
N2	0.20	0.23	15%	297.71	300.44	2.73
M2	1.18	1.36	13%	97.8	328.25	2.65
S2	0.45	0.49	1%	178.3	4.33	5.54
MN4	0.11	0.07	65%	25.02	358.33	26.69
M4	0.18	0.24	25%	59.37	28.68	30.69
MS4	0.12	0.19	34%	113.38	80.75	32.63
2MN6	0.15	0.07	126%	145.43	126.52	18.91
M6	0.18	0.16	6%	174.17	162.1	12.07
2MS6	0.22	0.22	7%	219.9	202.93	16.97

Table 3.2: Results of the harmonic analysis at Dockhead station.

major discrepancy in amplitude between model and observation (51-126 %) is obtained for the shallow-water constituent 2MN6, MN4 and the constituent K1.

The best accuracy for the phase is achieved in the simulation of the semi-diurnal constituents N2, M2 and S2 with a phase difference of less than 6 degrees between model and observations. The phase difference falls in the range of 26-32 degrees for the quarter-diurnal shallow water constituents MN4, M4 and MS4 and in the range of 12-18 degrees for the sixth-diurnal shallow-water constituents 2MN6, M6 and 2MS6. Least agreement is found for the diurnal constituents O1 and K1 with phase differences of 49.4 and 23.8 degrees respectively.

3.6.2 Portsmouth and Bournemouth

Two tide gauge stations are maintained by the Proudman Oceanographic Laboratory at Portsmouth and Bournemouth (see location on figure 3.1) and a long-term dataset was made available with a time resolution 15 minutes through the British Oceanographic Data Centre.

The tidal elevation profile obtained reproduces the tidal spatial variation. In the eastern part of the Solent, the tidal range is high (up to 4 m), and the 'young flood stand' and 'double high tide' is strongly attenuated (figure 3.7a) compared with Southampton Water (figure 3.6a). In the western part, the tidal range is lower (up to 2m) than in Southampton Water, however the distortion of the tidal wave is still marked with the presence of the 'double high water' and the 'young flood stand' (figure 3.8a). In the second high tide of day 120, a strong anomaly appears in the observation with a major difference between prediction and observations possibly due to meteorological effects. The model-data residual is in the range of 0.1 m to -0.5 m at Bournemouth (figure 3.8b) and in the range of -0.6 m to 0.4 m at Portsmouth (figure 3.7b). These residuals are lower than Dockhead (amplitude varying from -0.5m to 1m at Dockhead on figure 3.6b). At Portsmouth, this can be explained by a less distorted tidal curve and a better match of the 'young flood stand' and the extended high water. The variation in tidal residual varies during the course of the semi-diurnal period. At Bournemouth, the maximum difference between model and observed amplitude occurs during the second high tide at springs and during the first high tide at neaps (figure 3.7b). A better match is found at neaps, with the difference lower than at high tide at both stations.

Tidal harmonic analysis at Portsmouth is given in table 3.3. A good agreement between modelled and observed sea surface elevation is found for the semi-diurnal constituents (N2, M2 and S2) with an error of less than 10 % on the amplitude

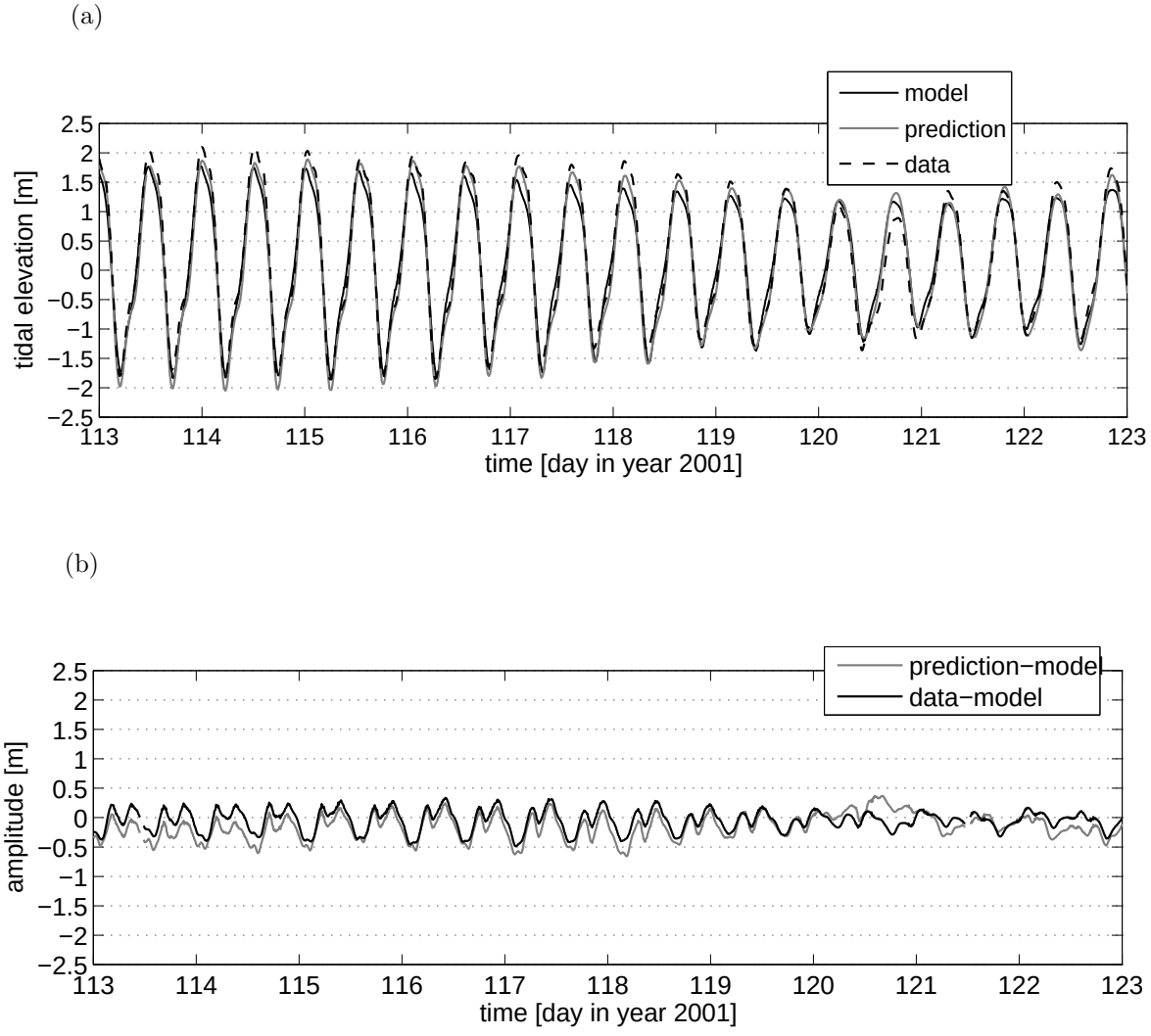

Figure 3.7: a) Sea surface elevation from model results (black line), from the Admiralty Tide Prediction (grey line) and from the tide gauge (dashed line) at Portsmouth. b) The grey line indicates the difference between model results and the Admiralty Tide Prediction. The black line indicates the difference between tide gauge measurements and the model results.

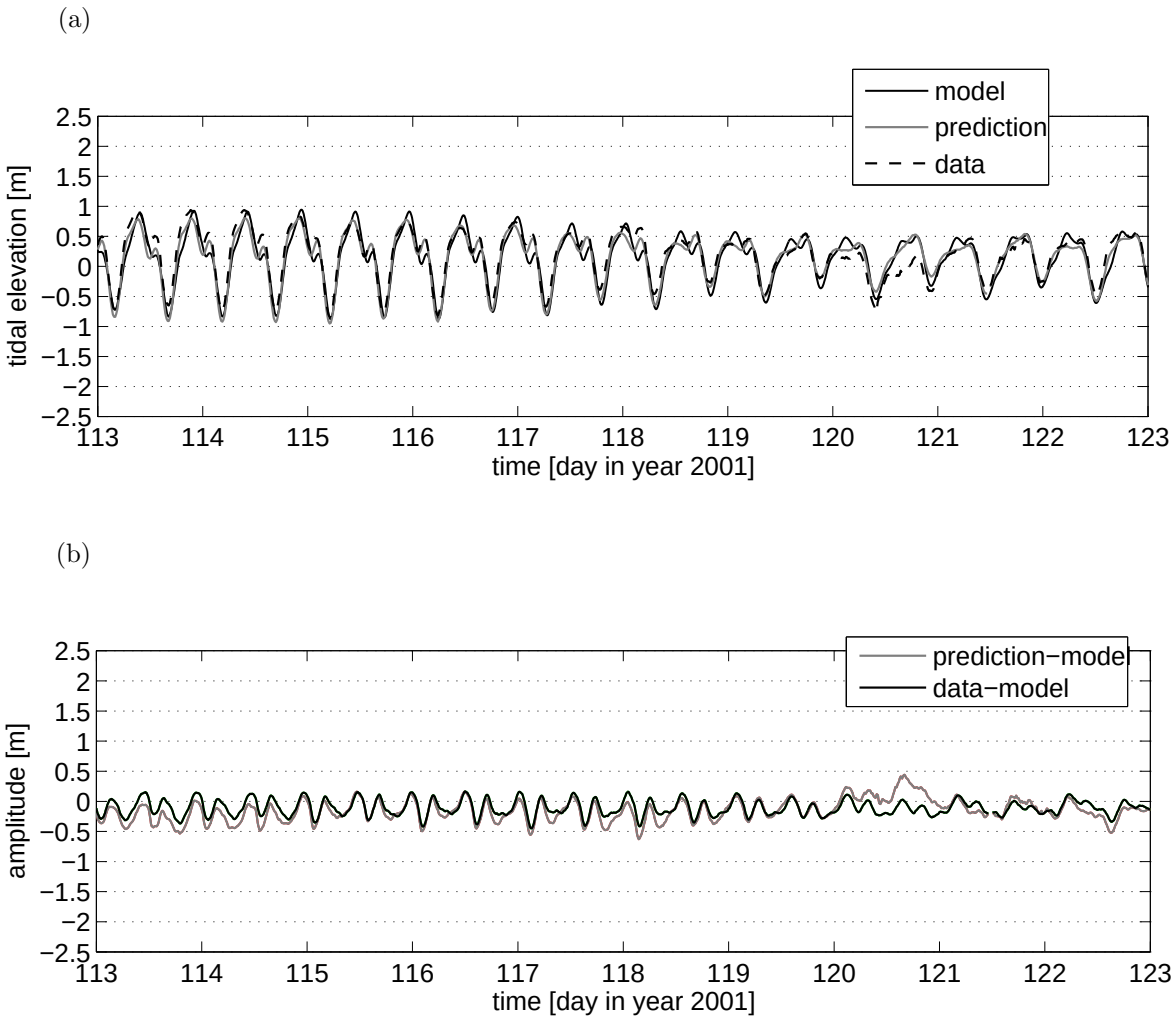

Figure 3.8: a) Sea surface elevation from model results (black line), from the Admiralty Tide Prediction (grey line) and from the tide gauge (dashed line) at Bournemouth. b) The grey line indicates the difference between model results and the Admiralty Tide Prediction. The black line indicates the difference between tide gauge measurements and the model results.

and less than 6 degrees in the phase. The highest errors are found for the diurnal (O1 and K1) and the quarter diurnal constituents (MN4, M4 and MS4) with errors in the amplitude above 10 % and a difference ranging from 11.4 to 31.2 degrees in the phase. The sixth diurnal constituents (2MN6, M6 and 2MS6) are affected by a poor agreement with data in the amplitude with an error higher than 20 %, however a good agreement is found in the phase with a phase difference of between 1.6 and 5.3 degrees.

tidal constituent	modelled amplitude [m]	observed amplitude [m]	amplitude error relative to observation	modelled phase [degree]	observed phase [degree]	phase difference [degree]
O1	0.045	0.02	78%	17.3	327.4	31.2
K1	0.036	0.065	44%	120.7	97.4	11.4
N2	0.204	0.223	8%	297.7	300.4	3.3
M2	1.24	1.293	10%	97.8	328.2	3.5
S2	0.48	0.417	5%	178.3	4.3	5.4
MN4	0.078	0.055	42%	25.0	358.3	25.4
M4	0.120	0.19	52%	59.4	28.7	20.7
MS4	0.08	0.14	42%	113.4	80.7	24.5
2MN6	0.075	0.049	52%	145.4	126.5	5.3
M6	0.084	0.105	20%	174.2	162.1	2.9
2MS6	0.102	0.146	30%	219.9	202.9	1.6

Table 3.3: Results of the harmonic analysis at Portsmouth tide gauge station.

tidal constituent	modelled amplitude [m]	observed amplitude [m]	amplitude error relative to observation	modelled phase [degree]	observed phase [degree]	phase difference [degree]
O1	0.054	0.034	58%	3.8	354.7	9.0
K1	0.044	0.067	34%	122.1	92.8	29.4
N2	0.1	0.099	2%	245.9	238.1	7.8
M2	0.48	0.4	20%	276.8	272.1	4.7
S2	0.23	0.20	7%	276.8	286.7	6.7
MN4	0.072	0.049	34%	13.8	343.81	30
M4	0.11	0.19	41%	52.2	22.48	30
MS4	0.07	0.13	47%	108.34	70.1	38.2
2MN6	0.072	0.033	103%	93.9	49.2	44.7
M6	0.080	0.07	22%	141.3	85.3	56.0
2MS6	0.022	0.081	75%	195.8	120.02	75.9

Table 3.4: Results of the harmonic analysis at the Bournemouth tide gauge station.

The tidal harmonic analysis at Bournemouth (table 3.4) gives similar results

with the best agreement between model and data obtained for the semi-diurnal components (N2,M2 and S2). A large error, ranging from 22 % to 106 % in the amplitude and ranging from 9 degrees to 75.9 degrees is obtained for the diurnal component (O1, K1), the quarter-diurnal components (MN4, M4 and MS4) and the sixth diurnal components (2MN6, M6 and 2MS6).

The highest errors in amplitude and phase are generally found at Bournemouth, compared with Portsmouth. For instance, the error on the amplitude of the M2 constituents is 10 % at Porsmouth compared with 20 % at Bournemouth.

3.7 Results for current velocity

Modelled velocity profiles were compared with observations made in Southampton Water (Cadlands, figure 3.1) in 2001 at springs (figure 3.9a) and at neaps (figure 3.10a). Tidal velocity reaches a higher magnitude during ebb than flood due to the tidal asymmetry which causes the flood to last longer than ebb, as described earlier (section 1.4.2). The maximum ebb current occurs in the surface layer up to 0.7 m s^{-1} on springs (figure 3.9a) and up to 0.5 m s^{-1} on neaps (figure 3.10a). The velocity field on spring tides is twice the magnitude during neap tides. The slack conditions of the young flood stand affect homogeneously the whole water column during spring tides, while at neaps the slack conditions affect mostly the surface water and the bottom layer and last longer. No flow reversal occurs at the 'young flood stand'. The maximum flood velocity occurs at mid-depth with a value of 0.4 m s^{-1} at springs (figure 3.9a) and 0.3 m s^{-1} at neaps (figure 3.10a).

A comparison has been made with measurements recorded by a four beam 1200kHz RD Instruments Acoustic Dopler Current Profiler (ADCP) moored at Cadland (figure 3.9b , figure 3.9c, figure 3.10 and figure 3.10). The vertical resolution is 0.25 m and the sampling rate 4 minutes. A separation has been made between surface and bottom current. For ADCP data, the surface current is the current 0.75 m below the surface and the bottom current is an average from the deepest current measurement at 1.5 m above the seabed up to the mid-depth measurements. The root mean square of the difference between modelled and measured velocity is 0.25 m s^{-1} at the surface (figure 3.9b) and 0.20 m s^{-1} at the bottom during spring tides (figure 3.9c). A better match is obtained during neap tides with a root mean square of the difference of 0.09 m s^{-1} at the surface (figure 3.10b) and 0.1 m s^{-1} at the bottom (figure 3.10c) respectively.

During flood both observations and models indicate a homogeneous profile with

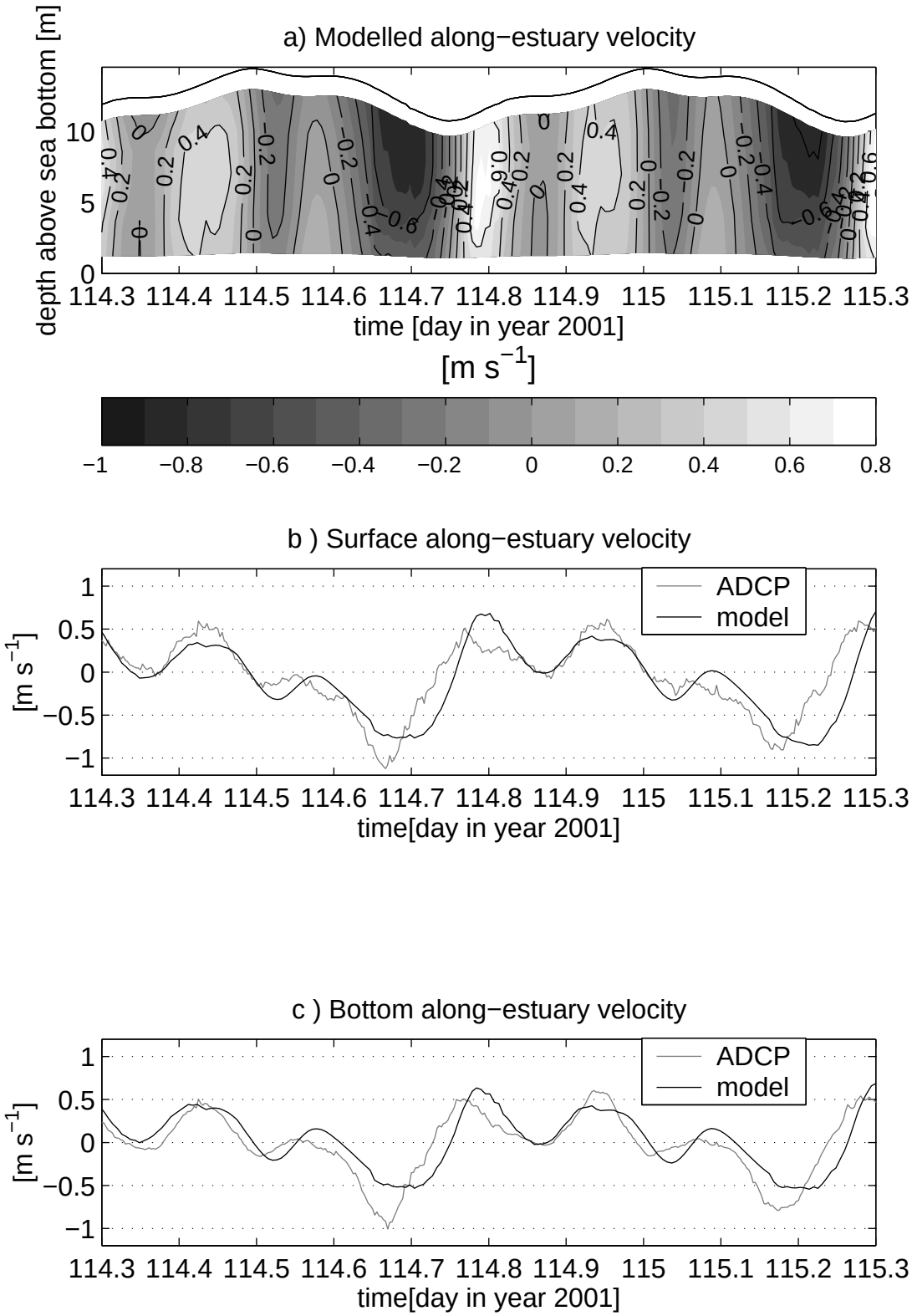

Figure 3.9: Along-estuary velocity at Cadland on spring tides. a) Vertical profile of modelled velocity. Isocontour intervals are labelled every 0.2 m s^{-1}. Variation in the modelled water depth is indicated with the black line. b) Surface velocity (grey line) and surface modelled velocity (black line). c) Bottom ADCP velocity (grey line) and bottom modelled velocity (black line).

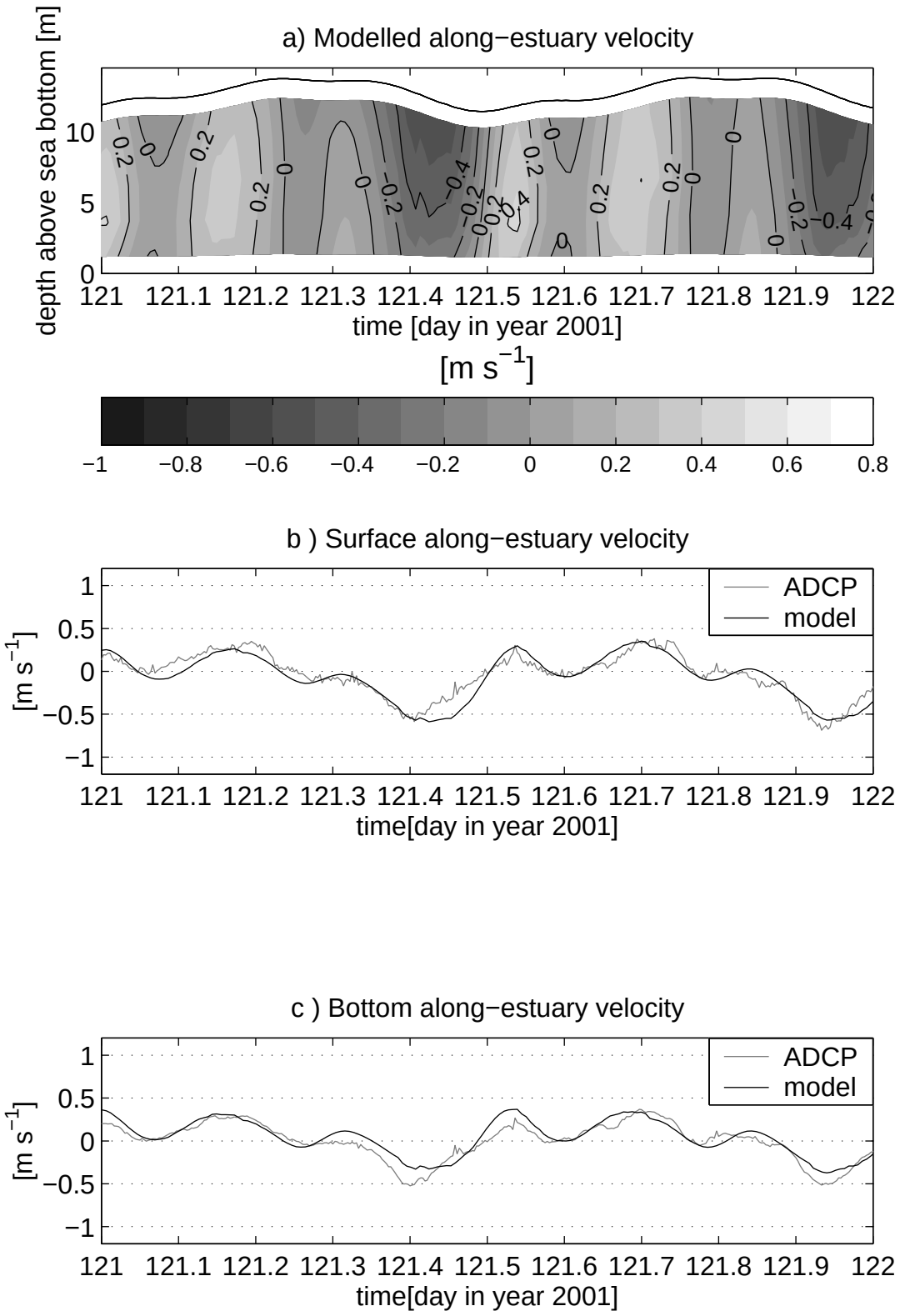

Figure 3.10: Along-estuary velocity at Cadland on neap tides. a) Vertical profile of modelled velocity. Isocontour intervals are labelled every 0.2m.s^{-1}. Variation in the modelled water depth is indicated with the black line. b) Surface velocity (grey line) and surface modelled velocity (black line). c) Bottom ADCP velocity (grey line) and bottom modelled velocity (black line).

similar velocities at the bottom and the surface. The maximum observed value is 0.5 m s^{-1} on spring tides (figure 3.9b and figure 3.9c) and 0.25 m s^{-1} on neap tides (figures 3.10b and 3.10c). During the first phase of the flood at spring (figure 3.9b and c), a difference in phase between modelled velocity and observed velocity suggests an error in the prediction of the phase of the M2 constituent by the model. The assymetry in the modelled velocity at flood (the maximum velocity is higher during the first phase of the flood compared with the second phase of the flood) does not appear in the observations (figures 3.9b and 3.9c). During ebb, the range of observed bottom velocities is lower in magnitude than the modelled values with a difference of up to 0.3 m s^{-1} at the surface (figure 3.9b) and 0.5 m s^{-1} at the bottom (figure 3.9c) during spring tide, which indicates an overestimation of the bottom friction in the modelled velocity. This difference is less during the neap tides.

3.8 Salinity

Modelled time-series of salinity at the three stations Cracknore (upper estuary), NWNetley and Calshot (coastal waters) are compared against measurements made in Southampton Water (see locations on figure 3.1). All measurements were made during the extended high water in order to standardise the tidal influence.

At Cracknore (figure 3.11 a), salinity variations in the model are affected by the semi-diurnal tidal cycle (time-scale of 12.42 hours), with the surface and bottom salinity gradually increasing at flood and decreasing at ebb. Tidal mixing is more intense during spring tides and reduces the degree of stratification (lower difference between bottom and surface salinity). This results in a spring-neap modulation of the simulated salinity difference between surface and bottom. The observations indicate a higher range of salinity values from surface to bottom (up to 10 units on day 116). Depth-averaged salinity agrees with modelled salinity on day 93 and day 116.

At NWNetley (figure 3.11b), partially-mixed conditions occur characterized by an alternation of stratified and non-stratified conditions in the water column depending on the stage of the tidal cycle. The short time-scale fluctuations in both surface and bottom salinity are driven by the semi-diurnal cycle, and reaches the amplitude of up to 4 units during spring tides (day 100 for example) and 1.5 units during neap tides (day 106 for example). At spring tide, no difference in salinity occurs between the bottom and the surface salinity as the simulation progresses in

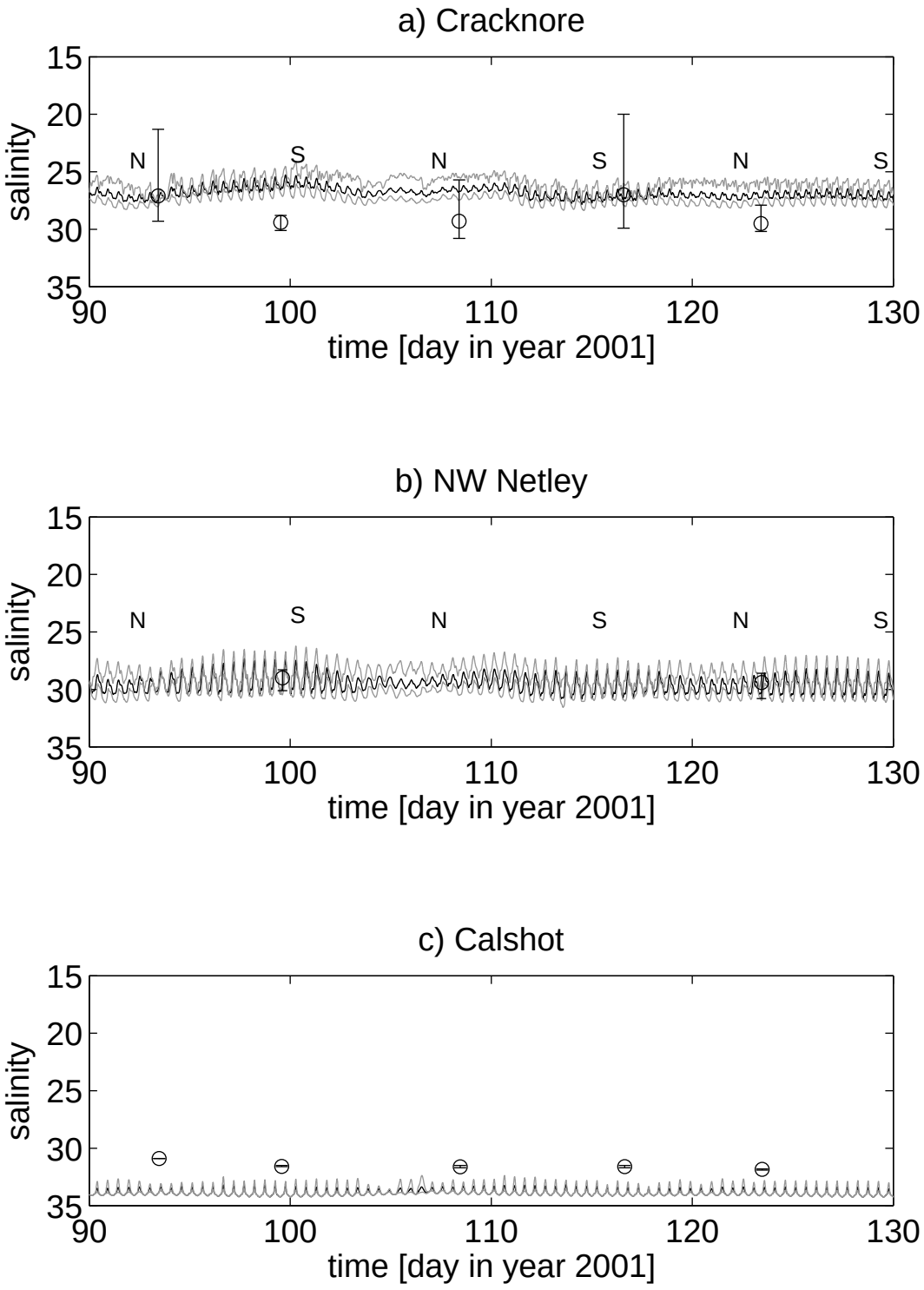

Figure 3.11: Time series of salinity for a) Cracknore, b) NWNetley c) Calshot. The black line indicates the depth-averaged values, the grey line indicates minimum (surface value) and maximum (bottom value) within each profile, circles indicate measurements with bars for minimum (surface values) and maximum (bottom values) within each profile. The labels 'N' and 'S' indicate neap and spring conditions, respectively.

time which indicates mixed conditions. At neap tide, the difference between the surface salinity and bottom salinity is in the range of 1.5 units (neap tides on day 122) to 2 units (strong neap tides of day 106). Comparison of modelled salinity with the observations indicates a good agreement.

At Calshot (figure 3.11 c), the salinity is mainly affected by the semi-diurnal tidal cycle modulated by the spring-neap tidal variation. Well-mixed conditions prevail at this location with a very small difference between bottom salinity and surface salinity.

The spatial gradient generated by the model is stronger (salinity ranging from approximately 26 at Cracknore to 34 at Calshot) compared with observations (approximately from 27 at Cracknore to 32 at Calshot). This indicates a slight overestimation of the modelled salinity intrusion from the Solent domain into Southampton Water.

3.9 Responses to wind stress

3.9.1 Effect of wind on sea surface elevation

The impact of wind forcing on the slope of the sea surface is evaluated by comparison between results of the simulation A1 (wind)and simulation C (no wind) (table 3.1). In estuaries variations in surface slope under the effect of the local wind modify the pressure gradient force which determines the secondary circulation. This effect has already been observed in other estuaries and has been reported to be the cause of wind-induced exchange of water which influences the export of freshwater to the coastal area (Wang et al., 1998; Hearn and Robson, 2002; Janzen and Wong, 2002; Wong and Valle-Levinson, 2002; Choi and Wilkin, 2006). For example, Hearn and Robson (2002) reported a variation in sea level of 0.08 m due to wind forcing for a mean daily seabreeze of about 7 m s^{-1} in the basin of the Harvey estuary, a microtidal estuary in southerwestern australia. This effect produces wind-induced channel exchange representing about 20 % of the exchange due to tides only.

When the wind blows perpendicular to a coastline, a surface slope forms in the same direction as the wind, which can be described analytically in one-dimension, starting from the balance between the pressure term and stress forces (Pugh, 1996). The equation found relates the variation in slope to the ratio of the intensity of the wind stress and the water depth:

$$\frac{\partial \xi}{\partial x} = \frac{C_d \rho_a W^2}{g \rho D} \tag{3.3}$$

where ξ is the sea surface elevation, C_d is the drag coefficient, ρ_a is the air density, g is the coriolis force, ρ is the seawater density and D is the water depth. The same equation can be used to estimate the variation in water level between the two ends of a narrow channel of constant depth or a lake by winds blowing in the along-channel direction (Ward, 1979; Pugh, 1996). Due to the presence of narrow channels interconnected (Southampton Water, Solent East, Solent West, Test and Itchen estuary) with various orientations (figure 3.1), the response of the water level in the channels is expected to be a combination of the remote effect of wind forcing and the local effect (Janzen and Wong, 2002; Wong and Valle-Levinson, 2002). Here a focus is made on estimating the amplitude of the sea level variation by local wind.

The contribution of the wind stress to the simulated sea surface elevation can be first evaluated by plotting the difference of ξ obtained in the case of a spatially uniform but temporally variable wind stress (run A1) and ξ obtained in the no wind case (run C) at the four reference stations Dockhead, Calshot, Bournemouth and Portsmouth along the coast (figure 3.1).

From day 110 to day 120, the wind was predominantly southwards (offshore wind) (figure 3.12a). The corresponding time-series of the difference in sea surface elevation between run C and run A1 is plotted figure 3.12b. A variation of up to 11 cm can be observed under the influence of the wind stress at Dockhead (on day 113 and day 117) compared with up to 5cm at the other stations Calshot, Bournemouth and Portsmouth. This result indicates that offshore wind tends to establish a small surface slope between the Solent and the head of Southampton Water. During periods of strong wind, short relaxation of the wind stress creates a reverse effect and the formation of water movement in the opposite direction to the wind direction (visible on day 115).

From day 120 to day 130, the wind was predominantly northwards (onshore wind) (figure 3.13a). The corresponding time-series of the difference in sea surface elevation between run C and run A1 is plotted figure 3.13b. A maximum variation of up to 4.5cm can be observed during this time period (day 120). The fluctuations in sea level are either small or non significant and can be related to the smaller intensity of the wind in this later period.

The difference in water level generated by the surface slope between the mouth of Southampton Water at Calshot (figure 3.14) and the head of Southampton

(a)

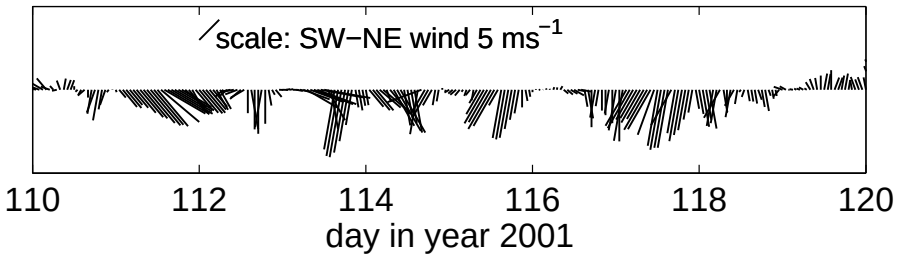

(b)

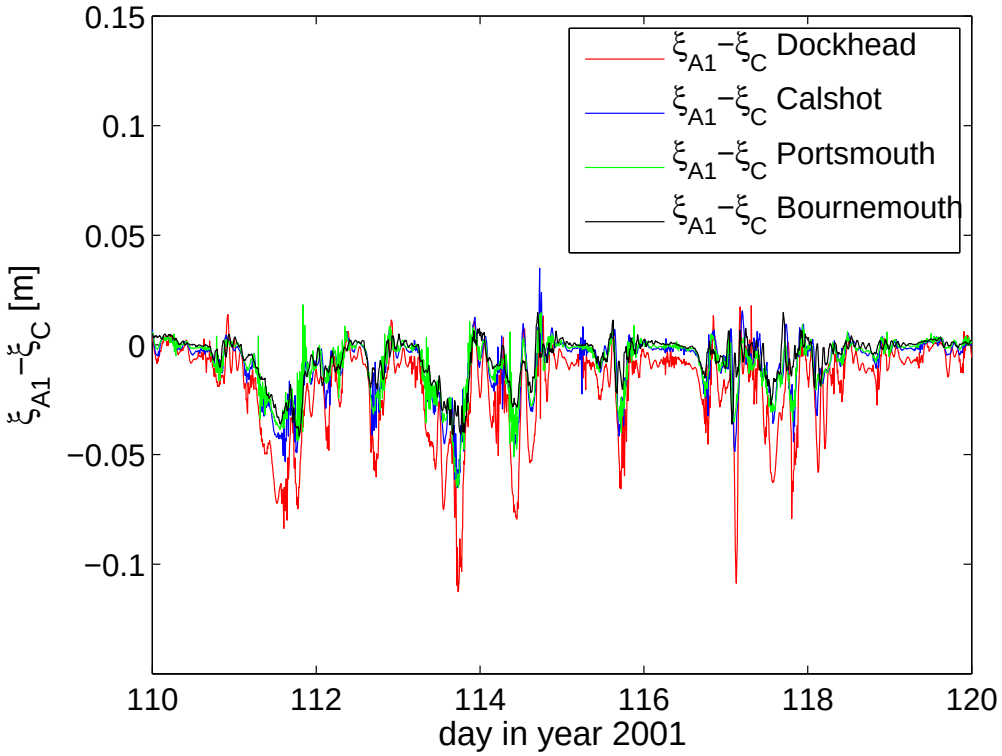

Figure 3.12: a) Stick diagram of the wind vector plotted from day 110 to day 120. The scale for the arrow is indicated for a southwesterly wind. b) Time series of the difference of sea surface elevation obtained with the simulation with wind stress (run A1) and the simulation with no wind stress (run C) at the four stations Dockhead (head of Southampton Water), Portsmouth, Bournemouth, and Calshot (mouth of Southampton Water) along the coast.

(a)

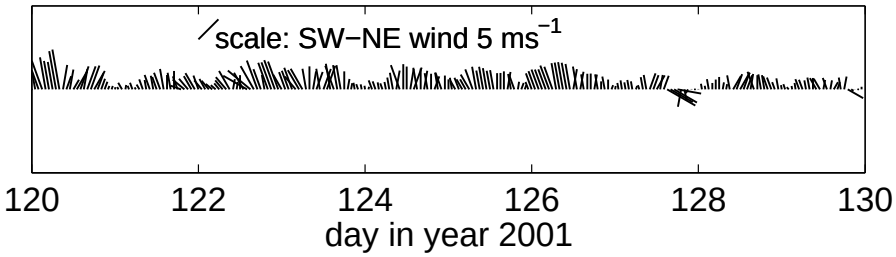

(b)

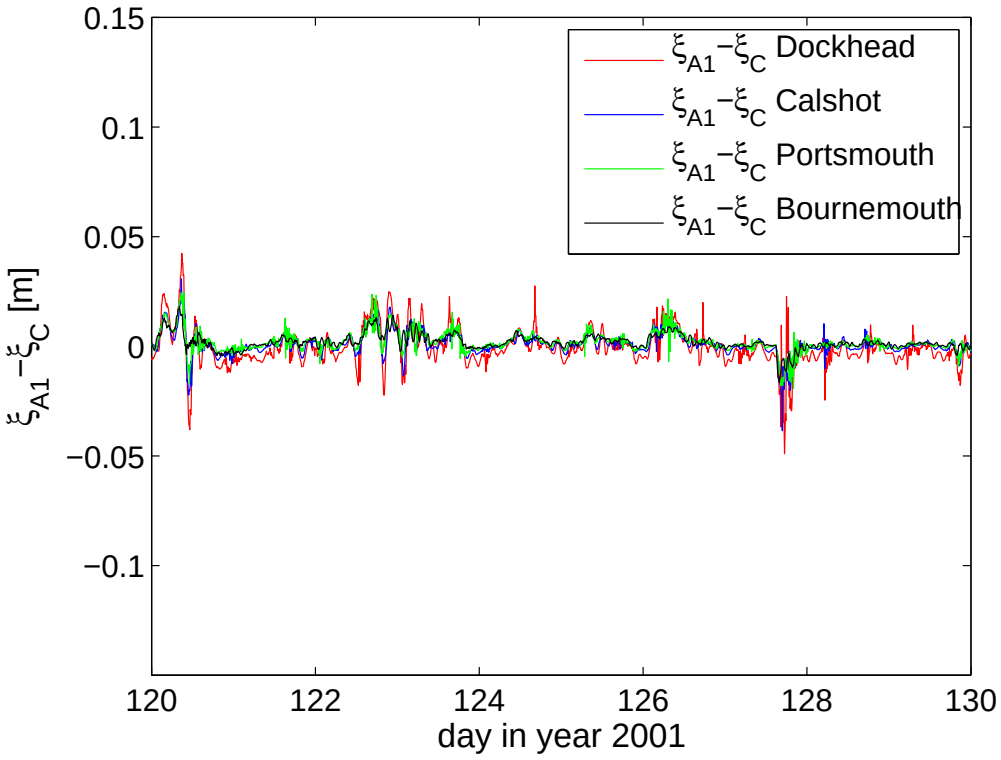

Figure 3.13: a) Stick diagram of the wind vector plotted from day 120 to day 130. The scale for the arrow is indicated on the top left corner (southeasterly wind). b) Time series of the difference of sea surface elevation obtained with the simulation with wind stress (run A1) and the simulation with no wind stress (run C) at the four stations Dockhead (head of Southampton Water), Portsmouth, Bournemouth, and Calshot (mouth of Southampton Water) along the coast.

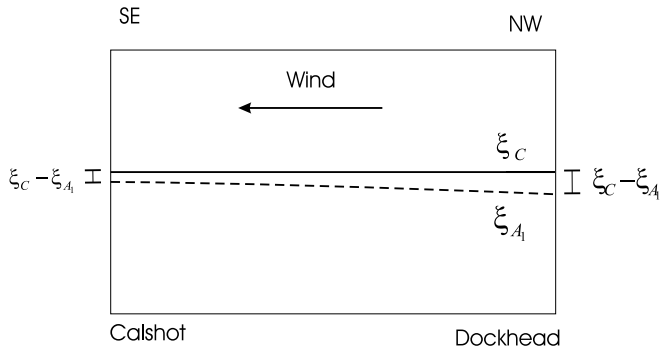

Figure 3.14: Schematic diagram of the formation of the surface slope in the main channel of Southampton Water.

Water at Dockhead is obtained by calculating:

$$\partial\xi_{A1} - \partial\xi_C = (\xi_{dockhead,A1} - \xi_{Calshot,A1}) - (\xi_{dockhead,C} - \xi_{Calshot,C}) \qquad (3.4)$$

This variation has been plotted together with the southerly (S-N) velocity component of the wind vector.

This estimation of the variation in the surface slope in Southampton Water (the difference in water level between the two stations Dockhead and Calshot) is given in figures 3.15a and 3.15b.

From day 110 to day 120, the temporal variation in the surface slope qualitatively covaries with the intensity of the southerly (S-N) wind component (figure 3.15a). A maximum difference in the sea surface elevation is 0.06 m is obtained on day 113 and day 117 with a wind magnitude of approximately 12 m s^{-1} and -9 m s^{-1}.

From day 120 to day 130, the temporal variation of the surface slope is as well qualitatively correlated to the intensity of the S-N wind component (figure 3.15b). The magnitude of the variation is less pronunced than the previous time-series, and the difference does not exceed 2 cm, except for day 127 when a sudden relaxation of the wind in the opposite direction generates a peak of 4cm. This lower magnitude can be related to the wind stress which is less intense (S-N component ranging from 0 to 7 m.s^{-1}) than the period from day 110 to day 120.

Coefficients of correlation over the whole time-series (from day 110 to day 130) have been calculated to determine the impact of wind direction on the amplitude of the sea surface slope ($\xi_{dockhead,A1} - \xi_{Calshot,A1}$) in Southampton Water. The sea surface elevation has been reduced to the same time resolution as the wind data by averaging over one hour. The highest correlation is found between the surface slope and southerly (S-N) wind, and between the surface slope and the

(a)

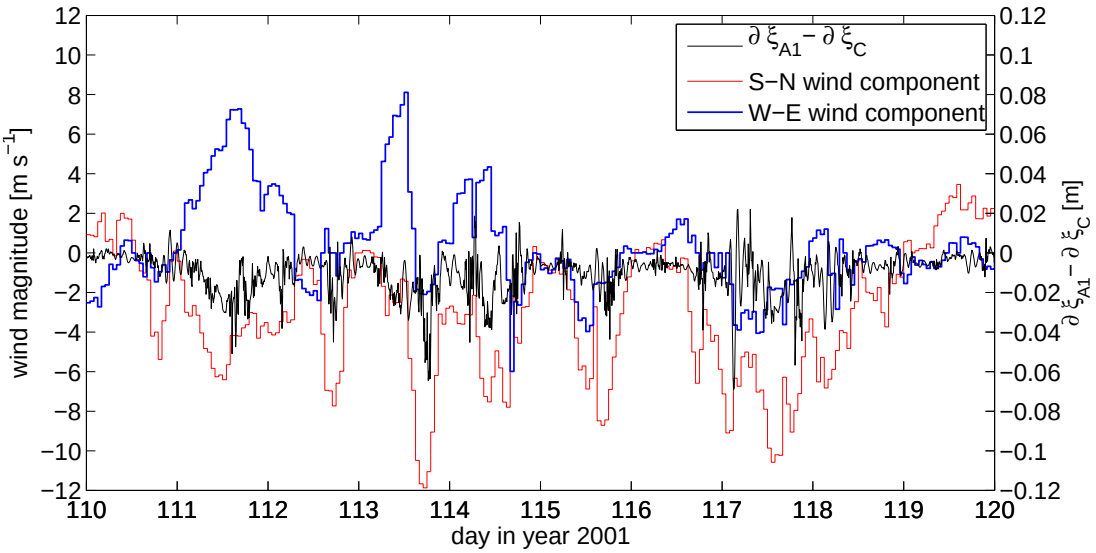

(b)

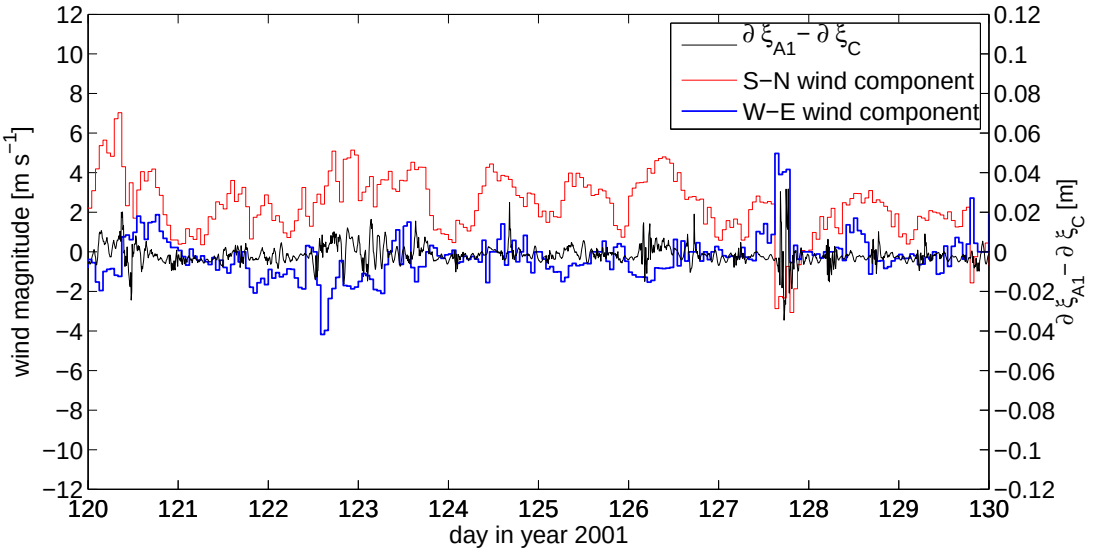

Figure 3.15: Time series of the difference of the slope obtained between Dockhead and Calshot (annotated $\partial\xi$ in the legend) obtained in the case with wind and the no wind case (black line). The southerly component (N-S) and the westerly component (W-E) of the wind vector are plotted on the right-hand axis (blue line and red line). a) from day 110 to day 120. b) from day 120 to day 130.

along-estuary (SE-NW) wind direction relative to Southampton Water with a coefficient of correlation of 0.662 and 0.647, respectively. The coefficient of correlation between the difference in surface slope and the wind intensity is 0.602. A lower correlation is found between the transverse wind component (SW-NE) and the surface slope with a coefficient of 0.524. Finally the lowest correlation is found between the W-E component and the difference in surface slope (-0.199). In summary, the S-N wind component is predominant in determining the amplitude of the surface slope in Southampton Water.

3.9.2 Effect of wind on vertical structure

3.9.2.1 Stratification parameter

The effect of the local wind stress on vertical structure has been estimated by calculation of the stratification parameter St (Hansen and Rattray, 1966; Dyer, 1997). St is defined as the ratio of the surface to bottom salinity divided by the averaged salinity:

$$St = \frac{\delta S}{< S >} \tag{3.5}$$

where δS is the difference between the salinity in the surface layer and the bottom layer, and $< S >$ is the vertically-averaged salinity. This stratification parameter is calculated at the two reference stations NWNetley (mid-estuary) and Calshot (mouth of Southampton Water) from run A1 and run C (table 3.1). A high value for the stratification parameter is associated with a strong stratification whereas a low value of the stratification parameter is associated with well-mixed conditions in the water column.

The range of variation of the difference between surface and bottom salinity δS for a given stratificiation parameter is plotted in figure 3.16 . The shaded area corresponds to the range of $< S >$ found at NWNetley and Calshot, which are respectively 27.4-30.80 and 32.7-34.1 from day 110 to day 130 of run C. This gives an indication that the surface to bottom salinity difference ranges from 1.37 to 1.5 when St=0.05, and from 2.74 to 3 when $St = 0.1$ at NWNetley. Therefore the time variation of St gives an indication of the degree of stratification in the water column.

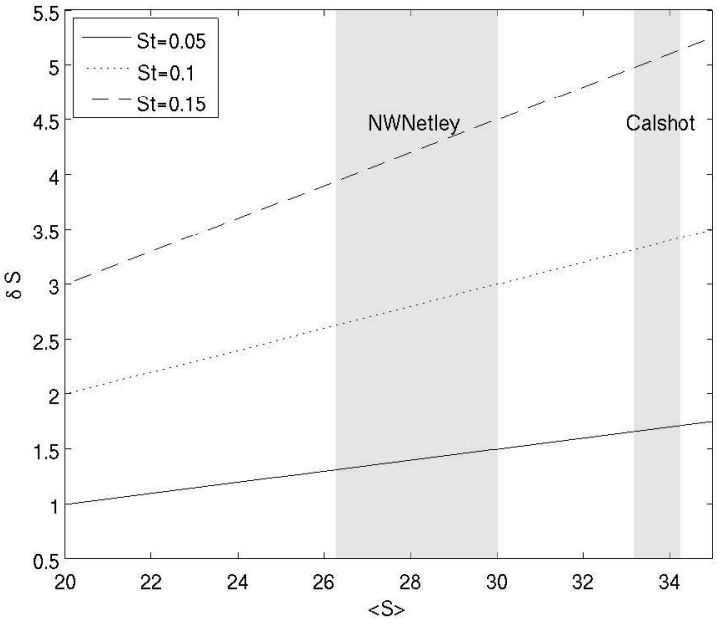

Figure 3.16: Variation of the stratification parameter. The shaded area represents the range of $< S >$ occuring at NWNetley and Calshot from day 110 to day 130 of simulation C (no wind).

3.9.2.2 Semi-diurnal variation

In absence of wind forcing, the degree of stratification is the result of the competition between the gravitational circulation (baroclinic exchange flow generated by the horizontal gradient of water density between the river and the sea), tidal stirring (mixing produced by small scale velocity shear) and tidal straining (bottom friction causes the velocity of the near-bed advective flow to be slower than the near-surface flow) (Simpson et al., 1990). Tidal straining reduces or increases stratification depending on the direction of the tidal current relative to the horizontal density gradient. At flood, tidal straining works against the gravitational circulation and alters stratification. At ebb, tidal straining strengthens the gravitational circulation and therefore stratification is stronger than at flood.

At NWNetley, modelled stratification in the no wind case (run C) shows a complex semi-diurnal variation in stratification, in relation to the unusual tidal cycle inducing variations in the tidal advection (figure 3.17a). Stratification is the highest at ebb, when both the gravitational circulation and the tidal straining stratify the water column. A peak of St occurs at mid-ebb when tidal advection is the fatest (figures 3.9a and 3.9a). At flood, tidal advection is in the opposite direction (towards the head of the estuary) to the gravitational circulation. Mixing

(a)

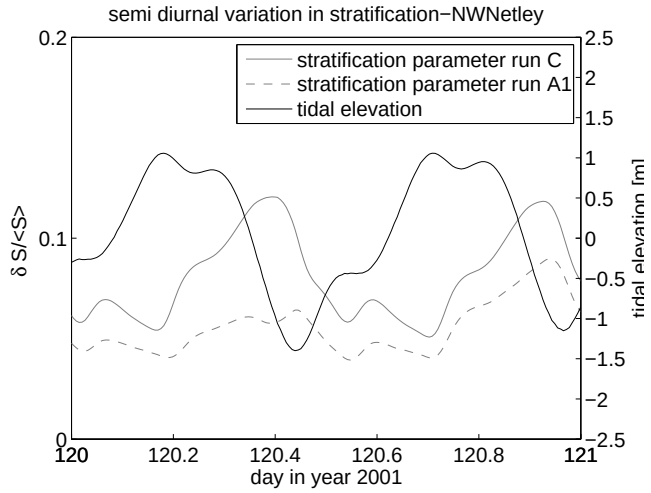

(b)

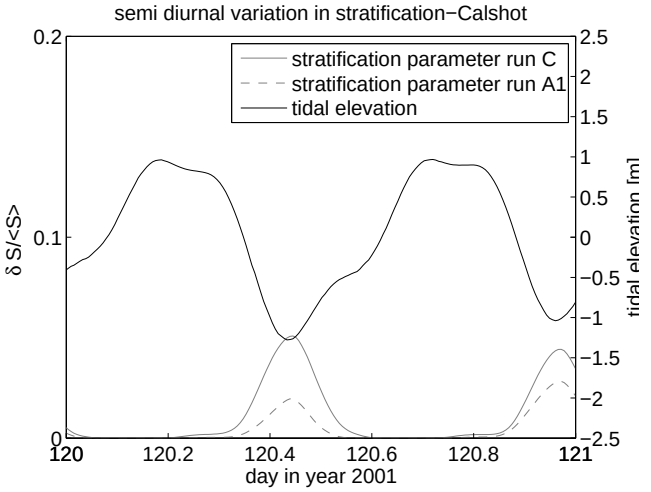

Figure 3.17: Semi-diurnal variation (typical neap tide) of the stratification parameter simulated in the case of run C (without wind forcing) and run A1 (with wind). a) NWNetley b) Cashot.

by straining gradually reduces the stratification, except at mid-flood when the sea water level rise pauses and a reverse effect occurs (the stratification parameter gradually increases during the young flood stand). Thus the weaker turbulence at slack water promotes an increase of the influence of the gravitational circulation which stratifies the water column. A similar effect occurs again at the first high tide, with a gradual increase in stratification due to the enhancement of the gravitational circulation. The difference between the simulation including the wind (run A1) compared with the no wind case (run C) consists of a reduction of the magnitude of the stratification parameter, due to the additional effect of wind-generated mixing. During the first semi-diurnal cycle (from day 120 to day 120.5), a delay is observed in the semi-diurnal variation of St in run A1 compared with run C, which results in a peak of the stratification parameter ocurring at low water rather than mid-ebb. In addition a short period of time (less than one hour) of reduction of St at mid ebb (day 120.4) occurs. Thus short-time scale (less than one hour) fluctuations of St are induced by wind variations and are superimposed on the semi-diurnal cycle of St.

At Calshot, the dynamics of the stratification parameter in the no wind case (run C) reflect the well-mixed conditions of the salinity stratification and St varies in the range of 0 to 0.05 (figure 3.17b). Stratification is thus weaker at Calshot than NWNetley. A semi-diurnal cycle in stratification occurs with a maximum of St occuring at slack water low tide. At flood, mixing conditions dominate and are not influenced by the pause in sea level rise at mid-flood. The stratification parameter in the wind case (run A1) shows a similar semi-diurnal cycle, however its magnitude is reduced and varies according to the intensity of the magnitude of the wind generated mixing, with a peak of St reaching 0.02 in the first low tide and 0.025 in the second low tide.

3.9.2.3 Time-series of 20 days

Figure 3.18a represents the modification of the stratification parameter under the effect of realistic wind forcing for a time-series of 20 days at NWNetley by comparison between run A1 (wind forcing) and run C (no wind forcing). Compared with run C, modelled stratification in run A1 is therefore controlled by wind stirring (wind acts as a source of kinetic energy which promotes mixing) in addition to the gravitational circulation, tidal straining and tidal stirring. Wind stirring efficiency depends on the alignment of the wind direction with the advection flow, and its persistence. Down-estuary wind (northwesterly wind) can

potentially generate wind straining (advection of near-surface flow) which reduces or overcomes mixing by wind stirring (Scully et al., 2005). The time-series shows semi-diurnal variations with the peak occuring at ebb as presented figure 3.17a. Wind forcing systematically generates a lower stratification parameter at all stages of the tidal cycle as indicated by the positive difference in the stratification parameter between the two model runs (figure 3.18b). Only on a few occasions in the time-series, (second semi-diurnal cycle on day 111, second semi-diurnal tidal cycle on day 113 and second semi-diurnal tidal cycle on day 127) does stratification appear increased in the run with wind forcing (run A1) and occurs during time of down-estuary wind forcing (northwesterly wind) in occurence with flood tide. These results reflect the predominance of wind-induced stirring which reduces the stratification. The highest deviation of stratification parameter occurs on day 115 and 117 and are coincident with peaks of wind intensity up to 10 m s^{-1} (figure 3.18b-c). However peaks in the difference of the stratification parameter occur during moderate wind intensity (for example δS up to 0.06 for a wind intensity of 8 m s^{-1} on day 120). This can be caused by the role of wind persistence and direction in addition to wind intensity in controlling the intensity of mixing in the water column Ribeiro (2004).

Section 3.9.2.2 has shown that mixing is more pronunced at ebb than flood and a semi-diurnal asymmetry of St appears in both run A1 and run C (figure 3.18a). Wind is more effective in reducing stratification at ebb than augmenting mixing at flood and therefore reduces the semi-diurnal asymmetry of the stratification as revealed by the semi-diurnal periodicity observed in the difference in St between run A1 and C (figure 3.18b).

On day 111, in spite of a persistent down-estuary (northwesterly) wind intensity up to 9 m.s^{-1}, the intensification of the mixing remains relatively low with a modification of the stratification parameter less than 0.02 at ebb (figure 3.18a and figure 3.18b). Down-estuary wind can promote stratification by advecting surface flow in the same direction to the gravitational circulation at ebb (Scully et al., 2005). A possible mechanism is the enhancement of the tidal straining by wind-induced straining reducing the effect of wind-generated turbulence.

A long term reduction of the stratification occurs as the simulation progresses in time towards summer, due to the impact of the seasonal variation in river inputs which gradually decreases (figure 3.18a). A spring-neap modulation in both simulations (runs A1 and C) is superimposed on this seasonal variation, with the range of the stratification parameter lower at neap tide (day 120 to day 124)

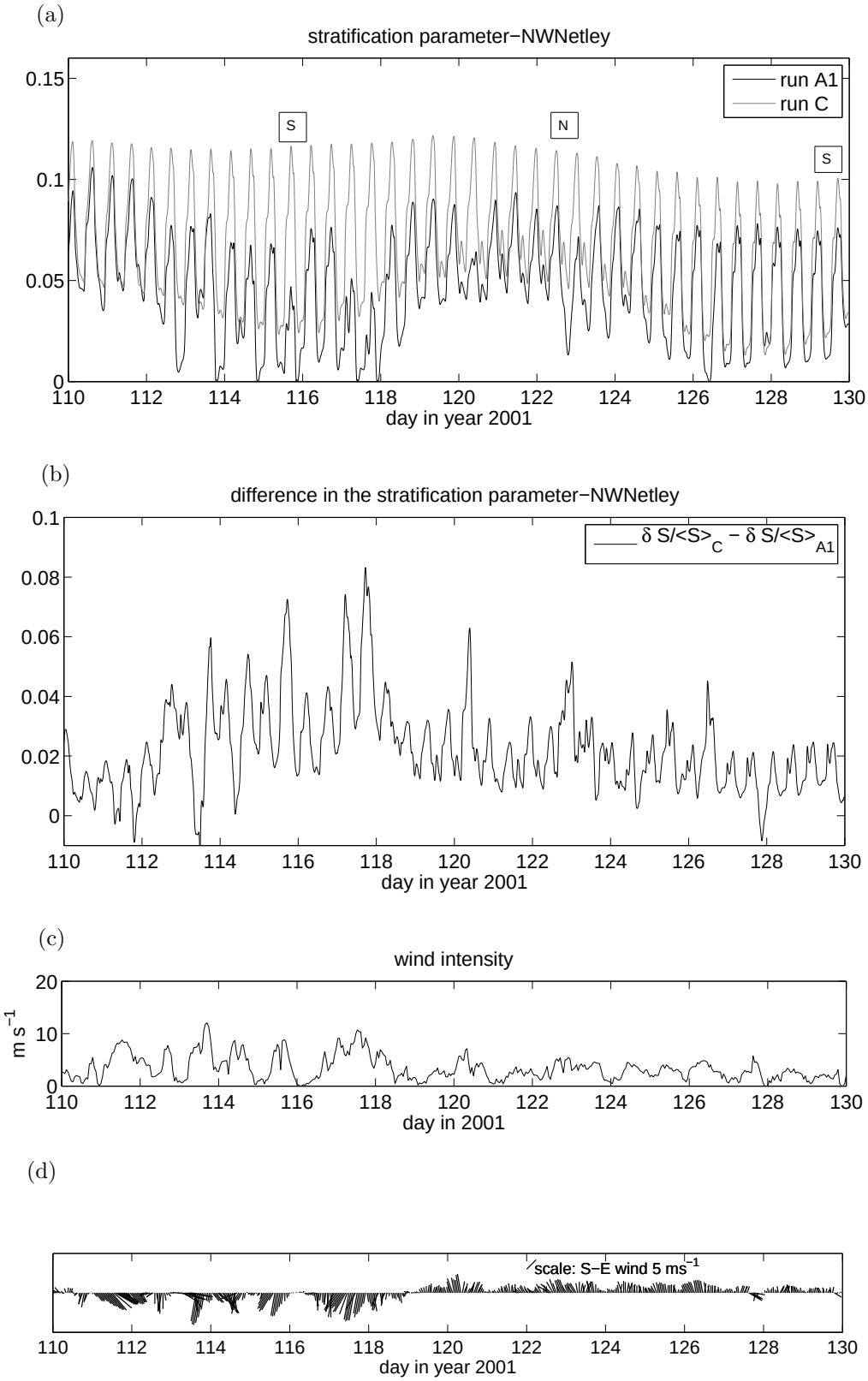

Figure 3.18: a) Time-series of the stratification parameter simulated in the case of run A1 (including wind forcing) and run C (no wind forcing) at NWNetley. b) difference between the stratification parameter in run A1 and run C .c) Wind intensity d) Stick diagram of wind direction and intensity.'N' and 'S' indicate spring and neap tide.

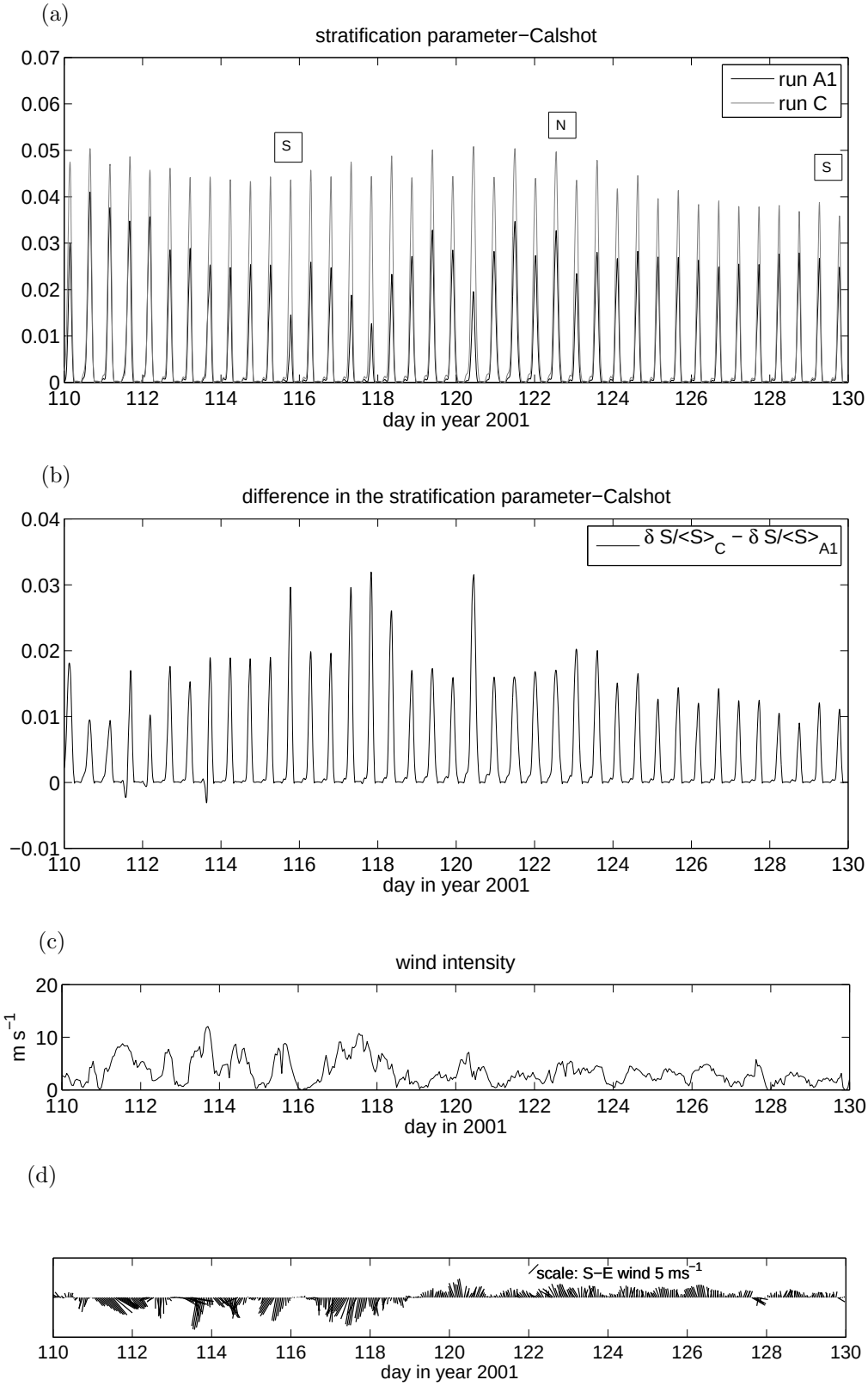

Figure 3.19: a) Time-series of the stratification parameter simulated in the case of run A1 (including wind forcing) and run C (no wind forcing) at Calshot. b) difference between the stratification parameter in run A1 and run C .c) Wind intensity d) Stick diagram of wind direction and intensity.'N' and 'S' indicate spring and neap tide.

compared to spring tide (day 114 to 118 and day 126 to day 130).

At Calshot, wind forcing generates a modulation of the semi-diurnal cycle of the salinity stratification: the slight stratification occuring at low water is reduced by wind forcing (figure 3.19a-b). Similarly to what was shown at NWNetley, the predominant effect of adding wind to the simulation is the overall more mixed conditions (the difference in the stratification parameter is positive) prevailing during the whole time-series. The highest difference of the stratification parameter between run C and A1 are associated with episodes of strong wind intensity, up to 10 m s^{-1} (day 115 and day 117 comparison between figures 3.19b and c). However the modulation of the effectiveness of the wind intensity in mixing the water column is further modulated by wind direction and persistence, as suggested by the moderate difference of the stratification parameter with wind intensity up to 10 m s^{-1} occuring on day 120 (figure 3.19b-c). Compared with NWNetley, the stratification parameter in run C is significantly influenced by a diurnal cycle (due to the K1 tidal harmonic constituent) as demonstrated by the variation with a period of one day superimposed on the semi-diurnal cycle (period of 12.42 hours) and the spring-neap cycle (fornightly fluctuations) (figure 3.19a). The variation generated by wind forcing tends to strongly weaken the spring-neap and the diurnal periodicity of the stratification (comparison between run A1 and run C on figure 3.19a).

3.9.3 Impact of wind on the mean flow

A least-square harmonic analysis of the modelled along-estuary velocity separates the velocity into a tidal component, referred to as the tidal velocity and a non tidal component, referred to as the residual velocity:

$$v_{model} = v_{tidal} + v_{res} \tag{3.6}$$

where v_{tidal} is the sum of the tidal harmonic constituents, defined as:

$$v_{tidal} = v_o + \sum_{i=1}^{N} (A_i cos(w_i t + \phi_i)) \tag{3.7}$$

where v_o is the mean velocity of the whole time-series, N is the number of tidal constituents used, A_i is the amplitude, w_i is the frequency, t is the time and ϕ_i is the phase. To make a comparison with the mean flow in Southampton Water calculated by Ribeiro et al. (2004), the same harmonic constituents (Mf, O1, P1,

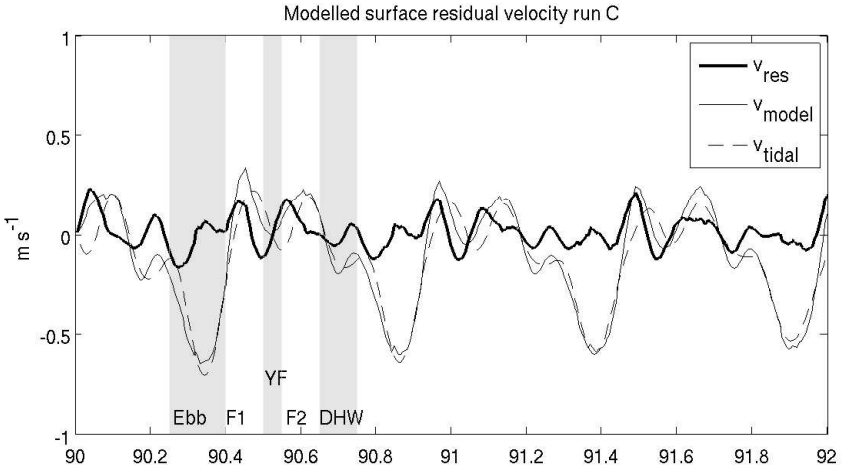

Figure 3.20: Illustration of the semi-diurnal modulation of the tidal residual. A typical semi-diurnal cycle is identified by the following abbreviations: Ebb for the ebb phase, F1 is the first phase of the flood, YFS is the young flood stand, F2 is the second phase of the flood and DHW is the double high water.

K1, N2, M2, S2, MN4, M4, MS4, 2MN6, M6, 2MS6, M8, M10, M12, M14) have been used. This calculation was made from day 90 to day 130, in the case of run A1 (including wind forcing), run C (without wind) and from the ADCP velocities at Cadland (see location in figure 3.1). Calculations in all three cases were separated into bottom and surface velocities.

In the absence of wind (run C plotted in figure 3.20), the residual current is affected by a semi-diurnal variation as illustrated for a 25 hour time-series starting from day 90. The residual current oscillates during a typical semi-diurnal tidal cycle and reaches four peaks: the first occurs during the first phase of the flood, the second occurs just after the young flood stand, a third occurs at the end of the double high water and the fourth is visible at the begining of the ebb phase.

Similar to Ribeiro et al. (2004), the least-square tidal harmonic analysis was carried out by running a 25 h window through the along-estuary depth-normalised velocity time series and sliding it forward by a 1 h time-step. This calculation filters out the semidiurnal variation of the residual velocity and results in an estimation of the mean flow. The mean flow characterises the bidirectional flow, with a flux of saltier water flowing landwards at the bottom and a flux of fresh water flowing seawards at the surface, at both the spring-neap and the seasonal time-scales.

The mean flow is examined first in the case of run C without wind forcing (figure 3.21a). The mean flow is positive at the surface (directed seawards) and negative at the bottom (directed landwards). The modelled surface mean flow

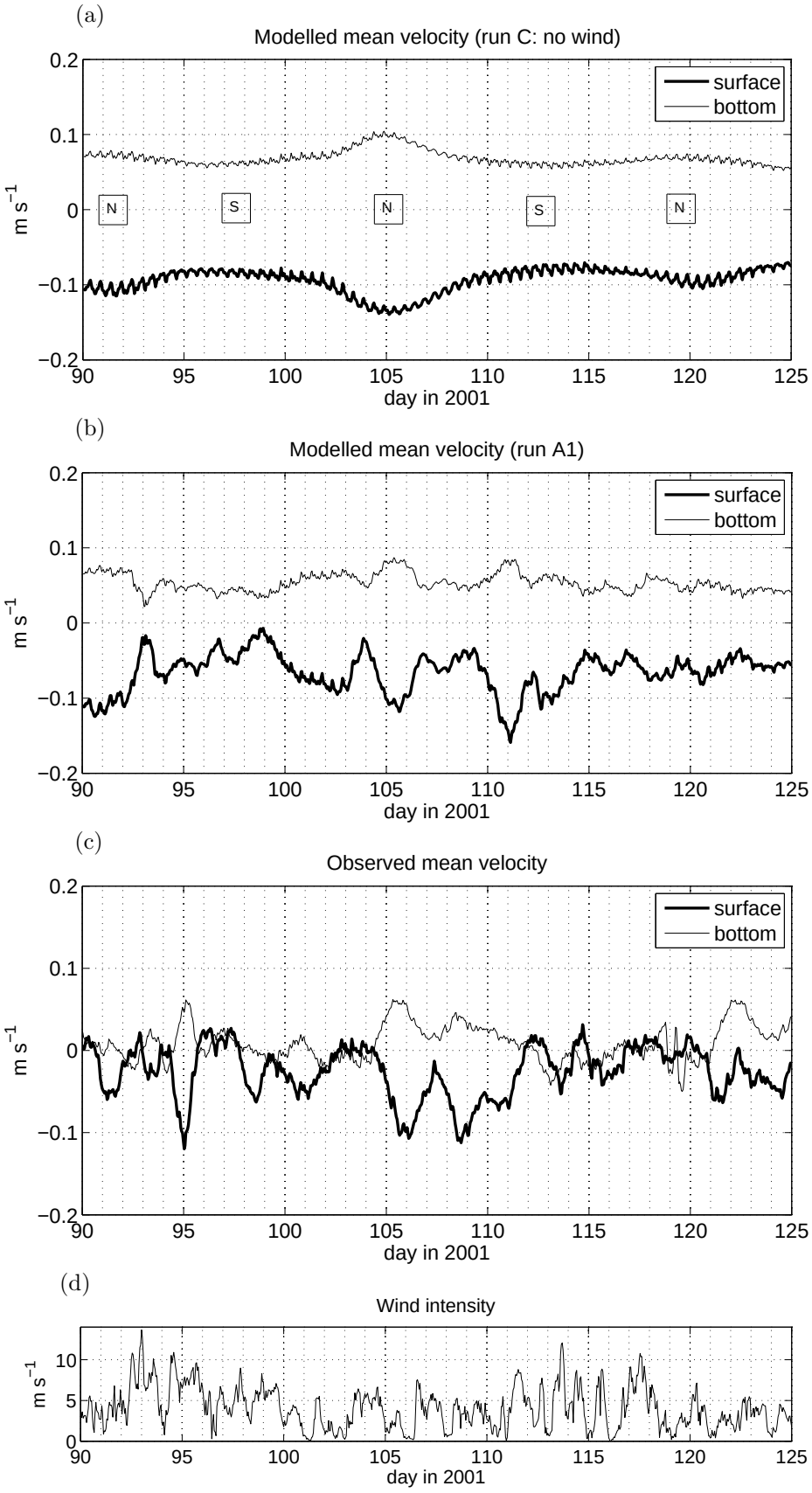

Figure 3.21: Mean flow corresponding to a 25h rolling average with a time-step of 1h of the residual currents. Positive and negative velocities are directed landwards and seawards, respectively. a) Surface and bottom modelled mean flow (simulation C) b) Surface and bottom modelled mean flow (simulation A1) c) Surface and bottom observed mean flow d) wind intensity.

ranges from -0.085 m s^{-1} to -0.13 m s^{-1} and the modelled bottom mean flows ranges from 0.06 m s^{-1} to 0.1 m s^{-1}, respectively. The spring-neap modulation of the mean flow reduces the difference between the modelled bottom and surface mean flow at springs compared with neaps (see 'N' and 'S' in figure 3.21a). This effect is caused by the tidal mixing being more intense at springs than neaps, which reduces the stratification by enhancing the vertical momentum exchange. The trend line calculated over two spring-neap cycles (28 days) gives $-0.160 + 0.0006 \times day$ for the surface mean flow, and $0.106 - 0.0004 \times day$ for the bottom flow, indicating the decrease in the intensity of the mean flow at the surface and the bottom. This result is consistent with the seasonal signal generated by flux of fresh water from the rivers which decreases as the simulation progresses in time towards the summer months and consequently reduces the intensity of the gravitational circulation.

A comparison between figures 3.21a-b illustrates the impact of wind forcing on the modelled mean flow. Wind forcing reduces the degree of stratification and therefore reduces the intensity of the mean flow both at the surface and the bottom. The averaged mean flow from day 90 to day 125 is -0.092 m s^{-1} at the surface and 0.067 m s^{-1} at the bottom in case of run C (no wind), compared with an averaged mean flow of -0.065 m s^{-1} at the surface and 0.053 m s^{-1} at the bottom in run A1 (with wind). The variation in modelled residual flow due to variations in wind forcing operates at the time-scales of a day, superimposed on the fluctuation due to the spring-neap tidal cycle. Peaks of gravitational circulation (defined as surface modelled mean velocities higher in magnitude than -0.1 m s^{-1}) occurs from day 90 to day 92, on day 105 and day 111 , when low wind intensity (< 5 m s^{-1}) persists for at least one day (figure 3.21d).

Modelled mean flow can be compared against observed mean flow by comparison of figure 3.21b with figure 3.21c. At the surface, the observed mean flow ranges from 0.02 m s^{-1} to -0.12 m s^{-1}, whereas the modelled mean velocity ranges from -0.01 m s^{-1} to -0.15 m s^{-1}. At the bottom, the observed mean flow ranges from -0.025 m s^{-1} to 0.06 m s^{-1}, compared with a modelled mean flow ranging from 0.03m s^{-1} to 0.09 m s^{-1}. Over the time-series (from day 90 to day 125), the difference between bottom and surface mean velocity is greater in the model compared with the observations: The modelled averaged bottom mean velocity and modelled averaged surface mean velocities are 0.053 m s^{-1} and -0.065 m s^{-1}, respectively, compared with the observed averaged bottom and surface mean velocities of 0.009 m s^{-1} and -0.026 m s^{-1}, respectively. This result indicates

a stronger gravitational circulation in the model compared to the observations. Differences exist between the fluctuation due to wind forcing in the modelled mean velocity and the observed mean velocity. For example, the pulse of gravitational circulation which occurred at the strong neap tide on day 105 is well-reproduced by the model, and the strong alteration of the gravitational circulation under the effect of the strong wind (up to 14 m s^{-1}) occuring on day 92-93 is reproduced by the model. In contrast, an increase of the bottom mean flow on day 123 is not reproduced by the model. Model simulation does not account for the effect of the spatial variation in the wind field over the whole model area (in particular the effect of the remote wind forcing), which may explain the differences between modelled and observed mean flow.

3.10 Summary and discussion

A 3D finite volume model of estuarine circulation has been described and applied to the Solent-Southampton Water estuarine system. The length of this simulation and the high temporal resolution allows the generation of physical processes occurring in Southampton Water from hourly to weekly time scales. The effect of the physical forcing on the equilibrium state has been examined. The time needed for the model to adjust to the initial density field has been estimated to be 50 days. This adjustment time can be reduced by using an initial spatially-varying salinity field instead of a constant salinity field.

Results from the model have been compared with observational datasets available for March-April-May 2001 in Southampton Water. The model generates a horizontal salinity gradient and the unique tidal regime of Southampton Water reproduced including the extended slack water period occuring at high water and the 'young flood stand' at mid flood. At Dockhead, an error assessment of the model solution using a tidal harmonic analysis indicates an error of less than 15 % in amplitude and an error less than 10 degrees in phase for the semi-diurnal tidal constituent M2, S2, N2. The largest error in amplitude appears for those constituents with an observed amplitude of less than 8 cm (K1, MN4 and 2MN6). While comparing the results of the tidal harmonic analysis with tide gauge data, least agreement is found in the western part of the model domain (Bournemouth) compared with the eastern part of the model domain (Portsmouth). The velocity field is better represented during neap rather than spring tide.

Evaluation of the POL CS3 model over the north-west Atlantic with 47 tides

gauges spread offshore over the North-West region indicates a very good accuracy for the N2 and M2 results and less satisfactory for the O1 and K1 constituents (Andersen, 1998) when compared with other ocean tidal models. The coarse resolution (approximately 12km) makes difficult an accurate representation of the near-shore tidal current and elevations. The major tidal constituent M2 is reproduced with a typical error of $\pm$ 10 % over the North-West continental shelf with higher error off the western tip of the Isle of Wight due the presence of the amphidromic point (Flather, 1987). This suggests that most of the error associated with the diurnal constituents and the semi-diurnal constituents in the Solent-Southampton Water are similar to the error found in the POL CS3 model, and therefore may be attributed to the error generated by the tidal inputs at the boundary.

The model results have been compared with salinity measurements for validation. The longitudinal variation in stratification, with partially-mixed conditions prevailing in the upper estuary and well-mixed conditions at the mouth is well represented. Comparisons with observations indicate an underestimation by the model of the vertical stratification in the upper estuary (Cracknore) and higher salinity (modelled salinity ranging from 33 to 34 compared with observations in the range of 31 to 32) at the mouth of Southampton Water. The discrete measurements can be characteristic of intermediate time scale features, where water masses with different chemical and physical properties are advected towards the mouth of the estuary and mixed with the surrounding water masses relatively slowly. This wide range of variation may originate from channel tortuosity, meteorological effects, brief spate in the river flow (Dyer, 1975), as well as water outflow from the nearshore industries (Webber, 1975). These effects, which are not represented in the model, could explain the wider range of fluctuation observed in the measurements at Cracknore. The weaker stratification at Cracknore may be caused by the closure scheme used in the model. However a numerical study using the Regional Ocean Modeling System in the Chesapeake Bay has demonstrated the low sensitivity of the modelled estuarine vertical gradient to the type of turbulence closure schemes (Li et al., 2005). Another factor to investigate is the coarse vertical resolution of the model, which can smooth out the sharp gradients occuring in the upper layer. The impact of doubling the number of vertical levels of the Massachusetts and Cape Cod Bays hydrodynamic model revealed an increase in the density stratification (Jiang and Zhou, 2006). However the same authors mentionned that augmenting the vertical resolution increases both the

vertical current shear (potentially generating vertical mixing) and the vertical stratification which has an opposite effects on the mixing intensity and therefore the impact on the final modelled stratification is uncertain.

The forcings which control the estuarine plume are tides, wind and the Coriolis force (Kourafalou et al., 1996; Cugier and Le Hir, 2002). The other important aspect of the formation of the salinity gradient is its dependance on fresh water inputs occuring over the past several months. Winter 2001 was affected by an unusual regime of high rates of precipitation (Iriarte and Purdie, 2004). One way of improving the modelled salinity field is to force it with a seasonal variation of salinity at the boundary in contrast to the constant value used here, another is to carry out longer simulations to take into account the seasonal variation of freshwater input, combined with an increase in vertical resolution. These could reduce the difference between modelled and observed salinity at Calshot. This issue is important for investigating biophysical interactions particularly with respect to simulations of nutrients concentrations.

A wind-induced setup is generated by the numerical model, and a water level difference up ± 6cm in the model simulation forms from the mouth to the head of Southampton Water (wind up to 12 m s^{-1} during the whole time-series). Using equation 3.3, with W =10 m s^{-1}, C_d =0.0014, ρ_a=1.29 kg m^{-3}, g=9.81 m.s^{-2} $\partial\xi$ = 12km and D =10m, a maximum value of $\partial\xi = 0.15$ m is found. Compared to the theory, the wind-induced setup by the model is possibly attenuated by friction effect, variation in bathymetry, stratification and the characteristic frequency of the wind events (Wong and Valle-Levinson, 2002). The amplitude of the surface slope mostly covaries with the S-N wind component. In Southampton Water, observations of the elevation of the sea level up to 0.4 m due to onshore strong wind has been reported (Ribeiro, 2004). Extreme wind events generating storm surges and seiches can contribute to a raise of the sea surface elevation up to 0.5 m in the Solent area (Wells et al., 2001, 2004). In conclusion, model results suggest that up to 15 % (0.06 m relative to 0.4 m) of the observed variation in sea level due to atmospheric effects can be attributed to the local wind-induced setup.

The salinity structure without wind forcing is characterized by a complex semi-diurnal cycle. At NWNetley, the peak of stratification is obtained at mid-ebb at the peak ebb velocity. At Calshot, the peak of stratification occurs at low water. The semi-diurnal periodic stratification at Calshot appears similar to the typical semi-diurnal stratification usually observed in regions of fresh water influence, affected by an increasing stratification at the ebb and progressive mixing on the

flood, with the highest stratification observed at low water (Sharples and Simpson, 1995; Simpson et al., 2002). By contrast, the stratification at NWNetley shows a more complex semi-diurnal cycle, with the progressive mixing occuring at flood interrupted by an increase of stratification at mid-flood during the 'young flood stand', and the highest stratification occuring at mid-ebb. The wind stirring is more effective in reducing the effect of tidal straining occuring at ebb, than at flood. Therefore the modelled semi-diurnal assymetry in stratification generated by tidal straining is attenuated by wind-generated turbulence.

The modelled mean flow varies at the time-scale of the semi-diurnal cycle, the spring-neap cycle and at the seasonal time scale. Without wind forcing, residual circulation is influenced by the vertical gradient in salinity and the longitudinal salinity gradient, as described by Park and Kuo (1996). The vertical tidal mixing has a direct impact as it modifies the vertical momentum exchange and therefore increased tidal mixing at spring tide reduces the mean flow. In addition, increased vertical mixing has an opposite indirect effect, consisting of modifying the salinity distribution (shortening salt intrusion at the bottom) which in turn strenghens the longitudinal salinity gradient. The gravitational circulation is more intense when the longitudinal salinity gradient increases. This indirect response is controlled by the time-scale of vertical mixing relative to the response time of the longitudinal salinity distribution. In a partially-mixed estuary, the fortnightly modulation of the tidal mixing operates over shorter time-scales than the variation in longitudinal salinity and therefore spring-neap modulation of the mean flow is the dominant effect. The contribution of the wind-induced residual flow to the mean residual flow is assessed in this study by comparing the mean flow in the case of run C (without wind forcing) and run A1 (with wind forcing). Wind (varying from 0 m s^{-1} to 14 m s^{-1}) reduces the mean flow at the surface (mean flow reduced from -0.092 m s^{-1} to -0.065 m s^{-1}) and at the bottom (mean flow reduced from 0.067 m s^{-1} to 0.052 m s^{-1}). Wind influences the residual circulation through a combination of remote and local wind effects, and the relative predominance of the local wind in determining this residual circulation varies according to the characteristic frequency of wind events and the degree of stratification of the estuary (Wong and Valle-Levinson, 2002). The spatial variation in wind forcing and the impact of the remote wind forcing (blowing over the Solent and the approaches to the Solent) are not simulated in the model. This may explain the discrepancy between modelled and observed mean flow (mean bottom flow of 0.008 m s^{-1} in the observations compared to the 0.052 m s^{-1} in the model and mean surface flow of -0.026 m s^{-1}

in the observations compared to the -0.052 m s^{-1} in the model).

The intensity of the gravitational circulation is related to the flushing rate of the estuary, which determines the time for sediment and phytoplankton to be transported out of the estuary. Simulations A1 and C have been extended until day 160 in year 2001, to assess the impact of the mean flow on the distribution of the phytoplankton bloom in the estuary as recorded by continuous monitoring of chlorophyll fluorescence from the ferrybox as an indicator of the phytoplankton concentrations between Dockhead and the Isle of Wight (see location in figure 3.1). No observations of ADCP velocities were recorded in the estuary during the major spring bloom event in 2001, however the simulation provides a predicted residual flow for this time period. The surface mean flow is an index of the stratification and the water column becomes less stratified when the magnitude of the mean flow reduces. A Hoevmuller diagram from day 120 to 160 reveals the spatial and temporal variation of the chlorophyll concentration in Southampton Water and the Solent in the along-estuary direction (figure 3.22a), and are compared with the time-series of surface mean flow at two locations in Southampton Water, upstream (50.87°N) and downstream (50.83°N).

- At the latitude 50.87°N (upstream) (comparison between figures 3.22a and b), two major spring bloom events (chlorophyll levels above 10 mg m^{-3}) occured in Southampton Water during the strong neap tide (from day 131 to day 139) and are simultaneous with a period of increase in the magnitude of modelled surface flow (which indicates an increase of the stratification). From day 132 to 134, the first bloom occured. During this time the modelled surface mean flow (run A1) continuously increased from -0.06 m s^{-1} up to -0.15 m s^{-1}). From day 134 to day 137, the second chlorophyll bloom appeared to diminish in Southampton Water (from 50.89°N to 50.83°N), in contrast to the bloom (above the threshold level of 10 mg m^{-3}) present in the Solent (from 50.83°N to 50.76°N). The modelled surface mean flow predicts an increase in mixing (decrease of the surface mean flow to a minimum of -0.025 m s^{-1}) from day 134 to day 138 in the upper estuary (mean flow plotted for location 50.85°N), which suggests that phytoplankton are no longer retained in the surface water and therefore phytoplankton bloom patches disperse, possibly explaining the lower level of chlorophyll concentration occuring during this time period (less than 8 mg m^{-3}). This synchronisation between the variation in intensity of the mean flow and the chlorophyll concentration is again visible on day 137, when an increase in

chlorophyll concentration above 10 mg m^{-3} occured from latitude 50.89°N to 50.85°N, (second chlorophyll peak) at the same time as a major increase in the magnitude of the modelled surface mean flow from -0.03 m^{-1} to -0.09 m s^{-1} (run A1).

- At the latitude 50.83°N (downstream) (comparison between figures 3.22a and c), only the first bloom occurred (day 131 to day 134) compared with the position in the upper estuary 50.87°N (upstream). The first bloom is coincident with an increase of the mean velocity from -0.05 m s^{-1} to -0.15 m s^{-1}, as shown previously at the location upstream. In spite of an increase in magnitude of the mean velocity from 0 m s^{-1} to -0.05 m s^{-1} at the downstream location from day 136 to day 138, no bloom develops. This suggests that the range of magnitude of the mean velocity is too low (less than -0.05 m s^{-1}) and thus mixing prevails over stratification which inhibits the development of the second phytoplankton bloom.

To summarise model results indicate that blooms in Southampton Water occured during periods of increasing residual circulation. Spatial variations of the bloom extension in the along-estuary direction have been shown to be simultaneous with the spatial variation in intensity of the surface mean flow. Both increased mean flow and bloom development originates from an increase in stratification. However, other predicted periods of increasing modelled surface mean velocity (from day 152 to day 154 and from day 156 to day 159) do not coincide with bloom development. This suggests that other factors regulating phytoplankton bloom development e. g. light availability, nutrient availability and grazing rate (Cloern, 1996) need to be accounted for.

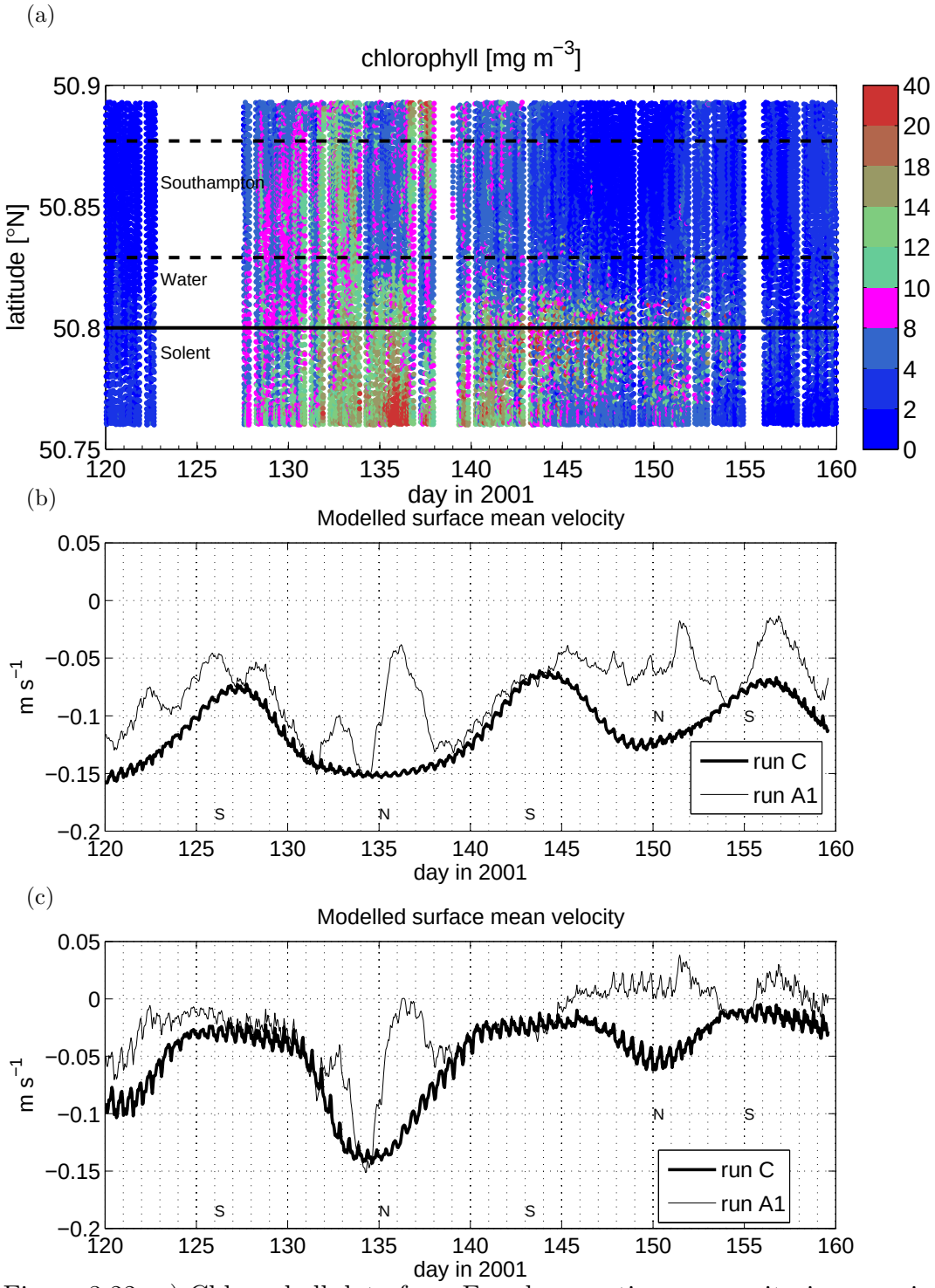

Figure 3.22: a) Chlorophyll data from Ferrybox continuous monitoring, y-axis indicates the position in the along-estuary direction. The solid line separates at 50.80°N Southampton Water (from 50.89 °N to 50.80°N) and the Solent (from 50.80°N to 50.77°N). The dashed line delineates the position in the along-estuary direction where is calculated the surface mean velocities. Observational data gap are illustrated by the white area. b) Modelled mean velocity (position along the estuary: 50.87 °N). Run C (without wind forcing) is plotted to illustrate Spring-Neap cycle. c) Modelled mean velocity (position along the estuary: 50.83 °N). Run C (without wind forcing) is plotted to illustrate Spring-Neap cycle. 'N' and 'S' indicates 'Neaps' and 'Springs' respectively.

Chapter 4

Observations of the temporal and spatial variability of light attenuation

4.1 Introduction

Light in seawater is attenuated as it propagates through the water column. As a consequence, light field variations impact on the distribution and species diversity of the primary producers living either in suspension in the water column or at the seafloor (Olesen, 1996; Charrier et al., 2000; Gattuso et al., 2006).

Two major processes contribute to light attenuation: absorption and scattering (figure 4.1 and figure 4.2). They can be defined as inherent properties of the medium and depend on the total content of dissolved and particulate matter (Preisendorfer, 1961).

Pure water alone contributes to absorption of the light field. Seawater contains dissolved matter which increases significantly the absorption spectrum of the light field. Decay of plant matter produces humic and fluvic acids referred to as coloured dissolved organic matter (CDOM) also known as gilvin or yellow substance (Kirk, 1994). Coastal waters are highly productive regions and receive a large amount of terrigeneous inputs from the land, and as a result contain a high percentage of suspended particulate matter (SPM). The SPM is divided into two categories: organic and inorganic particles or tripton. Particle size and abundance influence the attenuation of the light field in seawater. Organic particles contributing to absorption and scattering include (Mobley, 1996): viruses, colloids, bacteria, phytoplankton, organic detritus (or non-living particles) and large

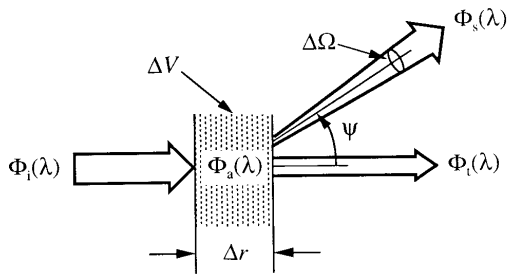

Figure 4.1: Optical quantities used to describe inherent optical properties, defined as the behaviour of a parallel beam of light incident upon a thin layer of medium, redrawn from Mobley (1996). By conservation of energy, the spectral radiant power of the incident light ϕ_i is equal to the sum of the spectral radiant power ϕ_a absorbed by an infinitesimal layer Δr, the spectral radiant power ϕ_s scattered and the spectral radiant power transmitted ϕ_t

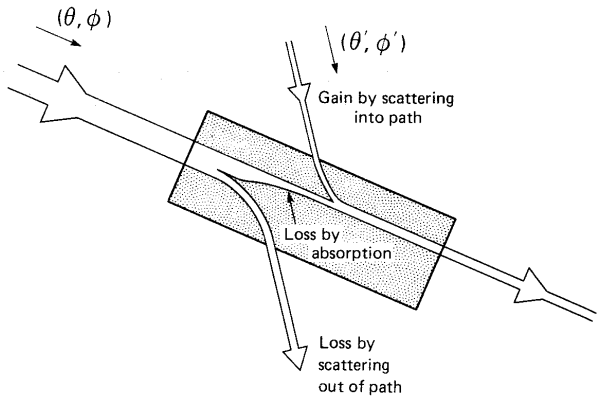

Figure 4.2: Net rate of change in the light flux in an infinitesimal layer of seawater. Part of the incident light corresponds to gain by scattering coming from other directions. The net rate of change in the infinitisimal layer corresponds to loss by scattering and absorption and gain by scattering into path and incident light. Redrawn from Kirk (1994)

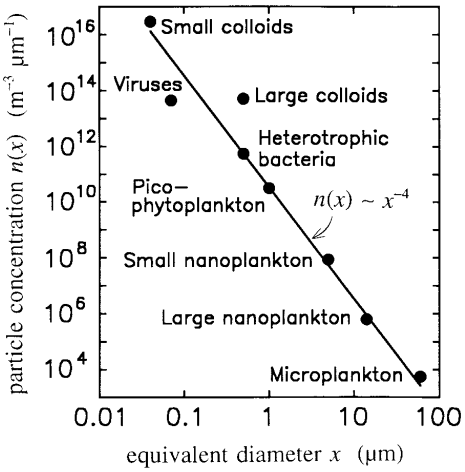

Figure 4.3: Concentration of biological particles in seawater in the open ocean. Redrawn from Mobley (1996)

particles which occur in the form of zooplankton and marine snow (figure 4.3). Inorganic particles are mostly formed from ground quartz, sand, clay minerals or metal oxides. The scattering and absorption properties of these particles vary depending on the wavelength.

The diffuse attenuation coefficient for downwelling irradiance or the downwelling diffuse attenuation coefficient $K_d(z, \lambda)$ determines the amount of light available at a certain depth and is defined as a function of the downward irradiance $E_d(z, \lambda)$ at each depth z and for each spectral band λ by :

$$K_d(z, \lambda) = -\frac{1}{E_d(z, \lambda)} \frac{dE_d(z, \lambda)}{dz} \tag{4.1}$$

$K_d(z, \lambda)$ is described as an apparent property of the field, since it is determined both by the inherent properties of the light field and changes in the incident radiation field at the sea surface during the course of the day (cloud conditions and sun angle).

The radiative transfer theory which describes the variation of the radiance field as it propagates through a medium allows the determination of a relationship between the coefficient of attenuation and the inherent optical properties of the medium. More specifically, by applying the Monte-Carlo procedure to solve the radiation transfer equation, $K_d(PAR)$ can be related to the absorption coefficient a and scattering coefficient b in units of m^{-1} (Kirk, 1981b,a, 1984) :

$$K_d(z, \lambda) = \frac{1}{\mu_o} \sqrt{a^2 + G(\mu_o) ab} \tag{4.2}$$

where μ_o is the angle of solar incidence and $G(\mu_o)$ is the relative contribution of scattering to vertical attenuation. Measurement of these inherent properties are difficult since it requires measurements with a high temporal, spatial, and spectral resolution (Schwarz, 2002). In practice, various simplified functions exist to predict a and b either based on their measurements at a specific wavelength, or as a cumulative function of the absorption coefficient for chlorophyll a, CDOM and other components, e. g. Babin et al. (2003).

A common simplified formulation is a partitioning of $K_d(z, \lambda)$ between the most important contributors of the attenuation in sea water and after integrating over the wavelength of the visible spectrum to give $K_d(z, PAR)$ where PAR is the Photosynthetic Available Radiation, ranging from 400-700nm of the total spectrum. This approximation is widely used in ecosystem models simulating attenuation of light in the open-ocean, since the contribution of the phytoplankton and the water colour is predominant, and gives the following equations:

$$K_d(z, PAR) = k_w + \frac{1}{z} \int_0^z k_c \times Chl dz \tag{4.3}$$

where k_w is the coefficient for contribution of water and gilvin in units of m^{-1}, k_c is the coefficient for the contribution of phytoplankton to attenuation in units of mg^{-1} m^2, and Chl is the concentration in chlorophyll a in units of mg m^{-3}. In coastal seas which are regions of freshwater influence, the contribution of non-living particles is non-negligible, and other site-specific semi-empirical relationships exist to simulate the temporal variation of $Kd(z, PAR)$, relating attenuation to environmental conditions or hydrographic conditions (Liu, 2005; Xu et al., 2005).

In Southampton Water, $K_d(z, \lambda)$ fluctuates throughout a semi-diurnal tidal cycle as described by Charrier et al. (1998a) and Charrier et al. (1998b). After averaging over the semi-diurnal cycle, values of K_d at 4m depth were found to be 1.14 m^{-1}, 0.79 m^{-1} and 1.04 m^{-1} for λ =443 nm, λ =555.6nm and λ =670.4 nm, respectively, which means that the light is rapidly attenuated and shifted towards the blue green band of the visible spectrum (Charrier et al., 1998a).

In this study, the depth-integrated PAR-averaged (integration over the range of wavelength of the visible spectrum) fraction of the coefficient of attenuation for downwelling irradiance is examined, in order to determine the temporal and spatial pattern of the light penetration in the Solent-Southampton Water estuarine system. This has important implications for the light-photosynthesis relationship which determines the rate of primary production, and its application to ecosystem models.

4.2 Seasonal variation in $K_d(PAR)$

4.2.1 Data

A set of discrete measurements collected in 2001, 2002 and 2003 at various locations has been combined to investigate the spatial and seasonal variation of the coefficient of attenuation in the Solent-Southampton Estuary. The four sample locations are Eling (50^{o}54.50N 1^{o}27.85W) at the mouth of the Test River, NWNetley (50^{o}51.97N,1^{o}22.64W) at the mid-estuary, Calshot (50^{o}49.51N 1^{o}18.20W) at the mouth of the estuary and Horse Elbow (50^{o}44.10, 1^{o}3.80W) in the coastal water as plotted on figure 4.4.

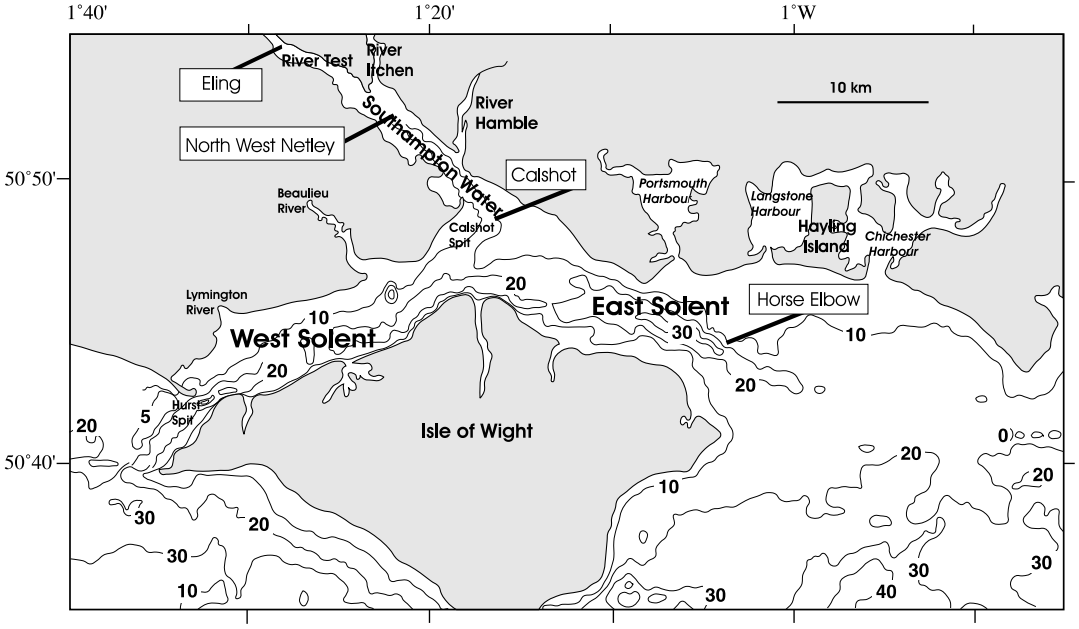

Figure 4.4: Sampling location of data collected in year 2001, 2002 and 2003.

Sampling frequency varied from one week to two weeks, and the sampling period covers the spring-summer-autumn period. This dataset includes $K_d(PAR)$, turbidity measurements and chlorophyll *a* concentrations. Hydrographic conditions are given by measurements of salinity and temperature. A summary of the data is given in table 4.1.

A LI-COR non spherical (or 2 π because it measures light coming from an hemisphere) underwater light quantum sensor (Model LI-1000) was used to measure surface incident and downwelling PAR irradiance field at 1m intervals from surface to bottom in 2001, 2002 and occasionally in 2003. In 2003 water transparency was measured with a secchi disk and its conversion to $K_d(PAR)$ is discussed in the following section.

year		2001	2002		2003
reference		Torres-Valdés and Purdie (2006) Torres-Valdés (2004)	Torres-Valdés and Purdie (2006) Torres-Valdés (2004)	Iriarte and Purdie (2004)	Iriarte and Purdie (2004)
location	Eling	✓	✓	×	×
	NWNetley	✓	✓	✓	✓
	Calshot	✓	✓	✓	✓
	Horse Elbow	×	×	✓	×
sampling period		April to October	April to October	March to July	February to December
sampling frequency		every two weeks,at spring tide	every two weeks,at spring tide	every week	every week
Kd(PAR) from	light profiles	√	✓	✓	✓ *
	secchi depth	×	×	✓	✓
Chl-a	chl-a surface/1m	✓	✓	✓	✓
	chl-a 2m	✓	✓	×	×
	chl-a 4m	✓	×	×	×
	chl-a 7m	✓	×	×	×
	chl-a 9m	✓	✓	×	×
turbidity	1-4m (surface)	✓	✓	✓	×
	depth-averaged	×	×	✓	×
salt	salt surf/1m	✓	✓	✓	✓
	salt 2m	✓	✓	×	×
	salt 4m	✓	×	×	×
	salt 7m	✓	×	×	×
	salt 9m	✓	✓	×	×

Table 4.1: Summary table of the discrete data. ✓ indicates samples collected or measured and × indicates samples not collected or not measured. * from May to September only.

Turbidity, salinity and temperature measurements have been derived from the YSI 6600 water quality probe. Salinity and temperature were occasionally measured with a T/S probe (Tetra-Con 325) when the multiprobe was not available.

Water samples to determine chlorophyll *a* were first filtered through Whatman GF/F filters and chlorophyll *a* concentration was extracted by sonification and centrifugation. Chlorophyll *a* concentration was obtained by measuring the fluorescence of the sample in a Tuner 10-AU fluorometer, calibrated with standard chlorophyll *a* measured with a Cecil CE 1010 spectrometer.

Additional environmental data include daily river inputs from the Environment Agency at the mouth of the Test and Itchen Rivers, and tidal range prediction at Dockhead and Portsmouth from Admiralty Charts.

4.2.2 Data homogenisation

Data homogeneity has been estimated by comparing the degree of linear correlation between $K_d(PAR)$ calculated from light measurements and secchi disk measurements when both measurements were made in 2002 and 2003 at Calshot, NWNetley and Horse Elbow. $K_d(PAR)$ is calculated by integrating over depth following the Beer-Lambert law:

$$E_z = E_o e^{-K_d(PAR)z} \tag{4.4}$$

which gives after transformation:

$$K_d(z, PAR) = \frac{1}{z} ln(\frac{E_o}{E_z}) \tag{4.5}$$

$K_d(PAR)$ (depth-mean value of $K_d(z, PAR)$) is conveniently obtained by linear regression between $ln(\frac{E_o}{E_z})$ and z .

The linear regression between $K_d(PAR)$ and the inverse ratio of Secchi depth (Figure 4.5) gives the function

$$K_d(PAR) = \frac{1.128}{SD} - 0.035 \tag{4.6}$$

with a coefficient of determination equal to 0.716. SD is the Secchi depth. The linear regression forced through origin gives the result:

$$K_d(PAR) = \frac{0.754}{SD} \tag{4.7}$$

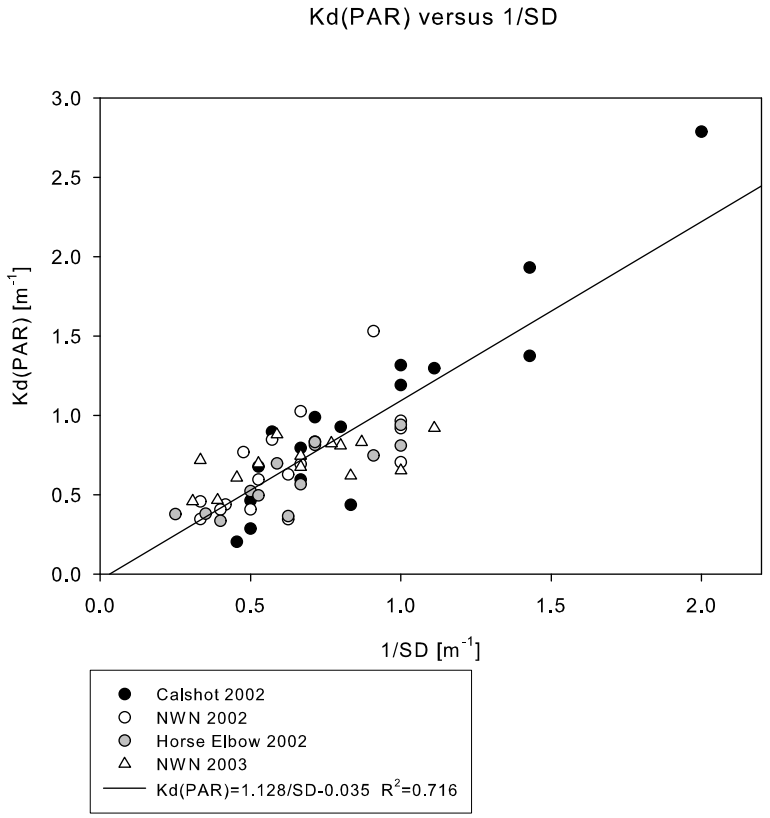

Figure 4.5: Scatterplot of the diffuse downwelling attenuation coefficient from light measurements and the inverse ratio of Secchi Depth. The results of the linear regression are shown in the legend.

station	a	yo	R^2
all datapoints	1.128 $\pm$ 6.316 10^{-2}	-0.035 $\pm$ 8.45 10^{-2}	0.716
all datapoints (regression through origin)	1.128 $\pm$ 6.397 10^{-2}	0 $\pm$ 6.397 10^{-2}	0.709
Calshot 2002	1.441 $\pm$ 1.417 10^{-1}	-0.269 $\pm$ 1.390 10^{-1}	0.777
NWN 2002	0.927 $\pm$ 2.558 10^{-1}	0.112 $\pm$1.715 10^{-1}	0.467
Horse Elbow 2002	0.752 $\pm$ 1.376 10^{-1}	0.128 $\pm$ 9.051 10^{-2}	0.717
NWN 2003	0.345 $\pm$ 1.019 10^{-1}	0.478 $\pm$ 6.766 10^{-2}	0.367

Table 4.2: Results of the coefficients and the standard deviation for the linear regression $K_d(PAR)$=yo+a/SD for the independent datasets.

with a coefficient of determination of 0.715 .

The uncertainty associated with Secchi disk transparency measurements originates from illumination conditions, sea surface roughness, sensitivity of the observer's eye and optical properties of the sea water (Kropotov, 1985; Preisendorfer, 1986). The high coefficient of determination found indicates that this uncertainty remains at a reasonable level, and for this reason, the linear function (equation 4.6) has been used to convert water transparency measurements (i.e. Secchi Depth) in 2003 to $K_d(PAR)$.

The coefficients of regression for each independant dataset are given in table 4.2. The variation in the coefficients illustrates the variation in time of the year covered by the individual dataset, and variation in hydrodynamic conditions between locations.

4.2.3 Time-series of light attenuation

After homogenisation between $K_d(PAR)$ derived from secchi depth measurements and $Kd(PAR)$ derived from irradiance profiles, results have been plotted for each station separately: Eling in figure 4.6, NWNetley in figure 4.7, Calshot in figure 4.8, and Horse Elbow in figure 4.9. A large scatter of data is visible, as a result of short time-scale variability and seasonal time-scale variability.

Short time-scale variability, at the scale of one week, is characterized by the presence of isolated peaks. Eling in 2001 and NWNetley in 2001 appear to be less affected by high scatter as suggested by their smoother curves. This could be explained by the homogeneity of the mixing conditions, since all measurements at Eling in 2001 and 2002 and at NWNetley in 2001 originate from the same dataset, when observations were made during spring tides, at high tide (Torres-Valdés and Purdie, 2006). By contrast, measurements at NWNetley, Calshot and Horse Elbow in 2002 and 2003 were not made at the same tidal state. Measurements occurred at less than one week intervals and thus occur either at Neaps or Springs at NWNetley and Calshot in 2002 and 2003. Tidal effects on resuspension can be assumed to be a factor in this high-frequency variability. Another factor of high frequency variability can be meteorological effects like rainfall and winds.

Temporal variability is affected by a seasonal trend which suggests that the lowest values occur in late spring and early in summer. This aspect is most visible at Horse Elbow (figure 4.9) and NWNetley (figure 4.7). Higher values are generally found in autumn and late winter. The higher frequency variability mentioned above affect the signal and tends to mask the seasonal trend. The minimum

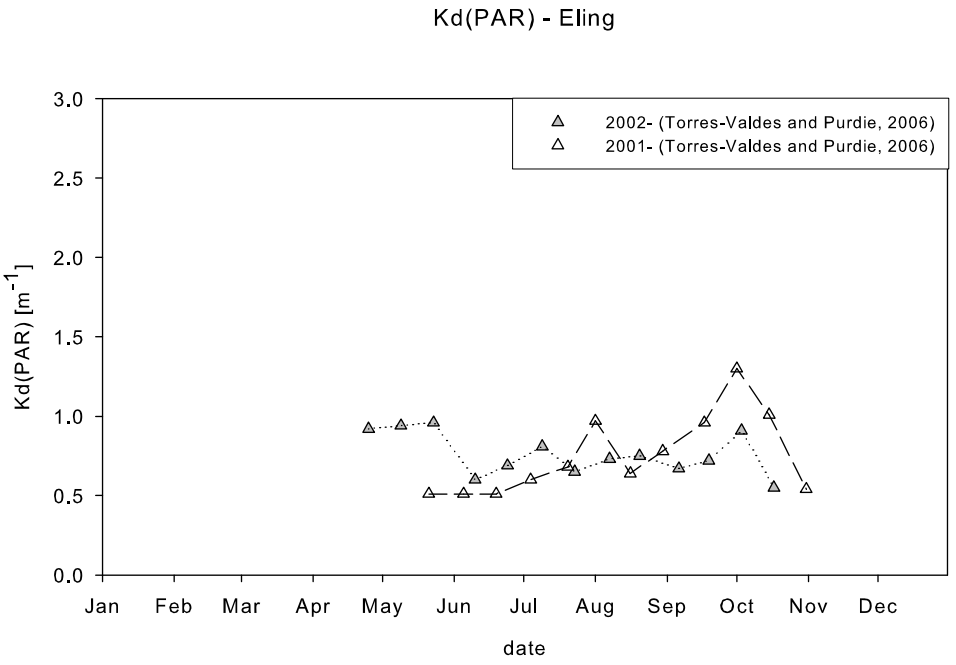

Figure 4.6: Time-series of the downwelling diffuse attenuation coefficient at Eling in 2001 (white triangles) and 2002 (grey triangles).

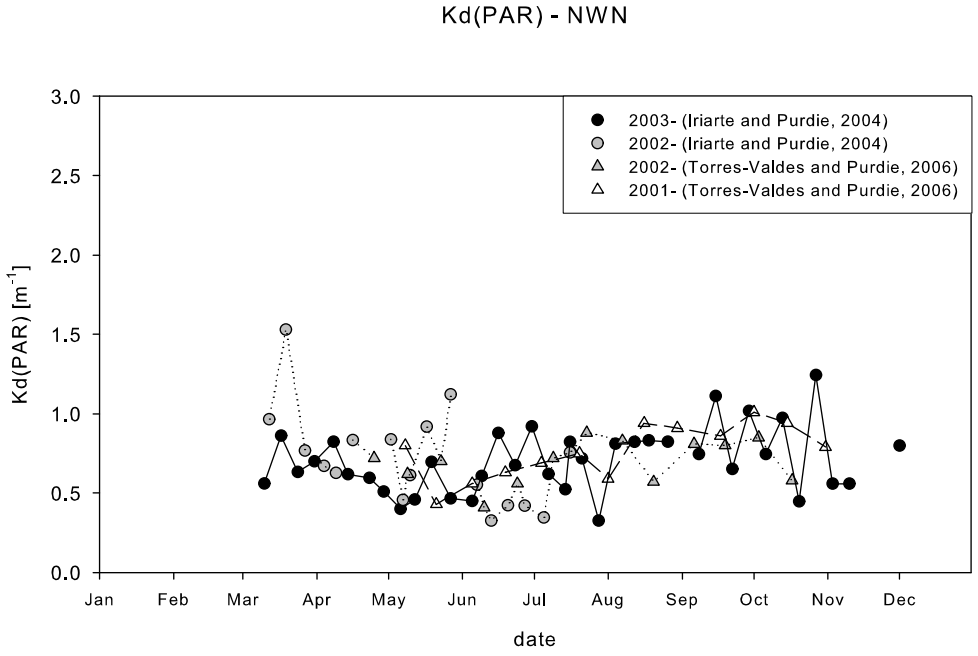

Figure 4.7: Time-series of the downwelling diffuse attenuation coefficient at NWNetley in 2001 (white triangles), 2002 (grey circles and triangles) and 2003 (black circles).

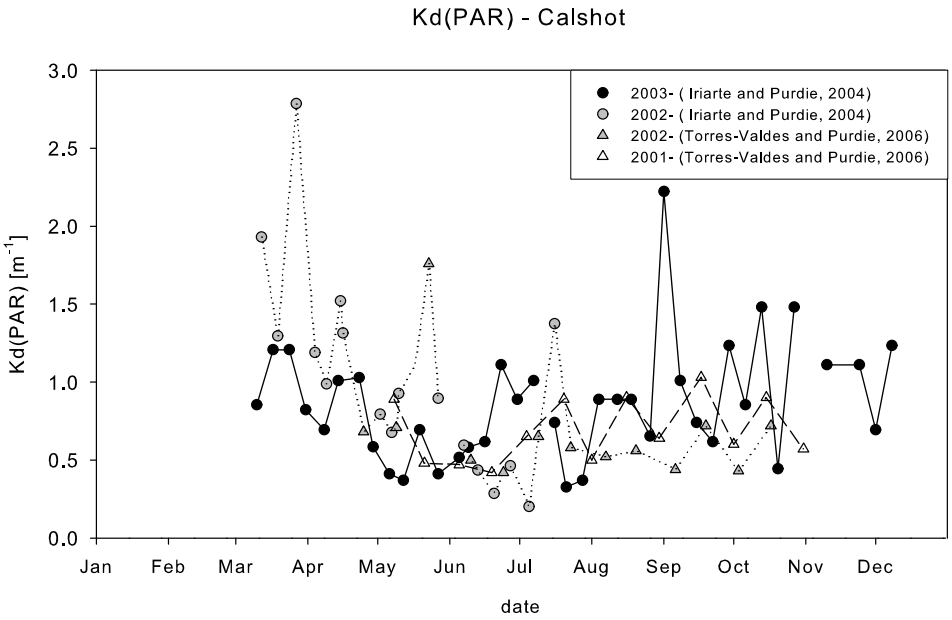

Figure 4.8: Time-series of the downwelling diffuse attenuation coefficient at Calshot in 2001 (white triangles), 2002 (grey circles and triangles) and 2003 (black circles).

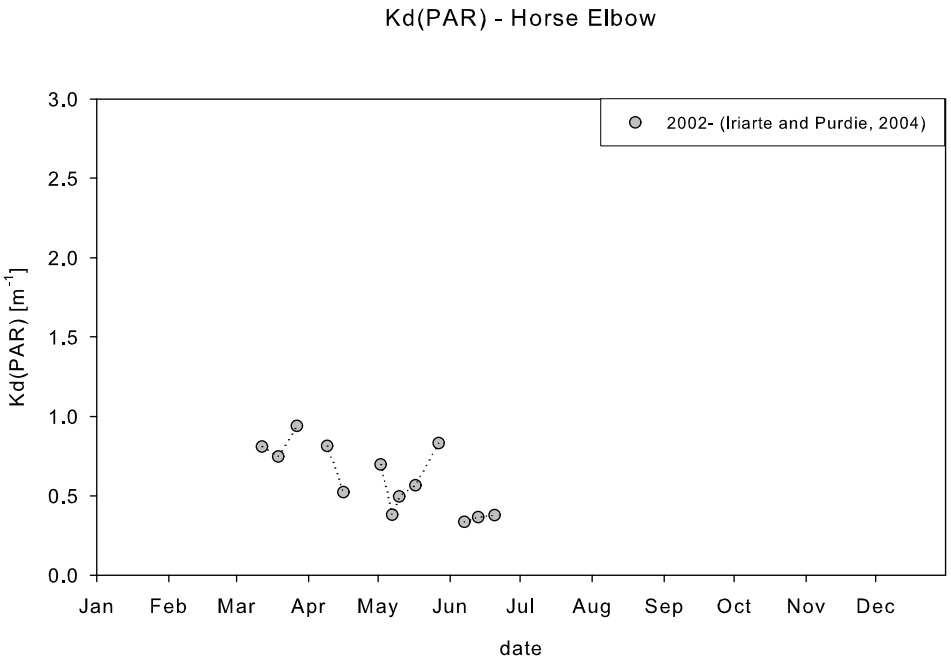

Figure 4.9: Time-series of the downwelling diffuse attenuation coefficient for downwelling irradiance at Horse Elbow in 2002 (grey circles).

$K_d(PAR)$ values are generally found in May-June in the inner estuary, and occur later in June-July at the mouth of Southampton Water with significant interranual variability: at Eling, this minimum value occurred on 8/5/2001 and on 10/6/2002. At North West Netley, this minimum value occurred on 21/5/2001, on 13/6/2002 and on 6/5/2003. At Calshot, the minimum value occurred on 19/6/2001, 5/7/2002 and 21/7/2002.

The range of $K_d(PAR)$ values is higher at Calshot with values from 0.20 to 2.78 m^{-1}, and is reduced towards the upper estuary with a range from 0.34 to 1.55 m^{-1} at NWNetley and 0.51 to 1.30 m^{-1} at Eling. Significant photosynthesis can take place above the euphotic depth, defined as the depth at which the downwelling irradiance $E_d(PAR)$ falls below 1 % of the surface downwelling irradiance $E_o(PAR)$ (Kirk, 1994). In the approximation of $Kd(PAR)$ being constant with depth, the euphotic depth is equal to $\frac{4.6}{K_d(PAR)}$. the range of euphotic depth is therefore from 1.65 to 23 m, from 2.96 m to 13.52 m and from 9.10 m to 3.53 m at Calshot, NWNetley and Eling, respectively. Calshot is more exposed than the other stations and is characterized by well-mixed conditions throughout the tidal cycle, which could explain the wider range of values obtained. The coefficient of attenuation at Horse Elbow ranges from 0.33 to 0.93 m^{-1} (figure 4.9), resulting in an euphotic depth varying from 4.94 m to 13.93 m. This narrow range is explained by the restriction of the dataset to a small portion of the annual cycle (spring).

4.2.4 Effect of environmental conditions on attenuation

To determine whether a relationship exists between light attenuation and environmental factors (tidal range, river flow, turbidity, chlorophyll *a*, surface salinity) for use in the ecosystem model (chapter 5), a statistical analysis based on the calculation of the coefficient of correlation has been carried out. Calculation of the coefficient of correlation between instantaneous wind (hourly measurements) and $K_d(PAR)$ measurements has not been made since the exact sampling time of $K_d(PAR)$ is not available. Environmental conditions vary at the different sites depending on the proximity of the freshwater sources, which determine hydrographic conditions, mixing intensity and nutrient inputs. For this reason, calculation has been performed for all years but separately for each station.

A high degree of correlation exists between turbidity and $K_d(PAR)$ (table 4.3): turbidity accounts for 52.7 %, 42.5 %, 64.5 % and 83.9 % of the variability of the attenuation at Eling, NWNetley, Calshot, and Horse Elbow respectively. A linear regression analysis using data points from all stations gives the linear relationship :

station	turbidity [1-4m]	averaged water column turbidity
Eling	0.726	×
NWNetley	0.652	0.539
Calshot	0.803	0.824
Horse Elbow	0.916	0.855

Table 4.3: Coefficient of correlation between $K_d(PAR)$ and turbidity.

station	coefficient of correlation between $Kd(PAR)$ and river flow (Test only)	coefficient of correlation between $Kd(PAR)$ and river flow (Test + Itchen)
Eling	-0.347	×
NWNetley	0.335	0.338
Calshot	0.338	0.452
Horse Elbow	0.625	0.659

Table 4.4: Coefficient of correlation between $K_d(PAR)$ and river flow.

station	coefficient of correlation between $Kd(PAR)$ and tidal range
Eling	0.130
NWNetley	0.116
Calshot	0.340
Horse Elbow	0.539

Table 4.5: Coefficient of correlation between $K_d(PAR)$ and tidal range.

station	coefficient of correlation between $Kd(PAR)$ and chlorophyll *a*
Eling	-0.154
NWNetley	-0.103
Calshot	-0.333
Horse Elbow	-0.116

Table 4.6: Coefficient of correlation between $K_d(PAR)$ and chlorophyll *a*.

station	coefficient of correlation between $Kd(PAR)$ and surface salinity
Eling	-0.024
NWNetley	0.379
Calshot	0.013
Horse Elbow	×

Table 4.7: Coefficient of correlation between $K_d(PAR)$ and surface salinity.

$$K_d(PAR) = 0.049 \times turb_{1-4m} + 0.340 \quad (4.8)$$

with a coefficient of determination of 0.607 (equivalent to a coefficient of correlation of 0.779), where $turb_{1-4m}$ is the turbidity from 1 to 4m.

Table 4.4 gives the results of the correlation between river flow variation and $K_d(PAR)$. River flow is positively correlated to $K_d(PAR)$ at NWNetley and Calshot with a coefficient of correlation above 0.330. At Eling, a negative correlation is found, which may be due to the time of the year considered: in Summer and Autumn, gravitational circulation weakens as part of the seasonal effect of a low fresh water input from the Test. This may favour resuspension of particles by turbulence under low stratification effects. River flow is mostly an index of seasonal inputs in suspended matter. At Horse Elbow, only a very limited part of the seasonal cycle is covered by the time-series and the high coefficient of correlation reveals that the river flow and the attenuation coefficient covary only during this time of the year.

Tidal range appears to explain more than 34 % of the variability in coastal areas (Calshot and Horse Elbow) and is positively correlated with $K_d(PAR)$ (table 4.5). In this area, tidal mixing plays a major role in sediment resuspension and controls the variability of the SPM concentration (Velegrakis et al., 1999b). The correlation coefficient is higher at Horse Elbow but this result may not apply to a longer time-series and indicates only that river flow and attenuation covary from March to June 2002.

Correlation between Chlorophyll *a* and $K_d(PAR)$ are presented in table 4.6. Chlorophyll *a* concentration accounts for less than 15 % of the variability of the coefficient of attenuation when considering the stations in the upper estuary (Eling and North West Netley). This result is in agreement with a previous study demonstrating phytoplankton as a minor component of the particle load of estuarine water, compared with terrigeneous particles (O'Mahony and Weeks, 2000). Chlorophyll *a* contribution is higher at Calshot, by a factor of four. This may be explained by the variation in the seasonal cycle in phytoplankton concentration between the head and the mouth of the estuary, which is dominated by a spring bloom in Calshot, whereas at NWNetley, blooms occurs over a longer period between spring and late summer.

Correlation between salinity and $K_d(PAR)$ is affected by strong variations between stations (table 4.7). At Eling, a very small degree of correlation exists between the two parameters, and this result is specific to the months of the

seasonal cycle covered (summer-autumn). At NWNetley, a higher positive correlation is found (coefficient of correlation of 0.379) certainly because a sufficient portion of the seasonal cycle is covered by the time-series compared with the results from Eling. This coefficient is similar to the correlation between $K_d(PAR)$ and river flow, which probably means that salinity variations reflect the seasonal cycle in river flow. No correlation is found between salinity and $K_d(PAR)$ at Calshot possibly because of an almost constant salinity occuring at this coastal station throughout the year. No salinity data are available at Horse Elbow.

The determination of a statistical model of $Kd(PAR)$ as a linear regression of the various parameter has proved to be not satisfactory. A low coefficient of determination was found and a different set of parameter was needed to get the best fit depending on the location.

4.2.5 Bimonthly average of the coefficient of attenuation

The whole dataset of attenuation coefficient $K_d(PAR)$ was processed by calculating bimonthly averages at each station and for each year in order to filter out the high frequency variability generated by meteorological effects and tidal effects, superimposed on the seasonal cycle. Results are plotted in figure 4.10 and the numerical values are given in table 4.8. This method leads to the calculation of each bimonthly averages from a minimum of 3 values.

Data from 2001 and 2003 (figure 4.10a and 4.10c) can be interpreted together: a minimum value for $K_d(PAR)$ is found in May-June at all stations (Eling, NWNetley and Calshot), while higher values occur in late autumn and March-April. This reveals a general trend with May-June being a 'window' of low attenuation, when phytoplankton experience the highest level of under water irradiance.

In 2002 (figure 4.10b) a similar seasonal pattern is observed at NWNetley, but does not occur at the other stations. At Horse Elbow, the lack of data in July and August does not indicate May-June 2002 as the minimum $K_d(PAR)$ value in the seasonal cycle, but an estimate in March-April 2002 indicates a decrease during spring in attenuation, in agreement with the general pattern described above. At Calshot and Eling in 2002, the lowest values for attenuation were found in summer and early in autumn.

No data are available to estimate $K_d(PAR)$ in January-February. Results from the coefficient of correlation analysis presented in the previous subsection (section 4.2.4) indicate that a strong correlation exists between $K_d(PAR)$ and the

		location			
bimonth	year	Eling	NWN	Cashot	Horse Elbow
Mar-Apr	2001				
	2002		**0.843** ±0.128 (7)	**1.463** ±0.229 (8)	**0.766** ±0.069 (5)
	2003		**0.662** ±0.044 (8)	**0.926** ±0.080 (8)	
May-Jun	2001	**0.51** ±0 (3)	**0.605** ±0.077 (4)	**0.565** ±0.218 (4)	
	2002	**0.797** ±0.090 (4)	**0.594** ±0.061 (13)	**0.705** ±0.112 (12)	**0.505** ±0.064 (8)
	2003		**0.617** ±0.064 (9)	**0.649** ±0.087 (8)	
Jul-Aug	2001	**0.734** ±0.066 (5)	**0.776** ±0.066 (5)	**0.716** ±0.148 (5)	
	2002	**0.735** ±0.033 (4)	**0.750** ±0.069 (4)	**0.578** ±0.027 (4)	
	2003		**0.700** ±0.059 (9)	**0.680** ±0.096 (7)	
Sep-Oct	2001	**0.952** ±0.157 (4)	**0.900** ±0.096 (4)	**0.775** ±0.116 (4)	
	2002	**0.712** ±0.075 (4)	**0.760** ±0.061 (4)	**0.578** ±0.082 (4)	
	2003		**0.867** ±0.093 (8)	**1.121** ±0.183 (9)	
Nov-Dec	2001				
	2002				
	2003		**0.639** ±0.080 (3)	**1.038** ±0.118 (4)	

Table 4.8: Results of the statistics year by year and site by site after grouping datapoints into bimonthly averages. Values in bold font, normal font and brackets are respectively the averages, the standard error and the number of datapoints.

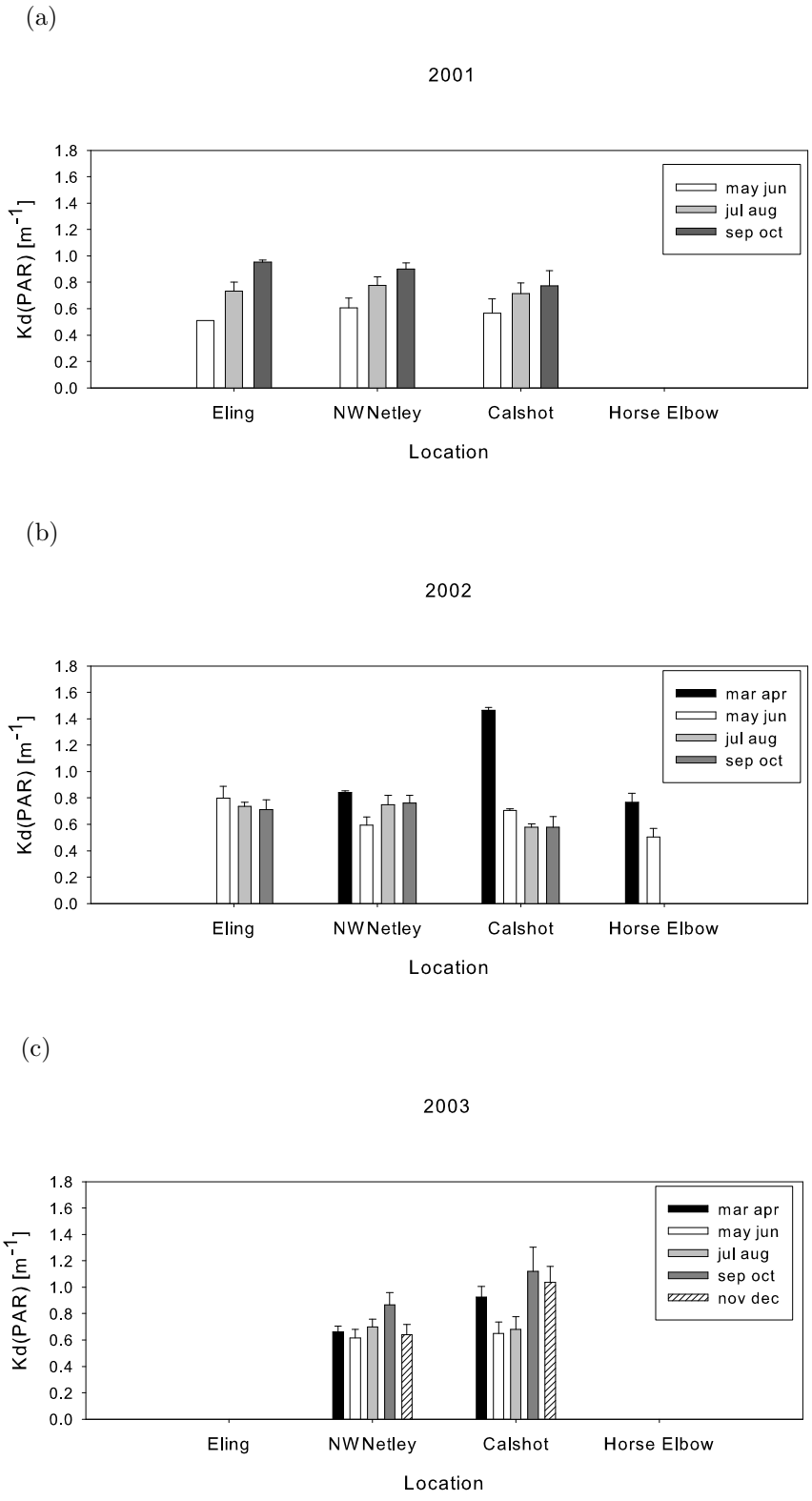

Figure 4.10: Bimonthly average of the attenuation coefficient for downwelling irradiance (numerical values from table 4.8). Error bars indicate the standard error.

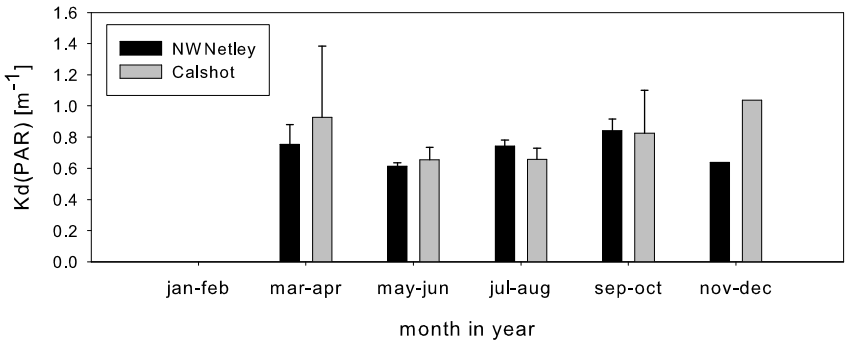

Figure 4.11: Seasonal cycle of $K_d(PAR)$, based on the datasets at Calshot and NWNetley. In November-December, no standard error is calculated since only one year of data is available.

concentration of suspended material in seawater. Previous measurements of suspended particulate matter in Southampton Water in winter indicate that high concentrations are measured at a similar or higher level than in March-April and a high $K_d(PAR)$ is expected during this time of the year (Shi, 2000).

The values obtained after averaging bimonthly have been further averaged over all years to highligh the typical long-term variation obtained for $K_d(PAR)$ at NWNetley and Calshot (figure 4.11). The typical seasonal cycle obtained confirm the presence of a low value in May-June. A large difference occurs between the two stations in November-December. However, the value in November-December is representative only of year 2003. The high standard error demonstrates the high level of interannual variability.

4.2.6 Curve fitting of $Kd(PAR)$

To simulate the seasonal decrease of the attenuation coefficient for downwelling irradiance ($K_d(PAR)$) in spring, two mathematical functions have been fitted to the dataset. The first function derives from a Weibull curve and takes the form:

$$K_d(PAR) = A_{min} + (A_{max} - A_{min})e^{-cT_d sin(\frac{t\pi}{T_d}+\phi))^4} \tag{4.9}$$

where T_d is the total number of day in a year and t is the time in days. This fitting function is characterized by four adjustable parameters: A_{min}, A_{max} in m^{-1}, c with no units and ϕ in degrees .

The second fitted function corresponds to the function used by Kratzer et al. (2003) to fit the seasonal cycle of suspended sediment concentration in the Menai Strait (UK).

$$K_d(PAR) = a_o + a_1 cos(\frac{2\pi}{T_d}t) + a_2 sin(\frac{2\pi}{T_d}t) \quad (4.10)$$

where a_o, a_1 and a_2 are the adjustable parameters. These parameters do not relate to the abiotic or biotic parameters, but are used to fit the long-term temporal variation of the diffuse attenuation coefficient throughout a year, more specifically the decrease in diffuse attenuation coefficient occuring in May and June. The first formulation has the advantage of being able to simulate two plateaus, but the disavantage of fitting 4 parameters instead of 3 for the Kratzer formulation. This fitting procedure allows for the extrapolation of the attenuation curves throughout the year to compensate for the lack of measurements in winter and to determine the annual average as employed by Kratzer et al. (2003).

The two functions (equations 4.9 and 4.10) have been fitted to the datasets available for Calshot and NWNetley in 2002 and 2003. $K_d(PAR)$ measurements available for Eling, Horse Elbow, NWNetley in 2001 and Calshot in 2001 do not cover a sufficient portion of the seasonal cycle to be fitted with the mathematical function. The fitting was done using a Marquardt-Levenberg algorithm included in the Sigmaplot software to find the coefficient that gives the best fit between equation and data (SigmaPlot 9 User's guide, 1998). Results of the fitting function are presented in figure 4.12, 4.13, 4.14 and 4.15. The parameter values for both functions, the annual average and the coefficients of the fitting function are given in tables 4.9 and 4.10. In addition, results for the best fit obtained with a linear function is given in table 4.11. For each case (NWN2002, Calshot 2002, NWN 2003 and Calshot 2003) the goodness of fit in the case of a linear function is always inferior compared with the goodness of fit obtained with the Weibull equation (table 4.9) and the kratzer equation (table 4.10). In all cases, the goodness of fit as indicated by the coefficient of determination is better for the first mathematical function (equation 4.9) than the Kratzer function (equation 4.10). For both functions and both stations, the fitting procedure gives a better fit in 2002 compared to 2003 (column R^2 in table 4.9 and table 4.10).

The calculation of the annual average by the two methods (fitting functions and) gives very similar results. A difference ranging from 0.0001 to 0.1 m^{-1} is found between column a_o in table 4.10 and column 'annual average' in table 4.9) while comparing site-by-site and year-by-year. The annual averages are higher at Calshot in comparison with NWNetley, in both years and for both fitting procedures. The average value can be related to observations of the spatial variation in SPM concentration in the estuary which indicates that the mouth of the estuary is more

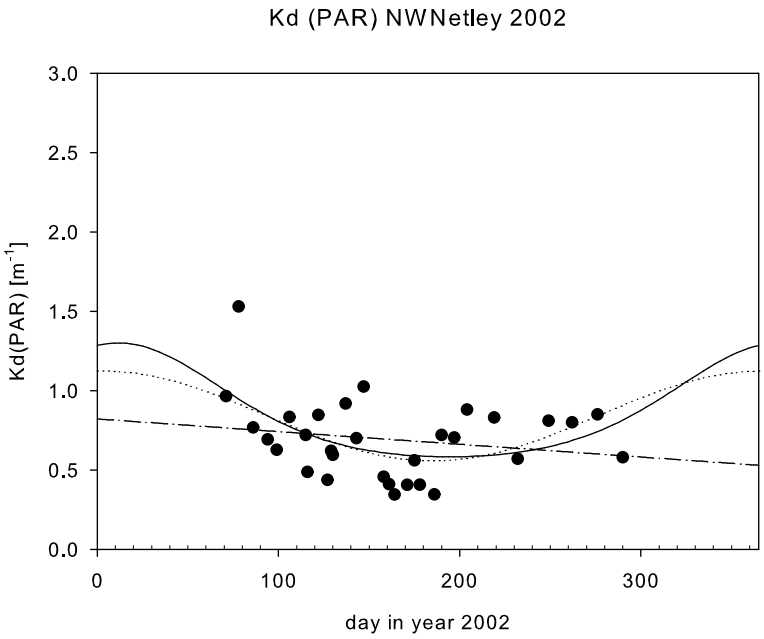

Figure 4.12: Result of the fitting procedure at NWNetley in 2002. The solid line is the best fit obtained with the Weibull function (equation 4.9). The dotted line is the best fit obtained with the Kratzer equation (equation 4.10). The dash-dotted line is the best fit obtained with the linear function.

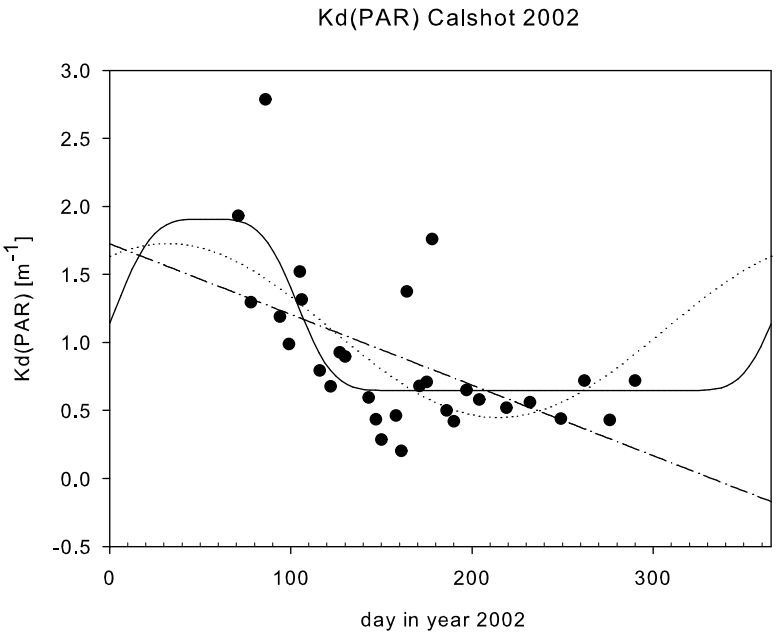

Figure 4.13: Result of the fitting procedure at Calshot in 2002. The solid line is the best fit obtained with the Weibull formulation (equation 4.9). The dotted line is the best fit obtained with the Kratzer equation (equation 4.10). The dash-dotted line is the best fit obtained with the linear function.

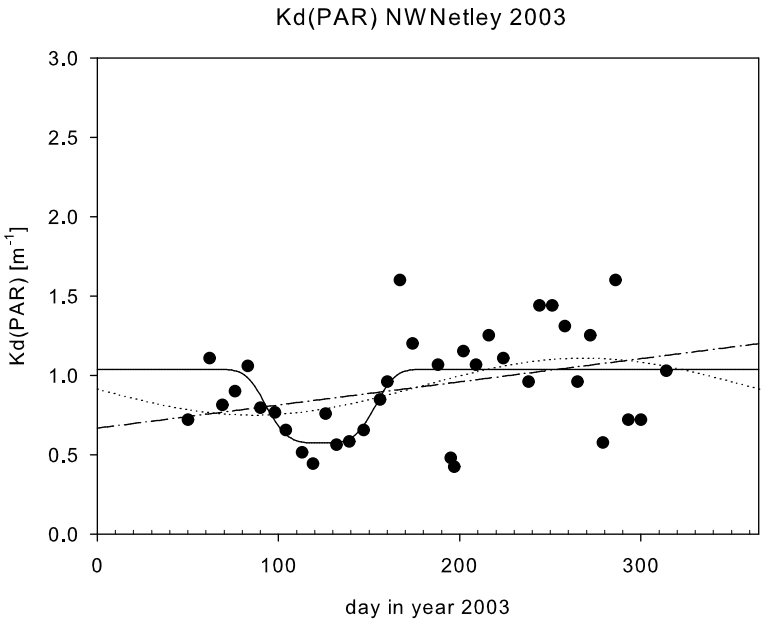

Figure 4.14: Result of the fitting procedure at NWNetley in 2003. The solid line is the best fit obtained with the Weibull formulation (equation 4.9). The dotted line is the best fit obtained with the Kratzer equation (equation 4.10). The dash-dotted line is the best fit obtained with the linear function.

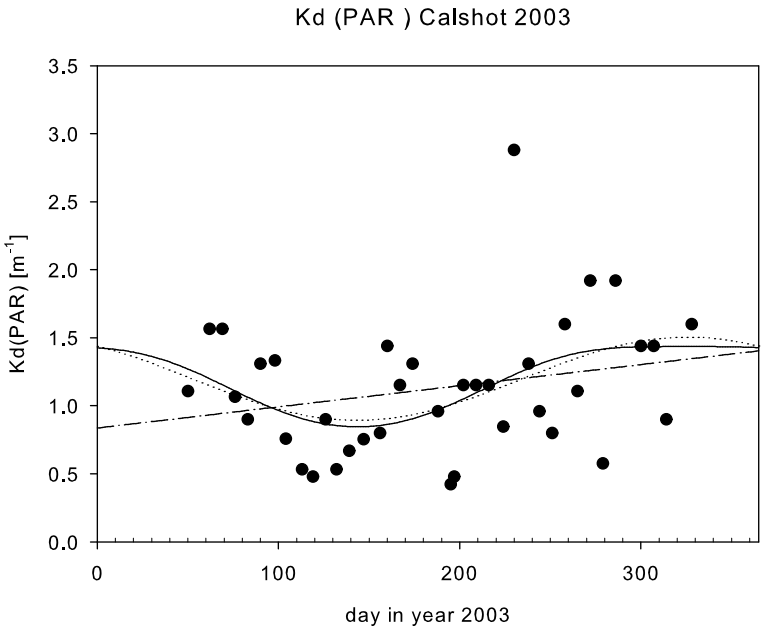

Figure 4.15: Result of the fitting procedure at Calshot in 2003.The solid line is the best fit obtained with the Weibull formulation (equation 4.9). The dotted line is the best fit obtained with the Kratzer formulation (equation 4.10). The dash-dotted line is the best fit obtained with the linear function.

turbid than the inner estuary. The combination of well-mixed conditions and the presence of a sand bank favour tidal resuspension of fine sediment and generate high turbidity at the mouth of the estuary (Lauria, 1998; Shi, 2000).

location and year	A_{min} [m^{-1}]	A_{max} [m^{-1}]	ϕ [no unit]	c [no unit]	annual average [m^{-1}]	R^2
NWN 2002	0.649	1.3	-0.668	0.0044	0.868	0.432
Calshot 2002	0.645	1.906	-0.465	0.0060	0.992	0.531
NWN 2003	1.0379	0.574	-1.061	0.0098	0.962	0.299
Calshot 2003	0.001	1.436	0.335	0.0023	1.199	0.195

Table 4.9: Results of the best fit obtained with equation 4.9. R^2 is the goodness of fit, expressed as the coefficient of determination.

location and year	a_o [m^{-1}]	a_1 [m^{-1}]	a_2 [m^{-1}]	R^2
NWN 2002	0.840	0.0109	0.0283	0.248
Calshot 2002	1.090	0.333	0.545	0.405
NWN 2003	0.928	-0.179	-0.0159	0.191
Calshot 2003	1.199	-0.191	0.238	0.170

Table 4.10: Results of the best fit obtained with the Kratzer formulation (equation 4.10). The average annual value is given by ao. R^2 is the goodness of fit, expressed as the coefficient of determination.

location and year	y_o [m^{-1}]	a [m^{-1}]	R^2
NWN 2002	0.821	-8 10^{-4}	0.037
Calshot 2002	1.724	-5.19 10^{-3}	0.300
NWN 2003	0.667	1.45 10^{-3}	0.120
Calshot 2003	0.837	1.55 10^{-3}	0.063

Table 4.11: Results of the best fit obtained with a linear function (Kd(PAR)=yo+at) where t is the time in day. R^2 is the goodness of fit, expressed as the coefficient of determination.

4.3 Spring-neap modulation of turbidity

4.3.1 Data

A strong correlation exists between downwelling irradiance and surface turbidity as demonstrated in section 4.2.4 (equation 4.8). To determine the cause of short-term variability in the downwelling diffuse attenuation coefficients, two datasets of high

temporal resolution (10 minutes) of turbidity, fluorescence and salinity measurements using continuous monitoring at Calshot in 2002 and Berth 49 in 2004 during the productive months have been examined. Calshot is located at the mouth of Southampton Water (figure 4.4) while Berth 49 is located in the Test estuary, close to Dockhead (figure 4.16). The tidal range is from Admiralty Charts. A summary table of these datasets is given in table 4.12.

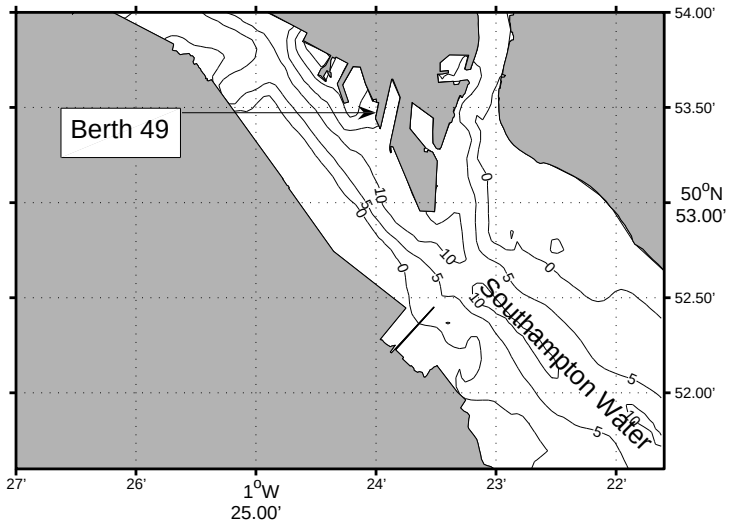

Figure 4.16: Location of Berth 49 in the Test estuary at the left-hand side of the Eastern Docks.

year		2002	2004
location	Berth 49	×	✓
	Calshot	✓	×
sampling period		15/4/2002 to 12/6/2002	7/7/2004 to 22/10/2004
sampling frequency		every 10 minutes	every 10 minutes
chorophyll *a*		✓	✓
turbidity		✓	✓
salinity		✓	✓

Table 4.12: Summary table of the discreet data. ✓ indicates samples collected or measured and × indicates samples not collected or not measured

.

In 2004 two YSI probes were deployed 1 meter below a surface float at Berth 49: One section of the mooring included a YSI backscatter turbidity sensor, a thermistor sensor to record temperature and a conductivity sonde to calculate salinity. The second section of the mooring included a fluorometer to derive

chlorophyll *a* concentrations, and similarly a temperature sonde and conductivity sonde. The sensors were cleaned to remove bio-fouling and calibrated against discrete water samples taken from both estuary and laboratory derived standards on a weekly basis.

In 2002, a YSI 6600 multiparameter sonde measuring water quality parameters was moored below the navigational buoy at Calshot, suspended by a chain and maintained below the water depth by a weight. The depth varied from 1.5m to 2.2m.

Values above the level of 400 NTU for turbidity and 50 mg m^{-3} for chlorophyll *a* have been filtered out from the time-series. They correspond to suspicious values which can be generated by transient effects like boat traffic near the sensor and biofouling (Pittam, 2004).

Turbidity measurements are strongly affected by cycles of resuspension and deposition during the course of a tidal cycle as usually observed in tidally-dominated environment (Weeks et al., 1993). In Southampton Water, this cycle is particularly complex due to the unusual tidal curve (Lloyd-Jones, 2002). To investigate the medium-term variation (at the scale of a day) of the turbidity measurements, an average of the turbidity over a tidal cycle (defined as the time period between two successive low tides) has been calculated. This time-series has been plotted against the semi-diurnal tidal range, beginning at low tide. Each averages are plotted at the time of high tide occuring between the two successive low tides considered for each semi-diurnal average.

4.3.2 Results

Time-series of the semi-diurnal averaged salinity, semi-diurnal averaged chlorophyll *a* concentration, semi-diurnal averaged turbidity and the tidal range at Calshot are plotted on figure 4.17. In 2002 at Calshot, blooms of phytoplankton detected by peaks of chlorophyll *a* occurred in June, later than the time period considered. Thus Chlorophyll *a* concentration remains at a low level (<6 mg m^{-3}), but tends to increase during springs and decrease during neaps. Turbidity is closely related to the tidal range. A linear regression analysis gives the relationship:

$$Turbidity = -6.85 + 6.38 \times T \tag{4.11}$$

where T is the tidal range, with a coefficient of determination of R^2=0.847 (figure 4.18). Consequently the medium-term variation in turbidity measurements

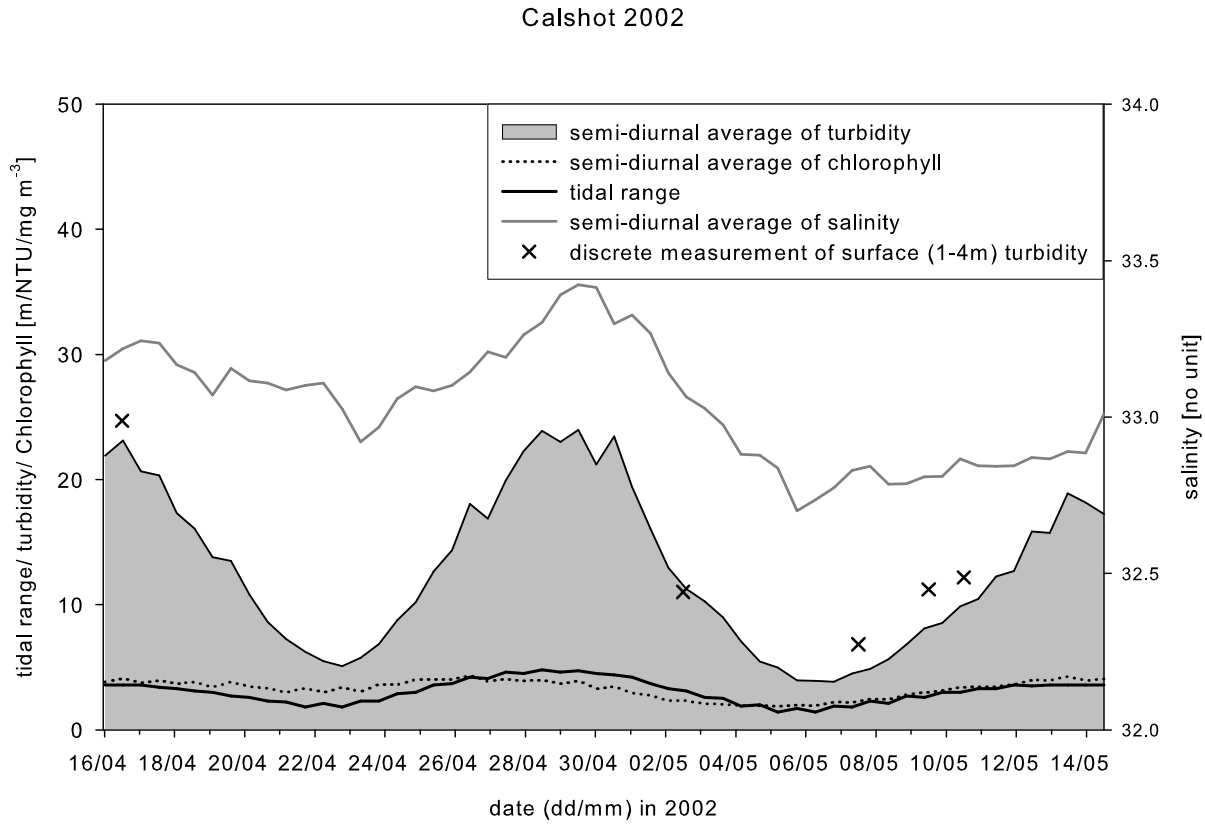

Figure 4.17: Time-series of measurement at Calshot, after averaging throughout a semi-diurnal cycle.

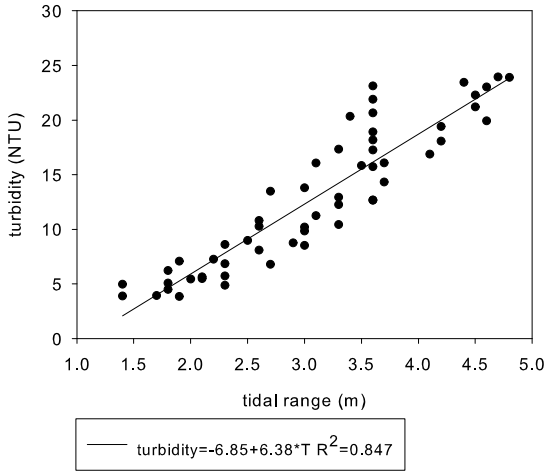

Figure 4.18: Scatter plot of tidal range and turbidity measurement at Calshot, after averaging over a semi-diurnal tidal cycle.

is dominated by the spring-neap modulation. Six discrete turbidity measurements presented in the previous section overlap this time-series. The relative error between discrete measurements and continuous measurements ranges from 1% to 28 %. This moderate error suggests the reliability of the continuous measurements of turbidity as a result of the calibration procedure.

Time-series for Berth 49 in 2004 are plotted on figure 4.19. Five blooms (defined as a peak of chlorophyll concentration above 10 mg m^{-3}) occured during this time period on 3/08, 13/8 19/8 23/8 and 10/9. The first two appear to be initiated at spring tide, while the last one occurs at neap tide. The 8-fold increase in chlorophyl concentration between 12 and 14 august was likely caused by the advection of pathces of phytoplankton that are known to exist in the estuary during *Mesodinium Rubrum* blooms (Crawford et al., 1997). Salinity is affected by transient variability, with a major freshening of the water occuring from 28/7 to 4/8, possibly generated by a high level of rainfall in the previous day which can generate patch of water with different hydrographic properties in the estuary, as demonstrated by Dyer (1975). The turbidity temporal variation matches the fortnightly modulation of the tidal cycle and the linear regression analysis gives the following relationship:

$$Turbidity = 2.11 + 0.812 \times T \tag{4.12}$$

where T is the tidal range, with a coefficient of determination of R^2=0.177 (figure 4.20a). This low coefficient of determination results from high frequency fluctuations affecting the signal. Applying the linear regression analysis to the time-series excluding the productive period (from day 27/7 to 21/9), a very similar linear function is obtained, but with a modest improvement of the coefficient of determination:

$$Turbidity = 1.28 + 1.08 \times T \tag{4.13}$$

with a coefficient of determination $R^2 = 0.309$ (figure 4.20b).This result is consistent with previous observations that phytoplankton concentration plays a minor role in total suspended matter (O'Mahony and Weeks, 2000) .

To compare the results from the two stations, a higher level of turbidity is obtained at Calshot with a range of 3.85-23.95 NTU to compare with the range of 1.76-7.95 NTU at NWNetley.

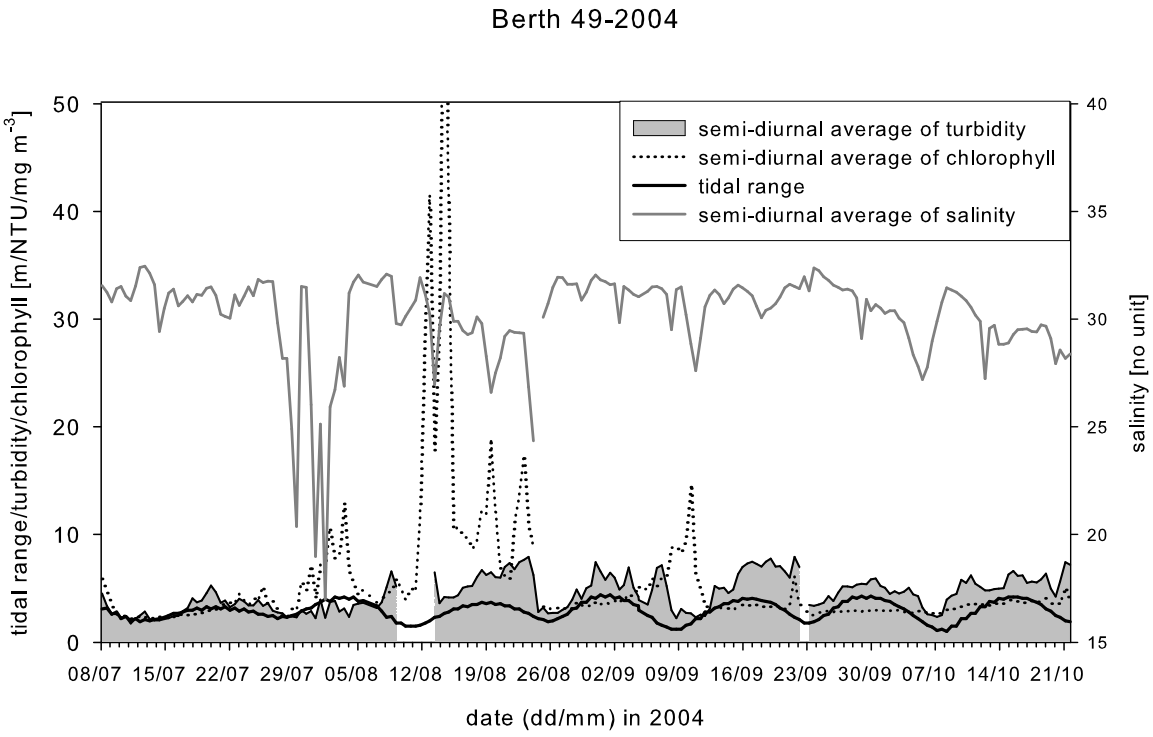

Figure 4.19: Time-series of measurements made at Berth 49, after averaging throughout a semi-diurnal cycle.

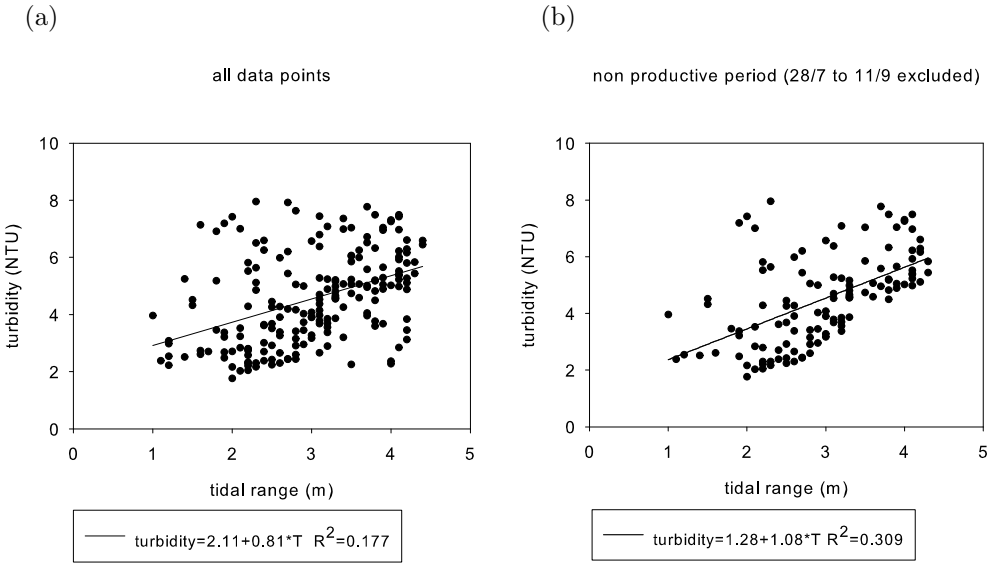

Figure 4.20: Scatter plot of tidal range and turbidity measurement at Berth49, after averaging over a semi diurnal tidal cycle.

4.4 Summary and discussion

Using the theory of Duntley-Preisendorfer (Duntley, 1963) describing the attenuation of contrast of a submerged object, Tyler (1968) demonstrated that the sum of the coefficient of attenuation for downwelling irradiance $Kd(PAR)$ and the beam attenuation coefficient (referred to as the contrast attenuation coefficient) are linearly related to the inverse ratio of the Secchi depth SD:

$$c + Kd = cst/SD \tag{4.14}$$

where cst is a constant which has been estimated in the range of 8.69 to 9.42 (Tyler, 1968; Holmes, 1970). In the present study, a linear relationship is found between $Kd(PAR)$ and $\frac{1}{SD}$, which suggests consequently that $K_d(PAR)$ and c covary. SD is predominantly governed by scattering, whereas $K_d(PAR)$ is dominated by both absorption by dissolved absorbers and scattering by particles in suspension (Koenings and Edmundson, 1991). As a result, the product $K_d(PAR) \times SD$ strongly varies depending on the contents of absorbers and scattering present in the water, as observed in lakes and some estuaries (Koenings and Edmundson, 1991; Liu, 2005). This study demonstrates that in Southampton Water, $K_d(PAR)$ and SD covary, and this result is explained by the predominance of one component in sea water determining the variation in attenuation and transparency, in this case turbidity (Kirk, 1994).

This study reveals that $K_d(PAR)$ is strongly affected by a seasonal cycle, and at the time scale of a week is strongly affected by spring-neap tidal variations by deduction from the continuous turbidity measurement. The results demonstrate that the spring-neap tidal variations can be described as a linear function of the tidal range. In the case of the long term variability, a seasonal cycling is observed, with a minimum in May-June and high concentration in late summer-autumn. This seasonal cycle is only poorly correlated to the rate of fluvial inputs, indicating the importance of the complex physical processes determining spatial and temporal variation of turbidity. For example, river flow may have a dual effect: high river flow brings higher concentration of terrigineous inputs, and at the same time tends to inhibit mixing by the tides and therefore resuspension of sediments in the water column. These competing processes makes it difficult to predict the long-term variation of the concentration of suspended particles in the water column as a function of the environmental physical parameters (salinity, tidal range and river flow) tested in this study. In the Irish Sea, a statistical model

defines the rate of suspended particulate matter concentration based on current speed, tidal displacement, and wind intensity and can explain 35 % of the variability of the turbidity (Weeks et al., 1993). Using a similar approach to Weeks et al. (1993) a statistical model has been developped to simulate the variation of the suspended matter throughout the semi-diurnal cycle in Southampton Water, which can explain 40.9 % of the variability of the SPM concentrations using current speed, tidal displacement, stratification and wind speed (Lloyd-Jones, 2002). A more general model exists to predict maximum turbidity concentration as a function of tidal intrusion length (mouth to limit of reversing tidal currents), tidal range and residence time determined with a datasets of 45 estuaries (Uncles et al., 2002). Further work could include these other estuarine parameters for the determination of an empirical relationship of the variability of $K_d(PAR)$.

Another source of variability in suspended sediment is the wind, which is not accounted for in this analysis, under the assumption that tidal effects and river flow are the dominant control of SPM variability. In Southampton water, wind speed was found to be a small contributor of the variability in turbidity (Lloyd-Jones, 2002). By contrast, wind-wave induced resuspension appears as a dominant factor in microtidal areas (Booth et al., 2000; Paphitis and Collins, 2005) and lakes (Bailey and Hamilton, 1997; Douglas and Rippey, 2000). Wind is one of the most complex environmental parameters to relate to SPM concentration in estuaries due to its stochastic variability . Wind effects can be related to both long-term changes and short term variability in SPM concentration. Changes in turbidity concentration have been correlated to changes in wind strength and the annual storm index in the Irish Sea (White et al., 2003). In the Bohai Sea, seasonal variations in wind intensity determine variations between spring and summer turbidity, as a result of intensification of bottom erosion by the effect of wind waves (Jiang et al., 2004). In the Tweed estuary, observations of turbidity are correlated to the swell waves height (Uncles and Stephens, 1997). Suspended sediment in the water column is determined by the degree of turbulence in the water column and the bed-shear stress at the interface of the sea bottom. Wind contributes to suspended sediment dynamics by generating turbulence, and wind-waves are determined by wind intensity, direction and fetch, all of which are generating bed-shear stress. A numerical study from May et al. (2003) demonstrated a complex interaction between the timing of the wind and the spring-neap cycle which significantly modulates the spring-neap variability in turbidity, and gives the conclusion that wind fetch plays a dominant role in creating spatial variation in

turbidity. Due to the complexity of the processes involved, assessment of the contribution of wind on turbidity in Southampton Water would require the use of a numerical model of sediment transport, which is beyond the scope of this study.

Both discrete $K_d(PAR)$ measurements and turbidity measurements provide evidence of higher attenuation occuring at the mouth of Southampton Water (Calshot) compared to the upper reaches of Southampton Water (NWNetley and Eling). The more likely mechanism to explain this spatial variation is the increased level of sediment resuspension occuring at the mouth of Southampton Water, where well-mixed conditions prevail. This suggests that in the upper reaches of Southampton Water, the proximity to the Test and Itchen river which is a major source of terrestrial sediment does not compensate for the inhibition of tidal resuspension by the increased stratification.

Further work could include the use of remote sensing to observe the long-term variability in $K_d(PAR)$. $K_d(PAR)$ is retrieved from the reflectance of seawater (Mueller, 2000). This algorithm currently in operation performs poorly in coastal areas, and two recent algorithms have been developped and reaches the accuracy of 14 % and 11 % for the estimate of $K_d(490)$ and $K_d(443)$, respectively (Lee et al., 2005; Doron et al., 2007). Additionnally, tests need to be carried out to determine the empirical formulation used to derive $K_d(PAR)$ from $K_d(490)$ for the same reason that it has been determined for the open-ocean (Morel et al., 2007). MOderate Resolution Imaging Spectroradiometer-Aqua (MODIS) and Sea-viewing Wide Field-of-view Sensor (SeaWiFS) provide $K_d(490)$ with 9 km and as monthly bins from daily observations. The spatial resolution is coarse and does not capture the spatial variations from the head to the mouth of Southampton Water. The time resolution is sufficiently high to examine the seasonal cycle of the attenuation coefficient. This work reveals the importance of the tidal cycle with a pronunced fortnightly variation superimposed on the seasonal variability of the attenuation coefficient. Therefore monthly bins could be affected by aliasing due to modulation in the spring-neap tidal cycle, which could be another source of error in the estimation of the temporal variation of $K_d(PAR)$.

Chapter 5

Effects of light attenuation on the spring phytoplankton bloom

5.1 Introduction

Freshwater runoff is responsible for the high concentration of nutrients in coastal areas which stimulates production of organic matter by primary producers. Phytoplankton dynamics play a key role in biogeochemical cycling and influences the entire food chain. One of the major features of phytoplankton dynamics is the formation of blooms, the largest of which generally occurs in spring in the northern hemisphere. Coastal ecosystems such as estuaries, lagoons and bays are usually highly populated areas and influenced by human activities. Determining what controls the variability of phytoplankton bloom dynamics is vital to be able to discriminate factors contributing to natural variability from anthropogenic changes.

Net primary production in coastal waters have been identified as a balance between primary production (limited by light and nutrients), and losses due to pelagic and benthic grazing and mortality generated by parasites and viruses (Cloern, 1996).

In shallow water environments, the optimal conditions for phytoplankton population growth are highly dependent on the local conditions prevailing in the water column. The degree of mixing, water depth and water turbidity are the main forcing functions which determine the relative importance of gains and losses of phytoplankton production. In estuaries, the high variability of hydrodynamic conditions and the complex interplay between mechanisms determining the rate of primary production makes the predictions of bloom occurrence a non-trivial question. For instance, turbulent mixing impacts on nutrient availability by

generating resuspension of sediment, which in turn modulates phytoplankton growth rate due to an increase in water turbidity and a reduction in the mean water column irradiance. In stratified waters, nutrients are generally more abundant at the bottom and light availability is the highest at the surface. A stratified water column reduces benthic grazing pressure (Koseff et al., 1993). Variations in water depth during the course of the tidal cycle determine the intensity of benthic grazing (inversely proportional to water depth) and light availability which decreases exponentially with depth (Lucas et al., 1999a; Lucas and Cloern, 2002). Spring bloom initiation is usually reported to coincide with three favourable factors of phytoplankton production: increased stratification, increased light irradiance and reduced water column turbidity (Cloern, 1996; Arndt et al., 2007).

Estuaries are often hypernutrified environments and nutrients are not usually a limiting factor to the spring phytoplankton bloom. Light attenuation has been demonstrated to be the controlling factor affecting spring phytoplankton bloom variability through the effect of cloud cover (Townsend et al., 1994), interranual variability in turbidity driven by wind effects, tidal mixing, river flow (May et al., 2003; Desmit et al., 2005) and effects of changing water depth during the course of the semi-diurnal tidal cycle (Lucas and Cloern, 2002). In Southampton Water, a comparison of time-series of chlorophyll *a* measurements and solar irradiance indicates that irradiance level higher than 380 W h m^{-2} d^{-1} during the week prior to the bloom is a necessary but not always sufficient condition for the onset of a bloom of magnitude above 10 mg m^{-3} (Iriarte and Purdie, 1994). The same study reveals that a decrease of the coefficient of attenuation below 0.5 m^{-1} is coincident with the generation of the major spring bloom event (Iriarte and Purdie, 1994). The spring-neap tidal cycle does not seem to determine bloom initiation, with spring blooms occuring either on neap tides or spring tides (Iriarte and Purdie, 1994).

In this section, the impact of the variability in light availability in the generation of the spring phytoplankton bloom is investigated using a simple zero-dimensional biogeochemical model, coupled to a benthic layer to account for nutrient regeneration. Interranual variation in the light penetration is simulated by various parameterisations of the attenuation coefficient, in order to examine its impact on the magnitude and timing of the spring bloom for different years. This modelling approach focuses on the essential *in situ* processes occuring in the water column for the determination of phytoplankton production, and short-term effects

generated by tidal variation in water column depth are ignored. A constant water depth is applied and stratification effects are not modelled, under the approximation that the semi-diurnal regime of periodic stratification in partially-mixed estuaries is closer to complete mixing than to persistent stratification for phytoplankton blooms (Lucas et al., 1998).

5.2 Description of the biomass model of pelagic ecosystem

A pelagic ecosystem model deriving from Fasham et al. (1990) containing 4 main state variables has been developed to simulate the dynamics of an idealised marine ecosystem. The four state variables are dissolved inorganic nitrogen (DIN), phytoplankton (P), zooplankton (Z) and detritus (D). Similar to Kelly-Gerreyn et al. (2004) and Anderson and Williams (1998), this model has been coupled to a sediment compartment (S) to account for the deposition of organic material to the seabed and a return flux of nutrients (DIN) to the pelagic domain, assuming implicit transformation (degradation and remineralization) of the sedimentary organic matter. DIN released to the overlying layer by benthic processes is a non-negligible source of nutrients to estuarine primary production due to the shallow depth (Boynton and Kemp, 1985; Heip et al., 1995). Phosphorus is generally the limiting nutrient in fresh water whereas nitrogen is the limiting nutrient in marine water in spring. Estuaries are a transition zone and both elements (phosphorus and nitrogen) can be considered as the limiting nutrient of the food chain (Wolanski, 2007). Here the assumption of nitrogen limitation in spring is made and all fluxes are expressed in nitrogen currency (mmol N m^{-3} for DIN, P, Z, D and mmol N m^{-2} for S). Chorophyll *a* concentration is a diagnostic variable and is calculated as a function of the phytoplankton concentration using a constant carbon to nitrogen ratio θ_P, the mass to weight conversion factor for carbon θ_C and the cellular carbon to chlorophyll ratio θ_{chl} (see parameter values in table 5.1):

$$Chl = \frac{\theta_c \theta_P P}{\theta_{chl}} \tag{5.1}$$

Fluxes of nitrogen between compartments are determined by the relevant biogeochemical processes (figure 5.1, tables 5.2 and 5.3). The system of partial differential equations determining the interations between the 5 ecosystem

symbol	definition	standard values	units
θ_P	molar C to N ratio in phytoplankton (Redfield ratio)	6.62 [a]	mmol C (mmol N)$^{-1}$
θ_C	Mass to weight conversion factor for carbon	12	mg C (mmol C)$^{-1}$
θ_N	Mass to weight conversion factor for nitrogen	14	mg N (mmol N)$^{-1}$
θ_{Chl}	ratio of phytoplankton cellular carbon to chlorophyll a	50 [c]	mg mg^{-1}
θ_{zoo}	percentage of Nitrogen: dry mass ratio in zooplankton	0.1[b]	mg N mg^{-1}

Table 5.1: Conversion factors used in the model. References: [a] Redfield et al. (1963), [b] Cushing et al. (1981), [c] Fasham et al. (1990).

symbol	variable	units
Chl	Chlorophyll a	mg Chl m^{-3}
D	Detritus	mmol N m^{-3}
DIN	Dissolved Inorganic Nitrogen	mmol N m^{-3}
I_o	PAR-fraction of surface irradiance	W m^{-2}
P	Phytoplankton	mmol N m^{-3}
S	Sediment	mmol N m^{-3}
Z	Zooplankton	mmol N m^{-3}

Table 5.2: List of model variables.

variables DIN, P, Z, D and S are described in detail below.

- Production of phytoplankton biomass is generated by the rate of primary production and depends on light, temperature and nutrient concentration. Losses include grazing by zooplankton, vertical sinking of phytoplankton, and non predatory mortality induced by senescence and bacterial decomposition of cells. The phytoplankton rate of change is described by equation 5.2:

$$\frac{dP}{dt} = Pr - Gp - Dep - Vep \tag{5.2}$$

  The phytoplankton growth rate Pr varies according to the availability of photosynthetically available light, determined by the photosynthesis-light relationship $F(I_{z,t})$ (Smith, 1936) integrated over the whole water column of depth H, and the supply of nutrient defined by the nutrient limitation factor Q:

$$Pr = J(I_{z,t})QP \tag{5.3}$$

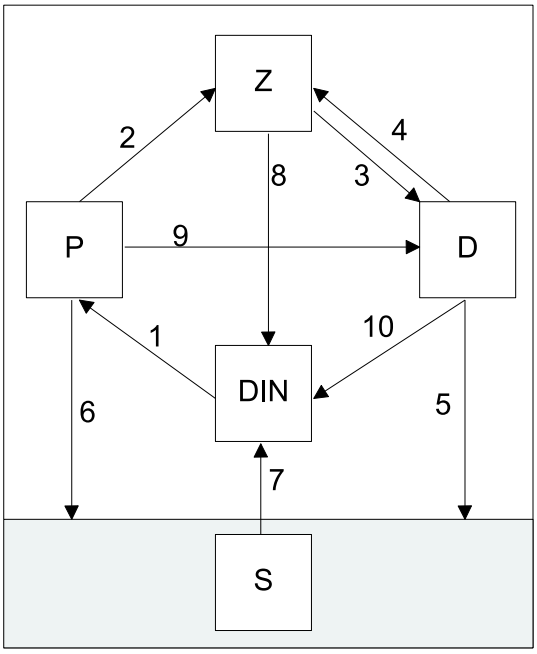

Figure 5.1: Ecosystem structure
1: nutrient uptake by phytoplankton, 2: zooplankton grazing, 3: zooplankton mortality, 4: zooplankton grazing, 5: sinking of detritus, 6: sinking of phytoplankton, 7: sediment return flux, 8: zooplankton excretion, 9: phytoplankton mortality, 10: detritus bacterial decomposition.

symbol	process	units
Ded	Detritus remineralisation	mmol N m^{-3} d^{-1}
Dep	Phytoplankton mortality	mmol N m^{-3} d^{-1}
Dez	Zooplankton mortality	mmol N m^{-3} d^{-1}
Exz	Zooplankton excretion	mmol N m^{-3} d^{-1}
Gd	Grazing of detritus	mmol N m^{-3} d^{-1}
Gp	Grazing of phytoplankton	mmol N m^{-3} d^{-1}
J	Light-limitation of phytoplankton growth	dimensionless
Pr	DIN-limited photosynthesis	mmol N m^{-3} d^{-1}
Q_{10fac}	Temperature dependency	dimensionless
Q	DIN limitation of phytoplankton growth	dimensionless
Ved	Vertical sinking of detritus	mmol N m^{-3} d^{-1}
Vep	Vertical sinking of phytoplankton	mmol N m^{-3} d^{-1}
V_p	Phytoplankton maximum growth rate	m^{-3} d^{-1}

Table 5.3: List of model processes.

$$J(I_{z,t}) = \frac{1}{H}\int_0^H F(I_{z,t})dz \tag{5.4}$$

$$F(I_{z,t}) = \frac{V_p \alpha I_{z,t}}{\sqrt{(V_p^2 + \alpha^2 I_{z,t})}} \tag{5.5}$$

$$I_{z,t} = I_0 e^{-kt} \tag{5.6}$$

where V_p is the growth rate as $I \to \infty$ with a temperature dependency (Eppley, 1972), $I_{z,t}$ is the irradiance and I_o is the PAR-fraction of surface irradiance.

$$V_p = 0.65 \times (1.066)^T \tag{5.7}$$

where T is the temperature. The nutrient limitation factor Q is based on the Michaelis-Menten type equation (Michaelis and Menten, 1913) .

$$Q = \frac{DIN}{k_{DIN} + DIN} \tag{5.8}$$

where k_{DIN} is the half-saturation phytoplankton DIN uptake. Vertical sinking and mortality affects the phytoplankton population at a constant rate m_p and w_p respectively :

$$Dep = m_p P \tag{5.9}$$

$$Vep = \frac{w_p}{H} P \tag{5.10}$$

The zooplankton grazing follows a Michaelis-Menten type formulation: the specific feeding rate depends on the zooplankton preference parameter on the food type (phytoplankton or detritus). The measure of the total food is simulated by the function F_1 and F_2.

$$Gp = \frac{g p_1 P^2 Z}{k_3 F_1 + F_2} \tag{5.11}$$

$$F_1 = p_1 P + p_2 D\,,\; F_2 = p_1 P^2 + p_2 D^2 \tag{5.12}$$

where k_3 is the zooplankton half-saturation for ingestion. p_1 and p_2 are the zooplankton preference parameter for food. g is the zooplankton maximum ingestion rate.

- Zooplankton accounts for the herbivorous and omnivorous fraction of the secondary producers which feed on phytoplankton and detritus. Losses of zooplankton biomass are generated by mortality and excretion of nutrients generated by grazing. The zooplankton rate of change is described by equation 5.13 :

$$\frac{dZ}{dt} = \beta(Gp + Gd) - Exz - Dez \tag{5.13}$$

Zooplankton grazing on detritus is the same formulation as that used for grazing on phytoplankton:

$$Gd = \frac{gp_2 D^2 Z}{k_3 F_1 + F_2} \tag{5.14}$$

The zooplankton mortality terms follows a hyperbolic function. This non-linear function reaches a saturation level at high concentration to account for the effect of zooplankton predation which is not explicitly modelled:

$$Dez = \frac{m_z Z^2}{k_z + Z} \tag{5.15}$$

where m_z is the zooplankton maximum loss rate and k_z is zooplankton half-saturation for loss rate. Zooplankton excretion rate (R_{exc}) is taken as a constant:

$$Exz = R_{exc} Z \tag{5.16}$$

where R_{exc} is the zooplankton excretion rate.

- The detritus pool is formed from dead phytoplankton, dead zooplankton and feacal pellets generated by zooplankton. Loss of detritus biomass is generated by zooplankton ingestion and sinking. Part of the remaining detritus is recycled implicitly by bacteria into nutrients. The detritus rate of change is described by equation 5.17:

$$\frac{dD}{dt} = (1 - \beta)(Gp + Gd) - Gd + Dep + Dez - Ded - Ved \tag{5.17}$$

Vertical sinking of detritus is a function of the depth and a constant sink rate

w_D:

$$Ved = \frac{w_D}{H} D \tag{5.18}$$

The detritus remineralisation rate (Ded) has an Arrhenius-type dependency on temperature Q_{10fac}.

$$Ded = Q_{10fac} k_d D \tag{5.19}$$

$$Q_{10fac} = e^{0.07(T-20)} \tag{5.20}$$

- The nutrients pool is consumed by the primary producer. Nutrient gains are formed by zooplankton excretion, remineralisation of detritus in the pelagic domain and remineralisation of sediments into DIN. The DIN rate of change is described by equation 5.21:

$$\frac{dDIN}{dt} = -Pr + Exz + Ded + Rs \tag{5.21}$$

At the sea floor, this organic material is remineralised into DIN and returned to the pelagic domain using a constant sediment remineralization rate modulated with an Arrhenius-type temperature dependency:

$$Rs = \frac{Rrem}{H} Q_{10fac} S \tag{5.22}$$

- The sediment pool is supplied by the fraction of phytoplankton and detritus which reach the seafloor by sinking. The loss is the return flux of DIN. The sediment rate of change is described by equation 5.23:

$$\frac{dSn}{dt} = w_P P + w_D D - R_{rem} Q_{10fac} S \tag{5.23}$$

The ecosystem model is forced with surface irradiance values. These data are provided as total hourly energy (kJ m^{-2} h^{-1}) by the National Oceanography Centre, Southampton meteorological station (see geographical location in figure 3.1) and converted to Photosynthetically Active Radiation (PAR) in W m^{-2}. For this conversion, 1 J s^{-1} is equal to 1 W and it is assumed that PAR constitutes 45 % of the total solar energy (Kirk, 1994). The model parameters are given in table 5.4.

The system of differential equations (equations 5.2, 5.13, 5.17, 5.21 and 5.17, 5.23) is solved using the fourth order Runge-Kutta technique with a time-step of

symbol	definition	standard value	unit
α	initial slope of P-I curve	0.045^b	(W m^2)$^{-1}$ d^{-1}
β	zooplankton assimilation efficiency	0.75^a	none
g	zooplankton maximum ingestion rate	0.21	d^{-1}
H	depth	10	m
k	extinction coefficient	variable	m^{-1}
k_3	zooplankton half-saturation for ingestion	1^a	d^{-1}
k_D	detrital breakdown rate	0.05^a	m d^{-1}
k_{DIN}	half-saturation phytoplankton DIN uptake	0.5^a	mmol N m^{-3}
k_z	zooplankton half-saturation for loss rate	0.2^a	mmol N m^{-3}
mp	phytoplankton mortality rate	0.045^b	d^{-1}
m_z	zooplankton max loss rate	0.03^b	d^{-1}
$p1, p2$	zooplankton preference parameters	0.5^b	none
R_{exc}	zooplankton excretion rate	0.1^a	d^{-1}
R_{rem}	sediment turnover rate for nitrogen	0.01^b	d^{-1}
T	Temperature	12.5	degree Celsius
w_D	detrital sinking rate	6^b	d^{-1}
wp	phytoplankton sinking rate	0.1^b	m d^{-1}

Table 5.4: List of model parameters. The references used to determine these values are a) Fasham et al. (1990) and b) Kelly-Gerreyn et al. (2004). zooplankton maximum ingestion rate is a tuned value. See text for T and H

one hour corresponding to the time resolution of the irradiance data used to force the ecosystem model. In this case the model resolves the day-night cycle. Preliminary results showed to be insensitive to a decrease of the time-step. A numerical integration based on the trapezoidal rule is performed over the vertical (equation 5.4) for a depth of 10 meters as an approximation of the averaged water depth found in the main channel of Southampton water yelding a zero-dimension domain. A constant temperature of 12.5^{o}C is used in all model runs, which is the annual mean value in Southampton Water (data accessed through the Centre for Environment, Fisheries and Aquaculture Science http://www.cefas.co.uk).

5.3 Sensitivity to light forcing and attenuation

5.3.1 List of simulations

Several groups of experiments were carried out, in order to determine the impact of the varying parameters (k, seasonal cycle in surface irradiance forcing and total inventory in nitrogen) on the timing and the magnitude of the spring bloom. A summary is given in table 5.5.

In scenarios 1-3, initial conditions are assigned the value P=1 mmol N m^{-3},

sc.	seasonal cycle of irradiance	k attenuation coefficient		total N inventory
		k formulation	parameter value	
1	2001	k=0.5 m^{-1}		362
2	2001	k=0.6 m^{-1}		362
3	2001	k=0.7 m^{-1}		362
4	2001	k=0.5 m^{-1}		562
5	2001	k=0.6 m^{-1}		562
6	2001	k=0.7 m^{-1}		562
7	2002	k=0.5 m^{-1}		362
8	2003	k=0.5 m^{-1}		362
9	2004	k=0.5 m^{-1}		362
10	2005	k=0.5 m^{-1}		362
11	2001	$k = k_w + k_c P$	[a] k_w=0.1m^{-1} [b] k_c=0.03 m^{-1}	362
12	2001	$k = A_{min} + (A_{max} - A_{min}) e^{-c(T_d sin(\frac{t\pi}{T_d} + \phi_1)^4)}$	ϕ_1=-0.4 A_{min}=0.5m^{-1} A_{max}=1.2m^{-1} c=0.004	362
13	2001	$k = A_{min} + (A_{max} - A_{min}) e^{-c(T_d sin(\frac{t\pi}{T_d} + \phi_2)^4)}$	ϕ_2=-0.2 A_{min}=0.5m^{-1} A_{max}=1.2m^{-1} c=0.004	362
14	2001	$k = A_{min} + (A_{max} - A_{min}) e^{-c(T_d sin(\frac{t\pi}{T_d} + \phi_3)^4)}$	ϕ_2=-0.01 A_{min}=0.5m^{-1} A_{max}=1.2m^{-1} c=0.004	362

Table 5.5: Summary table of the list of simulations. Simulations vary from the imposed seasonal cycle of irradiance, the parameterization of the coefficient of attenuation, and the total inventory of nitrogen. scenario is abbreviated by sc.

Z=0.1 mmol N m^{-3}, D=0.1 mmol N m^{-3}, S=150 mmol N m^{-2}, DIN=20 mmol N m^{-3} which gives a total inventory of nitrogen of 362 mmol N m^2. In scenarios 4-6 initial conditions are the same except for DIN which is set to 40 mmol N m^{-3} yielding a higher total nitrogen inventory of 562 mmol N m^{-2}. Scenarios 4-6 simulate the impact of higher nutrient load potentially generated by the proximity of river load in the upper estuary. Scenarios 7-10 test the result between changes in surface irradiance light forcing at similar attenuation conditions.

The impact of time-varying functions has also been tested and compared with the case of a constant k. In scenario 11, the typical formulation usually used in the open ocean, which corresponds to a lower range of value of the coefficient of attenuation (from k=0.15m^{-1} to 0.25 m^{-1}) is employed. Scenarios 12-14 investigate the impact of the time-varying function with a spring minimum in the attenuation (equation 4.9). Each scenario varies the timing of the spring minima with a variation in the parameter ϕ.

Each model run starts from day 1 of the year and is forced with a repeated seasonal cycle in irradiance forcing. A spin-up time of 3 years is necessary for the model to adjust to the initial conditions and forcing function, and results of year 4 have been analysed.

5.3.2 Repetition of the seasonal cycle

The seasonal cycle of irradiance used to force the ecosystem model generates a seasonal cycle of the 5 ecosystem variables. For a certain choice of parameter values, dynamical systems forced with an external seasonal periodic forcing produced a complex cyclical behaviour which takes the form of cycles at the frequency of more than one year, quasi periodic forcing and chaotic motion superimposed on the seasonal cycle, and sensitivity to the initial conditions (Popova et al., 1997). Part of the sensitivity analysis described above is to determine whether the model can reproduce identical successive seasonal cycles in the ecosystem variables succession at steady state for different values of k. This allows us to determine whether part of the interranual variability in the ecosystem model is generated by the intrinsic variability of the ecosystem model formulation and parameter choice. The range of k (k=0.5 m^{-1}, k=0.6 m^{-1} and k=0.7 m^{-1}) values tested in scenarios 1,2,3 corresponds to the range of values measured in spring in Southampton Water in year 2001, 2002, 2003 (table 4.8 in chapter 4).

A comparison of the seasonal succession in the ecosystem variables in the case of the low inventory of nitrogen is presented on figure 5.2a-e. A typical seasonal

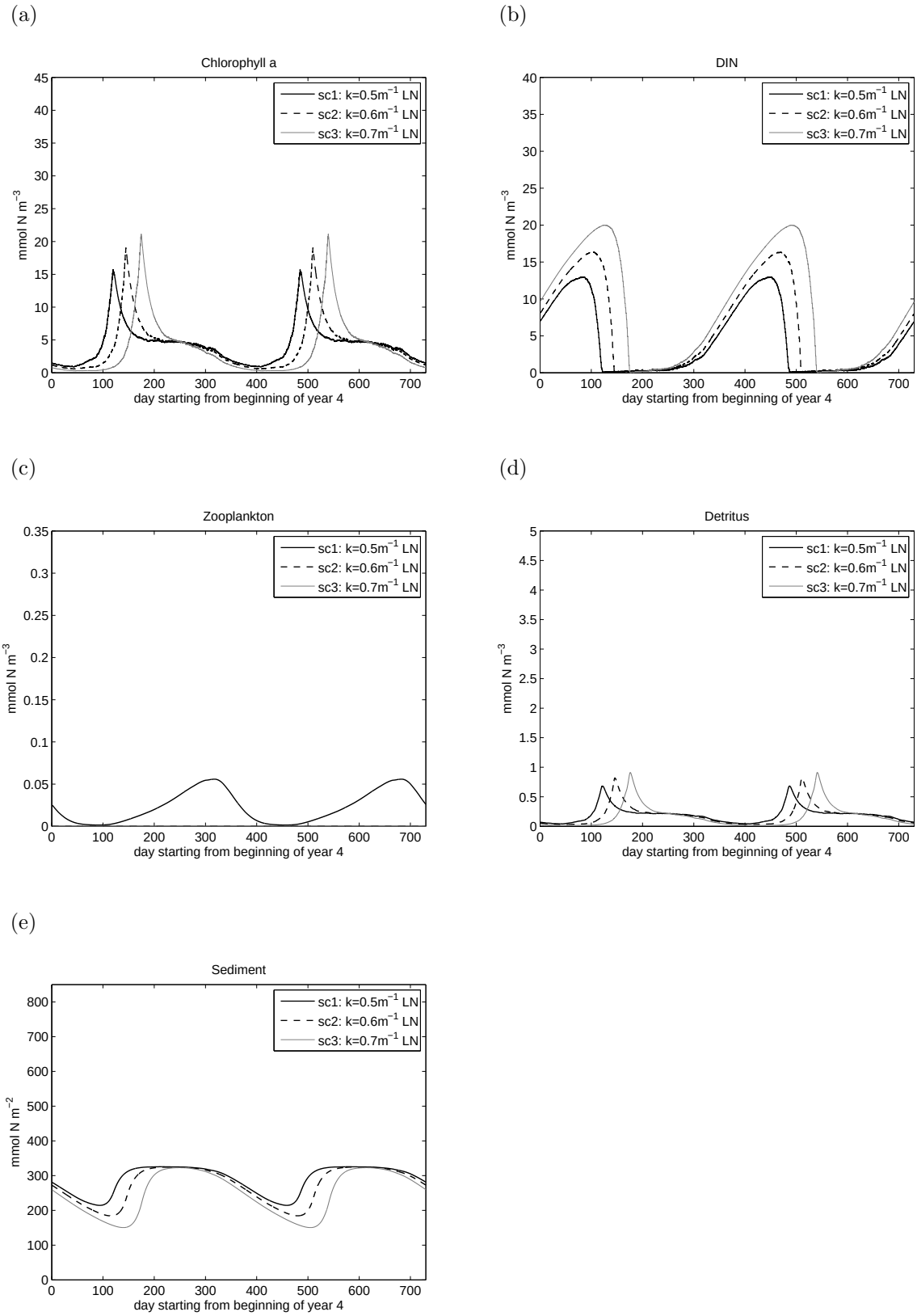

Figure 5.2: Seasonal cycle in the case of a low total inventory of nitrogen: scenario 1,2,3. These scenarios vary only by their k value and legend refers to the scenario (denoted sc.) as listed in table 5.5. LN=low inventory in nitrogen. Zooplankton concentration is zero in sc 2. and sc. 3 on subfigure (c).

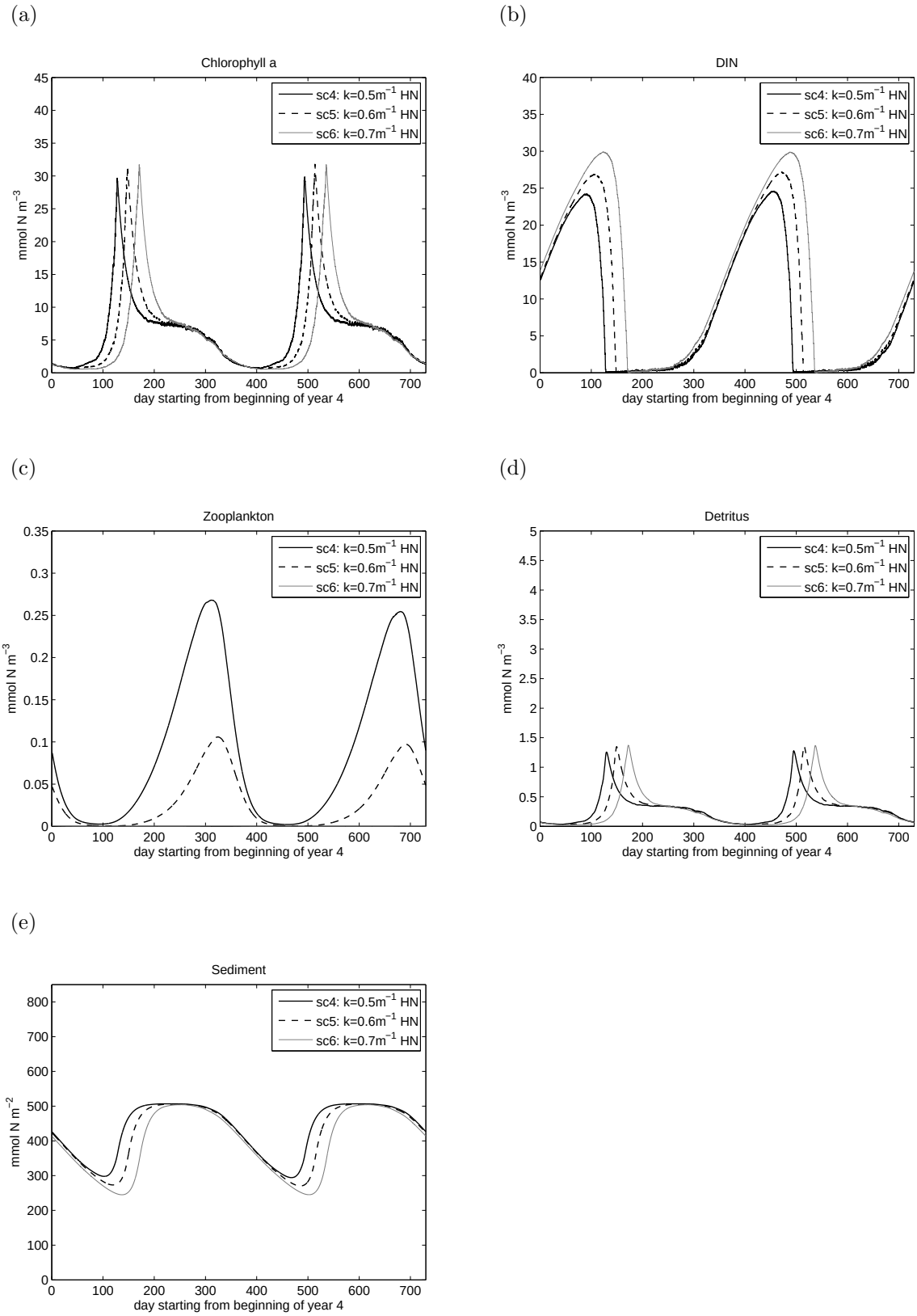

Figure 5.3: Seasonal cycle in the case of a high total inventory in nitrogen. These scenarios vary only by their k value and legend refers to the scenario (denoted sc.) as listed in table 5.5. HN=High inventory of nitrogen. Zooplankton concentration is zero in sc. 6 on subfigure (c).

cycle with the formation of a spring phytoplankton bloom is simulated (figure 5.2a), followed by an increase in the detritus (figure 5.2d) and later on by the zooplankton biomass (figure 5.2c). Phytoplankton biomass remains constant during summer (figure 5.2a). Nutrient regeneration occurs in winter when phytoplankton biomass is at the lowest level (figure 5.2b). The annual cycle in sediment nitrogen is characterized by a depletion during winter and a *plateau* during the summer and autumn (figure 5.2e). Sensitivity to k is the most striking for the zooplankton. For k=0.6 m^{-1} and k=0.7 m^{-1}, zooplankton levels are at zero, compared with the seasonality shown for k=0.5 m^{-1} (figure 5.2c). No deviation from a steady seasonal cycle is observed for all ecosystem variable between results of year 4 and result of year 5: A variation of less than 0.0035% is calculated between the peak of chlorophyll biomass in year 4 and the peak in chlorophyll biomass in year 5 (figure 5.2a, scenario 1 where k=0.5 m^{-1}).

Using a higher inventory in nitrogen, a similar succession in the seasonal cycle of the ecosystem variable is found (figures 5.3a-e). In contrast to scenarios with a smaller inventory of nitrogen (figure 5.2a-e), a small deviation from a steady seasonal cycle is observed for phytoplankton biomass (figure 5.3a) and for zooplankton biomass (figure 5.3c). This result is mainly due to the formation of a biannual cycle instead of an annual cycle. This effect is most visible in figure 5.3c where a variation of 5.2 % is found between the peak zooplankton bloom in year 4 and year 5 for k=0.5 m^{-1} . Zooplankton annual cycle is less strongly affected by the change in the k parameter to compare with the case of a low inventory of nitrogen: At the stage of k=0.7 m^{-1}, while comparing the results of the modelled seasonal cycle, we observe that zooplankton biomass is reduced to zero all year round (figure 5.3c).

These results reveal that the zooplankton compartment is the most sensitive to changes in the attenuation coefficient k. The model appears reasonably robust in the determination of the seasonal cycle for the other variables. A large degree of uncertainties exist in the initial concentration of nitrogen, and therefore in the total nitrogen concentration, due to a lack of observation of sediment flux in Southampton Water and detritus. Changing the total inventory of nitrogen demonstrates that a qualitatively similar seasonal cycle operates, however the dynamics of the system is affected by a slight deviation from the seasonal cycle. Additional runs of 50 years of simulation have been carried out and show the same biannual cycles.

5.3.3 Sensitivity to different constant values of k

Model results indicate that the major spring bloom is delayed and increased in magnitude as k is increased (figure 5.2a and 5.3a). The magnitude of the spring bloom ranges from 15.72 to 21.15 mg m^{-3} and the timing ranges from day 119 to day 174 of the year in the case of the low inventory of nitrogen (table 5.6). The magnitude of the spring bloom ranges from 29.87 to 31.77 mg m^{-3} and the timing ranges from day 128 to day 170 of the year in the case of the high inventory of nitrogen (table 5.7) This reveals that an increased level of attenuation systematically delays the bloom. In the case of the low inventory of nitrogen, an increase in k is always associated with higher chlorophyll maximum. It is not the case for the high inventory of nitrogen, due to the superimposition of the interannual variability generated by the intrinsic dynamics (biannual cycle) generated by the ecosystem model when k is increased.

sc	k (m^{-1})	Chlorophyll maximum $mg.m^{-3}$	day in year
1	0.5	15.72	119
2	0.6	19.03	144
3	0.7	21.15	174

Table 5.6: Timing and amplitude of the chlorophyll peak obtained in year 5 for various k values from figure 5.2. The total inventory in nitrogen is equal to 392 mmol N m^{-2}.

sc	k (m^{-1})	Chlorophyll maximum ($mg.m^{-3}$)	day in year
4	0.5	29.87	128
5	0.6	31.77	148
6	0.7	31.74	170

Table 5.7: Timing and amplitude of the chlorophyll peak obtained in year 5 for various k values from figure 5.3. The total inventory in nitrogen equal to 592 mmol N m^{-2}.

5.3.4 Effect of interranual variability in surface irradiance

The response of the phytoplankton seasonal cycle to interranual variability in irradiance field is shown in table 5.8 by comparing the results in the magnitude and timing of the maximum chlorophyll a concentration when different seasonal cycles in surface irradiance is imposed (comparison between scenario 1, 7, 8, 9 and 10 as described in table 5.5). k is fixed at the value k=0.5 m^{-1} for all simulations.

Figure 5.4 demonstrates the role played by the surface irradiance field in the interannual variability of the spring bloom, with the peak of the bloom ranging from day 106 to day 119 and the magnitude varying from 15.72 to 17.41 mg m^{-3} (table 5.8). A delay in the bloom does not systematically produce a bloom of higher magnitude, contrary to the case when only k is varied, with irradiance values kept the same between runs (section 5.3.3.

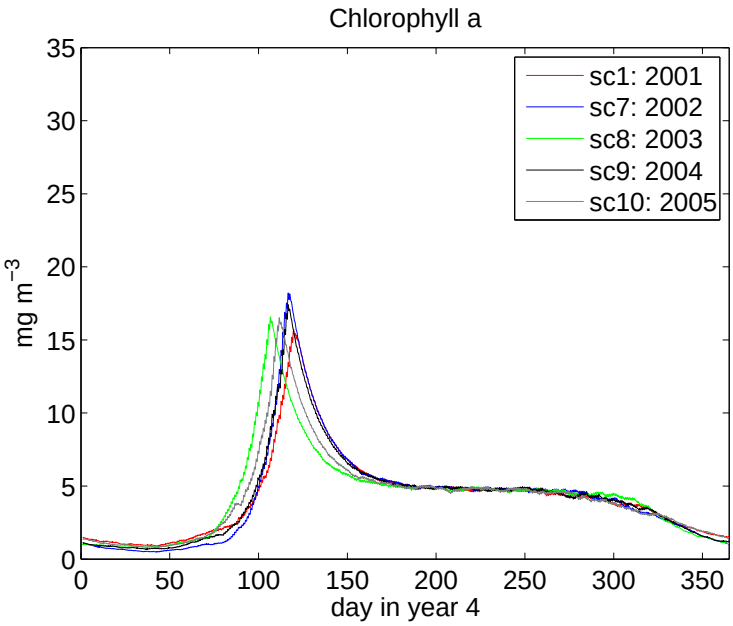

Figure 5.4: Annual cycle of chlorophyll concentration obtained with irradiance value for years 2001,2002,2003,2004,2005.

sc	year	Chlorophyll maximum (mg m^{-3})	day in year
1	2001	15.72	119
7	2002	18.21	116
8	2003	16.56	106
9	2004	17.41	116
10	2005	16.52	111
	average	16.88 ± 0.95	113.6±5

Table 5.8: Interranual variability in the magnitude and onset of the phytoplankton spring bloom for different seasonal cycle of irradiance. $k = 0.5m^{-1}$ for all scenarios.

Overall, changes in surface irradiance under the same attenuation conditions (k=0.5 m^{-1}) generate a peak of phytoplankton biomass on day 113.6±5 with a magnitude of 16.88± 0.95 mg m^{-3} (table 5.8).

5.3.5 Time-varying k

The impact of the attenuation coefficient is now assessed. Scenario 1 is a reference simulation where a constant parameter (k=0.5 m^{-1}) is used. In scenario 11, k varies in time as a linear function of the phytoplankton concentration to account only for the phytoplankton shelf-shading. This formulation is the typical formulation in the open-ocean, and corresponds to the assumption that phytoplankton is the major contributor to attenuation in seawater. Scenarios 12,13,14 use a function with a maxima in autumn-winter and a minima in spring-summer. Scenarios 12-14 vary in the timing of the transition from the minima to the maxima of the attenuation coefficient (figure 5.5a). These scenarios evaluate the impact of interranual changes in the spring decrease in attenuation, as identified from observation in Southampton Water (figure 4.11 in chapter 4).

In the standard run (scenario 1), the phytoplankton bloom occurs on day 119 with a magnitude of 15.72 mg m^{-3} (figure 5.5 b). In the case of the open-ocean coefficient function (scenario 11), the phytoplankton bloom occurs on day 58 with a magnitude of 8.65 mg m^{-3} (figure 5.5 b). This reveals the major role played by the elevated level of the attenuation coefficient in estuarine area, and supports the assumption that the high level of attenuation is the cause of the bloom occuring in late spring. A peak of chlorophyll biomass occur on day 134, 141, and 149 with peak of chlorophyll biomass of 22.27, 22.72 and 22.80 mg m^{-3} for scenario 12-14 respectively (figure 5.5b). Compared with scenario 1, this result demonstrates the importance of the seasonal cycle observed in Southampton Water is the determination of the timing of the bloom. The delay in the timing of the reduction in the attenuation in scenario 12,13,14 does not significantly change the bloom magnitude.

5.4 Model-data comparison

5.4.1 Observational data

Zooplankton data (Muxagata, 2005) covers the time period from January 2001 to August 2002 with a sampling frequency of three to four times a month from January to October 2001. In 2002, the sampling frequency was increased from 3 to 4 times per month during the productive period (March to July 2002) and only bimonthly or once a month during the less productive months. Zooplankton were sampled from surface to bottom at the two stations NWNetley and Calshot (figure

(a)

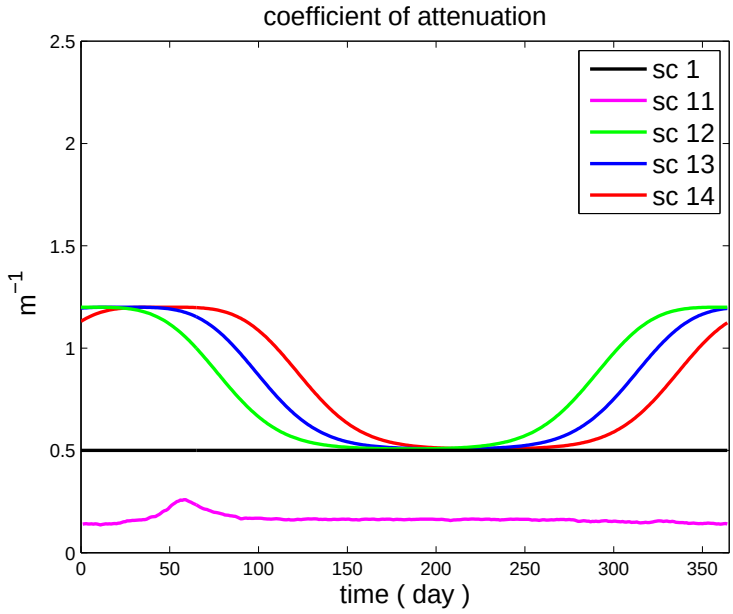

(b)

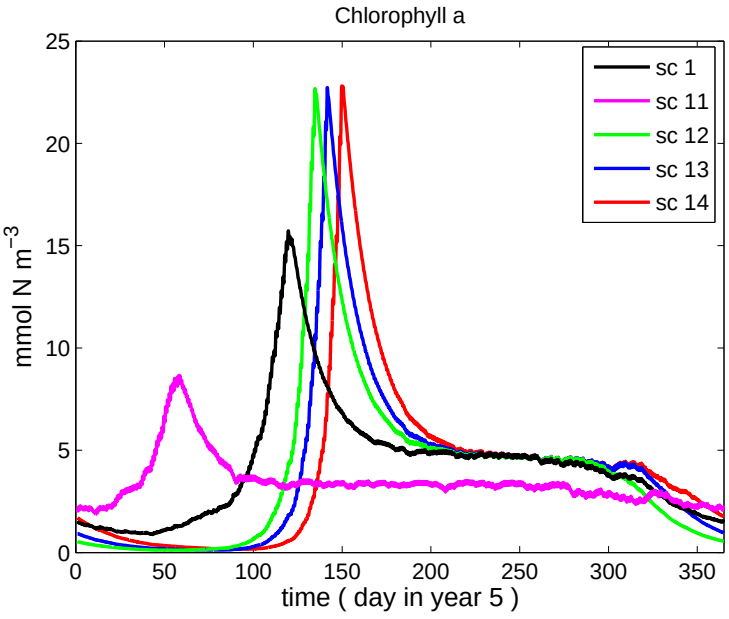

Figure 5.5: Comparison of the response of phytoplankton bloom in the case of the open ocean formulation (scenario 11), a constant k (scenario 1) and a time varying k (scenario 12,13,14).

species	Dry Weight
Acartia species (includes *A. Clausi A. bifilosa and A. discaudata*)	0.56
Oithona nana	0.54
Euterpina acutifrons	0.99
Copepoda nauplii	0.45

Table 5.9: Dry weight of the dominant species of copepoda.

4.4) with a 120 μm mesh size net. Zooplankton individuals were identified and the main species in terms of abundance (organisms m^{-3}) were *Acartia* species, *Oithona Nana, Euterpina Acutifrons, Copepoda nauplii, Polychaeta, Mollusca, Elminius Modestus*, *Balanus improvisus*, *Balanus crenatus* and *Semibalanus balanoides*, and *Urochordata*. To enable appropriate comparison with the model, zooplankton abundance was converted from abundance (organisms m^{-3}) into biomass (mmol N m^{-3}) :

$$Z = \frac{\theta_{zoo}}{\theta_N} \sum_{species} density \times DW \tag{5.24}$$

where density is the number of organisms per m^3 defined for each species, DW is the averaged dry weight (g) of an organism, θ_N is the atomic weight of nitrogen in mg N (mmol N)$^{-1}$ and θ_{zoo} is the ratio of Nitrogen to mass in zooplankton in mg N (mmol N)$^{-1}$(table 5.1). Carnivorous species (*Mollusca* and *Polychaeta*) have been omitted in the calculation, since the ecosystem model accounts only for the herbivorous fraction of zooplankton feeding on phytoplankton (figure 5.1). *Urochordata* was also omitted since no information exists on the percentage development stages and the dry weight for this dataset.

The DW of a zooplankton species varies according to larval development. An average DW for all stages is used for *copepoda* species (table 5.9). To account for the dominance of larval development stage II in the zooplankton abundance in terms of number of organisms in *cirripedia* species (table 5.10), the dry mass for a specific species is approximated by:

$$DW = \rho_{stage2} \times DW_{stage2} + (1 - \rho_{stage2}) \times DW_a \tag{5.25}$$

where ρ_{stage2} is the annual percentage of nauplii stage 2 for this species, DW_{stage2} is the dry mass for nauplii stage 2 of this species. DW_a is the calculated averaged dry mass for the remaining stages (stage III to VI).

species	naupliar stage 2 (%)	$DW_{stage2}(\mu g)$	$DW_a(\mu g)$
Eliminius modestus	50	0.29	1.17
Balanus improvisus	45	0.27	1.38
Balanus crenatus	83	0.46	2.60
Semibalanus balanoides	63	0.69	4.88

Table 5.10: Numerical value of the dry weight of the dominant species of *Cirripedia* found in Southampton Water and abundance of each larval stage thoughout the sampling survey. Numerical values are based on Muxagata (2005) and used to calculate the contribution of zooplankton species to herbivorous biomass.

Modelled phytoplankton biomass after conversion to chlorophyll *a* value (equation 5.1) is compared with surface chlorophyll *a* measurements. Data from Torres-Valdés and Purdie (2006) and Muxagata (2005) give a dataset covering the productive period (from March to October) in 2001, 2002 and 2003 with a frequency of approximately one week at the two main stations of NWNetley and Calshot. A description of the chlorophyll *a* measurements is given in section 4.3.1 of chapter 4.

Dissolved inorganic nitrogen in 2002 and 2003 have been estimated by summing nitrate and ammonium concentrations measured at Calshot and NWNetley (Torres-Valdés and Purdie, 2006). Nitrate values correspond to nitrate plus nitrite concentrations since they are not separated during the measurement process. This dataset covers the months April to October with a temporal frequency of two weeks and corresponds to surface values only.

5.4.2 NWNetley

Data available at NWNetley allows for the comparison of model simulations in 2001, 2002 and 2003 (chlorophyll *a* only). Model simulations vary only in their total inventory in nitrogen (N=352 mmol m^{-2} or N=552 mmol m^{-2}) and the value of the k coefficient: for each year, k is set as the k value obtained from this study (table 4.8 in chapter 4). The initial conditions are identical to section 5.3.1. Due to the lack of information on the sediment and detritus measurement to estimate the initial conditions of these two compartments and hence the total inventory of nitrogen, runs in the case of a total inventory of nitrogen of 352 mmol m^{-2} and N=552 mmol m^{-2} are also plotted. In 2002 and 2003, model runs where the fit obtained simulating the seasonal variation in attenuation has been used (scenarios 19-20 and scenarios 23-24). All scenarios tested are listed in table 5.11.

scenario	seasonal cycle of irradiance	k attenuation parameter		total N inventory
		k formulation	parameter value	
15	2001	k=0.6 m^{-1}		352
16	2001	k=0.6 m^{-1}		552
17	2002	k=0.6 m^{-1}		352
18	2002	k=0.6 m^{-1}		552
19	2002	$k = A_{min}+(A_{max}-A_{min})e^{-c(T_d sin(\frac{t\pi}{T_d}+\phi_1)^4)}$	ϕ_1=-0.668 A_{min}=0.65m^{-1} A_{max}=1.3m^{-1} c =0.0044	352
20	2002	$k = A_{min}+(A_{max}-A_{min})e^{-c(T_d sin(\frac{t\pi}{T_d}+\phi_1)^4)}$	ϕ_1=-0.668 A_{min}=0.65m^{-1} A_{max}=1.3m^{-1} c =0.0044	552
21	2003	k=0.65 m^{-1}		352
22	2003	k=0.65 m^{-1}		552
23	2003	$k = A_{min}+(A_{max}-A_{min})e^{-c(T_d sin(\frac{t\pi}{T_d}+\phi_1)^4)}$	ϕ_1=-1.061 A_{min}=1.04m^{-1} A_{max}=0.57m^{-1} c =0.0098	352
24	2003	$k = A_{min}+(A_{max}-A_{min})e^{-c(T_d sin(\frac{t\pi}{T_d}+\phi_1)^4)}$	ϕ_1=-1.061 A_{min}=1.04m^{-1} A_{max}=0.57m^{-1} c =0.0098	552

Table 5.11: List of simulations. Total inventory of nitrogen is in mmol N m^{-2}. Values of constant k are given by table 4.8 (value in May-June).

(a)

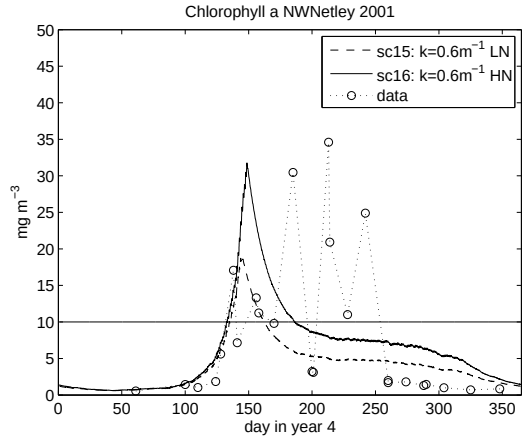

(b)

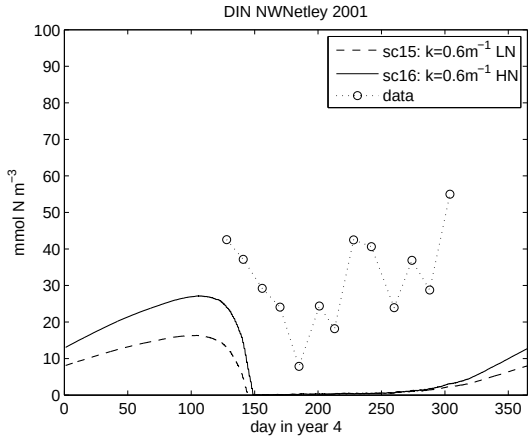

(c)

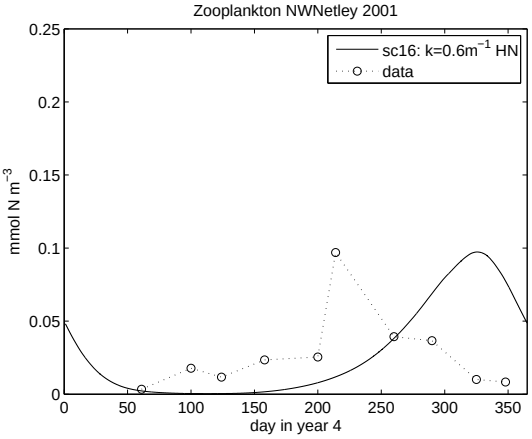

Figure 5.6: Comparison between model results and data available at NWNetley in 2001. A horizontal line delineates the minimum level of 10 mg Chl m^{-3} to identify a bloom. Zooplankton is zero all year round in case of scenario 15. LN=low inventory in nitrogen, HN=High inventory of nitrogen.

(a)

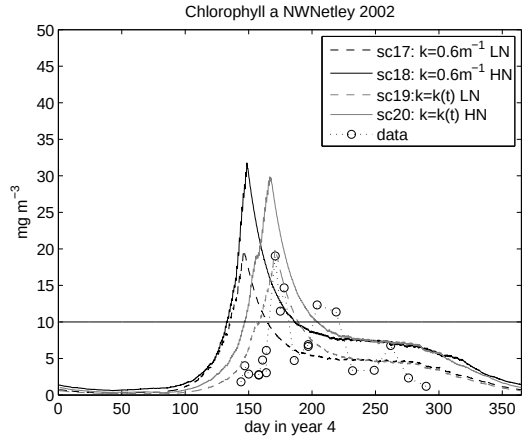

(b)

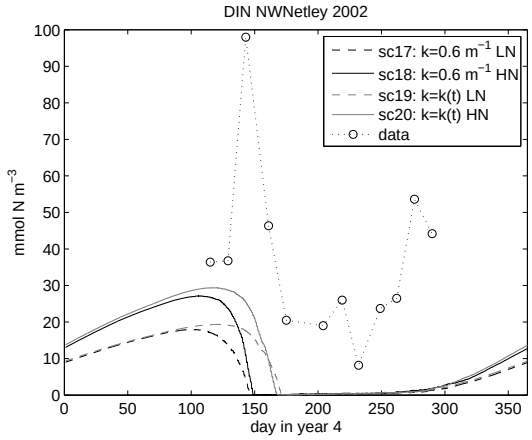

(c)

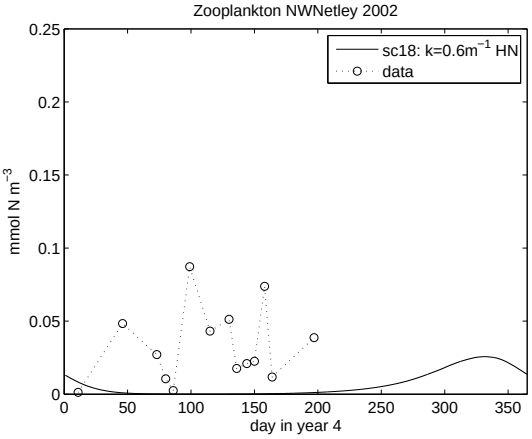

Figure 5.7: Comparison between model results and data available at NWNetley in 2002. A horizontal line delineates the minimum level of 10 mg Chl m^{-3} to identify a bloom. Zooplankton is zero all year round in case of scenario 17, 19 and 20. LN=low inventory in nitrogen, HN=High inventory of nitrogen.

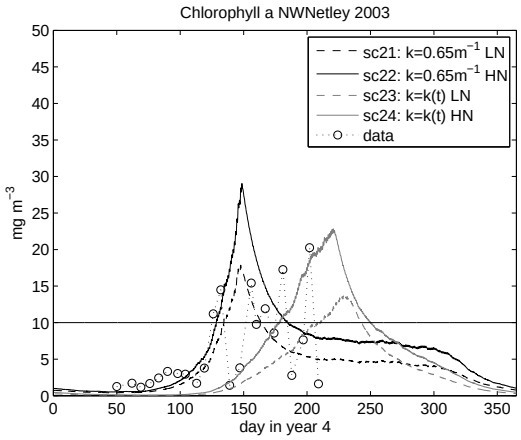

Figure 5.8: Comparison between model results and data available at NWNetley in 2003. A horizontal line delineates the minimum level of 10 mg Chl m^{-3} to identify a bloom. LN=low inventory in nitrogen, HN=High inventory of nitrogen. No data of DIN and zooplankton are available in 2003.

Figure 5.6a compares modelled results with observations of chlorophyll biomass at NWNetley in 2001. A phytoplankton bloom is identified by a chlorophyll peak above the threshold of 10 mg m^{-3} (Iriarte and Purdie, 2004). A first bloom is simulated in May with a bloom of chlorophyll *a* in agreement with observations: There is a difference of 6 days on the timing of the bloom (table 5.12). Four other blooms were observed until late in summer and are not simulated by the model. The experiment with the low inventory of nitrogen gives qualitatively a better match with the magnitude of the observed spring chlorophyll bloom.

Figure 5.6b is a comparison between DIN measured at the surface and modelled DIN. Modelled DIN concentration shows an idealised seasonal cycle of DIN concentration, with a regeneration in winter and a depletion in spring, whereas observations in DIN are affected by short term fluctuations superimposed on a similar seasonal cycle. Observations range from 8 to 42 mmol N m^{-3}, compared with a range of 0.05 to 27 mmol N m^{-3} in the model simulation (high inventory of nitrogen). Observed DIN is always higher than model simulation. This discrepancy is reduced by the use of the high nitrogen inventory.

Figure 5.6c compares modelled zooplankton biomass with the estimated zooplankton biomass from observations. A lag appears between the observed zooplankton biomass and the modelled zooplankton biomass. The range of values in model and data is similar: 0.005 to 0.09 mmol N m^{-3} in the observations and 0.001 to 0.1 mmol N m^{-3} (scenario 16). Simulation in the case of a high inventory of nitrogen leads to the destruction of the total depletion of the zooplankton biomass all year round, as seen previously in section 5.3.2 for a high k coefficient.

In 2002 (Figure 5.7a), four scenarios are plotted against the dataset, including simulations with the minimum observed k value in spring set as a constant, and simulation with a time-varying k fitted in year 2002. Observations indicate a bloom occuring on day 171 with a magnitude of 19 mg m^{-3}.A time-varying k (scenario 19-20) is the simulation which qualitatively gives the better fit to the dataset compared with the simulation with a constant k (scenario 17-18).

The model underestimation of DIN at NWN in 2002 is similar to 2001 (Figure 5.7b). An observed peak value of DIN above 95 mmol N m^{-3} occurs, possibly generated by a brief increase of river flow, since concentrations of nitrate are generally below 60 mmol N m^{-3} at NWNetley at this time of the year (Hydes et al., 2001). A time-varying k coefficient combined with a high inventory of nitrogen gives qualitatively the best fit to the data (scenario 20).

In figure 5.7c, only the first part of the seasonal cycle of zooplankton biomass (from day 0 to day 200) is covered by the dataset in contrast to 2001 (figure 5.6c). Peaks of concentration occurs on day 50, day 100, and day 150. A zooplankton seasonal cycle is simulated in the case of scenario 18 and indicates a peak in late autumn. Modelled zooplankton do not reproduce the observations.

In 2003 (figure 5.8), the first bloom was detected on day 132 with a magnitude of 14.5 mg m^{-3}. Contrary to the results of simulation in 2002, the best fit of the first spring bloom observed is obtained in the case of a constant k set as the minimum value.

		Model		Data		absolute difference	
sc.	year	amplitude (mg m^{-3})	day of year	amplitude (mg m^{-3})	day of year	amplitude (mg m^{-3})	days
15	2001	19.0	144	17.7	138	1.3	6
17	2002	19.5	146	19.0	171	0.5	25
21	2003	17.8	147	14.5	132	3.3	15

Table 5.12: Amplitude and timing of the first spring bloom as indicated by chlorophyll a concentration: Comparison between model prediction (simulation with k constant) and data at NWNetley.

In summary, these results demonstrate the model ability to predict the timing of the spring bloom with a reasonable agreement when a medium degree of realism is used (k set at the minimum spring value and forced with observed surface irradiance): differences in the timing of the bloom ranges from 6 to 25 days and magnitude ranges from 0.5 to 3.3 mg Chl m^{-3} (table 5.12).

5.4.3 Calshot

At Calshot, only model simulations with the lowest inventory in nitrogen have been plotted against data since at Calshot, blooms are generally of lower intensity than NWNetley (Hydes et al., 2001; Iriarte and Purdie, 2004). Simulations are listed in table 5.13. In 2003, the use of a time-varying k inhibits the formation of a seasonal cycle of phytoplankton and therefore this simulation is not included.

scenario	seasonal cycle of irradiance	k		total N
		k formulation	constant parameter	
25	2001	k=0.56 m^{-1}		
26	2002	k=0.70 m^{-1}		
27	2002	$k = A_{min}+(A_{max}-A_{min})e^{-c(T_d sin(\frac{t\pi}{T_d}+\phi_1)^4)}$	ϕ_1=-0.668 A_{min}=0.65m^{-1} A_{max}=1.91m^{-1} c =0.006	
28	2003	k=0.65 m^{-1}		

Table 5.13: List of simulations. Total inventory of nitrogen is equal to 362 mmol N m^{-2}. Values of constant k are given by table 4.8 (value in May-June).

Figure 5.9a compares model results with data in 2001. Two blooms were detected by the weekly sampling. The first occurs on day 141 with a magnitude of 11.9 mg m^{-3}. Model results closely match the spring phytoplankton bloom with a chlorophyll maxima predicted on day 135 with a magnitude of 17.7 mg m^{-3}. In contrast with NWNetley, no late summer bloom is detected at Calshot. Therefore the idealised modelled phytoplankton seasonal cycle matches closely the observations, compared to NWNetley.

Figure 5.9b compares measured DIN with simulated DIN. The model tend to underestimate nutrient concentration. Observed concentrations of DIN are lower than at NWNetley.

In figure 5.9c, observed zooplankton biomass shows a seasonal cycle with a peak in late summer. The model reproduces a seasonal cycle for zooplankton with a peak in late summer, which occur approximately 100 days after the observed peak.

In 2002, (figure 5.10a), only one spring phytoplankton bloom of 11.1 mg m^{-3} was detected on day 179. The modelled bloom in the case of a constant k value gives a better match (both in magnitude and timing) to the dataset than the modelled bloom forced with the time-varying k.

At the opposite, a comparison between modelled DIN and observed DIN

(a)

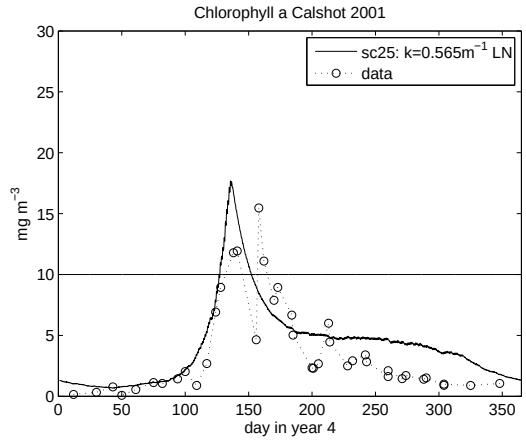

(b)

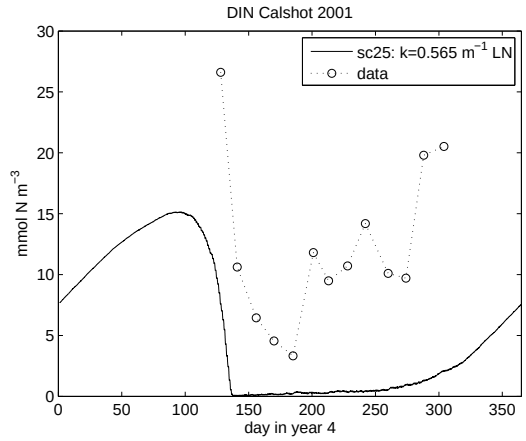

(c)

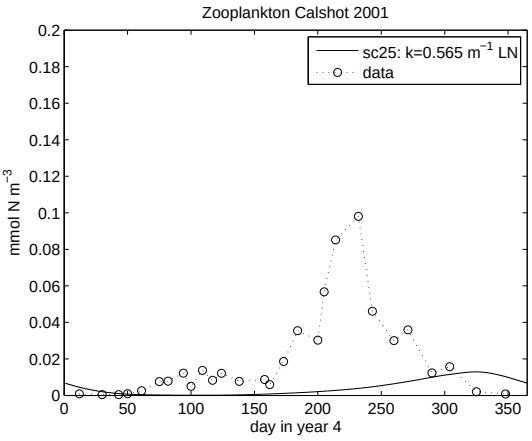

Figure 5.9: Comparison between model results and data at Calshot 2001. A horizontal line delineates the minimum level of 10 mg m^{-3} for a bloom to occur. LN=low inventory in nitrogen.

(a)

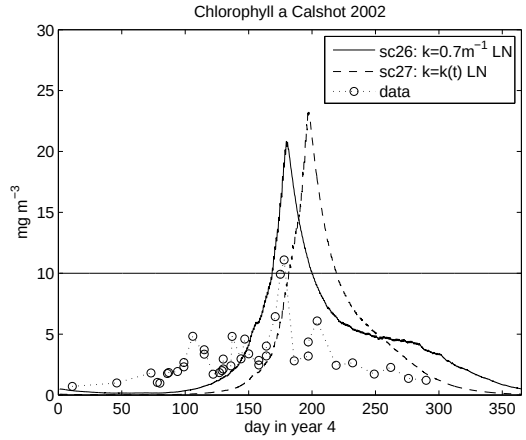

(b)

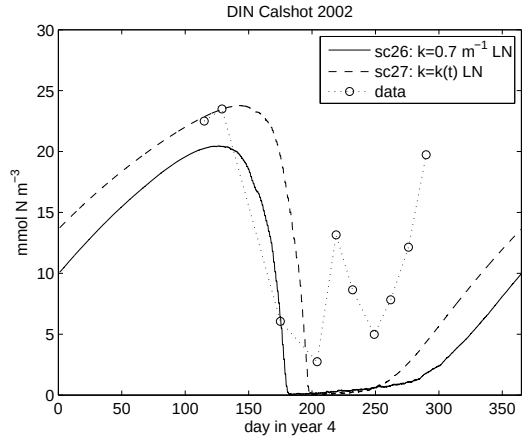

(c)

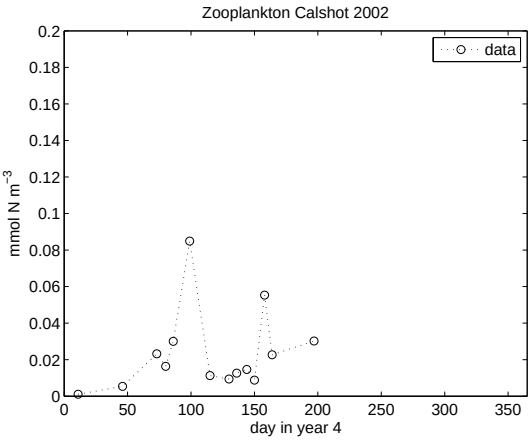

Figure 5.10: Comparison between model results and data at Calshot in 2002. A horizontal line delineates the minimum level of 10 mg m^{-3} for a bloom to occur.Zooplankton is zero all year round in case of scenario 26 and 27. LN=low inventory in nitrogen.

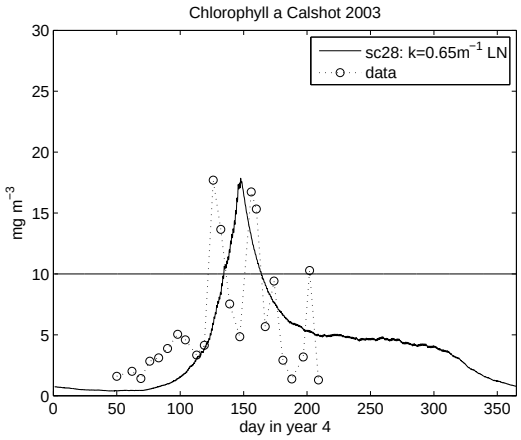

Figure 5.11: Comparison between model results and data at Calshot in 2003. A horizontal line delineates the minimum level of 10 mg m^{-3} for a bloom to occur. LN=low inventory in nitrogen. No data of DIN and zooplankton are available in 2003.

indicates that a reasonably good fit is obtained in the case of a time-varying k, both in the range of value and in the seasonal cycle obtained, especially in the spring depletion of DIN during the first portion of the seasonal cycle (figure 5.10b). However winter regeneration is still underestimated in late summer and autumn.

For the zooplankton compartment (figure 5.10c), no comparison can be made between measured zooplankton and modelled zooplankton, since the minimum k value in 2002 at Calshot and the time-varying k both leads to zero for the modelled zooplankton all year round. Two observed peaks of zooplankton occur at the beginning of spring, showing some similarity to NWNetley in 2002 (figure 5.7c)

Finally, phytoplankton seasonal cycle in year 2003 is shown in figure 5.11. Simulation with the time-varying k fitted at Calshot in 2003 gives a very high value and does not generate a phytoplankton bloom. For this reason, it is not compared to the dataset. In the case of a constant k coefficient, chlorophyll a peak is predicted after the first spring bloom (delay of 21 days), with a similar magnitude than observation.

In conclusion, the group of simulations at Calshot is affected by a difference between modelled and observed first spring bloom ranging from 1 to 21 days. The difference in the magnitude between model and observations ranges from 0.1 to 9.7 mg m^{-3} using the constant minimum spring k value (table 5.14).

		Model		Data		absolute difference	
sc.	year	amplitude (mg m^{-3})	day of year	amplitude (mg m^{-3})	day of year	amplitude (mg m^{-3})	days
25	2001	17.7	135	11.9	141	5.8	6
26	2002	20.8	179	11.1	178	9.7	1
28	2003	17.8	147	17.7	126	0.1	21

Table 5.14: Amplitude and timing of the first spring bloom: Comparison between model prediction (simulation with constant k value) and data at Calshot.

5.5 Parameter calibration at Calshot in 2001 using an objective analysis

Model to data comparisons reveal the model deficiency in determining qualitatively the DIN observations and zooplankton data (section 5.4). This discrepancy can originate from 1) the choice of parameters, 2) choice of model ecosystem structure and functionality 3) physical forcing and 4) errors in data. Here we focus on parameter calibration using an objective model fit analysis which consists of determining the best parameter set minimizing the model to data misfit. One year and one station has been selected for this test, Calshot in 2001, where zooplankton data are most abundant and show the clearest seasonal cycle. A fit of the model data at Calshot in 2001 has been carried out using the micro-genetic algorithm (Krishnakumar, 1989; Caroll, 1996), a global search technique which searches for the combination of parameters giving the minimum misfit between model results and observations. The micro-genetic algorithm first defines the set of model parameters (where the set is termed an individual) coded as a binary string, which are selected for reproduction in the next generation (or iteration) using a stochastic process, weighted by the model-to-data misfit function. At each iteration, a predefined number of individuals are generated, giving a population of individuals. At the end of the iteration, selected individuals are paired and recombined to create pairs of new individuals, a process called genetic crossover. The algorithm runs for a fixed number of generations. The fittest individual giving the smallest model to data-misfit in each generation is reproduced in the next. In contrast to a genetic algorithm, the micro-genetic algorithm does not use mutation, which consists of randomly modifying part of the individuals to generate a new population, therefore the search technique tends to converge on the fittest individuals. In the micro-genetic algorithm, if population variability (differences between individuals of the same population) falls below 5

%, a new population is randomly generated, to maintain the search across the wide range of parameter values. At each iterations, the ecosystem is run for 4 years using the irradiance light forcing in 2001 and the model to data misfit is calculated using modelled biological variables in year 4 (the first three years are spinup years). The misfit, in it simplest form, is the sum of the squared difference between model and observations across all data types (e.g. chlorophyll, zooplankton etc.) when observations are available (Fasham and Evans, 1995). In practice, various weighting terms can be used to account for the variation in magnitude between data types (Spitz et al., 1998) or the measurement uncertainty (Fennel et al., 2001; Schartau, 2001). In the present study, a non-weighted and a weighted cost function have been tested:

The non weighted cost function τ_M is

$$\tau_M = \frac{1}{2}\sum_{i=1}^{M}\frac{1}{N_i}\sum_{j=1}^{N_i}(y_{i,j,model} - y_{i,j,obs})^2 + \phi_M \tag{5.26}$$

$$\phi_M = \sum_{i=1}^{M}(y_{i,day_{1095},model} - y_{i,day_{1460},model})^2 \tag{5.27}$$

The weighted cost function $\tau_{w,M}$ accounts for the variation in magnitude between data type and is defined by:

$$\tau_{w,M} = \frac{1}{2}\sum_{i=1}^{M}\frac{1}{N_i}\sum_{j=1}^{N_i}\frac{(y_{i,j,model} - y_{i,j,obs})^2}{w_{i,obs}} + \phi_{w,M} \tag{5.28}$$

$$\phi_{w,M} = \sum_{i=1}^{M}\frac{(y_{i,day_{1095},model} - y_{i,day_{1460},model})^2}{w_{i,obs}} \tag{5.29}$$

where i is the sum over the number (M) of data types available for comparison, $y_{i,j,obs}$ is the measurement of datatype i on day j and $y_{i,j,model}$ is the modelled value for datatype i on day j. In the present case, the three data types DIN, phytoplankton, and zooplankton are available thus $M = 3$. The squared difference of model and observations is divided by a weighting term w_i. In equations 5.28 and 5.29 application, w_i is equal to the temporal average of the data type used to account for the variation in biomass between each biological variable. N_i is the number of observations existing for each data type. ϕ is a penalty term calculating the deviation of the model results between the beginning of year 3 and the end of year 4 and is added to contrained the ecosystem model to reproduce a seasonal cycle. 14 free parameters of the ecosystem model were optimized and compared

with the parameters from scenario 25 regarded as the standard run (table 5.15). Four parameters are kept constant in the optimization: temperature T, depth H, k which is determined by the observations (k =0.56 m^{-1} in May-June at Calshot in 2001, see table 4.8), and $p2$ which is not a free parameter ($p2 = 1 - p1$). At each generation the number of individuals was equal to the number of free parameters (14), as recommended by Schartau (2001) and Schartau and Oschlies (2003). A run of 2000 generations was performed.

symbol	lower-upper bound	weighted optimized parameter (τ_w)	deviation with weighted optimized parameter (%)	unweighted optimized parameter (τ)	deviation with weighted parameter (%)	standard value (sc. 25)	unit
α	0.0175-0.05 [a]	0.0500	11.1	0.0475	5.5	0.045[b]	$(Wm^2)^{-1}$ d^{-1}
β	0-1 [a]	0.3686	**50.8**	0.4510	39.9	0.75[a]	none
g	0.1-2.[a,b]	0.2659	26.6	0.8376	**298.8**	0.21	d^{-1}
k_3	0.5-1.2 [a]	0.7773	22.3	1.0380	3.8	1[a]	d^{-1}
k_D	0.025-0.1[a]	0.0253	49.4	0.0250	50.0	0.05[a]	m d^{-1}
k_{DIN}	0.25-0.75 [a]	0.7480	49.6	0.5010	0.2	0.5[a]	mmol N m^{-3}
k_z	0.5-1 [a]	0.8863	**343.1**	0.5098	**154.9**	0.2[a]	mmol N m^{-3}
mp	0.045-0.11[a]	0.0590	31.1	0.0491	9.1	0.045[b]	d^{-1}
m_z	0.01-1 [b]	0.0785	**161.7**	0.0901	**200.0**	0.03[b]	d^{-1}
$p1$	0-1 [c]	0.9569	**91.4**	0.0392	**92.1**	0.5[b]	none
R_{exc}	0.05-0.12 [a]	0.1005	0.5	0.0574	42.6	0.1[a]	d^{-1}
R_{rem}	0.001-0.1 [d]	0.0111	11.0	0.0130	30.0	0.01[b]	d^{-1}
w_D	0-10 [e]	9.4706	**57.8**	9.8941	**64.9**	6[b]	d^{-1}
w_P	0-1 [f]	0.1245	24.5	0.0649	35.1	0.1[b]	m d^{-1}
τ_3		×		10.8488		93.9626	
$\tau_{w,3}$		5.0424		×		9.1447	

Table 5.15: Results from the optimizations, compared with the standard run (scenario 25). The references used to determine the upper and lower bounds for the parameter search are from a) Fasham et al. (1990), b) Kelly-Gerreyn et al. (2004), c) percentage, d) (Anderson and Williams, 1998) uses 0.003 d^{-1} and (Billen and Lancelot, 1988) uses 0.05 d^{-1}, therefore an arbitrary range between 0.001 and 0.1 is used, e) (Anderson and Williams, 1998), and f) varies depending on phytoplankton species (Ross, 2004). The deviation (expressed as a percentage) is calculated as the relative error which is the absolute error between the optimized parameter value and the parameter value in scenario 25 divided the parameter value in scenario 25. Deviation above 50 % are in bold face.

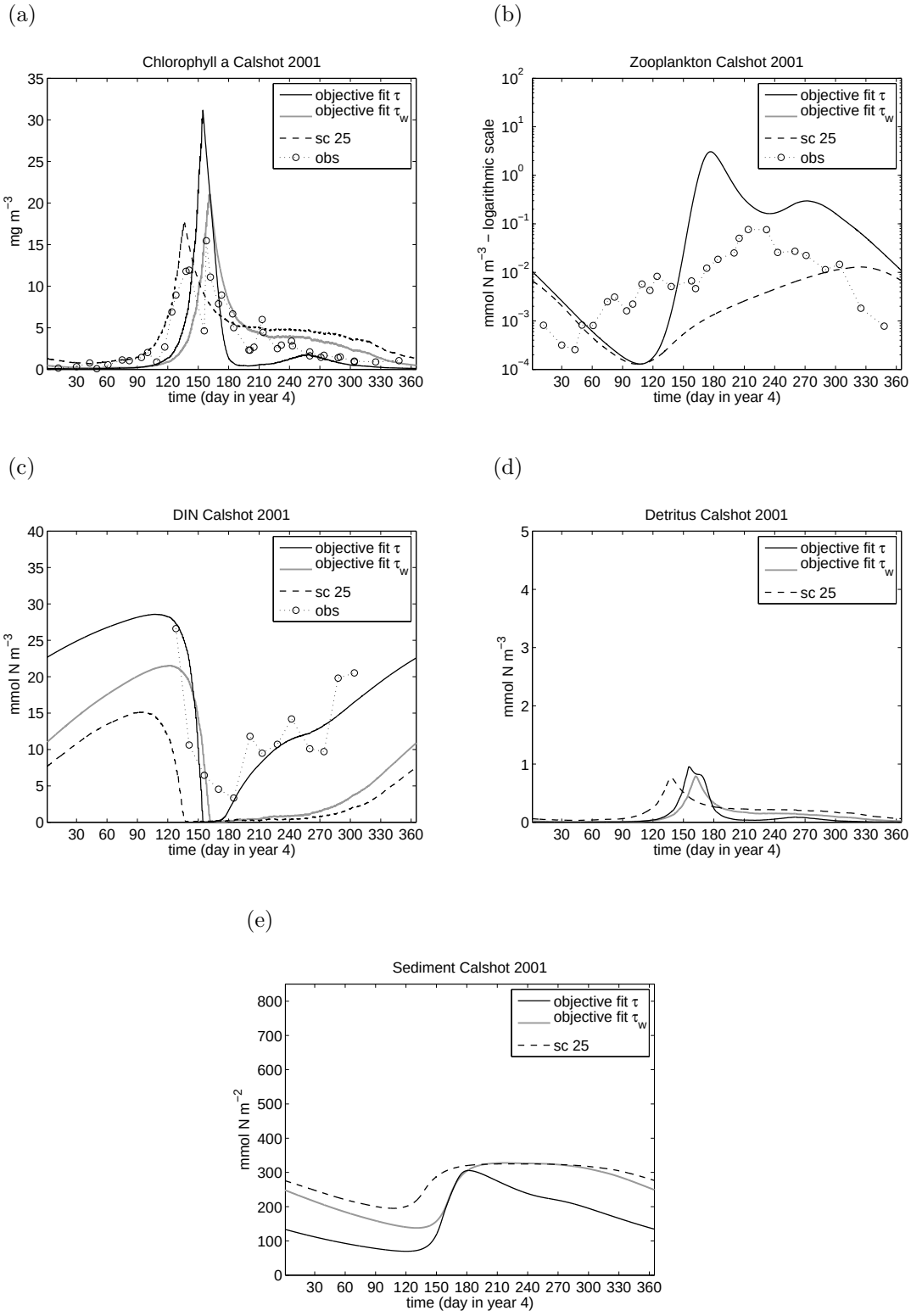

Figure 5.12: Comparison of seasonal cycle of the 5 ecosystem compartments (phytoplankton, zooplankton, DIN, detritus and sediment) with observations and results from the standard run (scenario 25). The black line is the results obtained using the unweighted cost function (equation 5.26) and the grey line is the result obtained with the weighted cost function (equation 5.28).

The parameter ranges were determined from the literature (table 5.15). The number of possibilities which determine the number of possible values between the lower and the upper bound is set to 256 for each parameter. The numerical values for the coefficients are given in table 5.15 and the results for the five state variables are compared against the standard run in figure 5.12.

Results of the optimization with the unweighted function reproduce two maxima in the modelled chlorophyll *a* (figure 5.12a). The first corresponds to the spring bloom and fits the second observed peak that occured on day 158, with a magnitude twice that of the observations. The second modelled maximum occurred later in the year on day 260. Modelled zooplankton biomass is characterized by two peaks, and shows greater variation compared to the observations (figure 5.12b). The fit of the modelled DIN to the observations appears to more closely follow the observations compared to the standard run, particularly in the regeneration of DIN after the spring bloom in summer and autumn (5.12c). Detritus is similarly affected by two peaks, however the seasonal range in magnitude appears similar to the standard run (figure 5.12d). Sediment nitrogen seasonal dynamics show a peak on day 180 followed by a constant decrease in late summer, autumn and winter indicating a constant regeneration to the water column, whereas the sediment pool in the standard run shows a summer steady state from day 180 to day 300 when sediment nitrogen remains constant at 300 mmol N m^{-2} (figure 5.12e). Sediment nitrogen in the optimized run is depleted relative to the standard run. Using the unweighted cost function, the model to data misfit is reduced from 93.96 (standard run) to 10.85 (table 5.15).

The optimized fit obtained using the weighted term is characterized by one maximum in chlorophyll *a* biomass which fits the second observed spring phytoplankton bloom (figure 5.12a). The set of optimized parameters does not improve the fit of the zooplankton data, instead zooplankton values are equal to zero all year round (figure 5.12b). DIN regeneration after the spring bloom is slightly greater compared to the standard run, but less than the unweighted optimized output (figure 5.12c). Detritus output is similar to the unweighted output and presents a peak at similar magnitude (0.85 mmol N m^{-3}) but is delayed to day 165 compared to the standard run (figure 5.12d). Sediment nitrogen concentrations reach similar levels in summer and autumn in both the optimized run and the standard run (approximately 300 mmol N m^{-2}) (figure 5.12e). In contrast, the objective fit using τ_w in winter-spring gives a lower accumulation of nitrogen than the standard run. This second optimization using

the weighted cost function results in a model-to-data misfit equal to 5.0424 compared with 9.1447 in the standard run (table 5.15).

The highest deviations (above 50 % between coefficients from optimizations and the standard run are obtained for k_z, m_z, $p1$, w_D (table 5.15). The zooplankton mortality term, determined by both k_z and m_z, appears to be a major factor modified by the calibration of the ecosystem model. In addition to these 4 coefficients, the optimized fit using τ_w gives a large difference in the parameter β compared with the standard run, and the optimized fit using τ gives a strong modification of the zooplankton grazing rate g relative to the standard run.

Both optimizations lead to an improvement of the DIN seasonal cycle. The optimization using the weighted cost function returns lower DIN levels, since relative to the unweighted cost function the weighted cost function gives more weight to the two other data types, which have a lower averaged nitrogen biomass (phytoplankton and zooplankton). As a result the weighted function compared to the unweighted function gives a better fit in terms of magnitude of the spring phytoplankton bloom, and the minimization of the zooplankton to data misfit is obtained when the zooplankton compartment is destroyed. Both optimized simulations still reproduce a similar seasonal dynamics than the standard run, with notably a spring phytoplankton bloom. Consequently from the sensitivity analysis shown in section 5.3, variations of the forcing function (coefficient of attenuation or variation in the seasonal cycle in irradiance) for this optimized set of parameter values are expected to give qualitatively the same result (a delay in the timing of the bloom in combination with an increase of the magnitude of the bloom in the case of an increase of the coefficient of attenuation).

5.6 Testing a Phytoplankton-Zooplankton model

As outlined at the beginning of section 5.5, the choice of model ecosystem compartments and the biogeochemical fluxes between them (i.e. model structure) may be a second source of error in model to data comparison. DIN observations at both stations in 2001 and 2002 reveals that DIN never falls below 7 mmol N m^{-3} (figures 5.9b and 5.10b), suggesting that nutrient may be a non-limiting factor in phytoplankton bloom development. To assess the importance of nutrient limitation in the dynamics of the spring phytoplankton bloom, a reduced version of the ecosystem (NPZDS) model, using only the phytoplankton and zooplankton compartments, has been tested. This new structure is analogous to a

predator-prey model which by definition incorporates 4 main functional terms: the growth rate of the prey, prey mortality rate due to predation, predator growth rate due to predation and predator mortality rate. The set of equations in the ecosystem model (section 5.2) is therefore reduced to the phytoplankton growth rate, grazing by zooplankton, zooplankton grazing on phytoplankton and the zooplankton mortality terms:

$$\frac{dP}{dt} = J(I_{z,t})P - Gp \tag{5.30}$$

$$\frac{dZ}{dt} = \beta Gp - Dez \tag{5.31}$$

The predator growth rate due to predation is proportional to the prey mortality rate, since only a fraction of the prey ingested is assimilated by the predator. The nutrient limitation Q is not included as the reduced ecosystem model regards nutrients as a non-limiting factor. The phytoplankton-zooplankton (PZ) model has been optimized using the microgenetic algorithm and the dataset available at Calshot in 2001. A similar optimization procedure was adopted (2000 generations, 256 possibilities for each parameters, 3 years of spinup and model to data misfit calculated with the results in year 4 of the model simulation), and resulted in the calibration of 7 parameters (table 5.16). The cost functions used for the simulation are the same as before (equations 5.26 and 5.28), but only two datatypes (chlorophyll *a* and zooplankton) are necessary for determining the misfit and thus $M = 2$.

The optimized coefficients indicate in both cases (optmization with the weighted and unweighted cost functions) a greater model to data misfit than obtained by the NPZDS model (table 5.16). In both fits, spring phytoplankton biomass reaches a maximum of 2.5 mg m^{-3} of chlorophyll *a* compared with observations above 10 mg m^{-3} (figure 5.13a). The PZ model overestimates zooplankton biomass (figure 5.13b). The best fit in seasonal abundance in zooplankton is obtained qualitatively in the case of the simulation using the PZ model in combination with the weighted function.

The model results tend to support the hypothesis that the phytoplankton bloom development is dependent on the seasonal fluctuation and trophic relationships with the other components (nutrient or DIN, detritus and sediment) included in the more complex model. The other possible explaination is that the interdependency between phytoplankton and zooplankton can not be reproduced

symbol	lower-upper bound	optimized parameter (τ_w)	optimized parameter (τ)	standard value (NPZDS)	unit
α	0.0175-0.05 [a]	0.0176	0.0213	0.045[b]	(W m^2)$^{-1}$ d^{-1}
β	0-1 [a]	0.0824	0.3137	0.75[a]	none
g	0.1-2.	1.4784	0.4502	0.21	d^{-1}
k_3	0.5-1.2 [a]	1.0627	1.1122	1[a]	d^{-1}
k_z	0.5-1 [a]	0.2000	0.4541	0.2[a]	mmol N m^{-3}
m_z	0.01-1 [b]	0.0996	0.0996	0.03[b]	d^{-1}
$p1$	0-1 [c]	0.5059	0.6412	0.5[b]	none
τ_2		×	4.6725	2.9571	
$\tau_{w,2}$		2.2581	×	0.8123	

Table 5.16: Results of the optimization for the phytoplankton-zooplankton model. The numerical value of the cost function for the standard run including only the two datatypes are included for comparison. References (a, b) for the choice of parameter range are given in table 5.15.

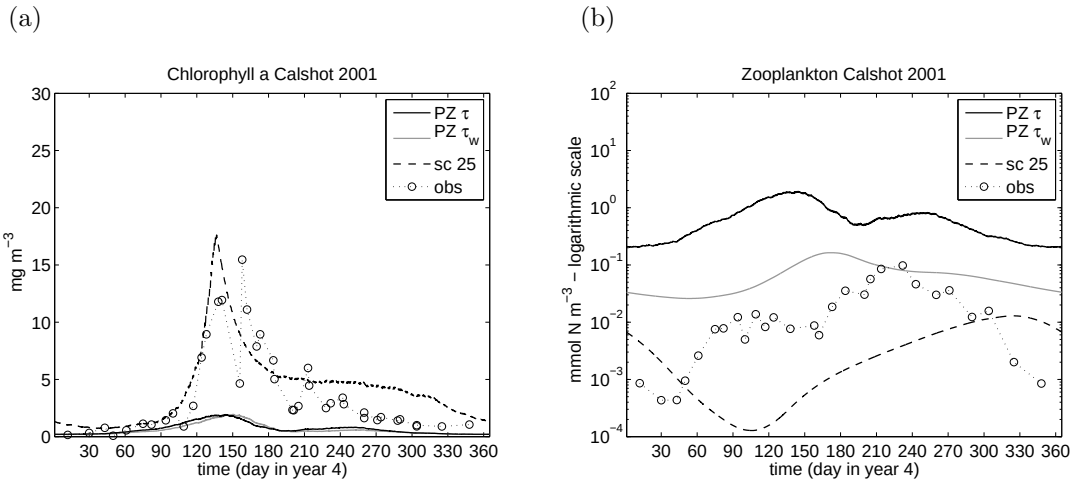

Figure 5.13: Comparison between model results (phytoplankton-zooplankton model), observations, and results from scenario 25 (standard run) for the two state variables phytoplankton and zooplankton.

by the reduced phytoplankton-zooplankton model and that this deficiency originates from the choice of biogeochemical functions used to simulate the predator-prey processes, and/or the forcing functions.

5.7 Summary and discussion

The sensitivity analysis of the ecosystem model indicates three main sources of interranual variability and by order of importance 1) k plays a key role in determining the interrannual variability with a higher attenuation coefficient generating a higher bloom in magnitude and a delay in the bloom. 2) The seasonal cycling of irradiance forcing is the second source of interranual variability of the spring bloom, but with a minor effect compared to k variation 3) At high level of nitrogen inventory, interranual variability is generated by the intrinsic dynamic of the ecosystem model which depends on the parameter k. This intrinsic variability takes the form of a biannual cycle.

The interranual variability generated by the intrinsic dynamic of the ecosystem model is not desirable, since it limits the prediction capabilities of the model outputs. The formation of the complex behaviour (a biannual cycle) occurs when the total inventory of nitrogen is increased and when the attenuation coefficient is high. Linear parameterizations of phytoplankton and zooplankton mortality has been suggested to be the cause of complex behaviours in other NPZ-type models (Popova et al., 1997). The replacement of a non-linear formulations for phytoplankton mortality could be investigated in the present model with the aim of reducing the sensitivity of the model to the formation of a biannual cycle.

An existing dataset of surface irradiance and the attenuation coefficient for years 2001, 2002 and 2003 has been used, in order to evaluate the impact a realistic light forcing function (k and I_o) has on the prediction of the timing and magnitude of the phytoplankton bloom. While comparing model and data, the use of a constant background coefficient of attenuation set as the averaged value for May-June of the year gives reasonable estimate of the timing and magnitude of the first spring bloom. This would tend to confirm the hypothesis that light-forcing is a major determinant of spring bloom interranual variability and therefore a high degree of realism of the light forcing function is necessary to model spring bloom dynamics. The mismatch observed between observed and modelled chlorophyll concentration could be generated by interranual variability in nutrient concentration, and other losses or gains not explicitly modelled in the present

study. The modelled results underestimate DIN concentration at NWNetley, but a better agreement is found when the nitrogen inventory is increased. A reasonably good agreement between modelled and observed DIN concentration is obtained at Calshot. Another model deficiency is the high sensitivity of the zooplankton concentration to the choice of the k value, with result in an unrealistic depletion of the zooplankton concentration all year round when k is set above 0.6 m^{-1}. The optimizations of the model parameters improve the DIN seasonal cycle but are still deficient in reproducing the zooplankton seasonal cycle. Reducing the ecosystem model to a two-compartment model (phytoplankton-zooplankton model) results in a higher model-to-data misfit. Therefore none of the ecosystem model version (standard 5-compartment model, optimized 5-compartment model or optimized phytoplankton-zooplankton model) provide a satisfactory results for all state variables.

The coarse temporal resolution of the discrete chlorophyll data (approximately every week) gives only an approximation of the timing and magnitude of the bloom. Therefore some caution needs to be made on the calculation between between modelled and observed spring bloom (timing and magnitude). A more precise determination of the observed spring phytoplankton bloom can be achieved by the use of continuous monitoring. This type of instrument requires a high level of maintenance (weekly calibration and cleaning), and the continuous time-series generated requires a careful data processing (filtering of outliers and comparison with boat surveys to determine the accuracy of calibration). In the present work only data from boat sampling were used, since it provides the most reliable and homogeneous dataset covering three consecutive years (2001-2002-2003) at two stations in the estuary (Holley et al., 2007).

At NWNetley, phytoplankton dynamics is more complex than Calshot with the formation of summer blooms in addition to the spring bloom. The role of other limiting elements (P and Si) are not accounted for in this modelling approach and could play a role in the formation and decline of the summer bloom at NWNetley (Hydes and Wright, 1999). However this study was focused on the first spring bloom and for this reason, the degree of complexity of the ecosystem model which include only one limiting nutrient was appropriate.

Part of the uncertainties in the reproduction of the spring phytoplankton bloom could be generated by other processes which are not accounted for in this simple ecosystem model. In the case of losses, another source of mortality is cell lysis caused by virus infections. Rate of cell lysis yelding to mortality of up to 0.3 d^{-1}

has been reported (Brussaard, 2004). In the North Sea, viral lysis has been reported to prevail over microzooplankton grazing at the end of the bloom of the species *Phaeocystis globosa* (Baudoux et al., 2006). In the present work, top-down control of primary production by zooplankton grazing is parameterized in a very simple formulation. Other authors have partitioned grazing into benthic and pelagic grazing in an estuarine ecosystem model resolving the vertical structure of the water column (Lucas et al., 1999a). To address the question of the role of zooplankton grazing, more field sampling are needed to estimate the regulation of phytoplankton population by zooplankton in Southampton Water.

Adding complexity into the present ecosystem model by accounting for vertical or horizontal displacement would allow the simulation of short-term variation originating from estuarine circulation in the physical forcing of spring phytoplankton blooms. Turbulence influences both light-forcing by determining sediment resuspension of particles and the rate of primary production depending on the position of phytoplankton, nutrient and grazers in the water column. For example, increasing the vertical turbulence regime or adding phytoplankton cell sinking lengthens the bloom time scale and consequently increases the limiting effect of seaward surface advection on phytoplankton biomass accumulation (Zakardjian et al., 2000). Simulation of individual planktonic organisms and their displacement in the water column give the results of photoadaptation processes generating 40 % increase of primary production at neap tide (Lizon et al., 1998). A recent modelling study has revealed the complex interaction between sediment dynamics, driven by tides and river flow and diatom growth in the Sheld estuary (Arndt et al., 2007). The modelling approach presented by Lucas et al. (1999b) indicates that estuarine tidal flow induces 5 transport-related mechanisms which interact with the phytoplankton dynamics and contribute to the determination of the timing and the location of a bloom. These five mechanisms are import of biomass, role of deeper channel as conduit, physical-biological phasing and lateral shoaling. The disadvantage of a coupled hydrodynamic-ecosystem model is the increased complexity of the model solution due to the multiplicity of processes modelled. Consequently, this makes it more difficult to analyse mechanisms of ecosystem variability compared with process-based studies using a simple model.

Chapter 6

Conclusion

The present work has focused on investigating the physical and biological variability of the Southampton Water-Solent estuary. The objectives were :

- 1) To study the impact of wind forcing on patterns of estuarine circulation.

A three-dimensional hydrodynamic model of the estuarine circulation of the Solent-Southampton Water estuarine system has been used for this purpose. An extended validation of the model of estuarine circulation is presented, using tide gauge data, ADCP velocity measurements and discrete salinity measurement. The model reproduces with a good agreement the specific features of the tides (the 'double high water' and the 'young flood stand') in Southampton Water and the Solent. The tidal analysis indicate that the model is less successful in predicting the shallow water components and the diurnal components. The use of a baroclinic model gives an accurate estimate of velocity, more specifically the vertical and temporal variation in the observed velocity field. The seasonal, the semi-diurnal variation and the spring-neap variation in bottom to surface salinity difference is well reproduced. The spatial gradient is overestimated by 1-2 salinity units, and could possibly be improved by the use of more realistic boundary conditions for salinity.

The effect of real wind forcing on the distribution of the water volume has been determined, in order to quantify the contribution of the local wind forcing on the variation in sea surface elevation. The numerical model establishes a 'wind setdown' when wind blows offshore and 'wind setup' when wind blows onshore. The formation of a wind setup and setdown by a time-varying wind forcing results in a variation of up to 11 cm in sea surface elevation at the head of Southampton Water, and up to 5 cm at the mouth of Southampton Water. Consequently, a sea surface slope (up to 6 cm) establishes in Southampton Water, which is mainly

controlled by the S-N wind component (the maximum wind intensity over the whole time-series is 12 m s^{-1}). This gives an estimate of the contribution of the local wind to the variation in water level. Wind forcing strongly influences the vertical salinity field. A two-fold reduction in stratification can be attributed to the wind. Wind is more efficient in reducing the stratification at ebb (when tidal straining enhances stratification) than flood. As a result wind appears to reduce the asymmetry of the semi-diurnal cycle in stratification.

- 2) To characterize the spatial and temporal variability of light penetration in Southampton Water.

A specific feature of the Solent-Southampton Water estuary is the predominance of suspended particulate matter (or turbidity) in determining light attenuation, and thus the negligible contribution of phytoplankton concentration on the seasonal cycle of the coefficient of attenuation for downwelling irradiance. Consequently light penetration is the estuary is governed by the dynamics of sediment resuspension. Seasonal variation in the coefficient of attenuation is characterized by a minimum in May-June and a maximum in October-November. A spring-neap variability in turbidity is observed after filtering out the semi-diurnal cycle from high temporal resolution turbidity measurements. This spring-neap variation is shown to be expressed as a linear function of the tidal range. The attenuation coefficient for downwelling irradiance ranges from 0.34 to 1.55 m^{-1} in the mid estuary (NWNetley), and from 0.20 to 2.78 m^{-1} at the mouth of Southampton Water (Calshot) throughout the year. Highest attenuation occurs occurs at the mouth of Southampton Water, suggesting the importance of both tidal resuspension in the determination of the suspended particulate matter in the water column, compared with the SPM originating from the rivers and SPM of marine origin.

- 3) To investigate the influence of light variability on the timing and magnitude of the spring phytoplankton bloom.

Based on the improvement of knowledge of the spatial and temporal variability of light penetration in the Southampton estuary demonstrated here, the impact of the variation of the coefficient of attenuation on the timing and the magnitude of the phytoplankton bloom has been quantified. For this purpose, a zero-dimensional five-compartment ecosystem model including a sediment compartment has been developed. Interranual variability in phytoplankton dynamics is generated by

intrinsic dynamics of the system, and depends, in part, on the total content of nitrogen in the model and the value used for the coefficient of attenuation (k), resulting in the formation of a biannual cycle. This effect is negligible at low nitrogen inventories. Sensitivity analysis demonstrates that the spring bloom responds significantly in time and magnitude to the choice of the non-varying coefficient of attenuation, with an increased constant coefficient generating a later spring bloom of higher magnitude. For changes in k in increments of 0.1 m^{-1}, a delay of up to 30 days in the timing and up to 3 mg m^{-3} in the magnitude of the spring chlorophyll maxima are predicted. Year-to-year variation in surface irradiance is a minor source of interranual variability compared with k variation, and produces a deviation of up to 5 days in the timing and of up to 0.95 mg m^{-3} of the spring chlorophyll maxima. Introducing the seasonal time-varying k generates a delayed and increased bloom compared with a constant k. The use of the formulation based on the observed seasonal cycle of the attenuation coefficient in some years in Southampton Water remains difficult due to the strong sensitivity of the ecosystem model to elevated level of attenuation which results in the formation of an irrealistic depletion of the modelled zooplankton. Compared to data, the idealised seasonal cycle in chlorophyll simulated using realistic surface irradiance forcing in combination with a constant k set at the averaged observed May-June $K_d(PAR)$ predicts the timing of the spring bloom to within 6 to 25 days and its magnitude to within 0.5 to 3.3 mg m^{-3} at NWNetley (mid-estuary) and from 1 to 21 days and from 0.1 to 9.7 mg m^{-3} at Calshot (estuary mouth). Comparison with DIN measurements shows an underestimation of the seasonal cycle. The modelled DIN level can be improved by using a higher inventory of total nitrogen, however this increases the discrepancy between the modelled and observed chlorophyll concentration. Modelled zooplankton shows the highest discrepancy with observations, which is more pronunced for higher k values.

Future work

- The model has proved useful to reproduce numerous processes occurring in these estuarine waters. The application of the numerical three-dimensional model of estuarine circulation to other estuaries is a possible prospect. This would require a new configuration (grid and forcing) to adapt the present model to a new area. One major limitation of the model is the strong constraint imposed by the grid size on the time-step, although it is not uncommon amongst three-dimensional models.

- The simple zero-dimensional model presented here could be considered as a first step in determining the factors influencing the formation of phytoplankton blooms in the estuary. Other issues like the formation of summer blooms in Southampton Water may require a more complex modelling approach. This could be addressed by adding more biological variables (e.g. additional phytoplankton group or limiting nutrient) to the ecosystem model, however this requires to evaluate the role of other components of the food chain to the phytoplankton dynamics by field observations. An other option is to embed the ecosystem model in the three-dimensional hydrodynamic model of estuarine circulation to account for the influence of the physical environment (stratification and advection processes).

- In this work, existing datasets have been used, which mainly consisted of discrete data collected in the estuary at three reference stations on a weekly or biweekly timescale. An important parameter to account for is the variability generated by the tidal cycle (semi-diurnal and spring-neap variation). Consistency in the data collected requires measurements to be made at similar tidal conditions. For practical reasons (boat availability and daytime measurement), it is not always feasible to make measurements under similar tidal conditions. However the recent development of continuous monitoring equipment should yield a better set of observations for investigating the temporal variability of physical, chemical and biological variables, although these data logging systems require high levels of maintenance. In conjunction with modelling tools, such as the ecosystem model developed in this work, a more comprehensive dataset would allow further analysis of the processes of variability controlling phytoplankton dynamics to be examined, as well as help to guide the level of model complexity necessary.

Bibliography

Algan, O. and Clayton, T. (1994). Estuarine mixing of clay minerals in the Solent region. *Sedimentary Geology*, 92:241–255.

Ali, E. M. (2003). *Processes and conditions influencing phytoplankton growth and bloom initiation in a macrotidal estuary, Southampton Water*. PhD thesis, University of Southampton, Southampton,UK.

Altisan, I. A. R. (2006). *Effects of Light and Nutrient Gradients on the Size Structure, Taxonomic Composition and physiological Status of the Phytoplankton Community Within a Temperate Eutrophic Estuary*. PhD thesis, University of Southampton, Southampton, UK.

Andersen, A. (1998). Intercomparison of recent ocean tide models. *Journal of Geophysical Research*, 100(C12):25261–25282.

Anderson, D. M., Glibert, P. M., and Burkholder, J. M. (2002). Harmful algal blooms and eutrophication: Nutrient sources, composition and consequences. *Estuaries*, 25(4B):704–726.

Anderson, T. R. and Williams, P. (1998). Modelling the seasonal cycle of dissolved organic carbon at the station e_1 in the english channel. *Estuarine and Coastal Shelf Science*, 46:93–109.

Andrews, J. (1989). British estuaries: an internationally important habitat for birds. *British wildlife*, 1.

Antoine, P., Coutard, A. D., Gibbard, P., Lautridou, J.-P., and Ozouf, J.-C. (2003). The pleistocene rivers of the english channel. *Journal of Quaternary Science*, 18(3-4):227–243.

Arndt, S., Vanderborght, J., and Regnier, P. (2007). Diatom growth response to physical forcing in a macrotidal estuary: Coupling hydrodynamics, sediment transport and biogeochemistry. *Journal of Geophysical research*, 112(C05045).

Babin, M., Stramski, D., Ferrari, G. M., Claustre, H., Bricaud, A., Obolensky, G., and Hoepffner, N. (2003). Variations in the light absorption coefficients of phytoplankton, non algal particles and dissolved organic matter in coastal waters around europe. *Journal of Geophysical Research*, 108(C7):4–1–4–20.

Bailey, M. C. and Hamilton, D. P. (1997). Wind induced sediment resuspension: a lake-wide model. *Ecological Modelling*, 99:217–228.

Balzano, A. (1998). Evaluation of methods for numerical simulation of wetting and drying in shallow water flow models. coastal engineering, 34:83:107. *Coastal Engineering*, 34:83–107.

Barnes, R. S. K., Cougilan, J., and Holmes, N. J. (1973). A preliminary survey of the macroscopic bottom fauna of the solent, with particular reference to *crepidula fornicata* and *ostrea edulis*. *Proceedings of the malocological Society of London*, 40.

Baudoux, A., Noordeloos, A. A. M., Veldhuis, M. J. W., and Brussaard, C. P. D. (2006). Virally induced mortality of *phaeocystis globosa* during two spring blooms in temperate coastal waters. *Aquatic microbial ecology*, 44.

Beaugrand, P. A. (2002). Reorganisation of north atlantic marine copepod biodiveristy and climate. *Science*, 296(5573):1692–1694.

Bianchi, A. P. (1994). *Studies of volatile organic compounds in the water and sediments of a British estuary - Southampton Water*. PhD thesis, The Open University, Milton Keynes, UK.

Bianchi, A. P. and Varney, M. S. (1998a). Volatile organic compounds in the surface waters of a british estuary. part 1. occurence, distribution and variation. *Water Research*, 32(2).

Bianchi, A. P. and Varney, M. S. (1998b). Volatile organic compounds in the surface waters of a british estuary. part 2. fate processes. *Water Research*, 32(2).

Billen, G. and Lancelot, C. (1988). Modelling benthic nitrogen cycling in temperate coastal ecosystems. In Blackburn, T. H. and SØrensen, J., editors, *Nitrogen cycling in coastal marine environments*, pages 341–378. John Wiley and Sons.

Bokuniewicz, H. (1995). Sedimentary systems of coastal-plain estuaries. In Perillo, G. M. E., editor, *Geomorphology and Sedimentology of Estuaries*, pages 49–111. Elsevier Science.

Booth, J. G., Miller, R. L., McKee, B. A., and Leathers, R. A. (2000). Wind-induced bottom sediment resuspension in a microtidal coastal environment. *Continental Shelf Research*, 20:785–806.

Boxall, S. R., Cabioch, L., D'Hieres, G. C., Collins, M., Guegueniat, P., Statham, J. C. S. P., and Wartel, M. (1995). FlUXMANCHE II, hydrodynamics, biogeochemical processes and fluxes in the Channel. In *Marine Science and technologies, Second MAST days and Euromar market*, volume 1. Official Publication of the European Communities.

Boxall, S. R. and Robinson, I. S. (1987). Shallow sea dynamics from CZCS imagery. *Advanced Space Research*, 7:237–246.

Boynton, W. R. and Kemp, W. M. (1985). Nutrient regeneration and oxygen consumption by sediments along an estuarine salinity gradients. *Marine Ecology Progress Series*, 23:45–55.

Bray, M. and Carter, D. (2003). SCOPAC sediment transport study 2003. Technical report, River and Coastal Environments Research, Department of Geography at the University of Portsmouth.

Brussaard, C. P. D. (2004). Viral control of phytoplankton populations -a review. *The Journal of Eukaryotic Microbiology*, 51(2).

Caroll, D. L. (1996). Chemical laser modeling with genertic algorithms. *American Institutes of Aeronautic and Astronautics*, 34.

Carr, J. F., de Turville, C. M., Jarman, R. T., and Spencer, J. F. (1980). Water temperatures in the solent estuarine system. In Burton, J. D., editor, *The Solent Estuarine System - an assessment of present knowledge*, number 22 in C, pages 36–43. N.E.R.C. Publication, Swindon.

Charrier, S., Weeks, A., Lewey, S., and Robinson, I. (2000). Underwater light in tidal waters: Possible impact on macro-algae communities. In Collins, M. and Ansell, K., editors, *Solent Science- A Review*, pages 283–294. Elsevier Science B.V.

Charrier, S. C., Weeks, A. R., Lewey, S., and Robinson, I. (1998a). The spatial and temporal distribution of simulated interidal underwater light. In Grattan, K., editor, *Applied Optics and optoelectronics 1998, Proceedings of the applied Optics Divisional Conference of the Institute of Physics*, Bristol, UK. Institute of Physics Publishing.

Charrier, S. C., Weeks, A. R., Robinson, I. S., and Lewey, S. A. (1998b). The optical characteristics of tidal waters. In *Proceedings of the Ocean Optics XIV conference*, USA. Office of Naval Research, Ocean, Atmosphere and Space Sciences and Technique.

Chen, C., Liu, H., and Beardsley, R. C. (2003). An unstructured grid, finite-volume, three-dimensional, primitive equations ocean model: Application to coastal ocean and estuaries. *Journal of Atmospheric and Oceanic Technology*, 20:159–186.

Choi, B. and Wilkin, J. K. L. (2006). The effect of wind on the dispersal of the hudson river plume. *Journal of Physical Oceanography*, 37:1878–1897.

Cloern, J. E. (1996). Phytoplankton bloom dynamics in coastal ecosystems: A review with some general lessons from sustained investigation of San Francisco bay, California. *Review of Geophysics*, 34(2):127–168.

Cloern, J. E. (2001). Our evolving conceptual model of the coastal eutrophication problem. *Marine Ecology Progress Series*, 210:223–253.

Collins, K. J. and Mallinson, J. (2000). Marine habitats and communities. In Collins, M. and Ansell, K., editors, *Solent Science- A Review*, pages 247–259. Elsevier Science B.V.

Crawford, D. W. and Purdie, D. A. (1992). Evidence for avoidance of flushing from an estuary by a planktonic, phototrophic ciliate. *Marine Ecology Progress Series*, 79:259–265.

Crawford, D. W., Purdie, D. A., Lockwood, A. P. M., and Weissman, P. (1997). Recurrent red-tides in the Southampton Water estuary caused by the phototrophic ciliate *mesodinium rubrum*. *Estuarine, Coastal and Shelf Science*, 45:799–812.

Crooks, S. (2004). The effect of sea-level rise on coastal geomorphology. *Ibis*, 146.

Croudace, I. W. and Cundy, A. B. (1997). Heavy metal and hydrocarbon pollution in recent sediments from southampton water, southern england: A geochemical and isotopic study. *Environmental Sciences & Technology*, 29:1288–1296.

Cugier, P. and Le Hir, P. (2002). Development of a 3D hydrodynamic model for coastal ecosystem modelling. Application to the plume of the seine river (France). *Estuarine, Coastal and Shelf Science*, 55:673–695.

Cundy, A. B., Croudace, I. W., Thomson, J., and Lewis, J. T. (1997). Reliability of salt marshes as "Geochemical Recorder" of pollution input : A case study from contrasting estuaries in southern England. *Environmental Sciences & Technology*, 31:1093–1101.

Cushing, D. H., Humphrey, G. H., Banse, G. H., and Laevastu, T. (1981). Report of the committee on terms and equivalents. Rapport Proces-Verbal de réunion 36, Conseil International pour l'exploration de la mer.

Davidson, N. C., Laffoley, D. D., Doody, J. P., Gordon, L. S., Key, R., Pienkowski, M. W., Mitchell, R., and Duff, K. L. (1991). Nature conservation and estuaries in great britain. Technical report, Nature Conservation and estuaries in Great Britain.

Davies, J. H. (1964). A morphogenetic approach to world shorelines. *Z. Geomorphol.*, 8.

Desmit, X., Vandervorght, J. P., Regnier, P., and Wollast, R. (2005). Control of phytoplankton production by physical forcing in a strongly tidal, well-mixed estuary. *Biogeosciences Discussions*, 2:37–75.

Doron, M., Babin, M., Mangin, A., and Hembise, O. (2007). Estimation of light penetration, and horizontal and vertical visibility of oceanic and coastal waters from surface reflectance. *Journal of Geophysical Research*, 112(C06003):785–806.

Douglas, R. W. and Rippey, B. (2000). The random redistribution of sediment by wind in a lake. *Limnology and oceanography*, 45(3):686–694.

Duntley, S. Q. (1963). Light in the sea. *Journal of Optical Society America*, 53:214–233.

Dyer, K. R. (1973). *Estuaries A Physical Introduction*. Wiley, Chichester.

Dyer, K. R. (1975). Localized mixing of low salinity patches in a partially-mixed estuary (southampton water, england). In Helliwell, P. R. and Bossanyi, J., editors, *Estuarine Comparisons.Proceedings of the 6th International Estuarine Research Conference, Gleneden Beach, Oregon.*, pages 21–35, New-York. Academic Press.

Dyer, K. R. (1980). Sedimentation and sediment transport. In Burton, J. D., editor, *The Solent Estuarine System - an assessment of present knowledge*, number 22 in C, pages 36–43. N.E.R.C. Publication, Swindon.

Dyer, K. R. (1997). *Estuaries A Physical Introduction*. Wiley, Chichester.

Eppley, R. W. (1972). Temperature and phytoplankton growth in the sea. *Fisheries Bulletin*, 70:1063–1085.

Fasham, M. J. R., Ducklow, H. W., and McKelvie, S. M. (1990). A nitrogen-based model of plankton dynamics in the oceanic mixed layer. *Journal of Marine Research*, 48:591–639.

Fasham, M. J. R. and Evans, G. T. (1995). The use of optimization techniques to model marine ecosystem dynamics at the JGOFS station at 47N 20W. *Philosophical Transaction of the royal society of London B*, 348:203–209.

Fennel, K., Losch, M., Schroter, J., and Wenzel, M. (2001). Testing a marine ecosystem model: Sensitivity analysis and parameter optimization. *Journal of Marine Systems*, 28.

Ferreira, J. G., W. J. Wolff, T. C. S., and Bricker, S. B. (2005). Does biodiversity of estuarine phytoplankton depend on hydrology. *Ecological Modelling*, 187:513–523.

Figueiras, F., Jones, K., Mosquera, A., Alvarez-Salgado, X., Edwards1, A., and MacDougall, N. (1994). Red tide assemblage formation in an estuarine upwelling ecosystem: Ria de vigo. *Journal of Plankton Research*, 16(7).

Flather, R. A. (1978). Recent results from a storm surge prediction scheme for the north sea. In Nihoul, J. C. J., editor, *Marine Forecasting. Proceedings of the 10th International Liège Colloquium on Ocean Hydrodynamics*, pages 385–409, Amsterdam. Elsevier Oceanographic Series 25.

Flather, R. A. (1987). Estimates of extreme conditions of tide and surge using a numerical model of the north-west european continental shelf. *Estuarine, Coastal and Shelf Science*, 24:69–93.

Flather, R. A., Proctor, R., and Wolf, J. (1979). Oceanographic forecast models. In Farmer, D. G. and Rycroft, M. J., editors, *Computer Modelling in the Environmental Sciences*, pages 15–30, Oxford, UK. Clarendon Press.

Flather, R. G. (2000). Existing operational oceanography. *Coastal Engineering*, 41:13–40.

Friedrichs, C. T. and Aubrey, D. G. (1988). Non-linear tidal distortion in shallow well-mixed estuaries: A synthesis. *Estuarine, Coastal and Shelf Science*, 27:521–545.

Galloway, T. S., Brown, R. J., Browne, M. A., Dissanayake, A., Lowe, D., Johns, M. B., and Depledge, M. H. (2004). A multibiomarker approach to environmental assessment. *Environmental Sciences & Technology*, 38:1723–1731.

Galperin, B., Kantha, L., Hassid, S., and Rosati, A. (1988). A quasi-equilibrium turbulent energy model for geophysical flows. *Journal of Atmospheric Sciences*, 45(1):55–62.

Garcia, C. A. E., Purdie, D. A., and Robinson, I. S. (1993). Mapping a bloom of the photosynthetic ciliate *mesodinium rubrum* in an estuary from Airborne Thematic Mapper Data. *Estuarine, Coastal and Shelf Science*, 97(3):287–298.

Gattuso, J.-P., Gentilli, B., Duarte, C. M., Kleypas, J. A., Middelburg, J. J., and Antoine, D. (2006). Light availibility in the coastal ocean: Impact on the distribution of the benthic photosynthetic organisms and their contribution to primary production. *Biogeoscience*, 3:489–513.

Gazeau, F., Quibier, C., Jansen, J. M., Gattuso, J.-P., Middelburg, J. J., and Heip, C. H. R. (2007). Impact of elevated co_2 on shellfish calcification. *Geophysical Research Letters*, 34.

Gazeau, F., Smith, S. V., Gentili, B., Frankignoulle, M., and Gattuso, J.-P. (2004). The european coastal zone: Characterization and first assessment of ecosystem metabolism. *Estuarine, Coastal and Shelf Science*, 60.

Gillanders, B. M. and Kingsford, M. J. (2002). Impact of changes in flow of freshwater on estuarine and open coastal habitats and the associated organisms. In Gibson, R. N., Barnes, M., and Atkinson, R. J. A., editors, *Oceanography and Marine Biology: an Annual Review*, pages 233–309. Taylor and Francis.

Hansen, D. V. and Rattray, M. J. (1966). New dimensions in estuary classification. *Limnology and oceanography*, 11:319–326.

Hearn, C. J. and Robson, B. J. (2002). On the effects of wind and tides on the hydrodynamics of a shallow mediterranean estuary. *Estuarine, Coastal and shelf science*, 22:2655–2672.

Heip, C., Goosen, N., Herman, P. M. J., Kromkamp, J., Middelburg, J., and Soetaert, K. (1995). Production and consumption of biological particles in temperate tidal estuaries. In Ansell, A., Gibson, R., and Barnes, M., editors, *Oceanography Marine Biology: An Annual Review*, pages 1–149. UCL Press.

Henderson, P. A. (2007). Discrete and continuous change in the fish community of the bristol channel in response to climate change. *Journal of the marine biological Association U. K.*, 87:589–598.

Hirst, A. G. (1996). *Zooplankton production and energy flow towards a biological model of Southampton water*. PhD thesis, University of Southampton, Southampton,UK.

Hirst, A. G., Sheader, M., and Williams, J. A. (1999). Annual pattern of calanoid copepod abundance, prosome length and minor role in pelagic flux in the Solent, UK. *Marine Ecology Progress Series*, 177:133–146.

Hiscock, K. (1998). *Marine nature conservation review: Benthic marine ecosystem of Great Britain and the north-east Atlantic*. Joint Nature Conservation Commitee, Peterborough, UK.

Holley, S. E. and Hydes, D. J. (2002). 'ferry-boxes' and data stations for improved monitoring and resolution of eutrophication-related processes: application in Southampton Water UK, a temperate latitude hypernutrified estuary. *Hydrobiologia*, 475/476:99–110.

Holley, S. E., Purdie, D. A., Hydes, D. J., and Hartman, M. C. (2007). 5 years of plankton monitoring in southampton water and the solent including ferrybox, dock monitor and discrete sample data. Research and Consultancy Report 82, National Oceanography Centre, Southampton.

Holmes, R. W. (1970). The secchi disk in turbid coastal waters. *Limnology Oceanography*, 15:688–694.

Howard, A. G., Comber, S. D. W., Kifle, D., Antai, E. E., and Purdie, D. A. (1995). Arsenic speciation and seasonal changes in nutrient availability and microplankton abundance in southampton water. *Estuarine, coastal and shelf science*, 40:435–450.

Hulme, M., Jenkins, G. J., Lun, G. J., Turnpenny, X., Mitchell, J. R., Jones, T. D., Murphy, R. G. L. J. M., Hassell, D., Boorman, P., McDonald, R., and Hill, S. (2006). Climate change for the united kingdom: the UKCIP02 scientific report. Scientific report, Tyndall Centre for Climate Change Research, School of Environmental Sciences, University of East Anglia.

Hydes, D. (2000). Nutrients in the Solent. In Collins, M. and Ansell, K., editors, *Solent Science- A Review*, pages 135–148. Elsevier Science B.V.

Hydes, D. J., Holley, S. E., Xiong, J., Gall, A. C. L., Kelly-Gerreyn, B. A., Purdie, L. S. D. A., Bonner, R. N., O'Mahony, J. H. T., and Weeks, A. R. (2001). The southern nutrient study phase two : Sonus-2. Research and Consultancy Report 52, Southampton Oceanography Center.

Hydes, D. J. and Wright, P. N. (1999). Sonus: the southern nutrients study 1995-1997. Research and Consultancy Report 7, Southampton Oceanography Center.

Iriarte, A. and Purdie, D. A. (1994). Size distribution of chlorophyll a biomass and primary production in a temperate estuary (Southampton Water). *Marine Ecology Progress Series*, 115:283–297.

Iriarte, A. and Purdie, D. A. (2004). Factors controlling the timing of major spring bloom events in an UK south coastal estuary. *Estuarine, Coastal and Shelf Science*, 61(4):679–690.

Janzen, C. D. and Wong, K. (2002). Wind-forced dynamics of the estuary-shelf interface of a large coastal plain estuary. *Journal of Geophysical research*, 107(3138).

Jiang, M. and Zhou, M. (2006). The massachusetts and cape cod bays hydrodynamic model: 2002-2004 simulation. Report ENQUAD 2006-12, Massachusetts Water Resources Authority.

Jiang, W., Pohlmann, T., Sun, J., and Starke, A. (2004). Spm tranport in the bohai sea: Field experiments and numerical modelling. *Journal of Marine Systems*, 44:175–188.

Jones, J. E. and Davies, A. M. (2005). An intercomparison between finite difference and finite element(TELEMAC) approaches to modelling west coast of britain tides. *Ocean dynamics*, 55:178–198.

Jones, T. E. and Odd, N. V. M. (1995). Southampton water and associated estuaries. calibration and sensitivity testing of two-dimensional-in-depth water quality models. Report EX 3253, HR Wallingford.

Kelly-Gerreyn, B. A., Anderson, T. R., Holt, J. T., Gowen, R. J., and Proctor, R. (2004). Phytoplankton community structure at contrasting sites in the irish sea: a modelling investigation. *Estuarine and Coastal Shelf Science*, 59(3):363–383.

Kelly-Gerreyn, B. A., Hydes, D. J., Jégou, A. M., Lazure, P., Fernand, L. J., Puillat, I., and Garcia-Soto, C. (2006). Low salinity intrusions in the western english channel. *Estuarine, coastal and shelf science*, 26(11):1241–1257.

Kifle, D. (1992). *Seasonal and spatial variations in species composition, abundance, biomass and primary production of phytoplankton in Southampton Water*. PhD thesis, University of Southampton, Southampton,UK.

Kifle, D. and Purdie, D. A. (1993). The seasonal abundance of the phototrophic ciliate *mesodinium-rubrum* in Southampton Water, England. *Journal of Plankton research*, 15(7):823–833.

Kirk, J. T. O. (1981a). Monte-carlo procedure for simulating the penetration of light into natural waters. Technical Report 36, CSIRO (Australia), Division of Plant Industry Technical Paper.

Kirk, J. T. O. (1981b). A monte-carlo study of the nature of the underwater light field in, and the relationships between optical properties of turbid of, yellow waters. *Austrialian Journal of Marine and Freshwater Research*, 32:517–532.

Kirk, J. T. O. (1984). Dependance of relationship between inherent and apparent optical properties on solar altitude. *Limnology and oceanography*, 29(2):350–356.

Kirk, J. T. O. (1994). *Light and photosynthesis in aquatic ecosystems*. Cambridge University Press, Cambridge.

Koenings, J. P. and Edmundson, J. A. (1991). Secchi disk and photometer estimates of light regimes in alaskan lakes: Effects of yellow color and turbidity. *limnology and oceanography*, 36(1):91–105.

Koseff, L. V., Holen, J. K., Monismith, S. G., and Cloern, J. E. (1993). Coupled effects of vertical mixing and benthic grazing on phytoplankton populations in shallow, turbid estuaries. *Journal of Marine Research*, 25(4A):497–507.

Kourafalou, V. H., Lee, T. N., Oey, L.-Y., and Wang, J. D. (1996). The fate of river discharge on the continental shelf 2. Transport of coastal low-salinity waters under realistic wind and tidal forcing. *Journal of Geophysical Research*, 101(C2):3435–3455.

Kratzer, S., Buchan, S., and Bowers, D. G. (2003). Testing long-term trends in turbidity in the menai strait, north wales. *Estuarine, coastal and shelf science*, 56:221–226.

Krishnakumar, K. (1989). Micro-genetic algorithms for stationary and non-stationary function optimization. *Intelligent Control and Adaptative System*, 1196.

Kropotov, S. I. (1985). The effect of observational conditions upon the accuracy of determination of water transparency, using a secchi disc. *Physical Oceanography*, 9(3):191–198.

Lauria, M. L. (1998). *Physical constraints on phytoplankton in estuaries and shallow coastal waters*. PhD thesis, University of Southampton, Southampton,UK.

Lauria, M. L., Purdie, D. A., and Sharples, J. (1998). Constrating phytoplankton distributions controlled by tidal turbulence in an estuary. *Journal of Marine Systems*, 21:189–197.

Le Pape, O., Holley, J., Guérault, D., and Désaunay, Y. (2003). Quality of coastal and estuarine essential fish habitats: estimations based on the size of juvenile common sole (*solea solea* l. *Estuarine, Coastal and Shelf Science*, 58.

Lee, Z.-P., Darecki, M., Carder, K. L., Davis, C. O., Stramski, D., and Rhea, W. J. (2005). Diffuse attenuation coefficient of downwelling irraidiance: An evaluation of remote sensing methods. *Journal of Geophysical Research*, 110(C02017):785–806.

Li, M., Zhong, L., and Boicourt, W. C. (2005). Simulations of chesepeake bay estuary: Sensitivity to turbulence mixing parameterizations and comparison with observations. *Journal of Geophysical Research*, 110(C12004).

Liu, W.-C. (2005). Water column light attenuation estimation to simulate phytoplankton population in tidal estuary. *Environmental Geology*, 49:280–292.

Lizon, F., Seuront, L., and Lagadeuc, Y. (1998). Photoadaptation and primary production study in tidally mixed coastal waters using a lagrangian model. *Marine Ecology Progress series*, 169.

Lloyd-Jones, D. (2002). *An investigation into the temporal variability of estuarine suspended sediments*. PhD thesis, Nottingham Trent University, Southampton,UK.

Lockwood, A. P. M. (1984). Southampton water and the solent : Biological effects of the multi-use of an estuarine system. In *La Baie de Seine (GRECO-MANCHE) - Université de Caen, 24-26 avril 1985 Actes de Colloques*, pages 421–430. IFREMER.

Lomas, M. W., Glibert, P. M., Shiah, F., and Smith, E. M. (2002). Microbial process and temperature in chesapeake bay: Current relationships and potential impacts of regional warming. *Global Chnage Biology*, 8.

Lowthion, D., Soulsby, P. G., and Houston, M. C. M. (1985). Investigation of a eutrophic tidal basin: Part 1 - factors affecting the distribution and biomass of macroalgae. *Marine Environmental Research*, 15:263–284.

Lozano, I., Devaoy, R. J. N., May, W., and Andersen, U. (2004). Storminess and vulnerability along the atlantic coastlines of europe: Analysis of storm records and of a grenhouse gases induced climate scenario. *Marine Geology*, 210:205–225.

Lucas, L. V. and Cloern, J. E. (2002). Effects of tidal shallowing and deepening on phytoplankton production dynamics: A modelling study. *Estuaries*, 25(4A):497–507.

Lucas, L. V., Cloern, J. E., Koseff, J. R., Monismith, S. G., and Thompson, J. K. (1998). Does the sverdrup critical depth model explain bloom dynamics inestuaries ? *Journal of Marine Research*, 56:375–415.

Lucas, L. V., Koseff, J. R., Cloern, J. E., Monismith, S. G., and Thompson, J. K. (1999a). Processes governing phytoplankton blooms in estuaries. I: The local production-loss balance. *Marine Ecology Progress Series*, 187:1–15.

Lucas, L. V., Koseff, J. R., Monismith, S. G., Cloern, J. E., and Thompson, J. K. (1999b). Processes governing phytoplankton blooms in estuaries. II: The role of horizontal transport. *Marine Ecology Progress Series*, 187:17–30.

May, C. L., Koseff, J. R., Lucas, L. V., Cloern, J. E., and Schoellhamer, D. H. (2003). Effects of spatial and temporal variability of turbidity on phytoplankton blooms. *Marine Ecology Progress Series*, 254:111–128.

May, S. (2000). Saltmarsh monitoring studies adjacent to the fawley refinery. In Collins, M. and Ansell, K., editors, *Solent Science- A Review*, pages 303–305. Elsevier Science B.V.

McLusky, D. S. (1999). Estuarine benthic ecology: A european perspective. *Australian Journal of Ecology*, 24:302–311.

McLusky, D. S. and Eliott, M. (2004). *The estuarine ecosystem. Ecology, Threats and Management.* Oxford University Press, Oxford.

Mellor, G. L. (2004). Users guide for a three-dimensional, primitive equation, numerical ocean model. Technical report, Princeton University.

Mellor, G. L. and Yamada, T. (1974). A hierarchy of turbulence closure models for planetary boundary layer. *Journal of Atmospheric Sciences*, 31:1791–1806.

Mellor, G. L. and Yamada, T. (1982). Development of a turbulence closure model for geophysical fluid problems. *Review of geophysics and space physics*, 20:851–875.

Michaelis, L. and Menten, M. I. (1913). Die kinetik der invirtinwirkung. *Biochemische Zeitschrift*, 49:333–369.

Millero, F. and Poisson, A. (1981). International one-atmosphere equation of seawater. *Deep-Sea Research*, A28(6):625–629.

Mobley, C. D. (1996). *Light and Water. Radiative transfer in Natural Waters.* Academic Press, San Diego.

Montgomery, H. A. C., Soulsby, P. G., Hart, I. C., and Wright, S. L. (1985). Investigation of a eutrophic tidal basin: Part 2 - nutrients and environmental aspects. *Marine Environmental Research*, 15:285–302.

Morel, A., Huot, Y., Gentili, B., Wedell, P. J., Hooker, S. B., and Franz, B. A. (2007). Examining the consistency of products derived from various ocean color sensors in open ocean (case 1) waters in the perspective of a multi-sensor approach. *Remote sensing of environment*, 111:69–88.

Mueller, J. L. (2000). Seawifs algorithm for the diffuse attenuation coefficient, k(490), using water-leaving radiances at 490 and 555nm. In Hooker, S. B., editor, *SeaWiFS Postlaunch Calibration and Validation Analyses*, pages 24–27. NASA Goddard SPace Flisht Center.

Muxagata, J. N. (2005). *Seasonal and spatial distribution of the mesozooplankton of Southampton Water with particular reference to the contribution of copepods and barnacle larvae to pelagic carbon flux*. PhD thesis, University of Southampton, Southampton,UK.

Nicholls, R. J., Wong, P. P., Burkett, V. R., J. O. Codignotto, J. E. H., McLean, R. F., Ragoonaden, S., and Woodroffe, C. D. (2007). Coastal systems and low-lying areas. In Parry, M. L., Canziani, O. F., Palutikof, J. P., van der Linden, P. J., and Hanson, C., editors, *Climate Change 2007: Impacts, Adaptation and Vulnerability. Contribution of Working Group II to the Fourth Assessment Report of the Intergovernmental Panel on Climate Change*, pages 315–356. Cambridge University Press, Cambridge,UK.

Nixon, S. W. (1995). Coastal marine eutrophication: a definition, social causes and futures concerns. *Ophelia*, 41.

Olesen, B. (1996). Regulation of light attenuation and eelgrass *zostera marina* depth distribution in a danish embayment. *Marine Ecology Progress Series*, 134:187–194.

O'Mahony, J. and Weeks, A. (2000). Phytoplankton - Annual sequences in the Hamble estuary. In Collins, M. and Ansell, K., editors, *Solent Science- A Review*, pages 287–294. Elsevier Science B.V.

Paphitis, D. and Collins, M. B. (2005). Sediment resuspension events within the (microtidal) coastal waters of thermaikos gulf, northern greece. *Continental Shelf Research*, 25:2350–2365.

Paphitis, D., Velegrakis, A. F., and Collins, M. B. (2000). Residual circulation and associated sediments dynamics in the eastern approaches to the solent. In Collins, M. and Ansell, K., editors, *Solent Science- A Review*, pages 36–43. Elsevier Science B.V.

Park, K. and Kuo, A. Y. (1996). Effect of variation in vertical mixing on residual circulation in narrow, weakly nonlinear estuary. In Aubrey, D. G. and Friedrichs, C. T., editors, *Coastal and Estuarine Studies*, pages 301–317. American Geophysical Union.

Pawlowicz, R., Beardsley, B., and Lentz, S. (2002). Classical tidal harmonic analysis including error estimates in matlab using T_TIDE. *Computers Geosciences*, 28:929–937.

Phillips, A. J. (1980). Distribution of chemical species. In Burton, J. D., editor, *The Solent Estuarine System - an assessment of present knowledge*, number 22 in C, pages 44–61. N.E.R.C. Publication, Swindon.

Pittam, N. A. (2004). Long-term marine environmental site monitoring: focus on defining background solid suspended levels. In Abbott, V. J. and Atkinson, H. L., editors, *Proceedings of hydro4: 14th Biennal International Symposium of the Hydrographic Society (International Federation of Hydrographic Societies) 'Diversity'*, pages 1–9. Hydrographic Society. paper 21.

Popova, E. E., Fasham, M. R., Opipov, A. V., and Ryabchenko, V. A. (1997). Chaotic behaviour of an ocean ecosystem model under seasonal external forcing. *Journal of Plankton Research*, 19(10):1495–1515.

Preisendorfer, R. W. (1961). Application of radiative transfer theory to light measurements in the sea. In *Symposium on Radiant Energy in the Sea, International Union of Geodesy and Geophysics*, pages 11–30, Paris. L'institut Géographique National. Monograph No. 10.

Preisendorfer, R. W. (1986). Secchi disk science: Visual optics of natural waters. *Limnology and Oceanography*, 31(5):909–926.

Price, D. and Townend, I. (2000). Hydrodynamic, sediment process and morphological modelling. In Collins, M. and Ansell, K., editors, *Solent Science- A Review*, pages 199–204. Elsevier Science B.V.

Pugh, D. T. (1996). *Tides Surges and Mean Sea Level A Handbook for Engineers and Scientists*. Wiley, Chichester.

Raven, J., Caldeira, K., Elderfield, H., Hoegh-Guldberg, O., Liss, P., Riebesell, U., Shepherd, J., Turley, C., and Watson, A. (2005). Ocean acidification due increasing carbon dioxide. Policy Document 12/05, Royal Society.

Redfield, A. C., Ketchum, B. H., and Richards, F. A. (1963). The influence of organisms on the composition of seawater. In Hill, M. N., editor, *The Sea*, volume 2, pages 26–77. John Wiley, New York.

Ribeiro, C. H. A. (2004). *Temporal variability of the gravitational circulation in a partially-mixed estuary*. PhD thesis, University of Southampton, Southampton,UK.

Ribeiro, C. H. A., Waniek, J. J., and Sharples, J. (2004). Observations of the spring-neap modulation of the gravitational circulation in a partially-mixed estuary. *Ocean Dynamics*, 54:299–306.

Riddle, A. M. and Lewis, R. E. (2000). Dispersion experiments in u. k. coastal waters. *Estuarine, Coastal and Shelf Science*, 51:243–254.

Riebersell, U., Zondervan, I., Rost, B., Tortell, P. D., Zeebe, R. E., and Morel, F. M. M. (2000). Reduced calcification of marine plankton in response to increased atmospheric co_2. *Geophysical Research Letters*, 34.

Ross, O. N. (2004). *Algal motility in variable turbulence*. PhD thesis, University of Southampton, Southampton,UK.

Salomon, J.-C. and Breton, M. (1993). An atlas of long-term currents in the channel. *Oceanologica Acta*, 16:439–448.

Samiaji, J. (2001). *The ecology of Zostera noltii bed ecosystem in the Solent*. PhD thesis, University of Southampton, Southampton,UK.

Savari, A., Lockwood, A. P. M., and Sheader, M. (1985). Effects of season and size (age) on heavy metal concentrations of the common cockle *cerasoderma edule l.* from southampton water. *Journal of molluscan studies*, 15:45–57.

Schartau, M. (2001). *Data-assimilation studies of marine, nitrogen-based, ecosystem models in the North Atlantic Ocean*. PhD thesis, Naturwissenschaftliche Fakultät des Christian-Albrechts-Universität zu Kiel, Kiel, Germany.

Schartau, M. and Oschlies, A. (2003). Simultaneous data-based optimization of a 1d-ecosystem model at three locations in the North Atlantic: Part I - methods and parameters estimates. *Journal of Marine Research*, 61(6).

Schwarz, J. N. (2002). *The use of spectral resolution in situ optical data for monitoring Case II (coastal) water quality*. PhD thesis, University of Southampton, Southampton,UK.

Scully, M. E., Friedrichs, C., and Brubaker, J. (2005). Control of estuarine stratification and mixing by wind-induced straining of the estuarine density field. *Estuaries*, 28(3):321–326.

Sharples, J. (2000). Water circulation in Southampton Water and the Solent. In Collins, M. and Ansell, K., editors, *Solent Science- A Review*, pages 45–53. Elsevier Science B.V.

Sharples, J. and Simpson, J. H. (1995). Semi-diurnal and longer period stability cylces in the liverpool bay region of freshwater influence. *Continental Shelf Research*, 15(2/3):295–313.

Shi, L. (1996). A three-dimensional model of estuarine and coastal sea with a hybrid method of fractional steps. *Journal of University of Qingdao*, 10:396–404. In Chinese, with English abstr.

Shi, L. (2000). *Development and Application of a three-dimensional Water quality Model in a partially Mixed Estuary, Southampton Water, UK*. PhD thesis, University of Southampton, Southampton, UK.

Shi, L. and Pangen, X. (1995). A hybrid method of fractional steps for numerical solution of three-dimensional hydrodynamical equations for estuarine and coastal seas. *Journal of University of Qingdao*, 25(2):162–172. In Chinese, with English Abstr.

Shi, L. and Purdie, D. (2000). M2 tidally-induced water mass transport and water exchange in Southampton Water and the Solent. In Collins, M. and Ansell, K., editors, *Solent Science- A Review*, pages 1999–204. Elsevier Science B.V.

SigmaPlot 9 User's guide (1998). *SigmaPlot 9 User's guide*. SPSS Inc. Chicago, Illinois, USA.

Simpson, J. H., Brown, J., Matthews, J. P., and Allen, G. (1990). Tidal straining, density currents and stirring in the control of estuarine stratification. *Estuaries*, 12:129–132.

Simpson, J. H., Burchard, H., Fisher, N., and Rippeth, T. P. (2002). The semi-diurnal cycle of dissipation in a rofi: model-measurement comparisons. *Continental Shelf Research*, 22:1615–1628.

Small, C. and Nicholls, R. J. (2003). A global analysis of human settlement in coastal zones. *Journal of Coastal Research*, 19:584–599.

Smith, E. L. (1936). Photosynthesis in relation to light and carbon dioxide. In *Proc. Nat. Acad. Sci.*, 22, pages 504–511, U.S.A.

Sommer, U. (1994). Are marine diatoms favoured by high Si:N ratios ? *Marine Ecology Progress Series*, 115:309–315.

Spitz, Y. H., Moisan, J. R., Abbott, M. R., and Richman, J. G. (1998). Data assimilation and a pelagic ecosystem ecosystem model: Parameterization using time series observations. *Journal of Marine System*, 16:51–68.

Statham, P. J. (2000). Trace metals in water, sediments and biota of the Solent system. In Collins, M. and Ansell, K., editors, *Solent Science- A Review*, pages 149–161. Elsevier Science B.V.

Sylaios, G. and Boxall, S. R. (1998). Circulation and mixing of a partially-mixed estuary. In *Physics of Estuaries and Coastal Seas*, pages 47–54. Dronkers and Scheffers.

Taylor, R., Fletcher, R. L., and Raven, J. A. (2001). Preliminary studies on the growth of selected 'green algae in laboratory culture: Effects of irradiance, temperature and nutrient on growth rate. *Botanica Marina*, 44(4):327–336.

Teles, A. P. D. S. (2003). *Tidal assymetry influence on sediment dynamics: The Solent Region*. PhD thesis, University of Southampton, Southampton,UK.

Torres-Valdés, S. (2004). *The Effect of Phytoplankton Growth on Nitrogen Cycling in a non-Turbing Estuary, Southampton Water, UK*. PhD thesis, University of Southampton, Southampton, UK.

Torres-Valdés, S. and Purdie, D. A. (2006). Nitrogen removal by phytoplankton uptake through a temperate non-turbid estuary. *Estuarine, Coastal and Shelf Science*, 70(3):473–486.

Townsend, D. W., Cammen, L., Holligan, P. M., Campbell, D. E., and Pettigrew, N. R. (1994). Causes and consequences of variability in the timing of spring phytoplankton blooms. *Deep-Sea Research I*, 41:747–765.

Tsimplis, M. N., Shaw, A. G. P., Flather, R. A., and Woolf, D. K. (2006). The influence of the north atlantic oscillation on the sea-level around the northern european coasts reconsidered: the thermosteric effects. *Philosophical Transactions of the Royal Society of London series A*, 364(1841):845–856.

Tyler, J. E. (1968). The secchi disk. *Limnology and oceanography*, 13:1–6.

Uncles, R. J. and Stephens, J. A. (1997). Dynamics of turbidity in the tweed estuary. *Estuarine, coastal and shelf science*, 45:745–758.

Uncles, R. J., Stephens, J. A., and Smith, R. E. (2002). The dependance of estuarine trubidity on tidal intrusion length, tidal range and residence time. *Continental Shelf Research*, 22:1835–1856.

Velegrakis, A. F. (2000). Geology, geomorphology and sediments of the Solent system. In Collins, M. and Ansell, K., editors, *Solent Science- A Review*, pages 21–43. Elsevier Science B.V.

Velegrakis, A. F., Dix, J. K., and Collins, M. B. (1999a). Late quarternary evolution of the upper reaches of the solent river, southern england, based upon marine geophysical evidence. *Journal of the Geological Society of London*, 156:73–87.

Velegrakis, A. F., Dix, J. K., and Collins, M. B. (2000). Late pleistocene/holocene evolution of the upstream section of the Solent river. In Collins, M. and Ansell, K., editors, *Solent Science- A Review*, pages 97–99. Elsevier Science B.V.

Velegrakis, A. F., Michel, D., Collins, M. B., Lafite, R., Oikonomou, E. K., Dupont, J.-P., Lecouturier, M. F. H. M., Salomon, J. C., and Bishop, C. (1999b). Sources, sinks and resuspension of suspended particulate matter in the eastern English Channel. *Continental Shelf Research*, 19:1933–1957.

Wang, J., Cheng, R. T., and Smith, P. C. (1998). Seasonal sea-level variations in san francisco bay in response to atmospheric forcing, 1980. *Estuarine coastal and shelf science*, 45:39–52.

Ward, P. R. B. (1979). Seiches, tides and wind set-up in lake kariba. *Limnology and Oceanography*, 24(1):151–157.

Webber, N. B. (1975). The tidal hydraulic of the solent and its estuaries. In Helliwell, P. R. and Bossanyi, J., editors, *Pollution criteria for estuaries*, 5, pages 1–27, London. Pentech Press.

Webber, N. B. (1980). Hydrography and water circulation in the Solent. In Burton, J. D., editor, *The Solent Estuarine System - an assessment of present knowledge*, number 22 in C, pages 25–35. N.E.R.C. Publication, Swindon.

Weeks, A. R., Simpsons, J. H., and Bowers, D. (1993). The relationship between concentrations of suspended particulate material and tidal processes in the irish sea. *Continental Shelf Research*, 13(12):1325–1334.

Wells, N. C., Baldwin, D., and Haigh, I. (2004). Seiches induced by storms in the english channel. *Journal of Atmosphere and Ocean Science*, 10:1–16.

Wells, N. C., Baldwin, D. J., Wang, J. Y., and Collins, M. B. (2001). Modelling of extreme storm surge events in the english channel for the period 14-18 december 1989. *Global Atmosphere and Ocean system*, 7(4):275–294.

White, M., Gaffmey, S., Bowers, D. J., and Bowyer, P. (2003). interannual variability in irish sea turbidity and relation to wind strength. In *Proceedings of the royal irish academy*, volume 103B, pages 83–89. Royal Irish Academy. No 2.

William, J. A. (1996). Bloom of *mesodinium rubrum* in Southampton Water-do they shape mesozooplankton distribution. *Journal of Plankton research*, 18(9):1685–1697.

Wolanski, E. (2007). *Estuarine Ecohydrology*. Elsevier, Amsterdam,.

Wolf, J., Wakelin, S. L., and Flather, R. A. (2002). Preliminary wave model results of climate change effects at the coast. In *Proceedings of The Twelfth International Offshore and Polar Engineering Conference*, pages 135–142. The International Society of Offshore and Polar Engineers.

Wong, K. and Valle-Levinson, A. (2002). On the relative importance of the remote and local wind effects on the subtidal exchange at the entrance to the chesapeake bay. *Journal of Marine Research*, 60:477–498.

Wright, P. N., Hydes, D. J., Lauria, M., Sharples, J., and Purdie, D. A. (1997). Data-buyo measurements of phytoplankton dynamics in Southampton Water, UK a temperate latitude estuary with high nutrient input. *German Journal of Hydrobiology*, 49(2/3):203–211.

Wu, J. and Chen, K. (1985). A hybrid method of fractional steps with L∞ -stability for numerical modelling of harbours and bays. In *International Conference on Numerical and Hydraulic Modelling of Ports and Harbours*, Birmingham, UK.

Xu, J., Hood, R. R., and Chao, S.-Y. (2005). A simple empirical optical model for simulating light attenuation variability in a partially mixed-estuary. *Estuaries*, 28(4):572–580.

Yanenko, N. N. (1971). *The method of fractional steps, the solution sof problems of mathematical physics in several variables*. Springer. translated from russian.

Zakardjian, B. A., Gratton, Y., and Vézina, A. F. (2000). Late psrig phytoplankton bloom in the lower st. lawrence estuary: the flushing hypothesis revisited. *Marine Ecology Progress Series*, 192.

Zinger, I. (1989). *Zooplankton community structure in Southampton Water an its potential response to estuary chronic oil pollution*. PhD thesis, University of Southampton, Southampton, UK.